



UTS

**UNIVERSITY
OF TECHNOLOGY
SYDNEY**

Faculty of Engineering & Information Technology

**CONDITION MONITORING OF
WOUND-ROTOR INDUCTION
MACHINES**

A thesis submitted for degree of

Doctor of Philosophy

AHMAD A. SALAH

October 2018



UTS

UNIVERSITY
OF TECHNOLOGY
SYDNEY

School of Electrical and Data Engineering
Faculty of Engineering & Information Technology

CONDITION MONITORING OF WOUND-ROTOR INDUCTION MACHINES

Done by: AHMAD A. SALAH

Supervisor: A/Prof. Youguang Guo

Co-supervisor: A/Prof. Li Li

External supervisor: Prof. David Dorrell

Course code: C02018

Subject Number: 49986 Doctor of Philosophy (PhD)

Dates: 10/08/2014 to 25/09/2018

University of Technology Sydney (UTS)

P.O. Box 123, Broadway, Ultimo, N.S.W. 2007

Australia

Certificate

I certify that the work in this thesis has not previously been submitted for a degree nor has it been submitted as part of requirements for a degree except as part of the collaborative doctoral degree and/or fully acknowledged within the text.

I also certify that the thesis has been written by me. Any help that I have received in my research work and the preparation of the thesis itself has been acknowledged. In addition, I certify that all information sources and literature used are indicated in the thesis.

Signature of Student:

Production Note:
Signature removed prior to publication.

Date: 25 September 2018

Acknowledgements

بِسْمِ اللَّهِ الرَّحْمَنِ الرَّحِيمِ
فَإِنَّ مَعَ الْعُسْرِ يُسْرًا (٥) إِنَّ مَعَ الْعُسْرِ يُسْرًا (٦) [سورة الشرح]
For indeed, with hardship [will be] ease (5). Indeed, with hardship [will be] ease (6).
[Quran, The Soothing/ash-Sharh 94]

First and foremost, my sincere thanks go to Allah, who has endowed me to complete this PhD degree. The research has been mainly financed by AL-Hussein bin Talal University, Ma'an, Jordan. Thanks must be made to them for their financial support of this project.

I would like to take this opportunity to thank the following people and organisations for their assistance and support during my candidature. My supervisor, Associate Professor Youguang Guo, has provided me invaluable knowledge and guidance, and together with external-supervisor, Professor David Dorrell, have guided me through this research and supported my work.

Most importantly, my wife, Nour, who is always by my side and helps me through thick and thin; I could not have done this without you. Of course, my family's advice and encouragement are indispensable. Last but not least, my UTS colleagues' knowledge, advice, and experience have encouraged me to do better and better, through this journey. Mohammad Shalby, Omar Elshaweesh, Sari Awwad, Mohamed Awadallah and many others were along the way.

Abstract

Condition monitoring enables diagnosis of the inception of fault mechanisms in electrical machines, thus averting failure and the need of expensive repairs. Therefore, it is valuable to develop efficient methods of condition monitoring. The idea would be relatively low cost and/or non-invasive system, which is still sufficiently powerful in terms of monitoring by online detection of developing faults. In this research, an overview of existing condition monitoring techniques is given, and issues related to induction machine faults are discussed. Therefore, this research develops a relatively simple yet powerful model for studying the behaviour of a wound rotor induction machine (WRIM) or doubly fed induction generator (DFIG) in healthy and faulty conditions based on the impedance matrix.

The first part of the work presented in this dissertation builds the fundamental impedance matrix that can predict the behaviour of the WRIM or DFIG in a healthy condition. A theoretical model is necessary so that any stator or rotor winding configuration in the machine can be incorporated. The effect of rotor skew is considered in this model. Then, the Motor-CAD package is employed to predict the electromagnetic behaviour of the induction machine during steady-state and transient-state operation. Motor-CAD has been used for examining the induction machine parameters.

The second part of the work develops the impedance matrix to detect unbalanced rotor-phase impedances. This can simulate rotor faults in the machine. The method leads to the calculation of stator current components when there are unbalanced rotor-phase impedances and it is verified experimentally using a four-pole wound rotor. The method is verified by inversion of the voltage matrix equation and solving for the currents in the

wound motor. Experimental results (torque and current characteristic) are compared with computer predictions for the test machine.

The third part of this thesis develops the fundamental impedance matrices for both rotor eccentricity detection and unbalanced magnetic pull (UMP) calculation. It puts forward a concept for detecting and measuring eccentricity faults in the WRIM. A simple and new approach using pole-specific search coils is introduced, and a theory is developed to illustrate that rotor eccentricity leads to the generation of air-gap flux waves with pole-pairs of $p_m \pm 1$, where p_m is the number of pole-pairs of the machine. Once again, this technique is used here to detect rotor eccentricity in a four-pole wound rotor machine and is verified experimentally using a rig for measuring UMP. The investigation uncovers several aspects of the damping effects of pole-specific search windings which can also be used to suppress UMP.

Keywords— Condition monitoring; doubly fed induction generator; DFIG; eccentric rotors; impedance matrix; induction motor; rotor eccentricity; squirrel cage induction machine; SCIM; unbalanced magnetic pull; UMP; wound rotor induction machine; WRIM.

Table of Contents

| | |
|-------------------------------------------------------------|------------|
| CONDITION MONITORING OF WOUND-ROTOR INDUCTION MACHINES | i |
| Doctor of Philosophy | i |
| CERTIFICATE | I |
| ACKNOWLEDGEMENTS..... | II |
| ABSTRACT | III |
| TABLE OF CONTENTS..... | V |
| LIST OF FIGURES | IX |
| LIST OF TABLES | XV |
| ACRONYMS AND ABBREVIATIONS..... | XVI |
| CHAPTER 1: INTRODUCTION..... | 1 |
| 1.1 Project Statement | 2 |
| 1.2 Project Objectives | 2 |
| 1.3 Structure of the Thesis | 3 |
| 1.4 Publications from this Thesis Work..... | 6 |
| 1.5 Novelties of the Project..... | 7 |
| CHAPTER 2: BACKGROUND AND LITERATURE REVIEW..... | 10 |
| 2.1 Introduction..... | 10 |
| 2.2 Basic Principles of the Induction Machines..... | 11 |
| 2.3 Operating Induction Machine in DFIG Mode..... | 20 |
| 2.4 Induction Motor Faults..... | 25 |
| 2.4.1 Bearing Faults | 27 |
| 2.4.2 Stator Faults | 28 |
| 2.4.3 Rotor Faults..... | 29 |
| 2.4.4 Rotor Eccentricity Fault | 30 |
| 2.5 Condition Monitoring of the Induction Machine..... | 32 |
| 2.6 Existing Condition Monitoring Techniques..... | 34 |
| 2.6.1 Current Monitoring | 35 |
| 2.6.2 Thermal Monitoring..... | 38 |
| 2.6.3 Vibration Monitoring | 39 |
| 2.6.4 Flux Monitoring | 40 |

| | | |
|--------------------------------------------------------------|-------------------------------------------------------------------------|-----------|
| 2.6.5 | Air-gap Torque Monitoring..... | 42 |
| 2.7 | Literature Review of Wound-Rotor Faults | 42 |
| 2.8 | Literature Review of Air-gap Eccentricity..... | 44 |
| 2.8.1 | Air-gap Eccentricity and UMP Calculation..... | 44 |
| 2.8.2 | Reduction of UMP | 47 |
| 2.9 | Literature Review Observations..... | 49 |
| 2.10 | Chapter Summary..... | 51 |
| CHAPTER 3: MACHINE MODELING BY IMPEDANCE MATRIX | | 52 |
| 3.1 | Introduction | 52 |
| 3.2 | Harmonic Field Analysis..... | 54 |
| 3.2.1 | Harmonic Conductor Density Distribution | 54 |
| 3.2.2 | Differences in the Rotor Current of SCIM and WRIM..... | 57 |
| 3.2.3 | Co-ordinate System of the Wound Rotor Induction Machine | 59 |
| 3.2.4 | The Flux Density Produced by Stator and Rotor Current Distribution..... | 61 |
| 3.3 | Impedance Matrix | 64 |
| 3.3.1 | Stator-Stator Coupling Impedance | 67 |
| 3.3.2 | Stator-Rotor Coupling Impedance | 68 |
| 3.3.3 | Rotor-Stator Coupling Impedance | 69 |
| 3.3.4 | Rotor-Rotor Coupling Impedance..... | 70 |
| 3.4 | Voltage Equations | 71 |
| 3.5 | Power and Torque Calculation..... | 72 |
| 3.6 | Wound-Rotor Equivalent Circuit | 74 |
| 3.7 | Inclusion of Rotor External Circuits | 76 |
| 3.8 | Chapter Summary..... | 80 |
| CHAPTER 4: PERFORMANCE ESTIMATION OF THE HEALTHY | | |
| MACHINE USING MATLAB..... | | 81 |
| 4.1 | Introduction to Motor-CAD | 81 |
| 4.2 | Induction Machine in Motor-CAD | 82 |
| 4.3 | Implementation of Induction Machine in Motor-CAD..... | 83 |
| 4.4 | Electromagnetic Model of Induction Machine | 87 |
| 4.5 | Machine Geometry..... | 91 |
| 4.6 | Implementation of Induction Machine in MATLAB..... | 92 |

| | | |
|-----------------------------------------------------------|--------------------------------------------------------------------------|-----|
| 4.7 | Simulation Results | 94 |
| 4.8 | Chapter Summary..... | 95 |
| CHAPTER 5: STUDY OF WOUND ROTOR INDUCTION MACHINES | | |
| INCLUDING ROTOR ASYMMETRY | | |
| 97 | | |
| 5.1 | Rotor Fault Analysis | 97 |
| 5.2 | Rotor Faults Detection Using Impedance Matrix | 99 |
| 5.2.1 | Coupling and Mutual Impedances Including General Rotor Asymmetry | 100 |
| 5.2.2 | Determination of Backward Components of Currents and Torque | 102 |
| 5.2.3 | Wound Rotor-Equivalent Circuit with Backward Components | 103 |
| 5.3 | Simulation of Wound Rotor Faults Using MATLAB..... | 105 |
| 5.3.1 | Implementation of Wound Rotor Faults | 105 |
| 5.3.2 | Results of Implementation of Wound Rotor Faults | 106 |
| 5.4 | Experimental Work and Results | 114 |
| 5.4.1 | Experimental Test Set-up and Testing Procedure..... | 114 |
| 5.4.2 | Results and Discussion..... | 117 |
| 5.5 | Chapter Summary..... | 121 |
| CHAPTER 6: STUDY OF WOUND ROTOR INDUCTION MACHINES | | |
| INCLUDING AIR-GAP ECCENTRICITY FAULT | | |
| 123 | | |
| 6.1 | Analysis of Air-gap Flux Changes Due to Eccentricity in Wound-Rotor | 123 |
| 6.2 | Variation of Air-gap Length Due to Eccentricity | 125 |
| 6.3 | Non-uniform Static Eccentricity | 127 |
| 6.4 | Permeance Harmonic Analysis | 129 |
| 6.5 | Generation of Additional Air-gap Flux Waves..... | 130 |
| 6.6 | Calculation of UMP Forces..... | 134 |
| 6.7 | New Approach to Eccentricity Detection Depending on Specific Search | |
| | windings | 140 |
| 6.7.1 | Eccentricity Detection..... | 142 |
| 6.7.2 | Development of the Impedance Matrix for Condition Monitoring..... | 143 |
| 6.7.3 | Development of the Impedance Matrix for UMP Control..... | 145 |
| 6.8 | Experimental Work Using New Test Rig | 148 |
| 6.8.1 | Laboratory Test Equipment..... | 148 |
| 6.8.2 | Implementation of Air-gap Eccentricity | 152 |

| | | |
|------------------------------------------------------------------------|------------------------------------------------------------------------|------------|
| 6.8.3 | Implementation of Auxiliary Windings | 153 |
| 6.8.4 | Measurement Setup and Testing Procedure | 155 |
| 6.8.5 | The Main Features of the Experimental Setup..... | 157 |
| 6.9 | Results and Discussion..... | 158 |
| 6.9.1 | Separate Static and Dynamic Eccentricity in the Test Machine | 160 |
| 6.9.2 | Separating Torque and UMP in the Test Machine..... | 162 |
| 6.9.3 | Non-constant Eccentricity and the Net Force Direction | 162 |
| 6.9.4 | Variation of UMP with Eccentricity for the Test Machine..... | 164 |
| 6.9.5 | Induced Voltages in the Simple Search Coils | 165 |
| 6.9.6 | Induced Voltages in the Functional Search Coils | 167 |
| 6.9.7 | Investigation on Non-constant Eccentricity | 170 |
| 6.9.8 | Production of Effective Damper Windings..... | 173 |
| 6.9.9 | Copper Losses in the Damper Windings..... | 176 |
| 6.9.10 | The Vibration Measurements..... | 177 |
| 6.9.11 | Investigation of Injecting a DC Current in the Auxiliary Windings..... | 179 |
| 6.10 | Chapter Summary..... | 180 |
| CHAPTER 7: CONCLUSIONS AND SUGGESTIONS FOR FURTHER | | |
| WORK | | 182 |
| 7.1 | Summary and Conclusions..... | 182 |
| 7.2 | Further Work..... | 185 |
| Appendix A : Internet Multimedia..... | | 187 |
| A.1 | Thesis Softcopy | 187 |
| A.2 | Thesis Figures | 187 |
| A.3 | Lab Videos and Photos | 187 |
| Appendix B : Rotor Skew..... | | 188 |
| Appendix C : Machine Specifications | | 189 |
| Appendix D : Induction Machine Equivalent Circuit Parameters | | 197 |
| D.1 | Stator and Rotor Resistances..... | 197 |
| D.2 | No load Test | 197 |
| D.3 | Locked Rotor Test..... | 198 |
| Appendix E : MATLAB/ Simulink Model of the Wound Rotor Induction Motor | | 199 |

List of Figures

| | |
|-----------------------------------------------------------------------------------------------------------------------------------------------------------------------------------------------------------------------|----|
| Figure 1.1. Thesis structure. | 4 |
| Figure 2.1. Torque characteristics for three values of external resistance (R_1 , R_2 , and R_0). | 12 |
| Figure 2.2. Magnetic pole system generated by currents in the stator and rotor windings. | 16 |
| Figure 2.3. Three-phase, 4-pole induction motor torque-speed curve for constant- voltage, | 17 |
| Figure 2.4. Per-phase induction machine equivalent circuit. | 18 |
| Figure 2.5. Simplified equivalent circuit. | 20 |
| Figure 2.6. Simple converter recovering energy from a rotor of doubly fed induction generator. | 21 |
| Figure 2.7. Equivalent circuit of doubly fed induction generator (DFIG). | 23 |
| Figure 2.8. Induction machine bearing. | 27 |
| Figure 2.9. Stator winding faults: phase to phase, turn to turn and phase to ground circuit. | 29 |
| Figure 2.10. Illustration of the different cases of eccentricity including static eccentricity and dynamic eccentricity. | 31 |
| Figure 2.11. Condition monitoring process. | 35 |
| Figure 2.13. Search coils used in condition monitoring of induction machine. | 41 |
| Figure 2.13. Phase winding of a four-pole induction machine, with two parallel paths involving three series connected coils each. This figure covers the coil numbers 1, 2, 6, 10, 11, and 15. | 48 |
| Figure 3.1. Single-coil located on the surface of the stator. | 55 |
| Figure 3.2. Single-coil located on the surface of the rotor. | 57 |
| Figure 3.3. Current distribution in the cage and wound rotors. In the rotor cage, this shows rotor-loop currents and the sharing of common paths. In the wound rotor, this shows the three phase windings. | 58 |
| Figure 3.4. Air-gap MMF and flux waves in terms of pole or harmonics number and frequency for a cage induction machine [146]. | 59 |
| Figure 3.5. Co-ordinate system for the stator and rotor. | 60 |

| | |
|---------------------------------------------------------------------------------------------------------------------------------------------------------------------------------------------------------------------------------------------------------------|-----|
| Figure 3.6. Applying Ampere’s law around a closed loop. | 63 |
| Figure 3.7. Experimental and predicted torque versus speed characteristics for balanced rotor for a four-pole wound rotor induction machine. | 74 |
| Figure 3.8. Equivalent circuit for wound-rotor induction machine as derived. | 76 |
| Figure 3.9. Wound-rotor induction machine with external resistors. | 78 |
| Figure 3.10. Simplified equivalent circuit for wound rotor induction machine connected to external impedance. | 79 |
| Figure 3.11. Four-pole wound-rotor induction machine torque-slip curves showing effect of adding external resistance to rotor-circuit resistance. | 79 |
| Figure 4.1. Radial and axial sections of the test machine. | 84 |
| Figure 4.2. Illustration of the stator conductors inside the slot. | 84 |
| Figure 4.3. Illustration of the winding layout (only phase 1 shown), and phase diagram. | 86 |
| Figure 4.4. Illustration of the mechanical harmonics for the test machine. | 86 |
| Figure 4.5. Illustration of the winding harmonic factors for the test machine. | 87 |
| Figure 4.6. A fast 2D FEM for locked rotor circuit flux distribution. | 88 |
| Figure 4.7. Results for different contour plots in the electromagnetic model: (a) locked-rotor and magnetic potential for locked rotor test (the penetration of the field in the rotor is usually negligible in these conditions) (b) no-load condition. | 89 |
| Figure 4.8. Equivalent circuit of the test machine in Motor-CAD. | 90 |
| Figure 4.9. Graphical results of the electromagnetic model in Motor-CAD. | 91 |
| Figure 4.10. Test machine, showing the stator frame during the rewinding process. | 92 |
| Figure 4.11. Predicted and measured torque developed by the test machine v.s. speed characteristics. | 94 |
| Figure 4.12. Simulated and measured rotor currents v.s. speed characteristics. | 95 |
| Figure 4.13. Simulated and measured losses v.s. speed characteristics. | 95 |
| Figure 5.1. Single-phase equivalent circuit containing ΔR in wound-rotor phase. | 104 |
| Figure 5.2. Simulation of wound rotor connected with external resistance. | 105 |
| Figure 5.3. Run-up torque with different loads. | 107 |
| Figure 5.4. Electromagnetic torque developed by the machine with rated load. | 107 |
| Figure 5.5. Simulated phase stator currents v.s. time response under different conditions. | 108 |

| | |
|--------------------------------------------------------------------------------------------------------------------------------------------------------------------------------------------------------------------------------|-----|
| Figure 5.6. Simulated rotor currents v.s. time response under different conditions. | 108 |
| Figure 5.7. Simulated stator power losses v.s. time under different conditions. | 109 |
| Figure 5.8. Characteristics of steady state torque developed by the machine v.s. speed..... | 111 |
| Figure 5.9. Predicted three phase rotor currents v.s. speed characteristics for balanced and unbalanced rotors. | 111 |
| Figure 5.10. The forward and backward components of stator current for balanced and unbalanced rotors. | 112 |
| Figure 5.11. Curve I_{sb}/I_{sf} versus slip for wound rotor machine with asymmetrical resistances. | 112 |
| Figure 5.12. Percentage of the backward component over forward component of stator current v.s slip for a machine connected to asymmetrical resistances, showing the drop point at half speed. | 113 |
| Figure 5.13. Stator and rotor losses vs. slip for a healthy machine, machine with asymmetrical resistances connected to the rotor, and machine with asymmetrical resistances connected to the rotor. | 113 |
| Figure 5.14. Laboratory set up of the experiment involving the test machine, external resistances, and measurement equipment. | 116 |
| Figure 5.15. Schematic diagram of the connection for load testing of the wound rotor..... | 116 |
| Figure 5.16. Variation of rotor current with speed for a healthy machine..... | 118 |
| Figure 5.17. Variation of line current with speed for a machine in healthy condition, and a faulty machine with one rotor phase connected with asymmetrical resistance ($2\ \Omega$). | 118 |
| Figure 5.18. Measured and predicted rotor phase currents for unbalanced rotor (one rotor phase connected with $2\ \Omega$, and the other two phases are short-circuited..... | 119 |
| Figure 5.19. Variation of rotor phase currents for the two fault conditions. In the first condition, one of the rotor phases was connected to $2\ \Omega$, and in the second condition it was connected to $5\ \Omega$ | 120 |
| Figure 5.20. Variation of measured and calculated steady torque with speed for machine connected with asymmetrical resistances ($2\ \Omega$). | 121 |

| | |
|----------------------------------------------------------------------------------------------------------------------------------------------------------------------------------------------------------------------------------------------------------------------------|-----|
| Figure 5.21. The backward components of stator current vs. slip for machine connected with asymmetrical resistances (2Ω), and that the machine runs with 100 V and 150 V respectively. | 121 |
| Figure 6.1. Air-gap flux waves accounted for in this study, showing linkages between MMF waves in a cage rotor machine and associated air-gap harmonic waves; for three-phase winding, $n = 1, 5, 7$, etc [50]..... | 125 |
| Figure 6.2. Air-gap flux waves accounted for in this study, showing linkages between MMF waves in a wound rotor machine and associated air-gap harmonic waves; for three-phase winding, $n = 1, 5, 7$, etc [50]..... | 125 |
| Figure 6.3. Schematic representation of air-gap eccentricity, showing the rotor and stator position..... | 127 |
| Figure 6.4. Definition of DE and NDE eccentricity..... | 128 |
| Figure 6.5. Amperes Law Applied to a Non-Uniform Air-Gap. (after 360 mechanical degrees, the air-gap length is again the same value)..... | 131 |
| Figure 6.6. Normal and tangential components of the flux density. | 136 |
| Figure 6.7. Radial magnetic forces in a 2 pole machine: (a) Radial magnetic forces in a symmetrical machine, and (b) machine with rotor displaced vertically downwards. | 138 |
| Figure 6.8. Two-phases distributed search winding: 6-pole search coils, 12 coils per phase, and 44 turns per coil and 2-pole search coils, 12 coils per phase, and 15 turns per coil – only one phase of each shown. | 140 |
| Figure 6.9. Flowchart of UMP and search coils voltages calculation..... | 141 |
| Figure 6.10. 72 slot wound rotor with 1 stator slot skew (removed slip rings). | 149 |
| Figure 6.11. Laboratory set up of the experiment involving the test machine (Dive End side), search coils, piezoelectric force transducers, and other measurement equipment..... | 150 |
| Figure 6.12. Transducers arrangement. The distance between the vertices of the shaft axis to the transducers is defined as x and the distance between shaft axis and the top point of the transducer is defined as y . (Transducers 1 and 2 in DE of the machine)..... | 151 |
| Figure 6.13. Experiment with test machine showing the air-gap adjustment using Clock gauges..... | 153 |

| | |
|-------------------------------------------------------------------------------------------------------------------------------------------------------------------|-----|
| Figure 6.14. Search coils being fitted: single 6-pole winding; red coils down top of slots; and blue coils wound round winding only next to the end of core. | 154 |
| Figure 6.15. Illustration of NDE and DE sides of the test machine, and UMP measurement rigs using piezoelectric transducers. | 157 |
| Figure 6.16. Open-circuit rotor UMP measurement results – comparison to adjust static eccentricity [48]. | 159 |
| Figure 6.17. Variation of UMP with line voltage for several eccentricities, at open- circuit condition [48]. | 160 |
| Figure 6.18. Short-circuit rotor UMP measurement results. | 160 |
| Figure 6.19. Axial variation of eccentricity and the direction of UMP. | 163 |
| Figure 6.20. Axial variation of eccentricity. | 163 |
| Figure 6.21. Variation of measured and predicted UMP with eccentricity degrees for the open-circuit test with 200 V. | 164 |
| Figure 6.22. Induced 6-pole search winding voltages with a variation of eccentricity, illustrating the predicted and measured values. | 165 |
| Figure 6.23. Variation of measured UMP with 6-pole induced voltages for the open-circuit test at 200 V. | 166 |
| Figure 6.24. Induced voltages with a variation of eccentricity with 2 and 6 pole search windings for open circuit operation. | 167 |
| Figure 6.25. Induced voltages in the functional coils with a variation of eccentricity. | 168 |
| Figure 6.26. Calculated and measured voltages in the search windings with a variation of eccentricity with an open-circuit rotor. | 169 |
| Figure 6.27. Variation of measured UMP with induced search windings voltages. | 169 |
| Figure 6.28. Variation of the rotor in stator bore and the illustration of 6 cases of movement strategies. | 171 |
| Figure 6.29. Average unbalanced magnetic pull due to rotor end movement with variation of eccentricity. | 172 |
| Figure 6.30. Unbalanced magnetic pull due to rotor end movement with variation of eccentricity. | 172 |
| Figure 6.31. Search coil voltages with motor end movement. | 173 |
| Figure 6.32. Calculated and measured currents in the functional search windings with variation of eccentricity. | 174 |

| | |
|-----------------------------------------------------------------------------------------------------------------------------------------------------------------------------------------------------------------------------|-----|
| Figure 6.33. Variation of measured UMP with eccentricity variation in the open circuit test and locked rotor test. | 175 |
| Figure 6.34. Comparison of calculated and measured UMP with a variation of eccentricity, and comparison of calculated and measured UMP with and without damping effect. The test was done with open-circuit operation. | 176 |
| Figure 6.35. Calculated and measured copper losses in the functional search winding with a variation of eccentricity..... | 177 |
| Figure 6.36. Vibration monitoring sensors position..... | 178 |
| Figure 6.37. Stator frame vibration zoom spectrum for a uniform air-gap, and 40% static eccentricity. | 178 |
| Figure 6.38. Illustration of the test where a DC current is input in the 2- and 6-pole search coils. | 179 |
| Figure 6.39. Variation of measured UMP with induction of a DC current in the 2-pole and 6-pole search coils..... | 180 |
| Figure B.1. Rotor surface with skewed slot. | 188 |
| Figure C.1. Double-layer winding, 4 poles, $q = 4$, $y/\tau = 11/12$, $N_s = 48$ slots, and $a = 1$ current path. | 192 |
| Figure C.2. Four pole main windings (Phase A only), blue wires located in the first layer, red wires located in the second layer, black wires illustrating the jumping to the next pole..... | 193 |
| Figure C.3. Two pole search windings, phase α | 194 |
| Figure C.4. Two pole search windings, phase β | 195 |
| Figure C.5. Six pole search windings, phases α and β | 196 |
| Figure E.1. MATLAB/simulink model of the three-phase wound rotor induction motor. | 199 |

List of Tables

| | |
|-----------------------------------------------------------------------------------------------------------------------------------|-----|
| Table 2.1. Survey of induction machine faults including percentage of failure, causes, and methods used for faults detection..... | 26 |
| Table 5.1. DC machine parameters. | 115 |
| Table 6.1. Comparing the analytical and numerical methods..... | 135 |
| Table 6.2. Winding parameters of main winding and functional search coils..... | 155 |
| Table 6.3. UMP measurements due to changing rotor position..... | 161 |
| Table C.1. Test machine specification. | 190 |

Acronyms and Abbreviations

Notations

| | |
|-----------------|---------------------------------------------------|
| k | Average air-gap radius |
| $e(y,t)$ | Axial electrical field of air gap |
| \bar{N}_r | Coefficient of rotor |
| \bar{N}_{st} | Coefficient of stator |
| c | Coil number of turns on stator |
| g | Effective air gap length |
| g_{av} | Effective air gap length when rotor is concentric |
| $g_{(x,y)}$ | Effective axial air gap length |
| R_a, R_b, R_c | External rotor resistances |
| F_x | Force at x component |
| F_y | Force at y component |
| F_z | Force at z component |
| $i_r(y,t)$ | Harmonic current density distribution of rotor |
| $i_s(y,t)$ | Harmonic current density distribution of stator |
| $i_x(t)$ | Harmonic current flow |
| V_D | Induced voltage |
| L_{st} | Length of the stator |
| σ_n | Maxwell stress (radially) |
| σ_t | Maxwell stress (tangentially) |
| ω_r | Mechanical angular frequency |
| P_{mech} | Mechanical power |
| n_r | Mechanical speed of rotor |
| T_{mech} | Mechanical torque |

| | |
|---------------|----------------------------------------------------------------------------|
| $b_n(y,t)$ | Normal radial flux density of air gap |
| k_s^n | n^{th} harmonic stator slot opening factor |
| c_ω | Number of conductors in the ω^{th} slot |
| p_m | Number of pole-pairs |
| P | Number of poles |
| N_R | Number of slot at which winding is located in rotor |
| N_S | Number of slot at which winding is located in stator |
| Λ | Permeance |
| μ_o | Permeance of free space |
| $b_s(y,t)$ | Radial flux density of air-gap |
| $b_r(y,t)$ | Rotor air-gap flux wave components |
| I_r | Rotor current |
| \bar{J}_r^n | Rotor current density coefficient of the n^{th} current harmonic |
| f_r | Rotor frequency |
| Ψ_r | Rotor magnetic field |
| R_r | Rotor resistance |
| b_r | Rotor slot opening |
| k_r^n | Rotor slot opening factor |
| V_r | Rotor voltage |
| $Z_{r,r}$ | Rotor-rotor coupling impedance |
| $Z_{s,r}$ | Rotor-stator coupling impedance |
| k_{sk} | Skew factor |
| s | Slip of the motor |
| K_s | Slot opening factor |
| α_s | Slot-angle of the stator in mechanical radians |
| \bar{J}_s^n | Stator current density coefficient of the n^{th} current harmonic |
| Ψ_s | Stator magnetic field |

| | |
|-------------|------------------------------------|
| b_{st} | Stator slot opening |
| V_s | Stator voltage |
| R_s | Stator winding resistance |
| $Z_{r,s}$ | Stator-rotor coupling impedance |
| t_{ratio} | Stator-rotor turns ratio |
| $Z_{s,s}$ | Stator-stator coupling impedance |
| f | Supply frequency |
| ω_s | Synchronous angular frequency |
| n_s | Synchronous speed |
| $b_t(y,t)$ | Tangential flux density of air gap |
| y | Variation in axial direction |
| n | Harmonic number |

Abbreviations Used in Thesis

| | |
|------|----------------------------------|
| BCW | Bridge configured winding |
| DE | Drive end |
| DFIG | Doubly fed induction generator |
| FEA | Finite element analysis |
| FFT | Fast Fourier transform |
| IM | Induction machine |
| MCSA | Motor current signature analysis |
| NDE | Non drive end |
| SCIM | Squirrel cage induction machine |
| UMP | Unbalanced magnetic pull |
| WRIM | Wound rotor induction machine |

Superscripts

| | |
|-----------|-----------------------------------------------------|
| av | Average |
| x | Axial distance along machine |
| b | Backward component |
| $1, 2, 3$ | Corresponding to stator and/or rotor phase windings |

| | |
|------|----------------------------------------------------------|
| f | Forwards component |
| y' | linear distance around air-gap in rotor reference frame |
| y | linear distance around air-gap in stator reference frame |
| r | Rotor |
| s | Stator |
| n | Stator harmonic |

Chapter 1: Introduction

The wound rotor induction machine has enjoyed a renaissance as the generator in many commercial wind turbines. It is used in a slip energy recovery manner so that it can generate at both below and above the synchronous speed.

Calculation of the machine performance has improved continuously for many decades. It is usually based on the equivalent circuits as well as modern electromagnetic finite element analysis. This has led to machine design becoming more systematic and operation more predictable.

There are still some challenges in detecting and calculating machine faults that cannot easily be predicted with reasonable accuracy. These often rely on techniques that are not adaptable to the wound rotor induction machine (WRIM) as described in Chapter 2. For instance, techniques need to be developed that can accurately predict rotor faults in the WRIM in the early stages of fault development. These rotor faults include air-gap eccentricity and external-connected rotor resistances.

This thesis contributes significant knowledge to the engineering community through the investigation of induction machine behaviour in healthy and faulty conditions, and the study of air-gap eccentricity and unbalanced rotor resistances in the WRIM and doubly fed induction generator (DFIG). The most significant and novel aspect of this research is to build an impedance matrix for both condition monitoring use and to calculate the unbalanced magnetic pull (UMP). Many other findings and original research contributions are detailed in the chapter summaries and in the conclusion of this thesis.

1.1 Project Statement

This work contributes to the development and verification of computationally efficient mathematical and experimental models that could be used for condition monitoring systems for the prediction of WRIM and DFIG behaviour under healthy and faulty operating conditions. The three most significant and novel aspects of this research are:

- [1] Development of a theoretical model to analyse WRIM behaviour.
- [2] Employment of Motor-CAD and MATLAB packages to predict the electromagnetic behaviour of an induction machine during steady-state and transient-state under various operational conditions.
- [3] Development of a new technique using special auxiliary windings to detect and damp the unbalanced magnetic pull in WRIM.

These are validated by experimental work.

1.2 Project Objectives

The main objectives of this project are:

- [1] Discussion of the main induction machine faults, and the techniques used to detect and diagnose these faults. This is followed by observations on the existing condition monitoring techniques.
- [2] Development of an impedance matrix that includes all the coupling and mutual impedances. This matrix represents an analytical approach to the three-phase wound-rotor motor. The analysis is based on rotating field theory and the coupling impedance concept. The impedance matrix is used to analyse the wound rotor induction machine behaviour in a healthy operating condition and then extended

to cover the faulty operating conditions such as unbalanced rotor-phase impedances.

- [3] Use of Motor-CAD and MATLAB packages to predict the electromagnetic behaviour of an induction machine during the steady-state and transient-state. Finite element analysis of an induction machine is carried out by using Motor-CAD in order to complete the comparison. The graphical interfaces of the Motor-CAD environment will be utilised to describe the machine geometry, winding harmonics, material properties, and air-gap flux.
- [4] A method is proposed for detecting and measuring rotor eccentricity in the WRIM. The analysis is fully developed in order to calculate the UMP, and then an experimental rig is described and measurements are taken. These are compared with the calculated values.
- [5] Introduction of a simple method using pole-specific search coils to detect and damp UMP. The impedance matrix is developed to predict the winding voltages as a function of eccentricity. The search coils can also be used to suppress UMP.
- [6] The experimental identification and study of the performance of the 3-phase 4-pole wound rotor induction machine in a variety of conditions.

1.3 Structure of the Thesis

In this thesis, detailed modelling and analysis methods are put forward that improve condition monitoring of the wound rotor induction machine. These help to aid readers in their understanding of the procedures applied, and to provide clarity and continuity of research. This thesis is divided into seven chapters. The chapters are subdivided into sections to maintain the flow of the chapters as shown in Figure 1.1. The rest of this thesis is organized as follows:

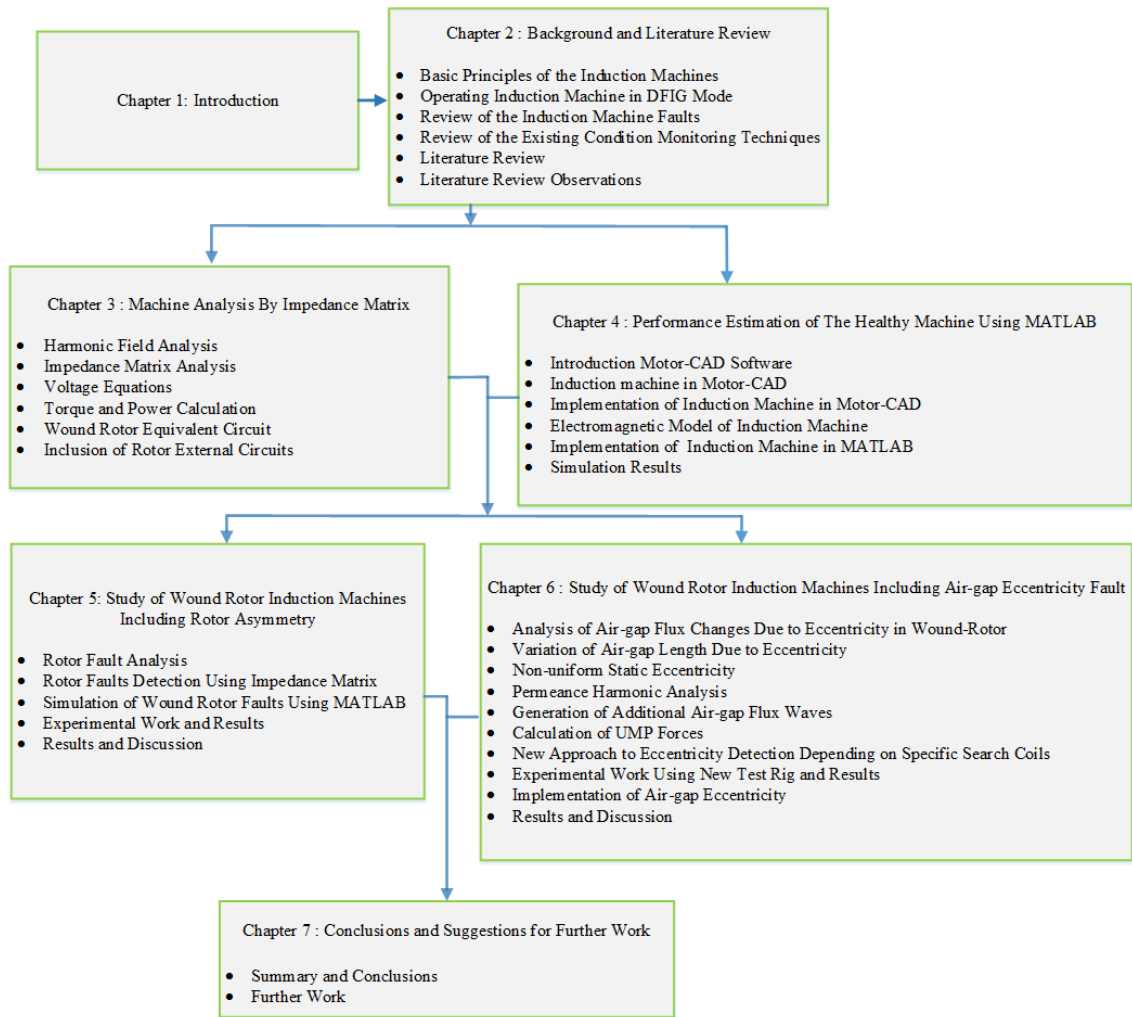


Figure 1.1. Thesis structure.

Chapter 2 provides a brief introduction to induction machines and condition monitoring techniques. The main induction machine faults are studied, followed by observations about the condition monitoring of induction machines. This represents the main literature review for the work. However, a brief exploration of the literature is performed in each chapter to address the important aspects of relevant previous research to the work in that chapter.

Chapter 3 addresses the theory related to harmonic field analysis of the wound rotor induction machine. The analysis develops expressions which can take into account any

stator or rotor winding. For completeness, a comparative study of the current distribution in the rotor of a squirrel cage induction machine (SCIM) and the WRIM is made. The developed electromagnetic torque can be determined from the stator and rotor current density distributions. The analysis outlined in the chapter leads to construction of the impedance matrix including all coupling and mutual impedances. An equivalent circuit for a wound rotor induction machine, which includes external rotor resistances, is derived in this chapter.

Chapter 4 provides a brief introduction to Motor-CAD software. Motor-CAD package is employed to predict the electromagnetic behaviour of the induction machine during steady-state and transient-state operation. In addition, it is used for examining the induction machine parameters. In this chapter, the implementation of an induction machine model in MATLAB is described in order to make some comparisons. These provide useful information and lead to a framework for understanding some results in the context of others.

Chapter 5 develops a relatively simple yet powerful model that can accurately analyse the behaviour of a WRIM or a DFIG with wound rotor faults. The model is based upon the calculation of the stator current components, which are obtained from an impedance matrix analysis that includes coupling impedances. This method is used here to detect unbalanced rotor-phase impedances for a four-pole wound rotor.

Chapter 6 puts forward a method for measuring rotor eccentricity in a WRIM. The investigated UMP sources are restricted to additional magnetic field components with one pole-pair below and above the main pole-pair number. A simple method using pole-specific search coils is introduced, and a theory is developed to illustrate rotor eccentricity. The radial forces in an induction machine are calculated, and the

characteristics of UMP are described. Then an experimental rig for measuring UMP is described and measurements are taken. The reader is assumed to be familiar with the fundamental air-gap magnetic flux density produced in the induction machines. However, background and basic characteristics are provided.

Chapter 7 reviews and summarises this thesis with a general summary of the contributions in the previous chapters, and discussing significant and novel results as well as identifying the important areas for further research.

1.4 Publications from this Thesis Work

A full list of papers are given below. It consists of two journal papers and seven conference papers and digests.

I. Journal papers

- [1] D. G. Dorrell, A. Salah, and Y. Guo, "The detection and suppression of unbalanced magnetic pull in wound rotor induction motors using pole-specific search coils and auxiliary windings," *IEEE Transactions on Industry Applications*, vol. 53, no. 3, pp. 2066-2076, 2017.
- [2] D. G. Dorrell and A. Salah, "Detection of rotor eccentricity in wound rotor induction machines using pole-specific search coils," *IEEE Transactions on Magnetics*, vol. 51, no. 11, pp. 1-4, 2015.

II. Conference papers

- [1] A. Salah, Y. Guo, and D. G. Dorrell, "Analysis of DFIG machine with rotor-wound faults", *IEEE AFRICON*, 2017, South Africa, pp. 1301-1306, 2017.
- [2] A. Salah, Y. Guo, and D. G. Dorrell, "Monitoring and damping unbalanced magnetic pull due to eccentricity fault in induction machines: A review"

International Conference on Electrical Machines and Systems, ICEMS, Sydney, Australia, pp. 1-6, 2017.

- [3] A. Salah, Y. Guo, and D. G. Dorrell, "Impedance matrix analysis technique in wound rotor induction machines including general rotor asymmetry," IEEE International Conference on Industrial Electronics, IECON, Florence, Italy, pp. 1821-1826, 2016.
- [4] D. G. Dorrell, A. Salah, and O. Kayani, "The detection and suppression of Unbalanced Magnetic Pull in Wound Rotor Induction Motors Using Pole-Specific Search Coils and Auxiliary Windings," IEEE Energy Conversion Congress and Exposition, ECCE, 2015, pp. 277–284. doi: 10.1109/ECCE.2015.7309699.
- [5] D. G. Dorrell and A. Salah, "Detection of rotor eccentricity in wound rotor induction machines using pole-specific search coils," IEEE International Magnetics Conference (INTERMAG), 2015, pp. 1-1, 2015.
- [6] A. Salah, Y. Guo, and D.G. Dorrell, "Rotor fault analysis in a doubly-fed induction generator using impedance matrix technique," IEEE International Magnetics Conference (INTERMAG), 2017, pp. 1-2, 2017.
- [7] A. Salah, Y. Guo, and D. G. Dorrell, "Predicting the behavior of induction machine using Motor-CAD and MATLAB packages," IEEE CPE-POWERENG, Doha, April 2018.

1.5 Novelties of the Project

This research is focused on developing a technique for detecting faults in the wound rotor machine at an early stage, in order to protect the machine or plant from catastrophic failure and reducing the cost of maintenance. In summary, the novelties of this project include the following:

- [1] Development a theoretical model for detecting wound-rotor faults using an impedance matrix. Considering the most of the existing theoretical models are couched in terms of cage induction machines which may not be applicable to wound rotor machines. In [1, 2], Williamson *et al.* utilised impedance matrices to detect the faults in cage rotor machines; however, the wound rotor machine runs at a higher slip than the cage rotor machine; and in the DFIG slip energy recovery, as described in Chapter 2, is used to get generation when sub synchronous and over a wide speed range. Faults in wound rotor machines can vary greatly from the cage-rotor equivalent.
- [2] Introduction of a new approach to evaluate the air-gap eccentricity using special search coils. Auxiliary windings are designed for this specific purpose, which enables measurement of the degree of air-gap eccentricity. The use of additional damper windings has been investigated in [3-6] and a similar theme is investigated here. However, this is combined with using pole-specific search coils to assess the degree of eccentricity.
- [3] Many researchers have addressed UMP; however, the challenge is how UMP can be accurately measured [7, 8]. Construction of a new experimental test rig that can be used to study the effect of air-gap eccentricity in the machines and calculate the UMP. Finally, to validate the mathematical models several experimental tests are conducted to evaluate the rotor faults. This enables verification of the work in this project.
- [4] Experimentally representation of different types of air-gap eccentricity including non-uniform eccentricity. A unique rig, which allows the study of non-uniform axial eccentricity, will be constructed.

- [5] Behavioural investigation of the wound rotor induction machine using specialist (Motor-CAD) and general purpose (MATLAB) software.

Chapter 2: Background and Literature Review

This chapter provides a brief introduction on the induction machine and condition monitoring techniques. The main induction machine faults are studied, followed by observations on the condition monitoring of induction machine.

2.1 Introduction

The induction machine is the established form of AC motor. It is used in 85 % of all industrial applications requiring an electric drive [9]. This high demand, which is increasing, appears to be improving the efficiency and availability of the induction machine. Recently, the wound rotor induction machine has enjoyed a renaissance as the generator in many commercial wind turbines and it is known as the doubly-fed induction generator (DFIG). It is used in a slip energy recovery manner so that it can generate at both below and above the synchronous speed. Therefore, it is important to devote more research to the study of induction machine behaviour during abnormal conditions due to various faults. The main goal here is to improve machine condition monitoring and fault diagnosis techniques.

There are many problems that can reduce the efficiency or cause a malfunction of an induction machine, such as load conditions, manufacture imperfections and installation issues. Industrial stress can lead to repair costs and losses because of increased unexpected downtime. The key is the ability to detect faults while they are still developing, which is called incipient failure detection [10]. By implementing efficient condition monitoring, it is possible to provide adequate warning of imminent failure. Thus, it is possible to schedule future preventive maintenance and repair work [11-13].

Different methods for fault identification have been developed and used effectively to detect machine faults at different stages using machine variables, such as current, voltage, speed, torque, noise and vibrations [13-17]. In most cases, faults produce one or more indicative signs, such as increased losses, excessive heating, torque pulsation, and unbalanced voltages and line currents. Rapid developments in signal processing and power electronic devices have made variable-speed induction generator applications more common. However, this brings with it significant challenges for building more sophisticated techniques, which are required for sensitive and reliable fault detection in the future. The shortcomings of existing condition monitoring methods are highlighted. The objective is to overcome the shortcomings related to these methods, so they can be improved and developed.

2.2 Basic Principles of the Induction Machines

The induction machine consists of a stationary part (the stator) and a rotating part (the rotor), which is supported by bearings concentric with the stator. The stator of the induction motor is wound with a balanced three-phase winding. When this winding is supplied from a balanced three-phase A.C voltage source, balanced three-phase currents flow. This produces a rotating magnetic field in the air-gap of the machine. The speed of rotation of this field is synchronous, determined by the number of pole pairs (p_m) of the winding, and the supply frequency [18].

There are two basic types of induction machines: squirrel cage induction machines (SCIM), and wound rotor induction machines (WRIM). The main difference between SCIM and WRIM is the design of the rotational part. The rotor of a SCIM is formed from copper or aluminium conducting bars short-circuited by rings at both ends. This “squirrel

“cage” is in slots in the rotor that can be open or closed. The rotor of a WRIM has a three-phase winding that is like the stator winding. However, the slot number will be different to prevent alignment torque. The winding will be star connected and the winding exit the rotor via three slip rings. The star point is hard-wired, and no access is given to it [19].

In the WRIM, the slip-ring brushes can be connected to variable resistors and the resistance of the rotor winding can be externally controlled, so it is possible to manipulate the torque/speed characteristic of the machine and control the output power. If the rotor circuit resistance is increased, then the pull-out speed of the wound induction machine decreases but the maximum torque remains constant. During run up, the torque can be increased, and the starting current decreased with additional external rotor resistances. Therefore, the rotor circuit resistance can be adjusted to produce the maximum torque at starting condition and it can then be decreased as the motor speeds up, making the maximum torque available over the whole accelerating range. As already mentioned, these external resistances decrease the stator starting current which is desirable in most applications. Figure 2.1 shows that by increasing the rotor resistance from R0 to R1 to R2, the starting torque is improved.

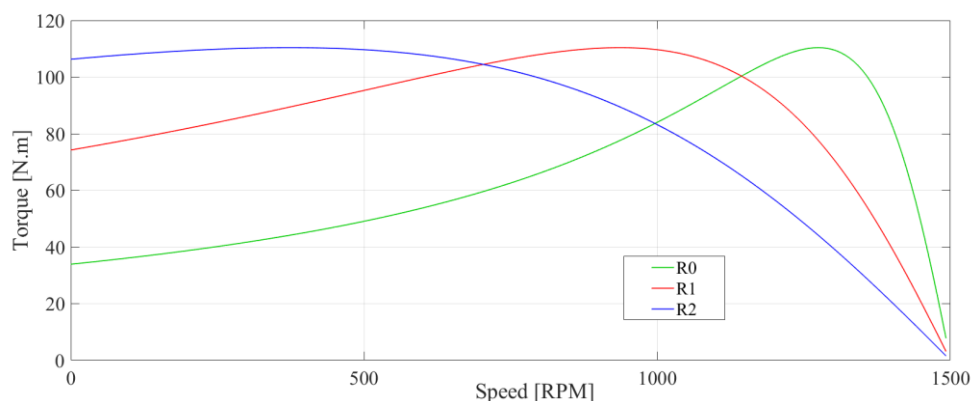


Figure 2.1. Torque characteristics for three values of external resistance (R1, R2, and R0).

The WRIM is a good choice of generator for a wind turbine because by changing the rotor resistor it is possible to change the operating point of the induction machine in order to get a better load match in start-up, weak wind conditions, and strong wind conditions. There are many useful discussions which compare the WRIM and SCIM [20, 21].

In terms of the control, the DFIG is more sophisticated than the WRIM because rather than dissipate energy in external resistors, the rotor is connected to the grid via back-to-back inverters. Below synchronous speed, if the machine is motoring, the energy exiting the rotor through the slip rings is regenerated back into the grid, or, in the case of a wind turbine, if energy is injected into rotor slip rings, the machine can generate more power at the terminals of the stator if mechanical power is turning the machine. Hence it can work as a generator across a wide speed range including sub synchronous speeds [22].

The transfer of energy from the stator to the rotor, either in the SCIM or WRIM, is by means of electromagnetic induction. Energy is transferred electromagnetically across the air-gap between the stator and the rotor windings. A very small air-gap can help to reduce reluctance. However, the length of the air-gap is constrained by allowable core losses as well as manufacturing tolerance and cost. It can be noted that air-gap eccentricity exists even in a healthy machine, but the permissible limit depends on the motor construction, e.g., 10 % for a healthy motor [23, 24]. The air-gap is typically between 0.35 and 0.50 mm for motors up to 10 kW, and between 0.5 and 0.8 mm for motor in the range of 10 to 100 kW [25]. One drawback of the wound rotor is that it needs a higher level of maintenance because of the brushes and slip rings compared with the squirrel cage motor. Induction machines operate at speeds away from the synchronous speed (n_s), therefore they are known as asynchronous machines. The difference between the synchronous speed and the rotor speed is commonly referred to the slip of the rotor; in this case, the

rotor slip is $n_s - n_r$ when measured in r/min. The per-unit slip of an induction motor is therefore defined as

$$s = \frac{n_s - n_r}{n_s} \quad (2.1)$$

where n_r is the mechanical speed of the rotor. The synchronous speed n_s is calculated from:

$$n_s = \frac{60f}{p_m} \quad (2.2)$$

where f is the supply frequency, and p_m is the fundamental pole-pair number of the machine. The relative motion of the stator flux and the rotor conductors induces voltages at the slip frequency f_r . This is defined by

$$f_r = sf \quad (2.3)$$

Hence, the rotor frequency is dependent on the slip of the motor, assuming the supply frequency remains constant. In inverter-fed SCIMs, the frequency f_s does vary to change the operating speed. This varies the synchronous speed and the machine will operate a few percent under this (or above it if it is generating).

The electrical behaviour of this machine is similar to that of a transformer but with an extra feature, frequency transformation produced by the relative motion of the stator and rotor windings. In fact, a wound-rotor induction machine can be used as a frequency changer.

When the stator winding is supplied by a three-phase voltage set, currents flow in the coils producing a magnetic field Ψ_s that rotates in one direction (the direction depends on the phase sequence). The rotating air-gap flux induces slip-frequency voltages in the rotor

windings. The rotor currents can be determined by the magnitudes of the induced voltages in the rotor and the rotor impedance at f_r . At the starting condition, the shaft is not moving ($n_s = 0$), the slip is unity ($s = 1$), and the rotor and stator frequencies are equal. The rotor field Ψ_r produced by the rotor currents, rotates at the stator field speed, resulting in a starting torque if there is a phase angle between the two field components. This torque turns the rotor in the direction of rotation of the stator field. If the torque is large enough to overcome the opposition to rotation created by the load, the motor will start rotating. The rotor speed can never equal the synchronous speed, since the rotor would then be steady with respect to the stator field. There would be no voltage induced in rotor windings so no current would flow, and hence, no torque would result. When open circuit, there is no rotor current and rotor field [26]. The electromagnetic torque is produced by an interaction of two fields, which can be expressed as

$$T \propto |\psi_s \times \psi_r| = |\psi_s| |\psi_r| \cos \theta_t \quad (2.4)$$

Both fields, the rotor magnetic field and stator magnetic field, rotate at the same synchronous speed. Torque is the vector product and results in a magnetic pole-pair due to the attraction of opposite polarity magnetic poles. When both vectors are normal to each other as shown in Figure 2.2, the maximum allowable torque is produced. It should be noted that the rotor (shaft) speed is asynchronous, whereas the rotational speed of rotor field is synchronous.

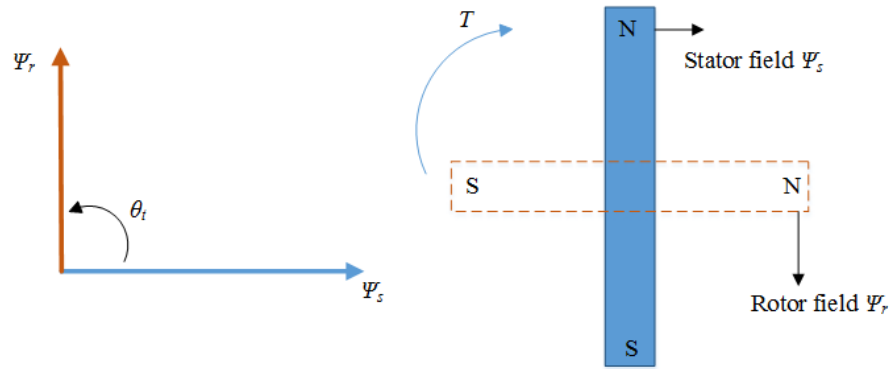


Figure 2.2. Magnetic pole system generated by currents in the stator and rotor windings.

The peak-torque slip is proportional to the rotor circuit resistance. For a squirrel-cage, the maximum steady-state slip is relatively small and much lower than the peak-torque slip - probably in the region of 1 to 4 % depending on the size of the machine. For this reason, the squirrel-cage machine is almost a constant-speed motor, experiencing only a few percentage points decrease in speed from no load to full load. The speed is varied by changing the synchronous speed via the supply frequency. However, in the wound-rotor machine, the rotor resistance is increased by inserting external resistance or an effective resistance; hence the slip at peak-torque increases, and thus the machine speed for a specified value of torque will decrease. Figure 2.3 shows an example of the torque-speed curve of a three-phase, four-pole induction machine, supplied at 50 Hz. The torque increases with increasing slip up to the breakdown torque, which is the pull-out point on the curve. The rated torque is less than the maximum torque, usually 30 to 50 % of the peak torque.

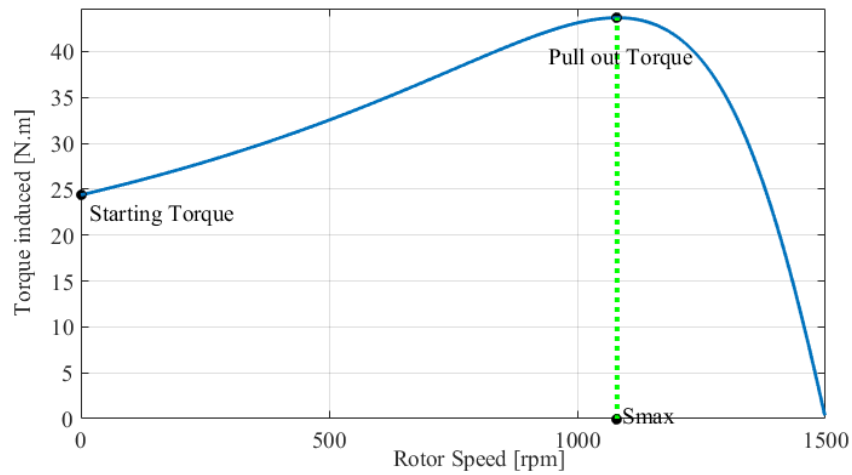


Figure 2.3. Three-phase, 4-pole induction motor torque-speed curve for constant-voltage, and frequency operation.

The mechanical torque rotates the shaft. The torque developed by the machine at any speed is given by

$$T_{mech} = \frac{P_{mech}}{\omega_r} \quad (2.5)$$

where, P_{mech} is the mechanical power that drives the load, and ω_r is the rotor speed and equal to $2\pi n_r \div 60$. The referred rotor resistance R_r in Figure 2.4 can be split into R_r which is the actual resistance, and $((1 - s)/s)R_r$, which is the component where electro-mechanical energy conversion takes place. Therefore, the output power can be calculated from

$$P_{mech} = 3 |I_r|^2 \left(\frac{1-s}{s} \right) R_r \quad (2.6)$$

Therefore the mechanical torque is dependent on the absorbed power in the rotor resistance component $((1 - s)/s)R_r$.

It was stated earlier that induction machine acts in a similar manner to a transformer. The stator part is equivalent to the primary coil of the transformer and has two components, R_s and X_s , which represent the resistance of the stator phase winding and the leakage inductance of the phase winding respectively. The leakage inductance represents the flux produced by the current in the stator windings that does not cross the air-gap of the machine and link the rotor windings, therefore it is not useful for the generation of torque. The magnetising reactance X_m represents the production of useful flux in the machine and this flux crosses the air-gap either from stator to rotor or vice-versa. The rotor is equivalent to the secondary part and has rotor leakage reactance, and rotor resistance. Therefore, the equivalent circuit for the induction machine is similar to that of the transformer. However, the secondary part in the induction machine is short-circuited in cage-rotor types and connected to a resistance circuit or inverter in wound-rotor types. The per-phase induction machine equivalent circuit can be simplified by eliminating the ideal transformer and referring the rotor resistance and reactance to the primary side as shown in Figure 2.4. The rotor circuit is reflected in the stator circuit side in the equivalent circuit (as in a transformer) whose turns-ratio depends on the actual turns ratio between the stator and rotor.

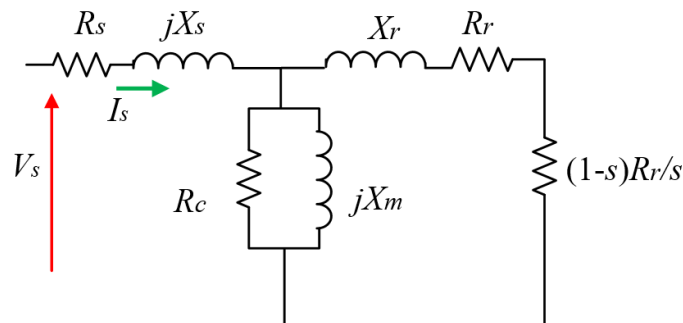


Figure 2.4. Per-phase induction machine equivalent circuit.

In the equivalent circuit R_s and R_r represent the resistances of the stator and referred resistances of rotor winding respectively. X_s and X_r represent the stator leakage reactance and referred rotor leakage reactance respectively. The magnetising reactance is required to cross the air-gap and link the two winding sets, which is represented by X_m . R_c represents the core loss (hysteresis and eddy current losses). The mechanical frequency can be obtained from

$$\omega_r = \frac{1-s}{p_m} \omega_s \quad (2.7)$$

Using the generated stator flux, where the voltage drop across the stator leakage and rotor leakage inductances and stator resistance are neglected:

$$\Psi_m = L_m i_m = \frac{V_s}{\omega_s} = \frac{|I_r| R_r}{s \omega_s} \quad (2.8)$$

This assumes that s is small. The mechanical torque can be expressed as

$$T_{mech} = 3 p_m \Psi_m |I_r| \quad (2.9)$$

The torque expression in (2.9) is an approximation but indicates that the rotor current and the generated stator flux can control the induced torque, as long as both vectors are maintained as shown in Figure 2.5. Obviously, the induced torque in a DFIG can be controlled by defining the physical position and magnitude of the stator winding flux. This can be done directly by monitoring stator voltage and adjusting the rotor currents [27].

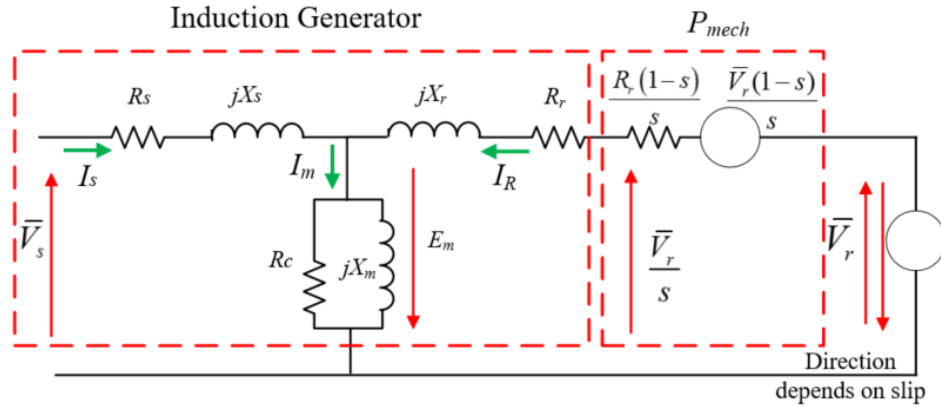


Figure 2.5. Simplified equivalent circuit.

2.3 Operating Induction Machine in DFIG Mode

The doubly fed induction generator (DFIG) is a wound rotor induction motor and typically acts as a generator when driven above the synchronous speed, however, sub-synchronous generation is possible as well. It is known as doubly fed because there are connections to both the stator and rotor. Thus, this research can be applied for both the DFIG, and the WRIM. The DFIG is a better choice for a variable speed wind turbine application since it has the ability to generate power at constant voltage and frequency while the rotor speed varies. This allows more adaptability in terms of the power conversion and more stability in frequency. The voltage in the power system that is linked to the DFIG can also be stabilized [28]. There is a reduction of the power losses and the cost of the converters, and filters [22, 29, 30].

The stator winding is connected to the grid or loads, and the rotor winding is connected to a back-to-back partially rated (20 % – 30 % rating) converter. Figure 2.6 shows that the converter (which is a back-to-back PWM inverter system as already mentioned) recovers energy from a rotor of doubly fed induction generator [28, 31-33]. The converter is utilised for exchanging the slip power to and from the grid for variable speed operation.

Below the synchronous speed, when $s > 0$, power flows into the rotor and this is effectively amplified by addition of power from the prime mover and flows out of the stator. Above the synchronous speed, when $s < 0$, power flows out of both the stator and rotor and at maximum power this is approximately split in the ratio 70 % to 30 %.

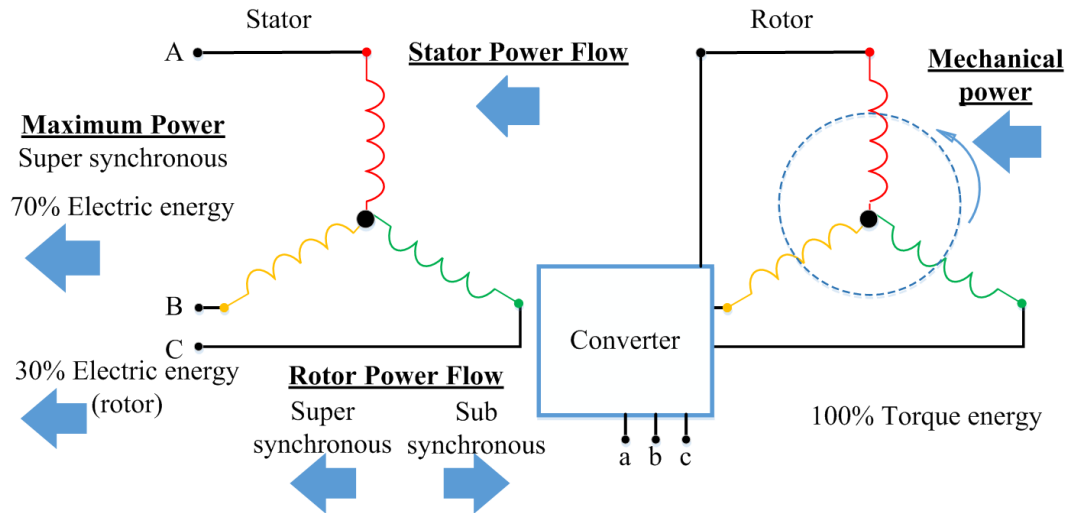


Figure 2.6. Simple converter recovering energy from a rotor of doubly fed induction generator.

The equivalent circuit of the doubly fed induction generator is shown in Figure 2.7. This is the coupled per-phase circuit with the additional rotor voltage source. These would be at slip frequency. As mentioned earlier, the induction motor may be viewed as an ideal transformer. Therefore, the electro-mechanical energy conversion will take place across the transformer component, including the turns transformation characteristic and frequency transformation. The frequency transformation leads to the electromechanical energy conversion. Across the transformer, the total air-gap power can be expressed as:

$$P_{airgap} = 3V_r I_r \cos(\phi - \theta) + P_{mech} + P_{R-cu} \quad (2.10)$$

where the motoring convention is used, and $(\phi - \theta)$ represents the difference between rotor voltage angle and rotor current angle. To make the machine generate then power has to

flow from the rotor to the stator so P_{airgap} has to be negative, even for sub-synchronous operation. Remember that

$$\begin{aligned} s &> 0, \text{ for sub-synchronous mode} \\ s &< 0, \text{ for super-synchronous mode} \end{aligned} \quad (2.11)$$

Assume that the stator and rotor turn ratio is equal to one. For normal induction machine operation with a closed or resistor-connected rotor circuit, the mechanical power is positive and from the stator to the rotor when sub-synchronous (motoring) and is negative and from the rotor to the stator when super-synchronous (generating). This means the rotor voltage source has to be used to generate below the synchronous speed. The current directions are defined as to the right, from stator to rotor. The referred rotor voltage V_r/s can be conveniently divided into an electrical source V_r and a source representing electro-mechanical energy conversion $(1-s)V_r/s$. V_r is the actual voltage applied to the rotor through the slip rings and it is at slip frequency. However, this voltage has to go through a frequency conversion since the equivalent circuit is at stator (grid) frequency so that the referred voltage applied to the rotor equivalent circuit is V_r/s . Hence

$$\frac{\bar{V}_r}{s} = \frac{(1-s)\bar{V}_r}{s} + \bar{V}_r \quad (2.12)$$

The rotor power P_{R-elec} at the rotor terminals (positive means power flowing out of rotor due to current convention), the mechanical power P_{mech} , and the rotor copper loss P_{cu} are given by

$$\begin{aligned} P_{R-elec} &= 3 \operatorname{Re}\{\bar{V}_r \bar{I}_r^*\} \\ P_{mech} &= 3 \frac{(1-s)}{s} \operatorname{Re}\{\bar{V}_r \bar{I}_r^*\} + 3 \frac{(1-s)}{s} |\bar{I}_r|^2 R_r \\ P_{cu} &= 3 |\bar{I}_r|^2 R_r \end{aligned} \quad (2.13)$$

By inspection, P_{cu} is always positive, i.e., a loss. The second term of P_{mech} when sub synchronous is always positive; this means power is flowing from electrical to mechanical systems. Therefore the first term must be negative and greater than the second term to allow for sub synchronous generation since this will mean power flowing from mechanical to electrical systems. But $s > 0$ and V_r must be positive to oppose V_s and balance the voltage equation. Hence, I_r must be negative. If this is the case, then P_{R-elec} must also be negative so power is flowing into the rotor.

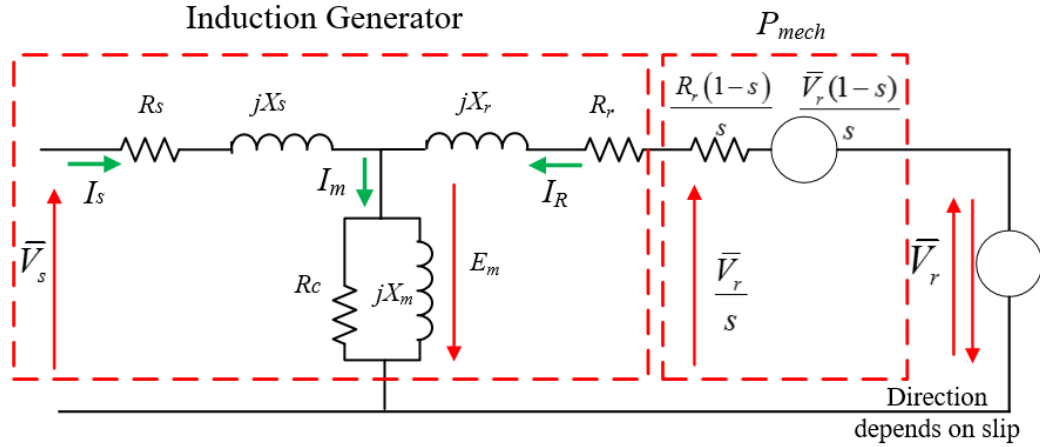


Figure 2.7. Equivalent circuit of doubly fed induction generator (DFIG).

The stator input power P_s (remember we are still using the motoring convention where positive power indicates that power flows into the stator and out of the rotor) and overall power generation P_{total} can be expressed as

$$\begin{aligned}
 P_s &= 3 \operatorname{Re} \left\{ \frac{\bar{V}_r}{s} \bar{I}_r^* \right\} + 3 |\bar{I}_r|^2 R_r + 3 |\bar{I}_s|^2 R_s \\
 P_s &= 3 \operatorname{Re} \left\{ \bar{V}_r \bar{I}_r^* \right\} + 3 \operatorname{Re} \left\{ \frac{(1-s)\bar{V}_r}{s} \bar{I}_r^* \right\} + 3 \frac{(1-s)}{s} |\bar{I}_r|^2 R_r + 3 |\bar{I}_r|^2 R_r + 3 |\bar{I}_s|^2 R_s \\
 P_{total} &= P_s - P_r = P_s - 3 \operatorname{Re} \left\{ \bar{V}_r \bar{I}_r^* \right\} \\
 P_{total} &= 3 \operatorname{Re} \left\{ \frac{(1-s)\bar{V}_r}{s} \bar{I}_r^* \right\} + 3 \frac{(1-s)}{s} |\bar{I}_r|^2 R_r + 3 |\bar{I}_r|^2 R_r + 3 |\bar{I}_s|^2 R_s
 \end{aligned} \tag{2.14}$$

In case of the sub-synchronous mode, and the requirement to generate, i.e., negative P_{total} , the input rotor power is amplified by the input mechanical power by $(1-s)/s$. At half synchronous speed, the first mechanical power conversion (first term on right hand side of P_{mech}) is equal to the electrical power at the rotor terminals [34]. When generating, then this means that the power coming out of the stator will be more than twice the input power to the rotor so that there is a lot of circulating energy and associated losses and loss of efficiency. This is because as the power flows through the circuit when generating, some power that will be returned to the mechanical source in the electro-mechanical resistance component (second term on right hand side of P_{mech}), and some will be dissipated in the circuit resistances (third and fourth terms on right hand side of P_{mech}). Hence, at high slip, the system will be inefficient because of the large amount of power cycling into the rotor and continuing through the stator and reduced through electro-mechanical energy conversion and loss.

Under super synchronous operation, $s < 0$ and when generating, the power will flow out of both the stator and rotor and operation will be much more efficient. The currents remain flowing in the same direction (against the arrows for I_s and I_r in the figure), but the rotor voltage is reversed.

The above discussion is in terms of generation. The current flows from right to left for generation against the motoring convention directions shown in the figure. For motoring operation, the current will now flow with the convention. This means power exits the rotor when sub synchronous and flows into the rotor when super synchronous.

The rotor is connected to back-to-back PWM inverters to the grid. The rotor side converter or resistors need a control system, which allows reliable operation of the machine under sub- and super-synchronous modes. One option is the rotor side converter

(RSC), where the RSC circuit controls the induced voltage and current of the rotor. In order to create torque in sub-synchronous mode of operation, it is important to control imposed current. When power flows out of the rotor then a line side converter (LSC) is needed to allow power to flow onto the grid. This will be for sub synchronous motoring and super synchronous generation. The LSC will also allow control of the power factor of the power onto the grid.

2.4 Induction Motor Faults

Induction machines are extensively used for most industrial applications over a large range of sizes because they have a simple construction and are reliable. On the other hand, faults may occur by exposure to non-ideal operating conditions in the industrial environment including overload, insufficient lubrication, frequent machine starts/stops, and cooling problems. The life cycle of an induction motor can be very long, so age will also be a factor. A variety of faults can occur within an induction machine within the course of normal operation. Sometimes these faults go undetected and can lead to catastrophic failure. Hence condition monitoring techniques have been developed for the detection and analysis of abnormal conditions [35].

In general, the induction machine faults are due to mechanical and electrical stresses [36]. Mechanical stresses are incurred by overloads and unforeseen load changes, which may cause bearing faults or a broken rotor bar. Electrical stresses are associated with the power supply, which may produce stator-winding short circuits. Fault mechanisms for induction machines have been extensively studied both by overseas and Australian researchers. According to IEEE and EPRI reports [20, 21], the most common faults in induction machines are distributed as shown in Table 2.1. These faults are briefly discussed on the

basis of their importance. There are some other faults related to the load, such as in large applications, because the induction machine is usually coupled with a mechanical load and gearbox. These faults often occur in the mechanical arrangement [37].

Table 2.1. Survey of induction machine faults including percentage of failure, causes, and methods used for faults detection.

| Major Components | Percentage (%) | | Causes | Detections Methods |
|---------------------------------------|----------------|------|----------------------------------------------|-----------------------------|
| | IEEE | EPRI | | |
| Electrical Faults | | | | |
| Rotor faults | 8 | 9 | Thermal-stresses | Stator current |
| | | | Corrosion | Axial flux |
| | | | Poor manufacturing | Vibration Torque, speed |
| Stator faults | 26 | 36 | Over heating | |
| | | | Over voltages | Axial flux |
| | | | Mechanical stresses | Stator current |
| Mechanical Faults | | | | |
| Bearing faults | 44 | 41 | Contamination | |
| | | | Improper- installation and lubrication | Stator current Vibration |
| | | | End of life | |
| Other faults (mainly eccentricity) | 22 | 14 | Bent rotor | Stator current |
| | | | Bearing wear | Vibration |
| | | | Misalignment | Axial flux |

Bearings are common elements of an electrical machine and Table 2.1 indicates that they are the single largest cause of machine failures. However, eccentricity and rotor faults represent a considerable proportion of all three-phase induction machine faults. This work addresses and tests these faults in wound-rotor since there has been little work focused on these faults in wound rotor machine. There are good examples in [11, 38].

2.4.1 Bearing Faults

Bearings are common elements of rotational machine, and they are the single largest cause of machine failures, as shown in Table 2.1. Bearings consists of two rings called the inner and the outer rings. A group of small balls or rollers are placed in raceways and rotate inside these rings as shown in Figure 2.8. A continuous stress on the bearings leads to fatigue failures at the rings, and these failures generate noticeable vibration and increased noise levels.

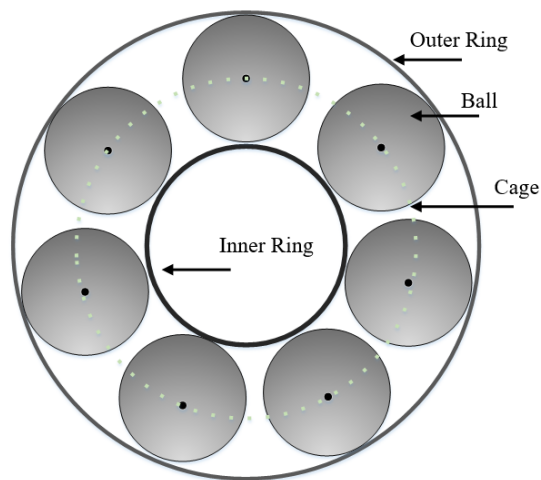


Figure 2.8. Induction machine bearing.

Improper lubrication, improper installation, and corrosion are further external factors that may increase the percentage of the failures. In addition, bearing failures could be

introduced by an abnormal change in voltage and current of the rotor, which results from asymmetrical flux distribution in the machine such as rotor eccentricity [13]. Bearing temperature is also one of the reasons for bearing failures. If the bearing exceeds a certain specific temperature level at rated condition, it will increase the percentage of the failures, According to [39], temperature measurements can provide helpful information about bearing health.

2.4.2 Stator Faults

Stator faults are essentially result of a breakdown of the stator winding insulation in adjacent turns of the stator coil [40], causing larger currents to flow in some turns. Figure 2.9 illustrates the three main types of stator winding faults including turn to turn faults, phase to phase faults, and phase to ground faults. A stator turn fault causes a large circulating current to flow and therefore produces excessive heat in the shorted turns. The heat is proportional to the square of flowing current, which may cause catastrophic failure [41]. If the machine is operating above the rated temperature, it will very likely fail even it has the good insulation. As a rule of thumb, the life of insulation is reduced by half for every 10°C increase above the stator windings temperature limit [42]. Therefore, many techniques were described in [43] for monitoring the stator winding temperature so that induction machines are prevented from running beyond their thermal capacity. Some other problems can accelerate insulation degradation including rotor unbalance, worn bearings, air gap eccentricity, and broken rotor bars.

The argument presented above makes it clear how important it is to detect mechanical failures early before they affect or damage the stator windings insulation [44, 45]. However, the turn to turn faults are the most difficult to detect at an early stage because

the other types of failures are often a consequence of turn faults. Many methods have been reported in [45, 46] to solve this problem.

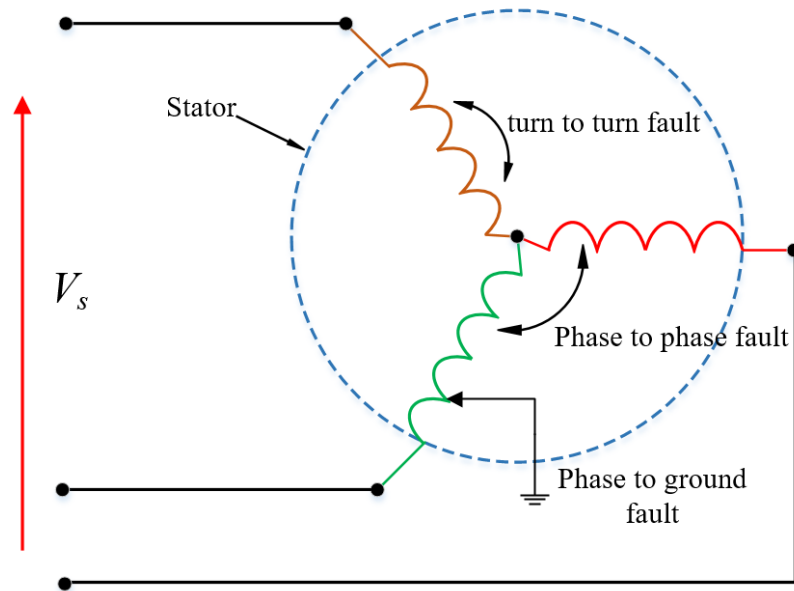


Figure 2.9. Stator winding faults: phase to phase, turn to turn and phase to ground circuit.

2.4.3 Rotor Faults

The rotor of induction machine is subjected to much lower voltage and much higher temperature than the stator. Therefore, the first common failure mode in the rotor is broken rotor bars in the SCIM and short-circuited rotor turns in the WRIM. This, in turn, can be caused by thermal or fatigue stresses. Such stresses in the rotor are commonly due to its design and construction [20, 21] such as poor manufacturing (defective casting or poor jointing).

The second common failure type is when rotor bars/windings are damaged and simultaneously the rotor is unbalanced. An asymmetrical distribution of the rotor current will result. This type of fault is related to air-gap eccentricity, which is presented in the

next section. Rotor current, flowed in the broken bars, will now flow in the two bars adjacent to it. Thus, the large thermal stresses may also damage the rotor. The temperature distribution across the rotor laminations is also affected by the rotor asymmetry. Rotor fault is briefly discussed here, and will be studied in more detail in Chapter 5.

2.4.4 Rotor Eccentricity Fault

An unequal distance in the air-gap between the stator and the rotor is known as eccentricity of the air-gap [3, 47, 48]. In cases of eccentricity in the air-gap, circuit inductances will vary, causing asymmetrical flux distribution in the air-gap. This imbalance produces electromagnetic forces between the stator and rotor. This electromagnetic force depends on the deviation of the rotor axis away from the stator axis, and the motion of the eccentric rotor in terms of its angular velocity. There are also considerable effects due to winding arrangement, loading and slotting. Eccentricity fault will briefly be discussed here and will be again studied in more detail in Chapter 6.

This force acts between rotor and stator in an irregular manner and pulls the rotor out of alignment. This is known as unbalanced magnetic pull (UMP). A high UMP may cause damage to the machine. Other vibrations can also be generated. Eccentricity often arises due to manufacturing tolerances. Inaccurate installation is another reason for increasing UMP, for example, when the bearings are incorrectly positioned or worn. A bent shaft, bearing wear and movement, or mechanical resonances at critical speeds can lead to dynamic eccentricity [49].

Assuming that the stator and rotor surfaces are perfectly circular, there are two main types of rotor eccentricity: static and dynamic [50]. Static eccentricity occurs when the axis of the rotor is at a constant distance from the centre of the stator, although the rotor still

rotates about its own axis. However dynamic eccentricity occurs when the rotational axis of the shaft is not the true axis, while it still rotates on the stator axis. Obviously, these conditions can occur simultaneously, and this phenomenon, called mixed eccentricity, is not necessarily constant down the bore [51]. The distribution of the magnetic flux density between the stator and the rotor will vary due to the eccentricity fault. When an air-gap asymmetry appears, a resultant radial force is produced on the rotor and stator, acting at the minimum air-gap [52]. Static eccentricity produces a steady pull on the rotor to one side while dynamic eccentricity produces a rotating force vector acting on the rotor and rotating with the rotor velocity. Figure 2.10 illustrates the different cases of eccentricity. The red areas in Figure 2.10 represent the minimum air-gap during the run-time.

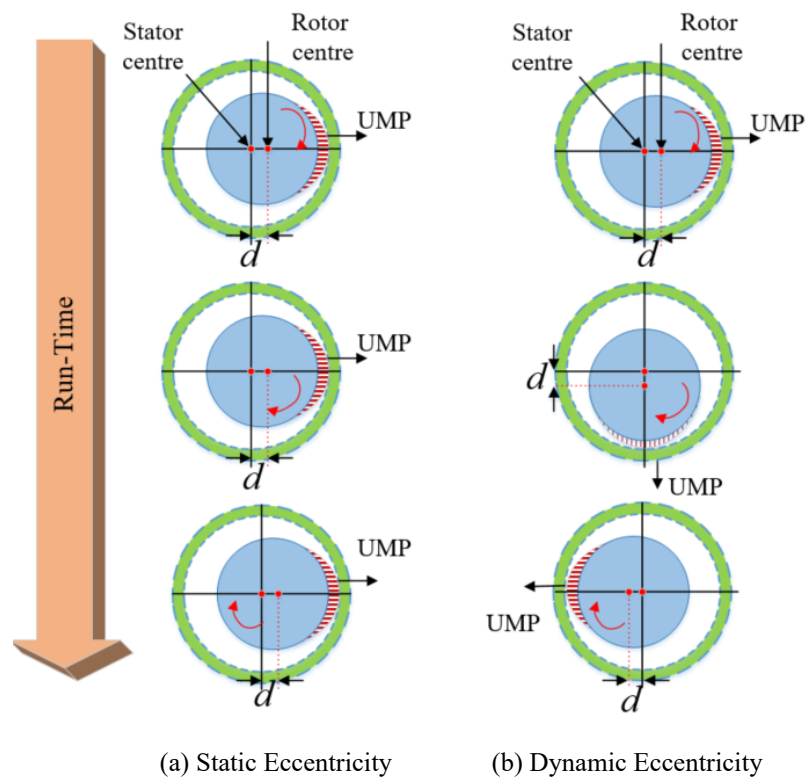


Figure 2.10. Illustration of the different cases of eccentricity including static eccentricity and dynamic eccentricity.

The UMP increases with the rotor diameter and the rotor length for a given air-gap eccentricity and flux density. For example, if the flux density increases from 1.0 T to 1.2 T, then the unbalanced pull forces will increase by 40-45% for a given eccentricity [53]. However, the power rating of the induction machine is usually improved by increasing the rotor length, rotor diameter for a given pole pair number, or by increasing the flux density in the air-gap.

By increasing the degree of air-gap eccentricity for a given machine design, rubbing can occur between the stator and rotor. For example, when there is a misalignment or bearing failure, the rotor can cause a puncture in the coil insulation of the coil laminations, resulting in the coil grounding. The rotor shaft has the smallest diameter in the rotor assembly and must be of sufficient diameter and mechanical stiffness to prevent rubbing between rotor to stator with a normal air-gap eccentricity level during starting and running. It should allow for some margin of error in case of any increase in operating air-gap eccentricity. It can be noted that air-gap eccentricity exists even in a healthy machine, but the permissible limit depends on the motor construction, e.g., 10 % for a healthy motor.

2.5 Condition Monitoring of the Induction Machine

Condition monitoring may be best defined as the continuous evaluation or periodic evaluation of the health of an electrical machine throughout its service life. The key is the ability to detect faults while they are still developing, a technique known as incipient failure detection [10]. By implementing efficient condition monitoring, it is possible to provide adequate warning of imminent failure. Thus, it is also possible to schedule future preventive maintenance and repair work [54]. As such, costs may be reduced by investing

in developing the condition monitoring of an induction machine. In order to improve reliability, productivity and safety, effective condition monitoring is critical.

Different methods for fault identification have been developed and used effectively to detect machine faults at different stages, using machine variables such as current, voltage, speed, torque, noise and vibrations [13, 15, 17, 55]. In the interests of safety and cost efficiency, it is important to monitor the behaviour of both large and small machines. In some applications, different techniques are used simultaneously to diagnose and monitor faults. Example of this are thermal measurements and chemical analysis [36]. In most cases, faults produce one or more indicative signs, such as:

- Unbalanced supply voltage and line currents.
- Changing in the torque pulsation and in the average torque.
- Increased power losses.
- Excessive heating.

Many diagnostic techniques used to analyse fault-related signals have been developed. These techniques involve a number of fields within science and technology [10, 54]. However, the most distinct condition monitoring methods are current monitoring, vibration monitoring, thermal monitoring, flux monitoring, and torque monitoring. In all the methods, the obtained signals from the machine are analysed continuously, thus identifying any significant change which would indicate a developing fault.

2.6 Existing Condition Monitoring Techniques

This section focuses on online condition monitoring techniques in an induction machine. A brief introduction to the different techniques available is first provided in this section.

When a fault occurs, it will introduce a change in some measured quantities that indicate the condition of an induction machine. Using a sensing element, these changes can be identified as shown in Figure 2.11. After data collection, a diagnostic process is necessary to characterise the fault. Different methods have been used to analyse the data, e.g., the fast Fourier transforms, wavelet transforms, fuzzy logic, neural networks, and Hilbert transforms [4, 55-59]. Many software tools [60] were developed to satisfy the requirements of faults detection and diagnosis. Detectable signs can be analysed in the time domain or frequency domain or in a combination of these (time-frequency analysis). In all the techniques, the obtained signals from the machine are analysed continuously, thus identifying any significant change that indicates a developing fault.

The scope of this project covers the first three stages in Figure 2.11: Faults, Fault Detection, and Signal Processing. However, it does not cover Expert Knowledge, Fault Diagnosis and Maintenance as shown in Figure 2.11.

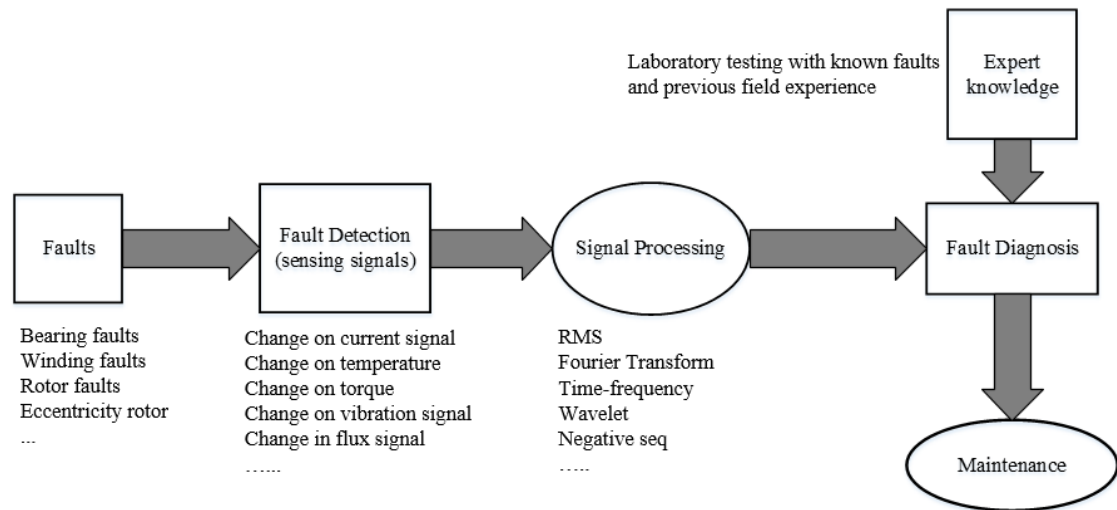


Figure 2.11. Condition monitoring process.

2.6.1 Current Monitoring

Current monitoring methods are the most attractive methods, essentially depending on monitoring the stator current in a non-invasive manner. This is also called current signature analysis [13, 61]. Current monitoring is widely used to diagnose faults such as broken rotor bars, abnormal levels of air-gap eccentricity, shorted turns in stator windings, and certain mechanical problems [14]. The stator current of an induction machine is available, and it can be analysed easily. In addition, current monitoring is a sensor-less detection method that can be implemented without any extra hardware [62]. These methods can be divided into three main groups: current spectral analysis, current Park's vector, negative-sequence and zero-sequence current monitoring.

There are numerous applications of utilised current spectral analysis, or MCSA, and it is the most commonly used method in the detection of rotor and stator faults. Essentially this method uses line current monitoring where the signature current sidebands are monitored. William *et al.* [63] have presented the fundamentals of using MCSA, and they

show that MCSA is a powerful online monitoring method for assessing the operational condition of a three-phase induction machine. Many industrial applications were addressed in [39, 43, 55, 64] that involved MCSA.

A clip-on current transformer can be used to measure the signal. Access to the machine is not required; the current can be measured in the supply side without disturbing to the operation of the motor [55]. Broken bars cause harmonics at the frequency given by

$$f_{bar} = f(1 \pm 2s) \quad (2.15)$$

in the stator current [55].

Thomson [55, 64] presented a classical analysis of the rotor slot passing frequency flux and current components that are spaced at twice the supply frequency $2f$ apart. These predict the current signature pattern that is a function of air-gap eccentricity. They are given by

$$f_{rs} = f \left\{ \frac{N_R}{p_m} (1-s) \pm n_{ws} \right\} \quad (2.16)$$

$$f_{ec} = f_{rs} \pm f_r$$

$$f_{ec} = f \left(\frac{N_R}{p_m} (s-1) \pm n_{ws} \right) \pm n_d \left(f \frac{(1-s)}{p_m} \right) \quad (2.17)$$

where f_{rs} are the frequency components due to rotor slotting, N_R is the number of rotor slots, $n_{ws} = 1,3,5,..$ corresponds to the fundamental component in the MMF waveform, and $n_d = 1,2,..$ is the air-gap eccentricity index. This gives the current components due to air-gap eccentricity at $\pm f_r$ around the rotor slot passing frequencies. Benbouzid [62, 65] studied the capability of MCSA analysis in the detection of various cage-rotor induction machine faults. Varieties of faults were successfully detected, such as asymmetrical

machine faults (including air-gap eccentricity and rotor asymmetrical resistances), broken bars, shaft speed oscillation, and bearing failure.

The second group is the Park's vector approach to the current analysis which is a two-dimensional representation of the three-phase line currents. Hence, it is essentially a description of the motor conditions. The stator current has no zero sequence component because the stator windings are usually not connected to a neutral point. In a healthy machine, balanced currents show a Park's vector that is a circular pattern centred at the origin of coordinates [66]. An automatic algorithm based on an unsupervised neural network for on-line analysis of three-phase induction machine stator faults was reported, and the detection of air-gap eccentricity in induction machine fault was studied in [67, 68]. The authors also reported that a Park's stator current vector approach can detect the air-gap eccentricity which was experimentally validated. According to this, the current stator equations of a three-phase induction machine can be converted into a two-phase d - q current set, which are stationary with respect to the stator and in quadrature. This is done through a matrix equation:

$$\begin{bmatrix} i_{ds} \\ i_{qs} \end{bmatrix} = \begin{bmatrix} \sqrt{\frac{2}{3}} & \frac{-1}{\sqrt{6}} & \frac{-1}{\sqrt{6}} \\ 0 & \frac{1}{\sqrt{2}} & \frac{-1}{\sqrt{2}} \end{bmatrix} \begin{bmatrix} i_A \\ i_B \\ i_C \end{bmatrix} \quad (2.18)$$

Recently much research has demonstrated how the Park's vector and the Concordia transform approach can enhance the detection of induction machine faults including rotor faults and bearing failure [66, 67, 69, 70]. However, with this technique comes a critical challenge, which is the ability to identify the types of faults, since they may cause similar stator current signatures [15].

The third group of analysis techniques consists of zero-sequence and negative-sequence current analysis techniques which are used to detect stator winding faults. When a stator fault occurs, such as a turn-to-turn short circuit, it creates an asymmetrical flux distribution in the air-gap of induction machine. This leads to zero-sequence and negative-sequence currents being generated, which can be detected by following the same procedure as in Park's vector method [71-73]. The accuracy of this method is questionable because such faults sometimes depend on mechanical load and operating conditions, causing misleading fault diagnosis.

Fault diagnosis can be done in real-time by analysing the frequency components of the stator current signals as stated earlier. This was discussed in [14, 61] and these systems allow precise and low-cost motor fault detection, and they are non-invasive. However, the methods developed are couched in terms of cage induction machines which may not be applicable to wound rotor machines. Wound rotor induction machine does not produce the same sideband currents as shown in [3].

Fault diagnosis can be performed using a variety of computer software. Some commonly used programs are MATLAB, ANSYS Maxwell, LabVIEW, Solid Works, as well as several others such as the Motor monitor program and fault tolerant software.

2.6.2 Thermal Monitoring

The thermal monitoring of induction machines can be carried out either by measuring the local or bulk temperatures of the motor or by parameter estimation. For example, when stator faults occur, they generate heat in the shorted turns. The heat extends until it reaches a destructive stage. The stator temperature can also be estimated based on stator resistance measurement as illustrated in [43, 74]. The researchers developed a thermal model of a

synchronous machine, and this thermal model was used to estimate the temperature of the motor and identify faults as shown in [75]. This model is based on finite element analysis (FEA) which is quite accurate, although it requires highly computational processes. Thermal measurements can be applied to detect rotor faults through rotor resistance identification [76]. In addition, this method needs comprehensive information about the machine including physical dimensions and construction materials, since the various materials have different characteristics.

Thermal measurements are very useful in detecting bearing faults because increased bearing wear increases the friction and temperature in the fault region. Thermal methods may be classified as indirect methods for evaluating some stator faults, and might be too slow to detect incipient faults inside the machine [77-79].

2.6.3 Vibration Monitoring

Noise and vibration are generated by all kinds of electric machines, and the condition of the machine during operation can be assessed by analysing the vibration. Vibration arises from mechanical forces, magnetic forces, and aerodynamics [80]. Electromagnetic radial forces are considered the most significant source of vibration in induction machines because the resultant MMF in the air-gap and permanence wave include the effect of any asymmetries in the machine. Vibration signals from a machine can be analysed to detect faults [81].

Vibration signal analysis has been widely used in fault detection of induction machines [59, 78, 82]. Faults create harmonics with different frequencies and power levels in the vibration signal. Consequently, the vibration signal is first sensed via a vibration sensor mounted on the stator frame, and then its spectrum is calculated using a Fourier transform

or a fast Fourier transform (FFT). The main source of noise production in induction machines is the UMP in the air-gap, since the resultant rotor MMF that was produced by unbalanced air gap flux waves contains the effect of any rotor and stator asymmetries. Cameron, *et al* [16] verified that air-gap eccentricity results in vibratory harmonics at frequencies of f_m , f_{m2} , f_{m3} , or f_{m4} . Imbalance in the rotor can also create rotating velocity vibration. Thus, it is not easy to detect the dynamic eccentricity individually by monitoring rotational velocity vibration. The high cost of vibration sensing is a drawback of the vibration monitoring technique. The acquisition of the vibration signals requires a significant investment. Vibration measurements are taken at each end of the motor, on the bearings, and in the horizontal and vertical axis positions.

2.6.4 Flux Monitoring

A flux monitoring method could offer reliable and accurate information on the condition of an electrical machine. Some reflected harmonic spectra would appear if any change occurs in the air-gap, winding, voltage, or current.

In [83] the authors studied the air-gap flux as a function of static eccentricity. A change in the air-gap flux can indicate a developing fault and can be reflected in the harmonic spectrum. Thomson, Rankin, and Dorrell [14, 84] investigated the relationships among air-gap flux, stator current, vibration signal, and air-gap eccentricity using complex analytical equations. These authors have undertaken many practical and analytical studies regarding detection of induction machine faults, especially eccentricity faults over the last 25 years.

The authors in [85] presented a technique for condition monitoring of electrical drives using special flux sensors. Rotor faults and air-gap eccentricity were detected using the

leakage flux in [86], which is obtained by means of a search coil placed at the rear end of the machine. In [87] specially designed search coils were placed under the stator winding wedges of the motor, and used for measuring the actual magnetic flux. Figure 2.12 shows an example of the use of search coils for condition monitoring. This represents the tested machine which has been used in this thesis. A search coil around the rotor shaft can also be used to evaluate axial flux components due to eccentricity [88, 89]. The resultant voltage of an axial search coil is proportional to the rate of change of the flux leakage, including some of fault frequencies. The main disadvantage is that it is not easy to install the search coil in the correct position to ensure that a reliable signal is obtained. A search-coil was used as a magnetic field sensor to measure the stray magnetic flux outside the motor in [57].

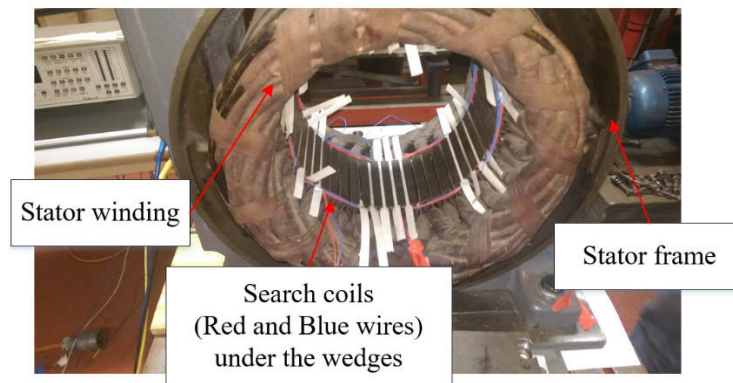


Figure 2.12. Search coils used in condition monitoring of induction machine.

Such flux measurement techniques are low cost and easy to implement. The main challenge for flux monitoring is the small air gap in most induction motors; the installation of search coils may require design modifications that may be difficult to implement.

2.6.5 Air-gap Torque Monitoring

The flux linkage and currents of an induction machine produce the air-gap torque. Faults create an unbalanced state, thereby influencing the air gap torque. Hsu [90] suggested a method for detecting defects such as cracked rotor bars and shorted stator coils. Air-gap torque can be measured while the motor is running. The zero frequency of the air-gap harmonics indicates that the machine is normal. A forward stator rotating field produces a steady torque. A backward stator field interacting with the rotor field creates an oscillating torque. Its frequency is given by:

$$\begin{aligned} \text{Frequency} &= \left[\begin{array}{l} \text{Stator field angular speed -} \\ \text{(Rotor field angular + Rotor field observed from Rotor)} \end{array} \right] \\ &= -\omega_s - \{ \omega_s (1-s) + s\omega_s \} = -2\omega_s \end{aligned} \quad (2.19)$$

A double slip frequency torque indicates an unbalanced rotor. However, once the leakage reactances and magnetic paths of the three phases become asymmetrical, errors are introduced and the calculation of air gap torque given in (2.19) is no longer accurate [91].

2.7 Literature Review of Wound-Rotor Faults

A understanding of the electric and mechanical behaviour of an induction machine in both healthy and faulty case is the key to creating an effective and reliable condition monitoring system [92]. The induction machine is a symmetrical machine, meaning that any fault can affect its symmetry and result in changes in its electric and/or mechanical behaviour [93]. Many authors have successfully introduced techniques for analysing asymmetrical wound rotor machines over several decades, including positive and

negative sequence equivalent circuits for the induction machine, stator current monitoring methods, and vibration signal analysis [55, 84, 94-96].

Elkasabgy *et al.* [97], Thomson and Stewart [98], and Filippetti *et al.* [99] focused on using motor current spectrum analysis (MCSA) in the cage-rotor machine to detect broken bar faults. In general, they have been developed using a Fourier analysis (FA) of the current or voltage at various speeds. Wound rotor machines have rarely been the focus of condition monitoring systems but are increasingly being used as wind turbine generators meaning there is a need to develop new condition monitoring techniques. These techniques must be appropriate to this machine. Smith [100] used a coupling impedance approach to evaluate the impact of MMF harmonics on the phase equivalent circuit of a slip-rig WRIM. The authors of [101] suggested a model for asymmetrical winding fault conditions using $d-q$ equations in a stationary reference frame and then compared the transient and steady state performance in healthy and faulty conditions. Vibration Monitoring for wound rotor induction machine was again investigated in [102]. However, this technique requires expensive monitoring tools. It makes use of load dependency of the identified fault components. Inter-turn short circuit faults in small WRIMs were studied in [103] through several analysis modes of signals from the numerical simulations.

In Section 2.5 there was a discussion about the symptoms of the rotor faults which can be observed using spectrum analysis of the stator current. However, fault frequency components can be present even in a healthy machine, making it difficult to detect some faults. The main target is to propose a relatively low cost and/or non-invasive system that could be used for condition monitoring systems for the prediction of WRIM and DFIG behaviour under healthy and faulty operating conditions. In this research, the impedance

matrix method will be used to detect rotor asymmetry faults. The impedance matrix for a healthy machine is developed in Chapter 3. The impedance technique has been used successfully in [3, 47] to investigate cage rotor machines with any number and distribution of bar and/or eccentricity faults. In [1, 2], Williamson *et al.* utilised impedance matrices to detect the faults in cage rotor machines; however, the wound rotor machine runs at a higher slip than the cage rotor machine; and in the DFIG slip energy recovery, as described in Section 2.3, is used to get generation when sub synchronous and over a wide speed range. Faults in wound rotor machines can vary greatly from the cage-rotor equivalent.

2.8 Literature Review of Air-gap Eccentricity

This section will be divided into two main parts; Air-gap Eccentricity and UMP Calculation, and Reduction of UMP.

2.8.1 Air-gap Eccentricity and UMP Calculation

Air-gap eccentricity is one of the more common faults of an induction machine. If the rotor is not concentric with the stator, an electromagnetic force is created in the direction of the minimum air gap, which could further increase the eccentricity [47]. Much of the recent eccentricity fault research is associated with condition monitoring and fault diagnostics. This electromagnetic force depends on the movement of the rotor axis away from stator axis, and the motion of the eccentric rotor in terms of its angular velocity. There are also considerable effects due to the winding arrangement, loading and slotting. This electromagnetic force is also called Unbalanced Magnetic Pull (UMP) as described earlier in Section 2.4. Studies of UMP first appeared around 1918. These works describe the air-gap eccentricity and calculate the generated UMP [104-107]. Rotating field theory

in a two-pole machine was used later, between 1955 and 1968, to introduce a method of UMP estimation [108-110]. It was concluded that static UMP produces vibrations at twice the supply frequency and dynamic UMP produces vibrations at twice the slip-frequency. Both Rai [111] and Cameron [112] investigated this experimentally and developed a general approach to detecting rotor eccentricity using high frequency noise.

Williamson and Eastham [113] developed winding analysis theory based on the study of machines using generalised harmonic analysis. This method has enabled calculation of an impedance matrix illustrating all stator and rotor currents and fields. Williamson and Smith [114] employed this method to identify rotor cage end-rings, inter-rings and stator windings faults. They linked various winding circuits and current flow to applied voltages, and successfully predicted UMP caused by broken rotor bars [100, 112, 115, 116].

Furthermore, Swann in [117] used an interesting conformal transformation technique for induction machine analysis. Dorrell and Smith in 1994 applied both methods of the generalised harmonic analysis and the conformal transformation to an induction machine to calculate the UMP. They used parallel stator windings and measured the resulting UMP [118]. Variation in the direction of UMP due to the parallel stator winding paths was observed in their studies. Tenhunen *et al.* in [119] investigated the effect of magnetic saturation on UMP using the Finite Element method. The main finding was that the magnetic saturation reduced the eccentricity harmonics and the UMP. Dorrell in [120] included saturation effects in the UMP calculation and concluded that saturation can cause considerable reduction of UMP.

In 1969, Heller and Jokl studied the magnetic fields in the air-gap using permeance harmonic analysis [121], which was then used to identify the integrated effects of rotor

saturation, eccentricity and slotting in magnetic field analysis [122, 123]. Berman 1993 [124] examined the equalisation of connection effects in stator coils of induction machines with rotor eccentricities using permeance harmonic analysis.

The WFA (Winding Function Approach) was used to study the stator and rotor currents and inductances in the induction machines [125, 126]. This approach was introduced in 1987 by Lipo [127], investigating the effect on inductance of a rise in MMF and rotor bar skewing. The MWFA (Modified Winding Function Approach) approach was developed in [128, 129]. It was then used to study the increase in MMF across the slots and rotor skewing in a machine with dynamic eccentricity [130].

Loading the machine produces an increase in the UMP, as investigated by Dorrell on the cage rotor induction machine [47, 131, 132]. He worked on UMP reduction, seeking the factors of parallel stator and rotor winding connections under variable frequency operation which can influence the UMP in eccentric rotor machines [3, 133].

Many researchers have addressed UMP; however, the challenge is how UMP can be accurately measured [7, 8]. In [134] UMP was measured by load cells, but this had drawbacks; for example, the eccentricity degree did not remain constant as force was exerted. In contrast, piezoelectric transducers were used to measure UMP in [135], being mounted separately for rotor and stator. This method was quite effective in UMP measurement since these transducers were mounted on a plate with the stator, and the rotor was mounted separately on pedestals. Dorrell also used finite element analysis (FEA) to predict the UMP in induction machine [34, 48]. Dorrell in [50] proved that UMP can be altered with varying load and voltage in an induction motor.

Andrej and Antero in [136] numerically investigated the UMP due to an eccentric cage rotor. They covered a wide whirling frequency range which becomes particularly

important when considering the electromechanical interactions in electrical machines. Again, they found the behavior of the UMP is determined mostly by the magnetic field harmonics introduced by the rotor eccentricity.

2.8.2 Reduction of UMP

In recent years the reduction of radial electromagnetic forces has been the objective of many studies. In order to damp the UMP in the case of an eccentric rotor, the additional air-gap flux waves of $p_m \pm 1$ should be eliminated or reduced. Three approaches have been previously suggested to achieve this; the use of equalising windings on the stator, the use of stator damper windings to reduce the side-band flux waves; and reconnecting the stator coils groups to build parallel paths from the winding current [52, 136, 137].

The reduction of UMP in induction motors is achieved by using a parallel connection of the stator coil groups in order to reduce the additional air-gap flux density due to eccentricity [3] as shown in Figure 2.13. The two parallel paths illustrate the equalising connections in the induction machine, and I_{q1} and I_{q2} represent the equalising current. Magnetic field harmonics due to rotor eccentricity generate currents circulating in the parallel paths of the rotor and stator windings. These currents equalise the magnetic field distribution in the air gap, and hence reduce the resultant UMP. [138, 139] studied the effect of parallel paths in the stator windings, finding that use of parallel paths can lead to a large reduction in UMP. It is worth mentioning that Finite Element Analysis assisted in the understanding of parallel paths in the stator windings.

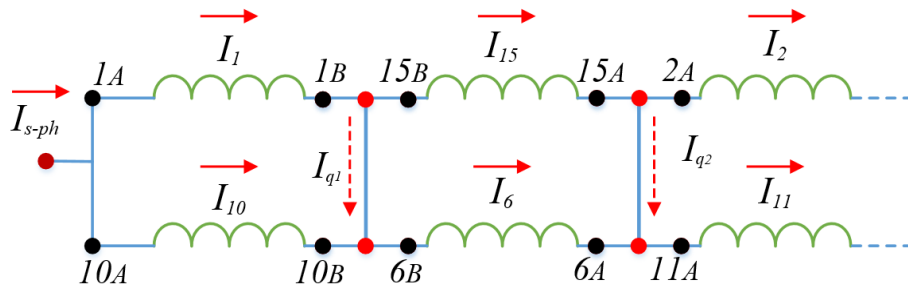


Figure 2.13. Phase winding of a four-pole induction machine, with two parallel paths involving three series connected coils each. This figure covers the coil numbers 1, 2, 6, 10, 11, and 15.

The results of the experiment in [140] show that parallel stator windings effectively attenuate the net eccentricity force by suppressing significantly the eccentricity harmonics related to the fundamental magnetic field. However, the stator winding normally contains fewer parallel paths. Therefore, the degree of UMP reduction may depend on the position of the rotor axis displacement.

There is a difference between the cage rotor and wound rotor in the generated UMP. The cage rotor will have a substantial differential which can add to the produced UMP but many parallel paths that can attenuate the UMP; while the wound-rotor machine will not have as many parallel paths like the cage that can damp $(p_m \pm 1)$ flux waves generated by the eccentricity. It has been illustrated that the wound rotor machine has much higher UMP compared to the cage machine [141]. Berman in [133] reported similar results of reducing UMP using parallel connections. The experimental findings have shown that using equalising connections in the stator, the UMP of an induction machine can be reduced by 25 times. The particular winding scheme has been called the bridge configured winding (BCW) scheme [142], where the currents flowing across this bridge are known

as equalising currents. This demonstrated the effect of equalising currents (applied to the bridge) on the magnetic field coupled with rotor eccentricity.

A two-pole induction machine was presented in [4], and was built with four-pole damper windings in stator. The test has shown that using the extra 4-pole stator winding to damp the four pole flux reduced the total vibration significantly and the test machine became more stable. The authors measured and predicted the unipolar flux in the machine. These techniques are still under investigation, consequently they are developed to include the damper windings to reduce the UMP. Other research has been focussed on the design and implementation of these coils such as a current sensor that aim to detect and reduce the eccentricity faults. [57, 143, 144].

2.9 Literature Review Observations

Building a reliable and accurate monitoring technique requires a deep understanding of the mechanical and electric characteristics of the induction machine. A healthy machine demonstrates different behaviours from a faulty machine. This literature review pointed out that current monitoring techniques are the most commonly used commercial techniques, since they are sensorless detection methods that can be implemented without any extra hardware.

The literature review has also shown that mechanical vibration can also appear in the stator current harmonic components. Increasing the vibration in the machine naturally increases the magnitude of these components.

The following observations were identified on the basis of information discussed in the literature review:

- a. There has been little research devoted to the detection of various faults in induction machine using one technique under varying loading conditions, i.e. the combination of eccentricity faults and rotor faults. Also, there has been little work focused on wound rotor machine faults. There are good examples in [11, 38]. Regarding this, theoretical and experimental works will be presented in Chapters 5 and 6.
- b. Focusing on eccentricity fault detection, the MCSA methods developed are couched in terms of cage induction machines which may not be applicable to wound rotor machines [48, 145]. Regarding this, more discussion and clarification will be presented in Sections 3.2.3 and 6.1.
- c. Vibration techniques pose challenges related to the cost. The vibration sensor and equipment are very expensive. Another drawback of vibration measurement is that the sensors need to be mounted on the frame of the machine, meaning that the machine needs to be accessible. This may not be possible at all times, especially in a complicated industrial application. Regarding this, more discussion and clarification will be presented in Section 6.9.11.
- d. There is still a need to investigate the reliability of condition monitoring techniques when they are applied to specific applications involving a large machine with low critical speeds. An example is the doubly fed induction generator (DFIG) when used in a wind turbine. Such these applications are often inaccessible and hence require special attention. Regarding this, more discussion and clarification will be presented in Sections 2.3 and 5.4.

2.10 Chapter Summary

This chapter briefly explored the basic concept of the induction machine. The literature review then discussed the main induction machine faults including bearing faults, rotor faults, stator faults and eccentricity faults. The purpose of condition monitoring was defined. Many plants are high cost capital investments or are involved in high turn-over production, so it is advantageous to invest in a monitoring system. With a condition monitoring system, faults can be detected at an early stage. Maintenance can then be carried out during planned downtime at an early stage, thereby protecting the machine or plant from catastrophic failures. There are many diagnostic methods for detecting faults in induction machines, which were outlined in the chapter.

Chapter 3: Machine Modeling by Impedance Matrix

This chapter provides the harmonic field analysis for the wound rotor induction machine. The aim of the analysis is to develop expressions which can consider any stator or rotor winding in order to predict the behaviour of the machine. The current distribution in the rotors of the SCIM and the WRIM is discussed; the calculation of these currents is the main aim of using the impedance matrix. The developed electromagnetic torque can also be determined from the stator and rotor current density distributions. The analysis outlined in this chapter leads to the building of the impedance matrix, which includes all coupling and mutual impedances. An equivalent circuit for a wound rotor induction machine, which includes external resistances, is derived. The matrix model is based on applying winding, rotating field, and coupling impedance theories.

3.1 Introduction

A survey of the literature covered several aspects related to detecting faults in these machines. Generally, stator winding connections and the influence of the rotor currents should be considered when evaluating the machine state in a healthy condition and a faulty condition. This involves the calculation of all machine currents from which the various field components and hence any asymmetry can be calculated.

The first stage of the project is directed towards the development of a model of the machine with stator and rotor windings. This was done using the permeance harmonic method, which was subsequently compared and verified experimentally. The major feature of this approach is the ability to produce analytical expressions for the field

harmonics in both symmetrical and asymmetrical cases, and to produce analytical expressions of UMP. The permeance harmonic method can be further developed to include various winding harmonics in the machine. The rotor skew and Carter correction factor can be included in these analytical expressions.

In this chapter, the conductor density method of analysing machine windings [47] is implemented to allow the calculation of currents in individual coil groupings. The main advantage of this analysis is that it can be used in two ways when dealing with a rotor which is concentric or not concentric with the stator. Hence this makes the harmonic conductor density method suitable for condition monitoring.

Determining the currents flowing in the various stator and rotor windings is the first stage in evaluating rotor symmetry or asymmetry. This can be done by using the coupling impedance method described in [47]. The machine analysis resolves the air-gap flux into a harmonic series of travelling waves with different pole numbers rotating in either direction. These can be derived using the currents and the spatial positioning of the rotor and stator conductors that are represented in the form of a harmonic Fourier series of surface current density. Finally, this produces an expression for the conductor density distribution in terms of a harmonic series and can be derived using complex Fourier analysis to account for the magnitude and positioning of conductors on the stator and rotor surfaces. The harmonic conductor density method of analysing machine windings has been used successfully in [47, 100] to analyse cage induction machines with any number and distribution of bar and/or eccentricity faults. In [1, 2], Williamson *et al.* used impedance matrices to detect the faults in cage rotor machines; however, the wound rotor machine works at a much higher slip than cage rotor machine, especially when used in a slip energy recovery scheme. The faults in these machines can vary greatly from their

cage-rotor equivalent [3] and they are substantially higher. Here, the method is developed to include rotor coil groupings for the wound rotor induction machine in the same way.

3.2 Harmonic Field Analysis

This analysis produces expressions which can consider any stator winding and is developed further to include the rotor winding. A comparison of current distribution in the cage rotor and the wound rotor is stated in this section to simplify the expressions that include the rotor winding currents. If it is assumed that there is poor coupling between the stator and rotor for the winding harmonics ($n > 1$) then these are ignored. Since the rotor is rotating, the relationship between the stator and rotor coordinates must be determined; the relationship is described here.

3.2.1 Harmonic Conductor Density Distribution

In an induction machine with asymmetrical stator windings, fields will be produced which may have sub-fundamental machine pole-numbers. It is easier to start by analysing a fundamental number of pole-pair of one ($p_m = 1$). Each group of stator series coils must be analysed individually. An expression for the complex conductor density distribution of a stator winding is derived by using a linearised machine. The winding distribution of the phase band is established, which is expressed in the form of a harmonic Fourier series of surface current density distribution.

Assume that a coil has C_s turns on a stator surface as shown in Figure 3.1. The conductor density over the slot opening b_s is the number of coil turns divided by the slot opening. Using complex Fourier series, the distribution can be represented as

$$\begin{aligned}
 n_s(y) &= \sum_{n=-\infty}^{\infty} (\bar{C}_s^n e^{-jnky}) \\
 \bar{C}_s^n &= \int_{y_1-b_s}^{y_1+b_s} \frac{C_s}{b_s} e^{jnky} dy - \int_{y_2-b_s}^{y_2+b_s} \frac{C_s}{b_s} e^{jnky} dy = \frac{k_s^n C_s}{2\pi r} (e^{jnky_1} - e^{jnky_2}) \\
 n &= 1, -5, 7, -11, \dots
 \end{aligned} \tag{3.1}$$

where the stator slot opening factor is given by

$$k_s^n = \frac{2 \sin(0.5 n p_m k b_s)}{n p_m k b_s} \tag{3.2}$$

where x is the variation in the axial direction, y is the variation in the tangential direction, z is the variation in the radial direction, $k = 1/r$ where r is the average of air-gap radius, and n is the stator harmonic conductor density distribution.

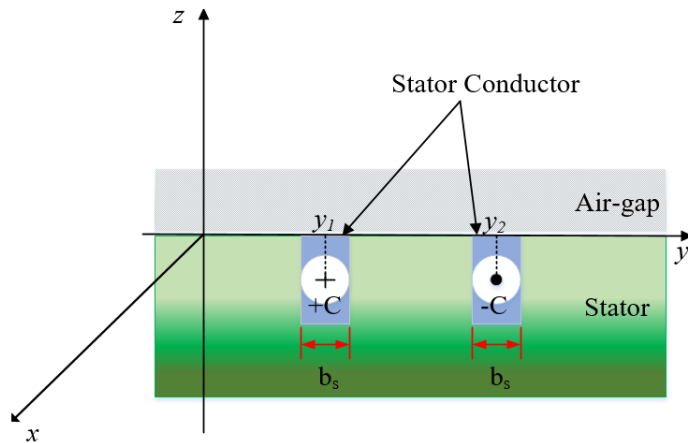


Figure 3.1. Single-coil located on the surface of the stator.

Using this summation to get expression for a number of series connected windings, the winding coefficient is obtained by the spatial distribution of all the coils so that

$$\bar{N}_{st}^n = \frac{1}{2\pi r} \sum_{w=1}^{N_s} k_s^n C_s e^{jnp_m ky} \tag{3.3}$$

where C_s is the number of conductors of the winding in the s^{th} slot (the sign will indicate whether the path is outgoing or returning) and N_s is the total number of slots. The current density distribution of the winding can be calculated from

$$j_s(y, t) = \text{Re} \left[\sum_{n=-\infty}^{\infty} \bar{I}_s \bar{N}_{st}^n e^{j(\omega t - nky)} \right] \quad (3.4)$$

and this will be used to derive an expression for the air-gap flux density as in [47].

Since the research focuses on the wound rotor machine, the rotor conductor distribution is calculated in a similar manner to the stator phase windings. Suppose $(+C, -C)$ is a coil in the first phase winding (r_1) in the rotor as in Figure 3.2, where x is the variation in the axial direction and y' is the variation in the tangential direction. If this is represented as having finite conductor width of b_r (the rotor slot opening), the conductor density over the slot opening is the number of coil turns divided by the slot opening. Its distribution can be then represented as a complex Fourier series as

$$\begin{aligned} n_{r_1}(y') &= \sum_{\nu=-\infty}^{\infty} (\bar{C}_{r_1}^{\nu} e^{-j\nu ky'}) \\ \bar{C}_{r_1}^{\nu} &= \int_{y'_1-b_r}^{y'_1+b_r} \frac{C_{r_1}}{b_r} e^{j\nu ky'} dy' - \int_{y'_2-b_r}^{y'_2+b_r} \frac{C_{r_1}}{b_r} e^{j\nu ky'} dy' = \frac{k_r C_{r_1}}{2\pi r} (e^{j\nu ky'_1} - e^{j\nu ky'_2}) \\ \nu &= \pm 1, \pm 3, \pm 5 \dots \end{aligned} \quad (3.5)$$

The harmonic number ν accounts for the fundamental plus winding harmonics. The winding coefficient is defined by the spatial distribution of all the coils

$$\bar{N}_{r_1}^{\nu} = \frac{1}{2\pi r} \sum_{w=1}^{N_R} k_r^{\nu} C_{r_1} e^{j\nu p_m ky'} \quad (3.6)$$

where N_R is the total number of rotor slots and C_r is the effective rotor turns per phase. The slot opening factor is defined by the rotor slot opening b_r so that

$$k_r^v = \frac{2 \sin(0.5 \nu p_m k b_r)}{\nu p_m k b_r} \quad (3.7)$$

Rotor skewing can be incorporated into this analysis, as explained in Appendix B. Skew can also be applied to the stator.

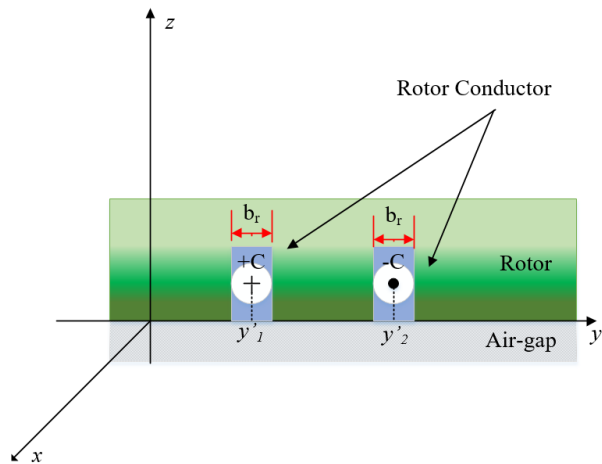


Figure 3.2. Single-coil located on the surface of the rotor.

3.2.2 Differences in the Rotor Current of SCIM and WRIM

When the rotor cage is symmetrical, the bar currents are of equal amplitude and the phase progression is fixed around the rotor periphery. The whole rotor cage current can then be represented by the current flowing in a single bar. It is clear that the rotor loop currents share common paths down the bars. Figure 3.3 shows that the number of currents required to specify the rotor current distribution fully. If a cage has N_b bars, there will be $2N_b$ nodes and $3N_b$ branches. The currents [114] flow in loops comprising two adjacent rotor bars and the end-ring segments that join them, together with a circulating current I_e in one of the end rings if there is an end ring fault.

However, the wound rotor has a complete set of three-phase windings that are similar to the windings on the stator, and the ends of the three rotor wires are connected to slip rings

on the rotor shaft, as mentioned earlier. They are usually permanently star connected on the rotor, otherwise six slip rings would be required rather than three. A similar expression can be obtained for the 3-phase winding in the rotor. The analysis is more straightforward than the cage rotor because the rotor loops currents (I_1 , I_2 and I_3) do not share any common paths, as shown in Figure 3.3.

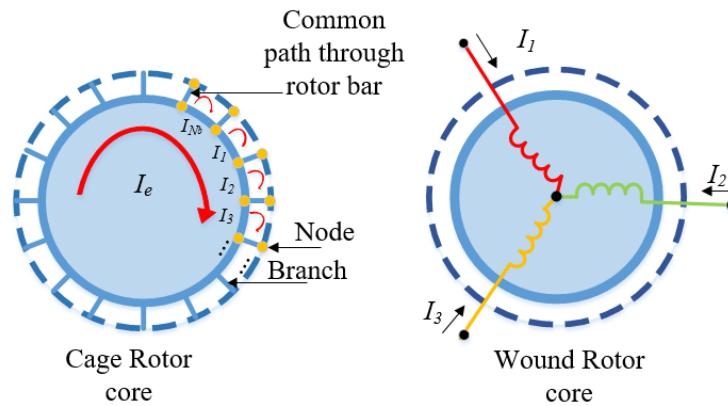


Figure 3.3. Current distribution in the cage and wound rotors. In the rotor cage, this shows rotor-loop currents and the sharing of common paths. In the wound rotor, this shows the three phase windings.

The literature review indicates that there is another difference between the wound-rotor and cage-rotor, which is related to the air-gap MMF. When the rotor is not centred in an induction machine, the unbalanced magnetic pull (UMP) can vary substantially with voltage and load [50] and this can be difficult to assess. In this research a wound rotor machine is investigated; the UMP in this type of machine can vary greatly from its cage-rotor equivalent [3] and it is substantially higher. Figure 3.4 illustrates this with a breakdown of the air-gap MMF and flux waves in terms of a 4-pole squirrel cage machine and this figure shows the interaction of these [146]. The main difference is the lack of 2-pole and 6-pole MMF waves on the rotor that can damp the additional flux waves generated by the rotor eccentricity, hence reducing the UMP. This is because the cage

structure has many effective parallel paths, which even out the air-gap flux and reduce the radial pull. The use of additional damper windings has been investigated [3, 85, 141] and a similar theme is investigated here.

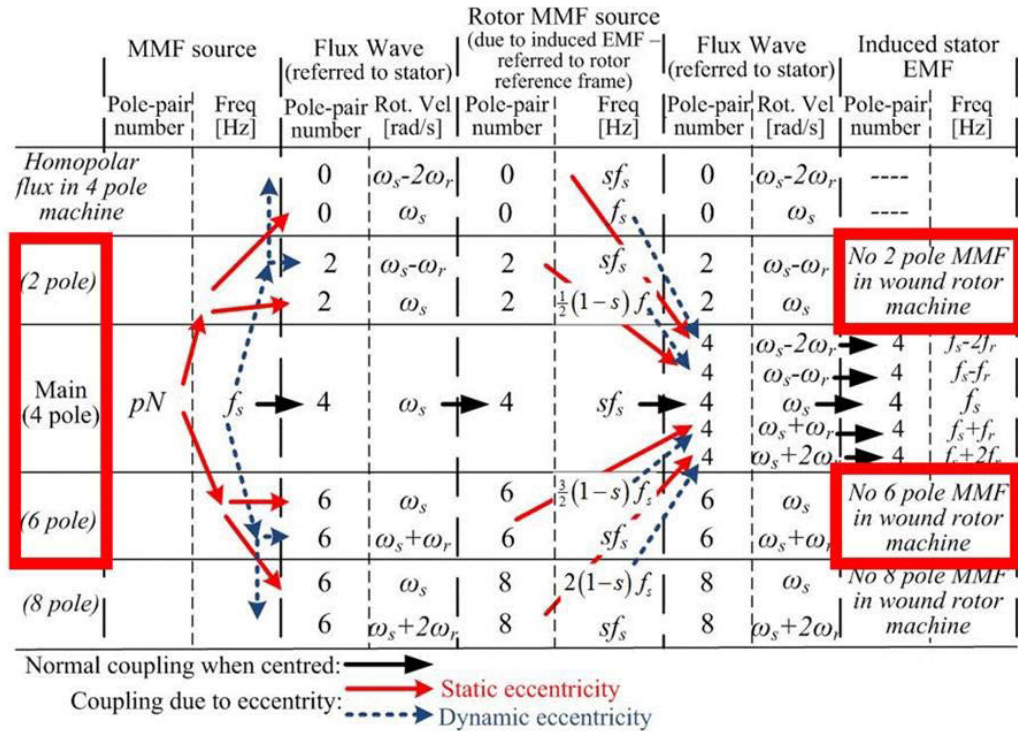


Figure 3.4. Air-gap MMF and flux waves in terms of pole or harmonics number and frequency for a cage induction machine [146].

3.2.3 Co-ordinate System of the Wound Rotor Induction Machine

The stator reference frame is used to represent equation (3.1). This is valid for the rotor if the machine stalled. However, the rotor is rotating at a specific speed with respect to the stator. It is necessary to set up a relationship between the stator and rotor co-ordinates. The co-ordinate system for the stator and rotor can be determined using the linearised machine [147] in Figure 3.5. It is assumed that the origin of the stator co-ordinates θ_1 lies on the magnetic axis S-S1 of the coil (+ C_s , - C_s). The axis R-R1 represents the rotor

reference axis, formed by the coil (+ C_R , - C_R) in the rotor. The circumferential location of any point in mechanical radians from the reference axis of the stator is represented as θ_1 , while its location in mechanical radians to the rotor axis is represented as θ_2 .

$\alpha_s = \frac{2\pi}{N_s}$: Slot-angle of the stator in mechanical radians,

and $\alpha_R = \frac{2\pi}{N_R}$: Slot-angle of the rotor in mechanical radius.

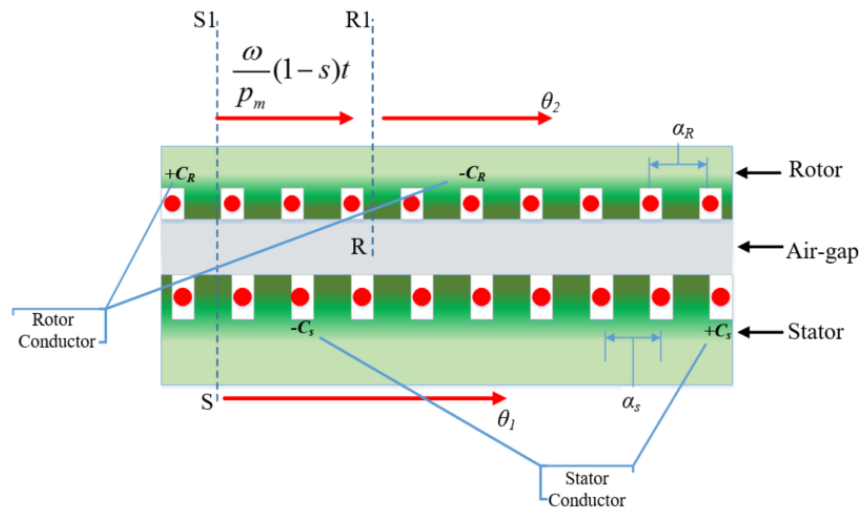


Figure 3.5. Co-ordinate system for the stator and rotor.

The rotor revolves with a speed of $\frac{\omega}{p_m}(1-s)$, so the relationship between θ_1 and θ_2 is

$$\theta_1 = \theta_2 + \frac{\omega}{p_m}(1-s)t \quad (3.8)$$

The distance y' denotes the tangential distance around the circumference of the rotor surface from a reference point on the rotor as stated earlier. The final expression of the stator and rotor reference frames is shown in (3.8). Assume $\theta_1 = ky$ and $\theta_2 = ky'$. The relationship holds between coordinate θ_1 and θ_2 where

$$y = y' + \left(\frac{\omega}{P_m} (1-s)r \right) t \quad (3.9)$$

3.2.4 The Flux Density Produced by Stator and Rotor Current

Distribution

The stator winding produces a series of MMF harmonic distributions when supplied by a balanced three-phase voltage source. The MMF distributions can be found by resolving the stator phase conductors into a complex Fourier conductor density distribution as derived by Dorrell in [47]. Using the expression of stator winding coefficient, defined earlier in (3.3), and assuming the three-phase supply is balanced with series connected stator windings, the MMF wave is given by

$$j_s(y, t) = \text{Re} \sum_{n=-\infty}^{\infty} \bar{J}_s^n e^{j(\omega t - np_m ky)} \quad (3.10)$$

For a balanced three-phase current set I_s , using the identity $a = e^{(j2\pi/3)}$, the MMF magnitude is

$$\bar{J}_s^n = \bar{N}_{st}^n (1 + a^{1-n} a^{n-1} + a^{n-1} a^{1-n}) \bar{I}_s = 3 \bar{N}_{st}^n \bar{I}_s \quad (3.11)$$

The rotor winding currents set up distributed rotating MMF waves, which can be expressed as

$$\bar{J}_r^{nv}(y', t) = \bar{I}_r^n \bar{N}_r^{nv} e^{j(s_n \omega t - np_m ky')} \quad (3.12)$$

s_n is the slip defined for the n^{th} harmonic field as in [100]. Transferring to a stator reference frame

$$\bar{J}_r^{nv}(y, t) = \bar{I}_r^n \bar{N}_r^{nv} e^{j(s_f \omega t - np_m ky)} \quad (3.13)$$

where $s_f = 1 - n(1 - v)(1 - s)$

A similar expression for balanced three-phase rotor currents is expressed in (3.12). Ampere's circuital law can be applied to obtain the air-gap flux density that is produced by the current distribution.

This is obtained from

$$b_s(y, t) = \int \mu_o \frac{j(y, t)}{g(y)} .dy \quad (3.14)$$

Subsequently, the electrical field in the air-gap can be calculated using

$$e(y, t) = \int \frac{db_s(y, t)}{dt} .dy \quad (3.15)$$

This expression can be used to calculate the EMF $u(t)$ induced into the winding using the conductor distribution. This is done using

$$u(t) = \text{Re} \int -e(y, t) n(y) .dy \quad (3.16)$$

where $n(y)$ is the winding distribution.

The stator and rotor cores are assumed to have infinite permeability so that only the MMF drop across the air-gap is considered, μ_o represent the permeability of free space, and the effects of saturation are ignored. The EMF equation in (3.16) can be used to calculate the coupling impedances, such as between two phase bands in the rotor or stator. In addition to this, the coupling impedances between the rotor windings and the stator windings can be derived in a similar fashion, as discussed next sections.

The harmonic conductor density distribution of the stator winding that was calculated in equation (3.3) results in the stator current density expressed in equation (3.10). The slot

opening factor K_s^n is assumed to be unity because the slot width is very thin compared with the stator surface size. Assume that the flux crosses the air-gap radially, since the air-gap is very small compared with the diameter. Ampere's law is applied in Figure 3.6 so that

$$\frac{g}{\mu_0} \left(b_s(y,t) + \frac{\delta b_s(y,t)}{\delta y} \Delta y - b_s(y,t) \right) = j_s(y,t) \Delta y \quad (3.17)$$

Using the derivative of equation (3.15) gives

$$\begin{aligned} db_s(y,t) &= \frac{\mu_0}{g} j_s(y,t) \cdot dy \\ b_s(y,t) &= \mu_0 \Lambda_s(x,y) \left[\int j_s(y,t) dy + C_{Homopolar} \right] \end{aligned} \quad (3.18)$$

where Λ_s is the inverse of the air-gap length g . The final expression is

$$b_s(y,t) = \text{Re} \left[\sum_{n=-\infty}^{\infty} \bar{B}_s^n e^{j(\omega t - np_m ky)} \right], \text{ and } \bar{B}_s^n = -\frac{j\mu_0}{knp_m g} \bar{N}_{st}^n \bar{I}_s \quad (3.19)$$

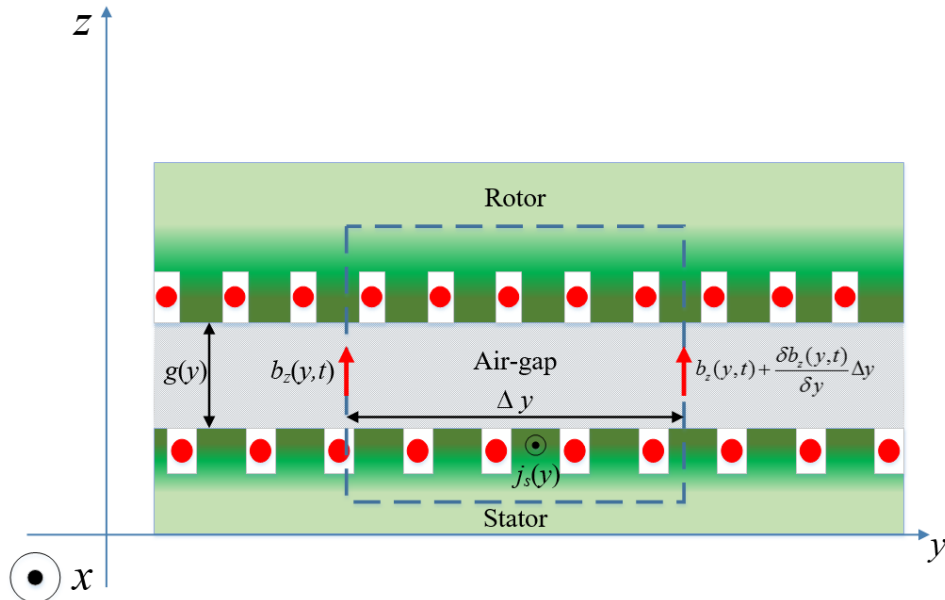


Figure 3.6. Applying Ampere's law around a closed loop.

The constant $C_{Homopolar}$ is included to control for any homopolar flux. This is a component of flux which crosses the air-gap only once and returns to the stator using alternative paths, such as the shaft, or the machine casing. This was investigated in [47, 131, 135]. It is negligible here since the rotor is mounted separately so that $C_{Homopolar}$ is ignored. In reality it is likely only to be significant in 2-pole machines where shaft voltages due to axial fluxes are noted in many machines.

The expression for the stator air-gap flux density waveform (3.19) can be used to calculate the rotor flux waves which contain waves of similar pole number and rotational velocity and their differential waves. The rotor air-gap flux wave components can also be obtained from

$$b_r(y, t) = \text{Re} \left[\sum_{n=-\infty}^{\infty} \sum_{\nu=-\infty}^{\infty} \bar{B}_r^{n\nu} e^{j(\omega_s t - \nu p_m k y)} \right] \text{ and } \bar{B}_r^{n\nu} = -\frac{j\mu_o}{k\nu p_m g} \bar{N}_r^{n\nu} \bar{I}_r^n \quad (3.20)$$

The air-gap field produced by the stator currents can now be used to determine the various coupling impedances in Section 3.3.

3.3 Impedance Matrix

Analysis methods for induction machines are either analytical or to use finite element analysis. Both methods are achieved using computational techniques to solve the magnetic circuit and produce performance predictions. The mechanical and electrical behaviour of the induction machine can be described using an impedance matrix. In this method, the currents are resolved and the torque obtained under steady-state operation for an applied supply voltage [146, 148-150]. The authors in [114] used the conductor density method to build the impedance matrix. This approach was used to evaluate the induction machine faults, such as broken bars [2], eccentricity [114, 148], and stator winding shorts

[62, 64, 151]. Dorrell [152] has applied this method to analyse brushless doubly-fed reluctance machines. The study in [72] introduced a robust, on-line turn-fault detection technique for induction machines based on monitoring the sequence components and an impedance matrix. In general, the impedance matrix technique can be utilised in the modelling and analysis of induction machine with faults. The study of induction machine in steady state, transient and fault cases necessitates accurate knowledge of equivalent circuit parameters. These parameters will change to reflect the severity of the fault. The finite element method (FEM) is extensively used for induction machine parameter identification in normal and fault conditions. However, all these studies focused on the cage rotor induction machine; here the wound rotor machine is investigated. The method will also include the effect of auxiliary windings to detect and control a rotor eccentricity fault.

This section establishes a steady-state impedance matrix of a three-phase induction machine including all mutual and coupling impedances. The impedance matrix is used to solve the circuits and cross-coupling in an induction machine. For an applied voltage, the currents are resolved, and the torque and the losses calculated under steady-state operation. This matrix analysis is valid for any combination of unbalanced winding. Here the analysis is developed for a balanced rotor; Chapter 5 and 6 deal with unbalance and faults where the impedance matrix is developed to account for rotor faults and where auxiliary stator windings (with two and six poles) and the main stator winding are considered separately. Thus, the matrix can be used to monitor and control eccentricity faults.

The matrix can include MMF harmonics so that the asynchronous torque dips due to the 3rd, 5th, 7th, etc. spatial MMF harmonics can be calculated for torque/speed curves. The

number of parallel windings in the stator and rotor will set the matrix size. If all windings are connected in series, then the matrix size will be 6×6 . These numbers represent the three-phase stator winding and the three-phase rotor winding. An impedance matrix of this size includes the self and mutual impedances between the stator and rotor phase windings. However, for a balanced machine this can be condensed by representation of just one of the phases in a balanced three-phase set and an assumption of replication for the other two with a 120-degree phase shift. Here, to illustrate this, only one phase of stator winding and all three phase of rotor windings are used to develop the impedance matrix, which reduces the matrix to a 4×4 size:

$$\begin{aligned}
 \begin{bmatrix} \bar{V}_s \\ 0 \\ 0 \\ 0 \end{bmatrix} &= \sum_n [\bar{Z}]^n \begin{bmatrix} \bar{I}_s \\ \bar{I}_{r_1}^n \\ \bar{I}_{r_2}^n \\ \bar{I}_{r_3}^n \end{bmatrix} = \sum_n \begin{bmatrix} \bar{Z}_{s,s}^n & \bar{Z}_{s,r_1}^n & \bar{Z}_{s,r_2}^n & \bar{Z}_{s,r_3}^n \\ \bar{Z}_{r_1,s}^n & \bar{Z}_{r_1,r_1}^n & \bar{Z}_{r_1,r_2}^n & \bar{Z}_{r_1,r_3}^n \\ \bar{Z}_{r_2,s}^n & \bar{Z}_{r_2,r_1}^n & \bar{Z}_{r_2,r_2}^n & \bar{Z}_{r_2,r_3}^n \\ \bar{Z}_{r_3,s}^n & \bar{Z}_{r_3,r_1}^n & \bar{Z}_{r_3,r_2}^n & \bar{Z}_{r_3,r_3}^n \end{bmatrix} \begin{bmatrix} \bar{I}_s \\ \bar{I}_{r_1}^n \\ \bar{I}_{r_2}^n \\ \bar{I}_{r_3}^n \end{bmatrix} \Big|_{n=1,-5,7,-11,13,\dots} \\
 &\approx \begin{bmatrix} \bar{Z}_{s,s} & \bar{Z}_{s,r_1} & \bar{Z}_{s,r_2} & \bar{Z}_{s,r_3} \\ \bar{Z}_{r_1,s} & \bar{Z}_{r_1,r_1} & \bar{Z}_{r_1,r_2} & \bar{Z}_{r_1,r_3} \\ \bar{Z}_{r_2,s} & \bar{Z}_{r_2,r_1} & \bar{Z}_{r_2,r_2} & \bar{Z}_{r_2,r_3} \\ \bar{Z}_{r_3,s} & \bar{Z}_{r_3,r_1} & \bar{Z}_{r_3,r_2} & \bar{Z}_{r_3,r_3} \end{bmatrix} \begin{bmatrix} \bar{I}_s \\ \bar{I}_{r_1} \\ \bar{I}_{r_2} \\ \bar{I}_{r_3} \end{bmatrix} \Big|_{n=1}
 \end{aligned} \tag{3.21}$$

Superscripts n represent the stator harmonic. The first line incorporates all the asynchronous harmonics. If it is assumed that there is poor coupling between the stator and rotor for the winding harmonics ($n > 1$) then these are ignored as illustrated in the second line. The voltage vector is split into stator and rotor terms. It is assumed that the rotor windings are short circuited (no external impedances); an external impedance will be added later. The symbols s , r_1 , r_2 , and r_3 correspond to stator and rotor phase windings respectively. The current vector includes the stator and rotor terms. I_s is the main stator current in phase 1, I_{r1} , I_{r2} , and I_{r3} are the currents in the rotor windings. $Z_{s,s}$ and $Z_{r,r}$ are the

stator-stator coupling impedance and the rotor-rotor coupling impedance respectively. These should still incorporate higher harmonics which act as differential leakage. $Z_{s,r}$ and $Z_{r,s}$ are the rotor-stator coupling impedance and the stator-rotor coupling impedance respectively. The rotor currents in (3.21) can be obtained from knowledge of the applied voltages when the matrix is solved. The rotor voltage set is zero because the three-phase rotor windings are short-circuited together. By following the approach in [100, 149], the coupling and mutual impedances for rotor and stator can be determined. The remainder of the section will be devoted to the determination of the impedances.

3.3.1 Stator-Stator Coupling Impedance

The air-gap field can be used to form a voltage equation (3.16) and hence the back-EMF in the stator winding can be calculated. This can then be related to all the winding currents. If the machine is balanced then this need only be defined by the stator-stator coupling impedance which incorporates the self and mutual inductances. For a balanced machine, the per-phase stator impedance can be written with reference to the winding resistance, leakage reactance and the main reactance where

$$\bar{Z}_{s,s} = R_s + jX_s + jX_{ss} \quad (3.22)$$

X_{ss} is the magnetising reactance for the three-phase winding. This can be obtained for a balanced machine using (3.16). To illustrate the derivation of the reactance then the working is shown from the electric field and winding harmonic to

$$\begin{aligned}
 u_{S1.Sm}(t) &= \text{Re} \int -e_{Sm}(y,t) n_{S1}(y) \cdot dy = \text{Re} \left[jX_{S1,Sm} \bar{I}_m e^{j\omega t} \right] \\
 u_{s,s}(t) &= u_{S1.S1}(t) + u_{S1.S2}(t) + u_{S1.S3}(t) \\
 u_{s,s}(t) &= \sum_n \text{Re} \left[jX_{S1,S1}^n \bar{I}_1 e^{j\omega t} + jX_{S1,S2}^n \bar{I}_2 e^{j\omega t} + jX_{S1,S3}^n \bar{I}_3 e^{j\omega t} \right] \\
 u_{s,s}(t) &= \sum_n \text{Re} \left[jX_{S1,S1}^n \bar{I}_1 e^{j\omega t} + jX_{S1,S2}^n a^{-1} \bar{I}_1 e^{j\omega t} + jX_{S1,S3}^n a \bar{I}_1 e^{j\omega t} \right] \quad (3.23) \\
 u_{s,s}(t) &= \sum_n \text{Re} \left[jX_{S1,S1}^n \bar{I}_1 e^{j\omega t} + ja^n X_{S1,S1}^n a^{-1} \bar{I}_1 e^{j\omega t} + ja^{-n} X_{S1,S1}^n a \bar{I}_1 e^{j\omega t} \right] \\
 u_{s,s}(t) &= \sum_n \text{Re} \left[j3X_{S1,S1}^n \bar{I}_1 e^{j\omega t} \right] = \text{Re} \left[jX_{ss} \bar{I}_1 e^{j\omega t} \right] \\
 X_{ss} &= 3 \sum_n \frac{2\pi\mu_0 \omega L_{st} \bar{N}_{st}^n}{k^3 n^2 p_m^2 g} (\bar{N}_{st}^n)^*
 \end{aligned}$$

where m is the m^{th} winding of the stator which has I_m current and n is the n^{th} winding harmonic where $n = 1, -5, 7, -11, 13$, etc. The symbols s_1, s_2 , and s_3 correspond to stator phase windings respectively. The 3 in the term for X_{ss} indicates a three-phase winding so this is a reactance that combines the self and mutual reactances between the difference stator windings. For a well distributed winding this can often be approximated to the fundamental magnetizing reactance where $n = 1$.

3.3.2 Stator-Rotor Coupling Impedance

Taking (3.19) to provide an expression for the air-gap field produced by the stator winding, and transferring this to a rotor reference frame, it becomes:

$$b_{rt}(y', t) = \text{Re} \sum_{n=-\infty}^{\infty} \left[\bar{B}_{st}^n e^{j(s_n \omega t - np_m ky')} \right] \quad (3.24)$$

where s_n is the slip defined for the n^{th} stator harmonic field

$$s_n = 1 - n(1 - s) \quad (3.25)$$

The stator-rotor coupling impedance is

$$\bar{Z}_{r_1,s}^n = 3 \frac{j2\pi\mu_0\omega s_n L_{st} k_{sk} \bar{N}_{st}^n}{k^3 n^2 p_m^2 g} (\bar{N}_{r1}^n)^* \quad (3.26)$$

and it includes a conventional rotor skew factor k_{sk} where

$$k_{sk} = \frac{\sin\left(\frac{np_m\theta_{sk}}{2}\right)}{\left(\frac{np_m\theta_{sk}}{2}\right)} \quad (3.27)$$

The conventional rotor skew factor k_{sk} is explained in Appendix B. The coupling impedances for the other rotor phases are related to $\bar{Z}_{r_1,s}^n$ via

$$\bar{Z}_{r_2,s}^n = a^n \bar{Z}_{r_1,s}^n \quad \text{and} \quad \bar{Z}_{r_3,s}^n = a^{-n} \bar{Z}_{r_1,s}^n \quad (3.28)$$

Again, often only the fundamental coupling is considered where $n = 1$.

3.3.3 Rotor-Stator Coupling Impedance

The rotor phase windings will have currents at slip frequency, which is appropriate to the stator field which induces it. The current in the rotor will be obtained from (3.12) and transformed to the stator reference frame as in (3.14). The rotor-stator coupling impedance is \bar{Z}_{s,r_1}^n , so that

$$\bar{Z}_{s,r_1}^n = \frac{j2\pi\mu_0\omega L_{st} k_{sk} \bar{N}_{r_1}^n}{k^3 n^2 p_m^2 g} (\bar{N}_{st}^n)^* \quad (3.29)$$

$$\bar{Z}_{s,r_2}^n = a^n \bar{Z}_{s,r_1}^n \quad \text{and} \quad \bar{Z}_{s,r_3}^n = a^{-n} \bar{Z}_{s,r_1}^n \quad (3.30)$$

Note the lack of the 3 term in (3.29) since this is now one individual rotor phase inducing an EMF into phase 1 of the stator. The $n=1$ harmonic is often only considered.

3.3.4 Rotor-Rotor Coupling Impedance

The rotor current produces a harmonic series distribution, which induces back-EMFs in the rotor windings. Every rotor phase is consequently inductively coupled with every other phase via the rotor air-gap flux. These induced voltages can be summed together to produce an impedance in the same way in the stator winding. Rotor-rotor coupling impedances will be

$$\bar{Z}_{r_1, r_1}^n = \bar{Z}_{r_2, r_2}^n = \bar{Z}_{r_3, r_3}^n = \frac{2}{3} j s_n \sum_v X_{rr}^{nv} \quad (3.31)$$

where X_{rr}^{nv} represents the ν^{th} differential harmonic of the n^{th} harmonic rotor magnetising reactance. The factor (2/3) converts magnetising reactance from a three-phase winding to a single phase winding. The mutual coupling impedances between the rotor phases are determined from

$$\bar{Z}_{r_2, r_1}^n = \bar{Z}_{r_3, r_2}^n = \frac{2}{3} j s_n \sum_m \cos(2\pi n\nu / 3) X_{rr}^{mv} \quad (3.32)$$

where X_{rr}^{mv} is the 3-phase reactance similar to (3.23):

$$X_{rr}^{mv} = 3 \frac{2\pi\mu_0 \omega s_n L_{st} k_{sk} \bar{N}_r^{nv}}{k^3 n^2 \nu^2 p_m^2 g} (\bar{N}_r^{mv})^* \quad (3.33)$$

The rotor self-impedances are modified to include resistance and the leakage inductance so that

$$\bar{Z}_{r_1, r_1}^n = \bar{Z}_{r_2, r_2}^n = \bar{Z}_{r_3, r_3}^n = (R_r + j s_n X_r) + \frac{2}{3} j s_n \sum_v X_{rr}^{nv} \quad (3.34)$$

The use of the term m allows differential terms of the different n^{th} rotor winding harmonics and this can often be attenuated to a series $\nu = 1$.

3.4 Voltage Equations

The system of N complex linear equations, where N is the number of rows in the matrix (3.21), can be solved by any convenient means to find the N unknown currents.

The 4×4 impedance matrix technique described above can be used to find the steady-state equivalent circuit for the wound rotor machine with balanced rotor currents. If it is unbalanced there will be a backwards rotating $2s - 1$ stator EMF induced into the stator which is explored later. As illustrated in (3.21), the impedance matrix can be further reduced to

$$\begin{bmatrix} \bar{V}_s \\ 0 \end{bmatrix} = \begin{bmatrix} \bar{Z}_{s,s}^1 & \bar{Z}_{s,r}^1 \\ \bar{Z}_{r,s}^1 & \bar{Z}_{r,r}^1 \end{bmatrix} \begin{bmatrix} \bar{I}_s \\ \bar{I}_r \end{bmatrix} \quad (3.35)$$

for a single rotor phase when the rotor has balanced phases set. This is similar to the treatment of the stator winding so that

$$\begin{aligned} \bar{Z}_{r,r}^1 &= (R_r + js_1 X_r) + js_1 \sum_v X_{rv} \\ \bar{Z}_{r,s}^1 &= 3 \frac{j2\pi\mu_0 \omega s_1 L_{st} k_{sk} \bar{N}_{st}^1}{k^3 p_m^2 \mathcal{G}} (\bar{N}_{r_1}^1)^* \\ \bar{Z}_{s,r}^1 &= 3 \frac{j2\pi\mu_0 \omega L_{st} k_{sk} \bar{N}_{r_1}^1}{k^3 p_m^2 \mathcal{G}} (\bar{N}_{st}^1)^* \end{aligned}$$

This gives the voltage equations

$$\begin{aligned} \bar{V}_s &= \bar{Z}_{s,s}^1 \bar{I}_s + \bar{Z}_{s,r}^1 \bar{I}_r \\ 0 &= \bar{Z}_{r,s}^1 \bar{I}_s + \bar{Z}_{r,r}^1 \bar{I}_r \end{aligned} \quad (3.36)$$

which leads to the rotor current

$$\bar{I}_{r_1} = \left(\frac{-\bar{Z}_{s,r}^1}{\bar{Z}_{r,r}^1} \right) \bar{I}_s \quad (3.37)$$

so that

$$\bar{V}_s = \left(\bar{Z}_{s,s}^1 - \frac{\bar{Z}_{s,r}^1 \bar{Z}_{r,s}^1}{\bar{Z}_{r,r}^1} \right) \bar{I}_s \quad (3.38)$$

which can easily be solved for the current. This can also be used to obtain the standard per-phase equivalent circuit.

3.5 Power and Torque Calculation

The impedance matrix is first assembled, and then adjusted to create the desired fault condition which will require development of the basic impedance matrix described in Section 3.4. The input power and reactive power may be calculated in a straightforward manner from the stator voltage and current since the stator supply is assumed to be ideal where

$$\bar{S} = 3\bar{V}_s \bar{I}_s^* \quad (3.39)$$

The input power can be calculated from the positive sequence mains frequency current using

$$P_i = \text{Re}\{3\bar{V}_s \bar{I}_s^*\} \quad (3.40)$$

The developed electromagnetic torque can be determined from the stator and rotor current density distributions, which are generated as a result of the interaction between the stator and rotor fields [115]. The stator and rotor current densities are $j_s(y,t)$ and $j_r(y,t)$ respectively, which includes only the forward components for the healthy condition and neglecting of higher terms. However, in Chapter 6, there will be backward components in these expressions when a machine has an eccentric rotor. The torque is given by

$$T = \frac{2\pi r^2 \mu_o L_{st}}{p_m \mathcal{G}} \text{Re}\{j(\bar{J}_s \bar{J}_r^*)\} \quad (3.41)$$

This torque includes the state steady developed by the machine. Note the j operator in the Real term calculation. This shows that torque is developed by the stator and rotor current waves that are orthogonal to each other. Using these parameters, an impedance matrix was built. The torque was measured with a short-circuited rotor. Figure 3.7 presents the measured and predicted values of the torque for a healthy machine, neglecting the harmonic components. This is a good approximation to demonstrate the validity of the analysis including the neglecting of the asynchronous torque dips. The measured torque is lower than predicted, and there is a difference in pull out torque points. There are several possible reasons for this, including friction and windage which are not measured and iron losses which are not included, and refinement of leakage inductance would also help in improving the calculation accuracy. The referred rotor current for the first phase can be obtained from

$$I_{R_1} = -\left(\frac{T_{ratio}}{k_{sk}}\right) I_{r_1} \quad (3.42)$$

as well as for I_{R2} , and I_{R3} , where t_{ratio} is the stator-rotor turns ratio given by

$$t_{ratio} = \frac{N_{st}}{N_r} \quad (3.43)$$

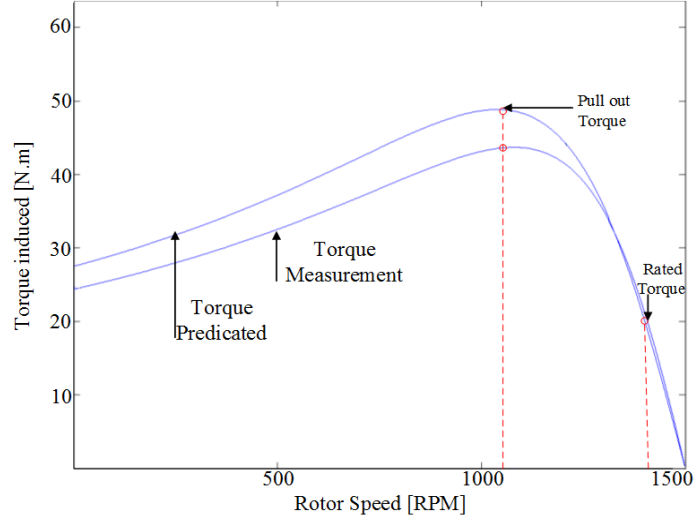


Figure 3.7. Experimental and predicted torque versus speed characteristics for balanced rotor for a four-pole wound rotor induction machine.

3.6 Wound-Rotor Equivalent Circuit

The voltage equation in (3.36) can be obviously used to find the steady state equivalent circuit of the induction machine. By breaking down the voltage equations in (3.36)

$$\vec{V}_s = \left(R_s + jX_s + jX_{ss} - \frac{\bar{Z}_{s,r_1}^1 \bar{Z}_{r_1,s}^1}{\bar{Z}_{r_1,r_1}^1} \right) \vec{I}_s \quad (3.44)$$

So that

$$\vec{V}_s = \left(R_s + jX_s + \frac{jX_{ss} \bar{Z}_{r_1,r_1}^1 - \bar{Z}_{s,r_1}^1 \bar{Z}_{r_1,s}^1}{\bar{Z}_{r_1,r_1}^1} \right) \vec{I}_s \quad (3.45)$$

Hence

$$\vec{V}_s = \left(R_s + jX_s + \frac{(jX_{ss})^2}{jX_{s,r_1} jX_{r_1,s}} \left[\frac{jX_{s,r_1} jX_{r_1,s}}{jX_{ss}} \left(\bar{Z}_{r_1,r_1}^1 - \frac{jX_{s,r_1} jX_{r_1,s}}{jX_{ss}} \right) \right] \right) \vec{I}_s \quad (3.46)$$

where, for clarity, in numerator of the fraction term in (3.45)

$$jX_{ss} \bar{Z}_{r_1, r_1}^1 - \bar{Z}_{s, r_1}^1 \bar{Z}_{r_1, s}^1 = \frac{(jX_{ss})^2}{jX_{s, r_1} jX_{r_1, s}} \frac{jX_{s, r_1} jX_{r_1, s}}{jX_{ss}} \left(\bar{Z}_{r_1, r_1}^1 - \frac{jX_{s, r_1} jX_{r_1, s}}{jX_{ss}} \right)$$

And the denominator is

$$\bar{Z}_{r_1, r_1}^1 = \frac{jX_{s, r_1} jX_{r_1, s}}{jX_{ss}} + \left(\bar{Z}_{r_1, r_1}^1 - \frac{jX_{s, r_1} jX_{r_1, s}}{jX_{ss}} \right)$$

Simplifying equation (3.46) by multiplying the top and bottom of the square bracketed

term by $\frac{(jX_{ss})^2}{jX_{s, r_1} jX_{r_1, s}}$ gives

$$\bar{V}_s = \left(R_s + jX_s + \frac{(jX_{ss})^2}{jX_{s, r_1} jX_{r_1, s}} \left[\frac{jX_{ss} \left(\bar{Z}_{r_1, r_1}^1 - \frac{jX_{s, r_1} jX_{r_1, s}}{jX_{ss}} \right)}{jX_{ss} + \frac{(jX_{ss})^2}{jX_{s, r_1} jX_{r_1, s}} \left(\bar{Z}_{r_1, r_1}^1 - \frac{jX_{s, r_1} jX_{r_1, s}}{jX_{ss}} \right)} \right] \right) \bar{I}_s \quad (3.47)$$

The manipulations in the above equations are necessary to find terms that can be linked to the equivalent circuit per phase [149]. In this circuit, the rotor components are referred to the stator. In (3.47) a turns-ratio can be defined squaring the terms relating the stator and rotor circuits as in (3.48), which is derived from the expression defined in (3.43)

$$\begin{aligned} \frac{(jX_{ss})^2}{jX_{s, r_1} jX_{r_1, s}} &= \frac{\left(j3 \frac{2\pi\mu_0 \omega L_{st} \bar{N}_{st}^n}{k^3 n^2 p_m^2 g} (\bar{N}_{st}^n)^* \right)^2}{\left(3 \frac{j2\pi\mu_0 \omega s_f L_{st} k_{sk} \bar{N}_{r_1}^1}{k^3 p_m^2 g} (\bar{N}_{st}^1)^* \right) \left(3 \frac{j2\pi\mu_0 \omega L_{st} k_{sk} \bar{N}_{r_1}^1}{k^3 p_m^2 g} (\bar{N}_{st}^1)^* \right)} \quad (3.48) \\ &= \frac{1}{s_f} \left(\frac{N_{st}}{N_r} \right)^2 = \frac{(t_{ratio})^2}{s_f k_{sk}^2} = \frac{(t_{ratio})^2}{s_n k_{sk}^2} \Bigg|_{\substack{v=1 \\ s_f=s_n}} \end{aligned}$$

The rotor impedance is then given by

$$\left(\frac{(jX_{ss})^2}{jX_{s,r_1}jX_{r_1,s}} \left(\bar{Z}_{r_1,r_1}^{-1} - \frac{jX_{s,r_1}jX_{r_1,s}}{jX_{ss}} \right) \right) = \left(\frac{R_r}{s_n k_{sk}^2} + \frac{jX_r}{k_{sk}^2} \right) + jX'_{ss} \frac{(1-k_{sk}^2)}{k_{sk}^2} \quad (3.49)$$

Hence the referred rotor impedance is

$$\frac{R'_r}{s_n} + jX'_r = \frac{(T_{ratio})^2}{s_n} (R_1 + jX_r) \quad (3.50)$$

The third term in (3.49) is called the rotor skew reactance term [153]. X_{ss} is much higher than the skew reactance term because the skew factor is usually close to one. If the skew factor is unity (i.e., no skew) the skew reactance disappears. The equivalent circuit is then given in Figure 3.8. Also, the core loss resistance is incorporated in the circuit.

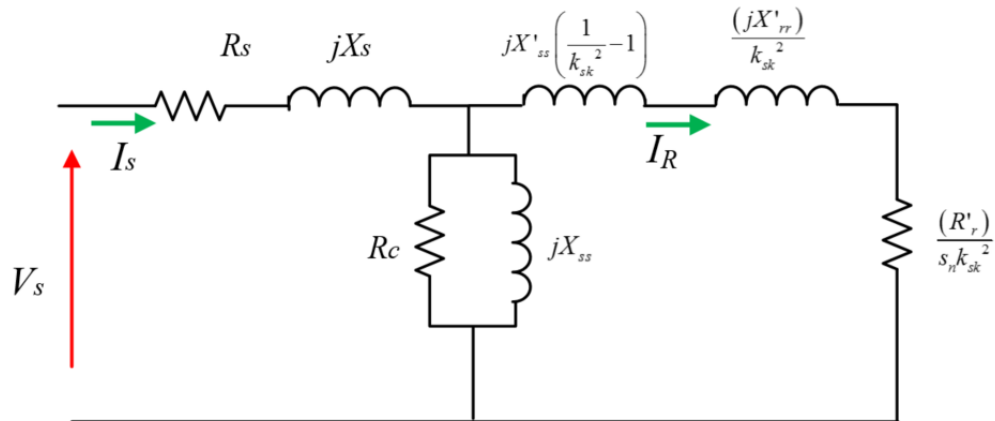


Figure 3.8. Equivalent circuit for wound-rotor induction machine as derived.

3.7 Inclusion of Rotor External Circuits

The currents in the stator and rotor winding are related to the main supply voltage by means of the matrix equation as given in (3.21). Hence this matrix equation represents the complete rotor, before any fault has occurred. The matrix equation defined in (3.21)

assumes that the rotor windings are short-circuited. In order to consider any additional circuitry associated with non-supply frequency source impedance (stator winding), soft starting (extra rotor impedance), and slip energy recovery voltages from an inverter, then (3.21) can be further developed to become

$$\begin{bmatrix} \bar{V}_s \\ \bar{V}_{r1} \\ \bar{V}_{r2} \\ \bar{V}_{r3} \end{bmatrix} = [\bar{Z}] \begin{bmatrix} \bar{I}_s \\ \bar{I}_{r1} \\ \bar{I}_{r2} \\ \bar{I}_{r3} \end{bmatrix} = \begin{bmatrix} \bar{Z}_{s,s} & \bar{Z}_{s,r1} & \bar{Z}_{s,r2} & \bar{Z}_{s,r3} \\ \bar{Z}_{r1,s} & \bar{Z}'_{r1,r1} & \bar{Z}_{r1,r2} & \bar{Z}_{r1,r3} \\ \bar{Z}_{r2,s} & \bar{Z}_{r2,r1} & \bar{Z}'_{r2,r2} & \bar{Z}_{r2,r3} \\ \bar{Z}_{r3,s} & \bar{Z}_{r3,r1} & \bar{Z}_{r3,r2} & \bar{Z}'_{r3,r3} \end{bmatrix} \begin{bmatrix} \bar{I}_s \\ \bar{I}_{r1} \\ \bar{I}_{r2} \\ \bar{I}_{r3} \end{bmatrix} \quad (3.51)$$

where

$$\begin{aligned} \bar{Z}'_{r1,r1} &= \bar{Z}_{r1,r1} + Z_{ex,r1} \\ \bar{Z}'_{r2,r2} &= \bar{Z}_{r2,r2} + Z_{ex,r2} \\ \bar{Z}'_{r3,r3} &= \bar{Z}_{r3,r3} + Z_{ex,r3} \end{aligned} \quad (3.52)$$

The wound rotor machine with external rotor resistances (R_a , R_b , and R_c) is shown in Figure 3.9. The referred external impedance is symmetrical about one phase and this phase is connected with R_a . Hence, if the magnetising current is neglected, the resistance terms are considered dominant,

$$\begin{aligned} R_b &= R_c \neq R_a \\ R_0 &= \frac{1}{3}(R_a + R_b + R_c) \\ R_1 &= \frac{1}{3}(R_a + aR_b + a^2R_c) \\ R_2 &= \frac{1}{3}(R_a + a^2R_b + aR_c) \end{aligned} \quad (3.53)$$

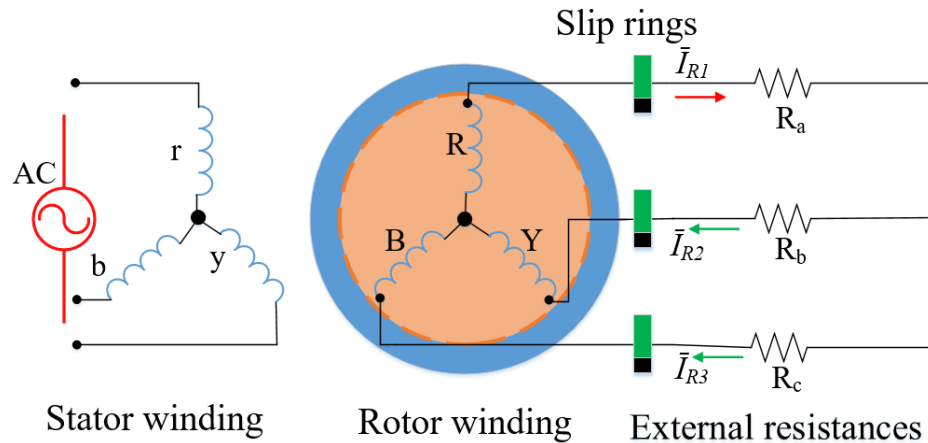


Figure 3.9. Wound-rotor induction machine with external resistors.

The simplified equivalent circuit is transformed to the primary side, with the mutual impedance replaced by its equivalent T-network [154-156]. The resultant equivalent circuit converted to constant frequency, is shown in Figure 3.10. This is considered essential for evaluation and detection of the wound-rotor faults. Speed variation can be obtained by applying external resistance to the rotor circuit; the impact of increased rotor resistance on the torque-speed characteristic is shown by the curves in Figure 3.11. For such a machine, significant speed variations can be achieved using the various rotor resistance given by $R_2''' > R_2'' > R_2' > R_2$ in Figure 3.11.

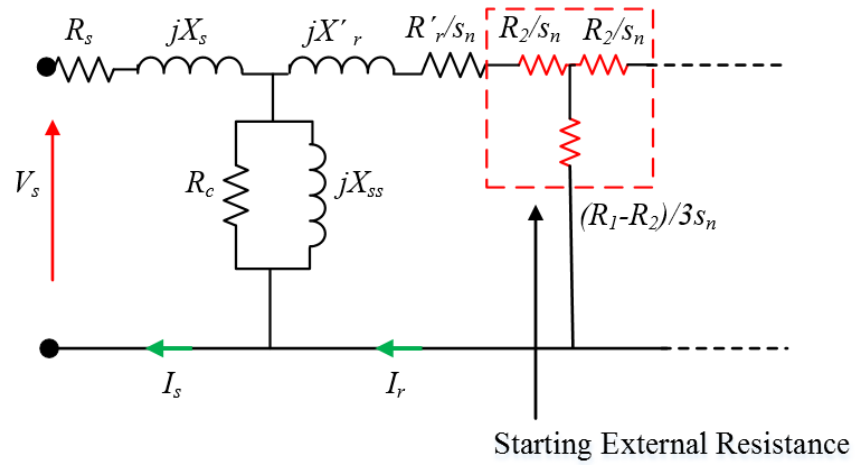


Figure 3.10. Simplified equivalent circuit for wound rotor induction machine connected to external impedance.

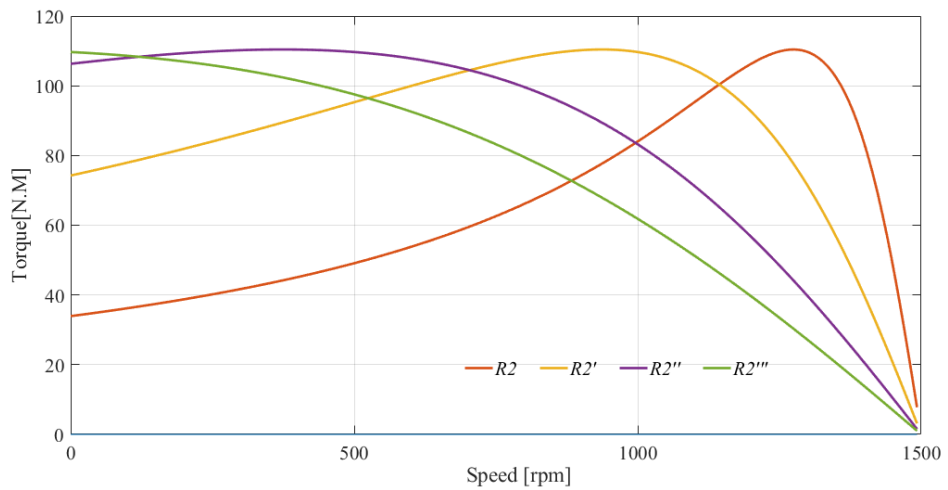


Figure 3.11. Four-pole wound-rotor induction machine torque-slip curves showing effect of adding external resistance to rotor-circuit resistance.

3.8 Chapter Summary

The harmonic conductor density approach of analysing machine windings [47] was implemented to allow the calculation of currents in individual coil groupings and is described in this chapter. The main advantage of this analytical approach is that it can be used in two ways: when dealing with a healthy machine and dealing with a machine where the rotor is not concentric with the stator. A full derivation is put forward for the healthy rotor case in this chapter to illustrate the technique. It is a suitable approach for detecting the faults in IM and further analysis will be put forward in later chapters.

As already stated, this chapter has developed models using a linearising machine for stator and rotor windings in a healthy machine which is extended to include faults. The purpose is to ultimately develop a relatively simple, yet powerful model that can accurately analyse the behaviour of DFIG.

Chapter 4: Performance Estimation of the Healthy Machine Using MATLAB

IN this chapter, MATLAB is employed to predict the electromagnetic behaviour of the induction machine during steady-state and transient-state. Implementation of the induction machine in MATLAB will be conducted in order to make comparisons, which can provide useful information and create a framework for understanding results. This chapter provides a brief introduction about Motor-CAD software [157]. In addition, Motor-CAD and MATLAB will be used for examining the induction machine parameters.

4.1 Introduction to Motor-CAD

Modern design methods for induction machines often use Computer-Aided Design. Cage induction machines are now used widely in inverter-fed variable-speed drive systems and supplanted DC machines in many applications. The wound rotor induction machine has enjoyed a renaissance as the generator in many commercial wind turbines.

There are several software packages that can predict the electromagnetic behaviour of an induction machine during steady-state and transient-state conditions. Most of these software packages use finite element analysis to evaluate and examine electrical machine parameters although packages such as *SPEED*, as developed by The University of Glasgow, use lumped magnetic circuits to provide fast solutions; *SPEED* also has a finite element analysis package for solution refinement. Finite element methods are commonly used to estimate the electromagnetic performance of electrical machines since these methods are particularly suitable for developing good design calculations for the current density distribution [47, 84, 158]. An analysis package for the induction machine is provided by Motor-CAD simulation software which combines thermal and magnetic

lumped circuit analysis with finite element analysis so that it solves in less time than other software. Motor-CAD also solves for other machines, such as the brushless permanent magnet (BPM) motor, outer rotor BPM motor, switched reluctance motor and permanent magnet DC machine [159, 160]. Generally, the machine performance, losses, and temperatures for an induction machine can be calculated in few minutes in the Motor-CAD environment. Furthermore, it allows the designers to optimise their designs for energy efficiency and size and cost reduction, offering a link between the electromagnetic design and thermal analysis of motors. It allows quick and easy evaluation of different cooling options during the design process for both the steady-state and transient thermal analysis.

4.2 Induction Machine in Motor-CAD

This section will investigate how to design a three-phase, four-pole induction machine using Motor-CAD, and the electromagnetic performance of the machine. As a comparison, the impedance matrix technique including all coupling and mutual impedances which was described in Chapter 3 will be used in modelling and analysis of the same induction machine. It is not easy to obtain this impedance matrix using hand calculations, so it is reasonable to use MATLAB for calculations. The results of the matrix method are verified by inversion of the voltage matrix equation and solving of the currents for the applied voltages to the induction machine after programming it in MATLAB. This allows the machine losses to be presented. The results (torque, current characteristic, power losses) are compared for the test machine.

The graphical interfaces of the Motor-CAD environment will be utilised to describe the machine geometry, winding harmonics, material properties, and air-gap flux. The

predicted results are validated by experiment. Power losses are calculated for the test machine, and then the results are explained.

4.3 Implementation of Induction Machine in Motor-CAD

Motor-CAD software has been introduced to provide a fast method for analysing design changes on the behaviour of the machine. Thus, the designer can identify variables such as the geometry of the machine, material, and cooling type, which have the greatest influence on the machine performance. Numerical methods are used in Motor-CAD to solve the electromagnetic circuit in the machines over the full torque/speed range. The use of intelligent loss algorithms makes it suitable for many applications, for example, traction applications which have complex duty cycle loads.

The Motor-CAD software has a very simple user-interface, so that the designer just needs to identify the geometry of the machine and set up a several winding, drive, and material options. The machine geometry for the three-phase four-pole induction machine was set up, and the final figuration is shown in Figure 4.1. One of the drawbacks of Motor-CAD is that it does not include wound rotor induction machine topology so that an equivalent cage rotor was used. This has an identical slot shape to the wound rotor machine and the end-ring shape and rotor conductor resistivity were adjusted to obtain the same referred rotor resistance. However, the leakage will still be different, but this seemed to give a fair approximation. The skew of the rotor is one stator slot from end to end. The rotor is shown later in Figure 6.11.

Details about the test machine are given in Appendix C. Here Motor-CAD is described though in earlier studies *SPEED* was used to obtain parameters [23] and Appendix C includes some of these parameters. The coils were designed with three strands in hand for

each turn in the slot. Figure 4.2 shows the stator conductors inside the slot. The separation distance between the conductors is 0.1 mm. The wire size is defined using the copper slot fill factor and this value is set to 0.523 mm. The diameter of the wire was 1.21 mm. The geometry of the machine is set to have 48 stator slots, 72 rotor slots, and 4 poles.

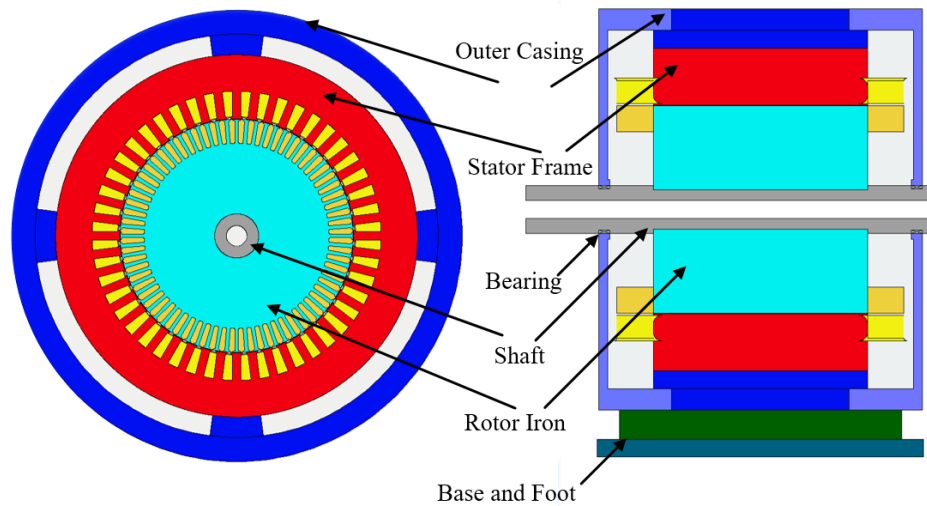


Figure 4.1. Radial and axial sections of the test machine.

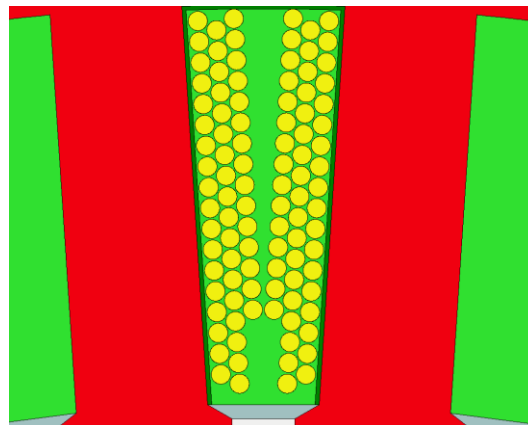


Figure 4.2. Illustration of the stator conductors inside the slot.

The next step is to define the control parameters, so the software can calculate the machine performance. The software allows to evaluate the electromagnetic performance

when the machine acts as either a motor or a generator. In addition, the skew angle can be set, which is utilised to reduce the machine harmonics. Then the winding pattern of the machine will be adjusted according to the initial geometry layout. Modifying the pattern for the slot/pole combination is also possible in Motor-CAD as illustrated in Figure 4.3. The winding factors, phasor diagrams and winding harmonics for the phase winding are shown in Figure 4.4 and 4.5. These charts generally provide an accurate comparison between different winding specifications, such as single layer and double layer windings. The peak harmonics amplitudes are reduced when the double layer is used instead of the single layer in the machine. A large of material database is available for modelling the materials commonly used in electrical machine manufacturing. Furthermore, the software has a capability for other materials to be added. Different cooling type options are available and complex heat transfer data are calculated automatically. Motor-CAD provides an exhaustive understanding of the cooling system and facilitates optimisation.

One more feature for the software is that geometries can be imported from, and exported to, other software environments. Motor-CAD can be linked to *SPEED*, *FLUX*, and *PORTUNUS* software, and to other design tools.

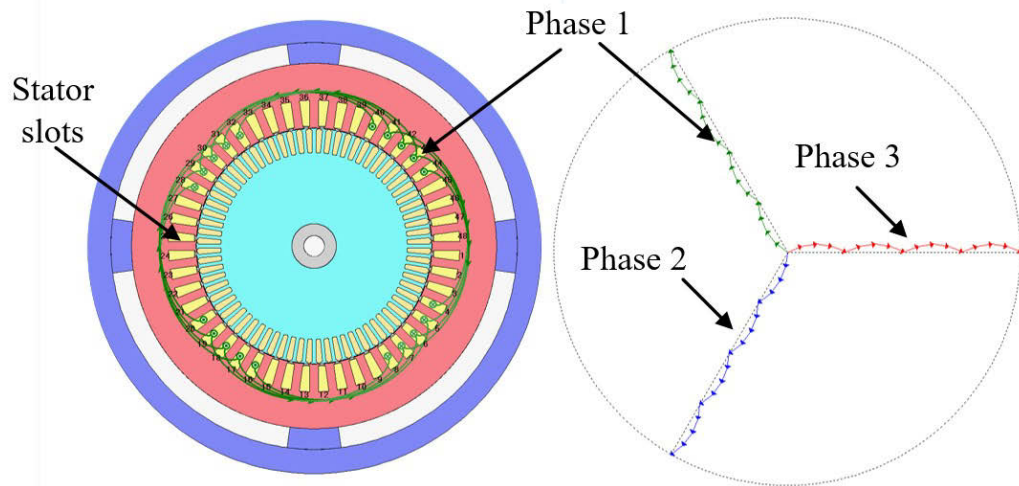


Figure 4.3. Illustration of the winding layout (only phase 1 shown), and phase diagram.

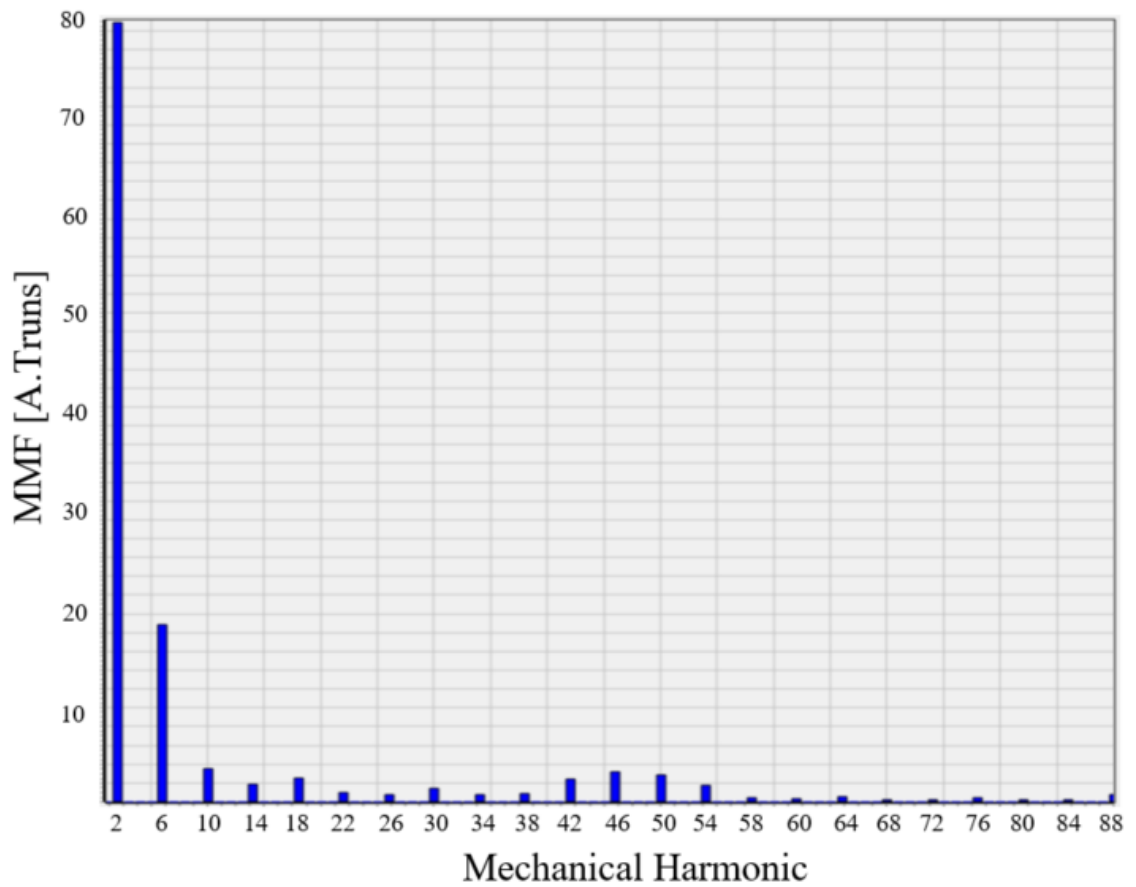


Figure 4.4. Illustration of the mechanical harmonics for the test machine.

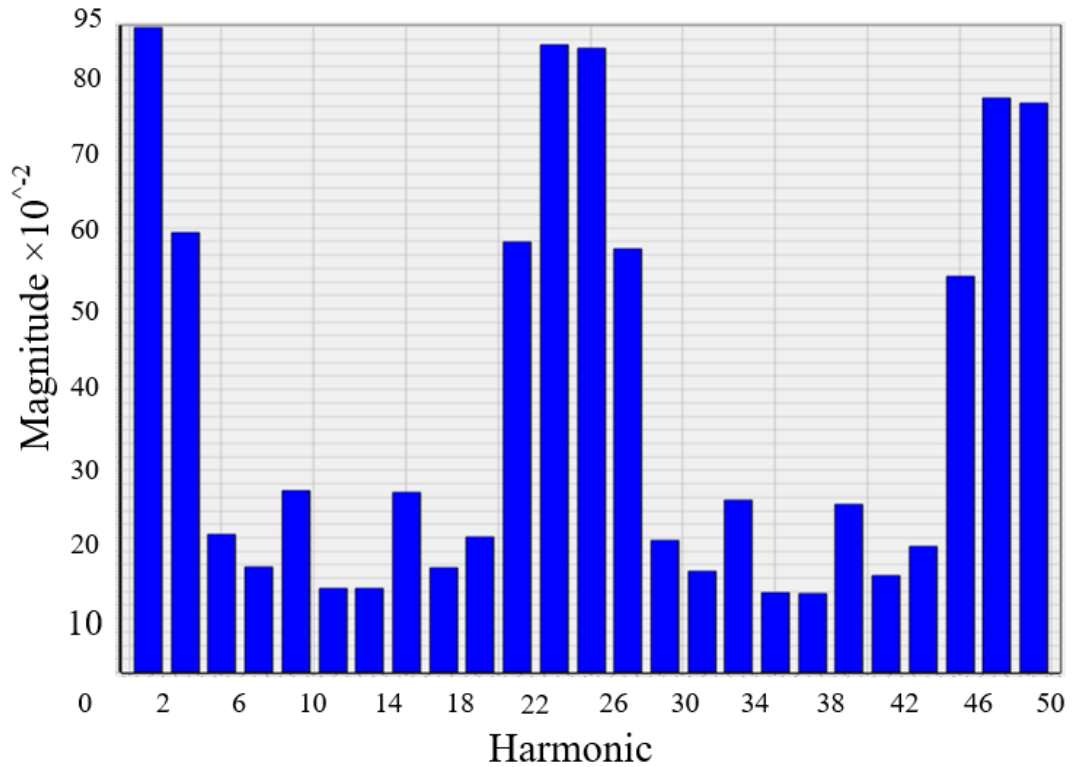


Figure 4.5. Illustration of the winding harmonic factors for the test machine.

4.4 Electromagnetic Model of Induction Machine

In Motor-CAD, the air-gap of the machine can be split into two or more layered sections that represent the stator air-gap and the rotor air-gap during meshing. The mesh points and boundary of the combining site are exactly the same for the coupling calculation of stator and rotor. At each point in time, the equations of the magnetic field and electric field are calculated together in an iterative manner. The matrix counter is refreshed at each subsequent point in time. The electromagnetic model for the induction machine is calculated and the results of the analysis are depicted in Figure 4.6. Flux density contour plots and plots of constant magnetic potential enable the investigation of any region in the machine, for example, flux distribution on the stator or rotor surfaces.

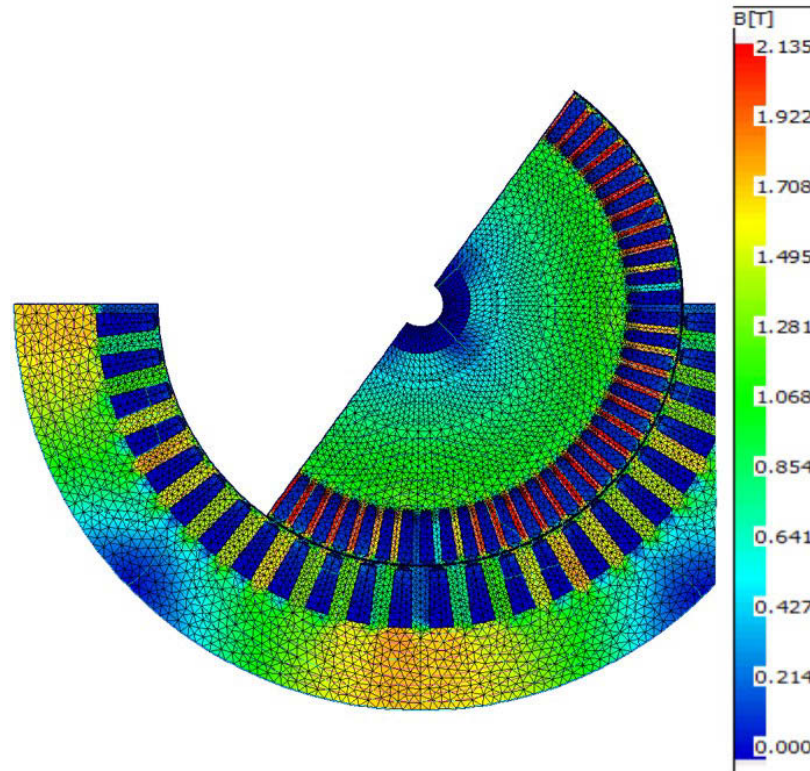


Figure 4.6. A fast 2D FEM for locked rotor circuit flux distribution.

The test machine was simulated over a 0.12 s period with 1 ms time intervals to investigate the electromagnetic model of the machine at 400 V and 5 A. The locked rotor and open rotor test were also applied. The supply current and terminal voltage can be presented graphically in Motor-CAD.

The electromagnetic model in motor-CAD enables the designer to inspect not only the total air-gap flux but also the stator flux and rotor flux separately which is useful for calculating the torque in BPM machines and looking at the flux vectors in induction machines. For the induction motor, the flux density can be calculated under locked rotor and no-load conditions. Figure 4.7 shows the results for different contour plots that are available in the electromagnetic model in the locked-rotor and no-load cases.

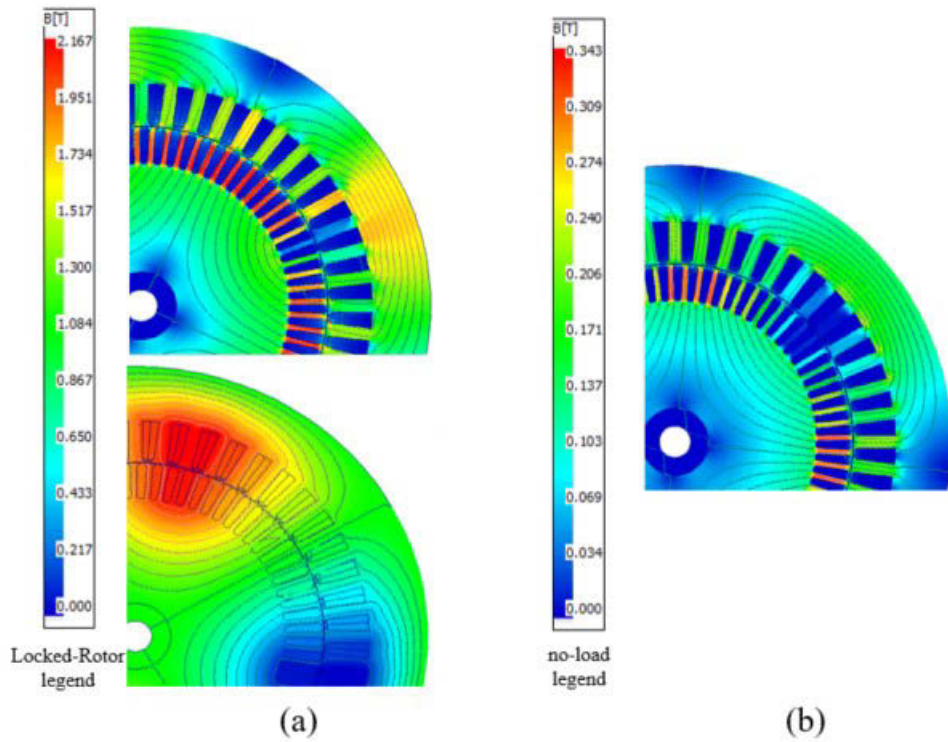


Figure 4.7. Results for different contour plots in the electromagnetic model: (a) locked-rotor and magnetic potential for locked rotor test (the penetration of the field in the rotor is usually negligible in these conditions), (b) no-load condition.

All these components are taken into account when calculating the equivalent circuit parameters of the induction machine after the solving is finished. Furthermore, the core loss resistance can be included in the equivalent circuit as a post processing iron loss calculation as illustrated in Figure 4.8. The equivalent circuit parameters (R_s , R_r , R_c , and X_m) shown in the figure were compared with the results in Appendices C and D. The good matching has clearly appeared. The core resistance of the test machine was predicted to be lower than the measured value at rated slip because it is an old machine.

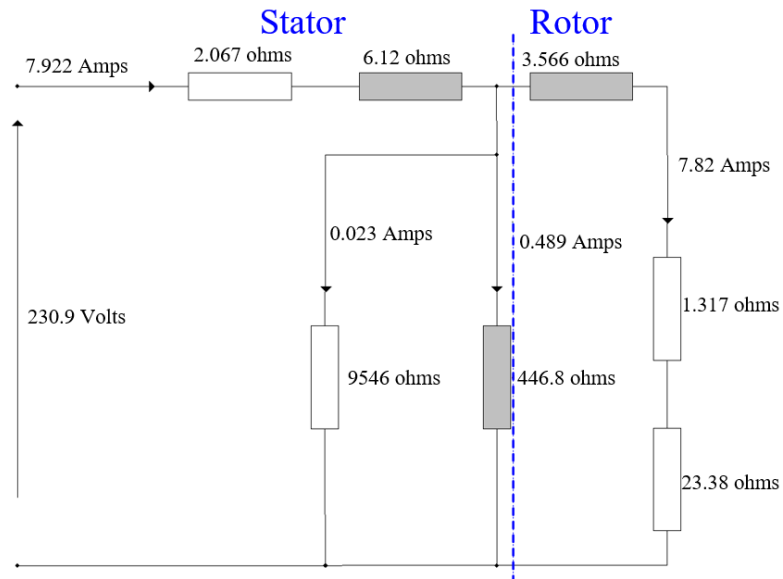


Figure 4.8. Equivalent circuit of the test machine in Motor-CAD.

Figure 4.9 (a) shows flux density in the air-gap of the test machine under saturated and unsaturated conditions, providing more details about modelling of the magnetic circuit saturation. This relates to the treatment of the material used. The magnetisation curve of the machine material can be treated as linear (with a set relative permeability) or with a knee due to saturation. The output power, power factor, and various machine inductances are calculated in this set of curves to illustrate that other results can be obtained in addition to a torque/speed curve. In (b) the power factor of the test machine was predicted to be low at rated slip because it is an old machine; however, it will increase to a maximum as the load is reduced before rapidly dropping of close to no-load. The designer can compare the different approaches to the design, which demonstrates the influence of the geometry of the machine within the model assumptions. The models allow the designer to observe the run-up power curves as shown in (c). This will help in understand the transient start-up. Self and mutual inductances are calculated for set current and load points as illustrated in (d). This is at no load with increasing voltage.

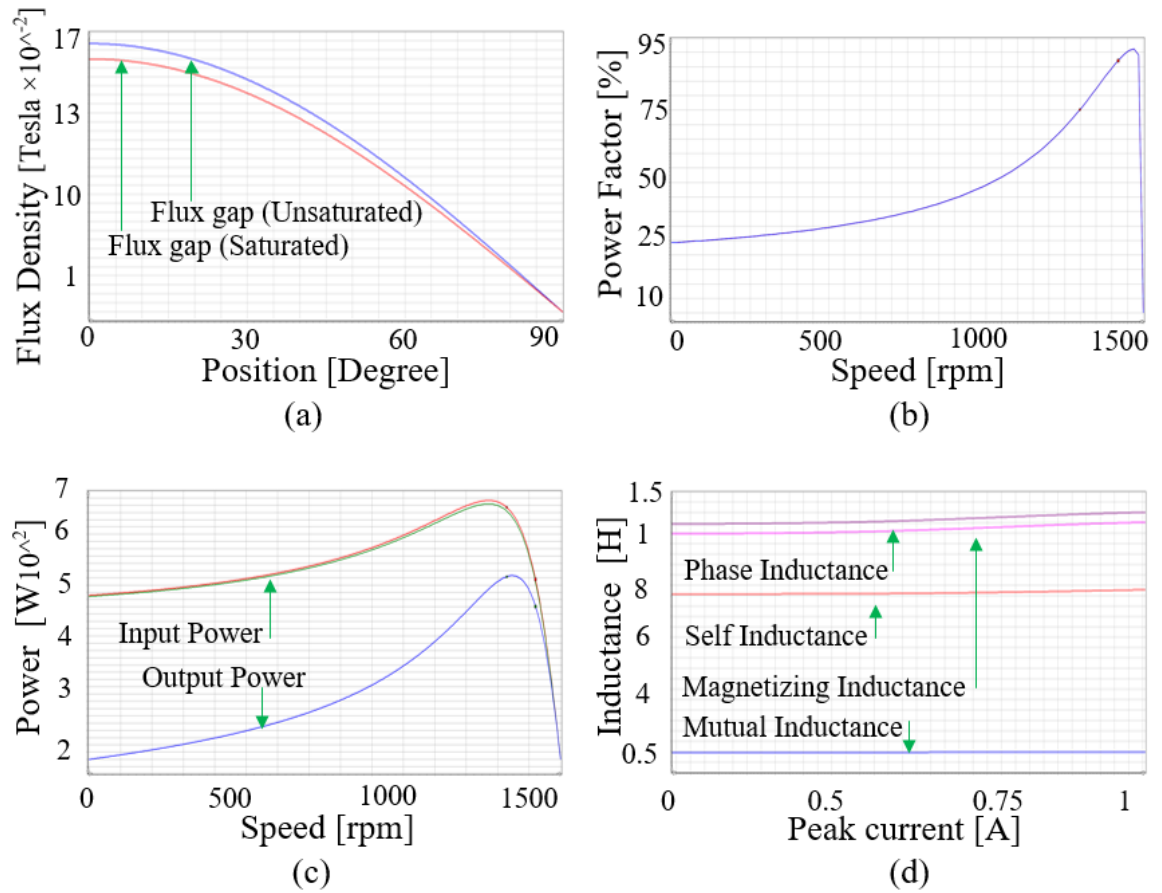


Figure 4.9. Graphical results of the electromagnetic model in Motor-CAD.

4.5 Machine Geometry

The basic 4-pole wound rotor machine specification is given in Appendix C. The geometry of the machine is set to 48 stator slots, 72 rotor slots, and 4 poles. It is an old machine, in which the stator was rewound with a double layer winding. In the stator, the number of coils per phase equals 16, and the number of coils per pole per phase equals 4 (two coil sides per slot). There are 16 slots occupied by one phase in each layer, 8 with inward and 8 with outward current directions. The induction machine is shown in Figure 4.10.

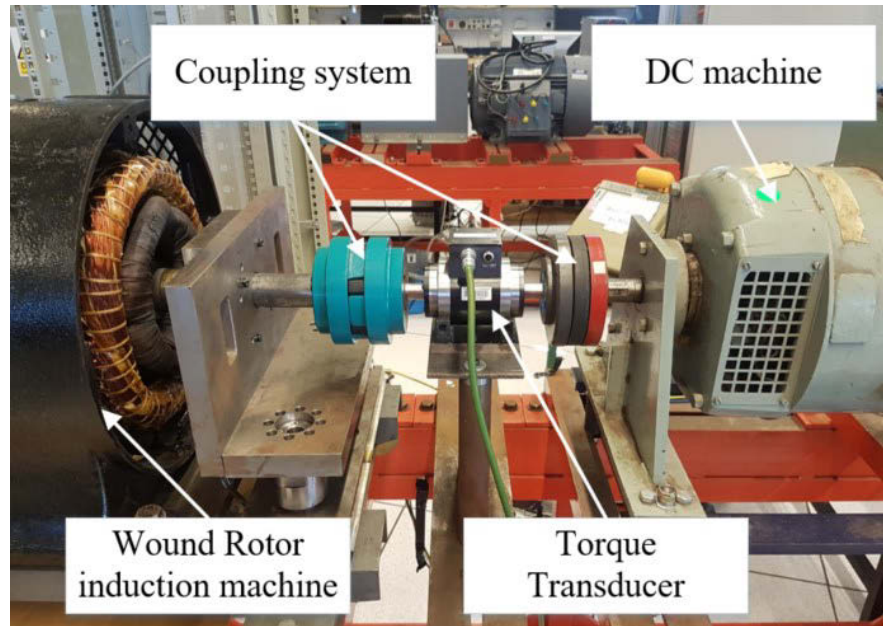


Figure 4.10. Test machine, showing the stator frame during the rewinding process.

4.6 Implementation of Induction Machine in MATLAB

In this section the impedance matrix is programmed in MATLAB. Since this is test implementation to compare to the Motor-CAD model then an equivalent cage-rotor machine is programmed in addition to the wound rotor machine. MATLAB is increasingly used in modelling and simulation of the machines. MATLAB/Simulink implementation for an induction machine allows the designer to test various control strategies. The model equations are written in the form of a matrix to find the steady state equivalent circuit for the wound rotor induction machine, as described in Chapter 3, equation (3.21). The currents in the stator and rotor winding are linked to the supply voltage by means of the matrix equation as described in (3.35); here it is coded as

$$\begin{bmatrix} \bar{V}_s \\ 0 \\ \vdots \\ 0 \end{bmatrix} = \begin{bmatrix} \bar{Z}_{s,s} & \bar{Z}_{s,1} & \cdots \\ \bar{Z}_{1,s} & \bar{Z}_{1,1} & \cdots \\ \vdots & \vdots & \vdots \\ \bar{Z}_{N_b,s} & \bar{Z}_{N_b,1} & \cdots \end{bmatrix} \begin{bmatrix} \bar{I}_s \\ \bar{I}_1 \\ \vdots \\ \bar{I}_{N_b} \end{bmatrix} \quad (4.1)$$

so it is applicable for both the cage rotor and the wound rotor.

The impedance matrix was developed to enhance condition monitoring of the induction machine. For the cage rotor equivalent machine, the matrix equation in (4.1) assumes that the rotor bars/phases are short-circuited. N_b is the total number of the bars/phase windings in rotor. The system of N_b complex linear equations, where $(N_b + 1)$ is the number of rows in the matrix, can be solved by any convenient means to find the N_b unknown currents.

The impedance matrix can be assembled and then the input and output power may be calculated in a straightforward manner using the stator voltage and current since the stator supply has been assumed to be ideal where

$$P_i = \text{Re}\{3\bar{V}_s I_s^*\} \quad (4.2)$$

The losses in the rotor or stator can be calculated from I^2R losses in the rotor cage or stator winding and hence the mechanical output power for each harmonic and torque can be calculated. The electromagnetic torque of the induction machine is generated through the interaction between the stator and rotor fields and can be obtained by applying equation (3.41). This algorithm is easily implementable in the MATLAB software package and provides a modern form of induction machine analytical analysis.

4.7 Simulation Results

The three-phase four-pole induction machine (test machine) shown in Figure 4.10 was tested using a rig. This will run the machine up to synchronous speed from a supply terminal voltage and loading the machine in a controlled manner. The speed is reduced to standstill, and then allowed to return back to synchronous speed. During this testing, the parameters such as stator current, power, power factor and torque can be recorded.

The developed torque and rotor current are shown in Figure 4.11 and Figure 4.12 for the two simulation techniques and measured values. These are sufficiently close to indicate that Motor-CAD and MATLAB can accurately and smoothly predict the behaviour of the induction machine. Similar values of the current induced into the rotor are shown in Figure 4.12. Again, the increase in machine losses is related to the stator and rotor resistances which are considered high compared with the modern induction machine, these are shown in Figure 4.13. As expected, the losses are in good agreement, the differences being attributed to tolerances in the magnetic properties of the chosen steel and neglecting of the iron loss in the MATLAB simulation.

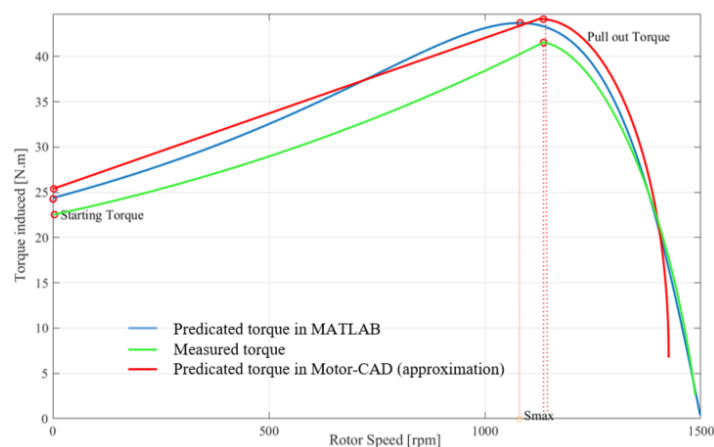


Figure 4.11. Predicted and measured torque developed by the test machine v.s. speed characteristics.

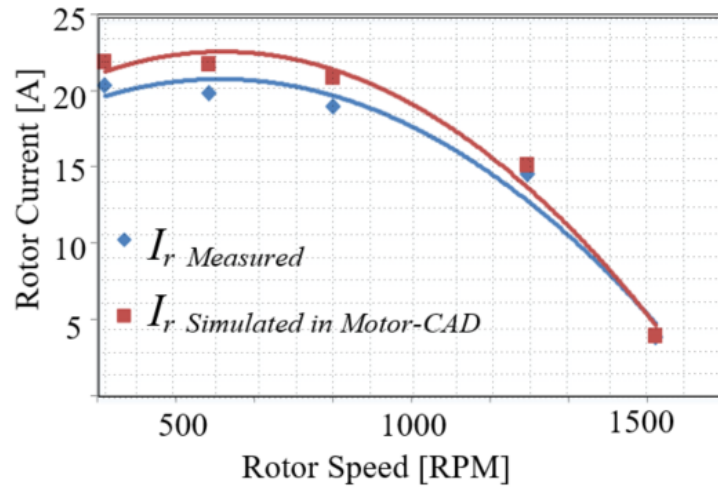


Figure 4.12. Simulated and measured rotor currents v.s. speed characteristics.

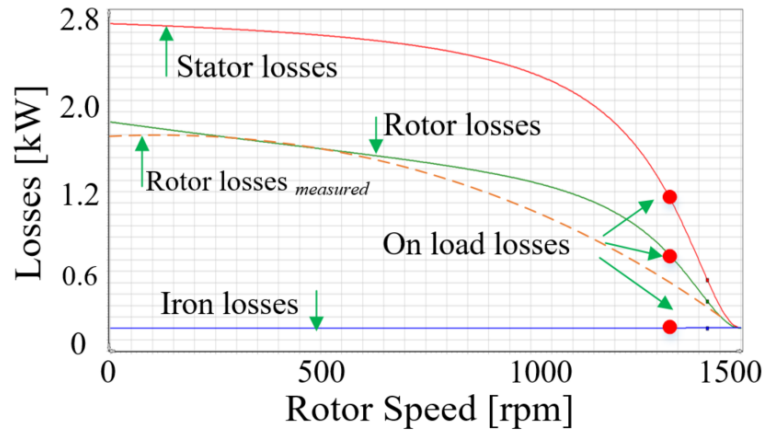


Figure 4.13. Simulated and measured losses v.s. speed characteristics.

4.8 Chapter Summary

Simulation models of the induction machine using MATLAB are presented in this chapter in detail. These models can predict and characterise the behaviour of the induction machine. The main purpose is to improve design approaches, and ultimately to improve the efficacy and reliability of the induction machine. The parameter estimation of the induction machine can then be done at an early stage of the design process, including the structures of the stator and rotor, even for the wound rotor machine if an equivalent cage-rotor design is used.

A comparison has been done between two separate models and the corresponding experimental results. These models, while for a cage machine, use an equivalent machine with similar rotor equivalent circuit parameters as the wound rotor machine. MATLAB has the capacity to predict and evaluate induction machine behaviour, although it has to be programmed. Motor-CAD is specific and focuses only on electric machine design. It provides a very simple user-interface which simplifies the machine design and training and is used to provide visualisation in large research projects. However, for fault monitoring and detection, specific simulation methods need to be used which require a more flexible approach than the MATLAB method allows.

Chapter 5: Study of Wound Rotor Induction Machines Including Rotor Asymmetry

This chapter develops a relatively simple yet powerful model that can accurately analyse the behaviour of a WRIM or DFIG with rotor faults. The model is based upon the calculation of the stator current components, which are needed to build the impedance matrix that includes coupling impedances. This method is used here to detect the electrical asymmetry of the external-connected rotor resistances on a four-pole wound rotor.

5.1 Rotor Fault Analysis

When the stator terminals are supplied by a balanced positive-sequence voltage, each individual phase winding in the stator generates a pulsating field in the air gap, and the combination of all three phases produces a forwards-rotating air gap field which induces slip frequency electromagnetic forces (EMFs) in the rotor windings. There will also be winding harmonics that produce asynchronous torques. The EMFs will create currents in the rotor windings, which will produce an air-gap magnetic field that contains a field component fundamentally distributed and rotating in the forward direction. It also contains the higher pole number differential fields. If there is rotor asymmetry, then a fundamental field component of with a smaller amplitude and rotating backwards with respect to the rotor is generated which will be reflected back to the stator. Both these field components will rotate at slip speed with respect to the rotor but in opposite directions.

The backwards rotating field rotates at slip speed with respect to the rotor, but rotates forwards with respect to the stator with speed $(1-2s)$ of the synchronous speed for low slip. This rotating field induces EMFs in the stator windings with a frequency of $(1-2s)f$.

This EMF can produce current in the rotor since there windings are effectively shorted through the supply by the source transformer at this frequency. A non-synchronous air-gap flux wave is then produced. The analysis so far only accounts for a $(1-2s)f$ sideband current in stator but a $(1+2s)f$ sideband also exists that is commonly monitored. This is because the $(1-2s)f$ air-gap field reacts with the main stator MMF to produce a $2sf$ pulsating torque that leads to a small speed oscillation. This leads to modulation and the generation of a $(1+2s)f$ EMF in the main stator winding and associated sideband current as described in [161]. This upper sideband current tends to much lower in magnitude and is a function of voltage and slip [161, 162].

In addition to the above mechanism for producing the $(1+2s)f$ sideband current, the third-order spatial flux density saturation wave in the air-gap produces $3sf$ EMFs in the rotor, which can also induce $(1+2s)f$ EMFs in the stator [163, 164]. The $(1+2s)f$ component always exists in maintenance diagnostic tests, but this saturation mechanism for $(1+2s)f$ sideband harmonic current produces only low harmonics.

It should be stated there is $(1+2s)f$ component appears in the cases of broken rotor bar and asymmetric wound rotor. This component has been used to detect such faults in large cage induction machine. The authors in [161] investigated experimentally the behaviour of the $(1+2s)f$ sideband current component using a cage rotor. This upper sideband component has been found to be due to both speed ripple and third-order special saturation flux density waves. They proved theoretically this upper sideband component proportional to the cube of the supply voltage. The main conclusion of the work in [161] is that the $(1+2s)f$ component is significant in the case of high voltage or the low inertia, and the magnitude of the sidebands increases with the number of broken bars. It has been shown that the twice slip frequency sideband components of the supply current can be

used to detect broken bars in a cage rotor induction motor [86]. But it was shown that the $(1+2s)f$ component is much less than the $(1-2s)f$ components and the $(1-2s)f$ of sideband current dominates in the most cases [162]. Therefore $(1+2s)f$ component is not present in the analysis.

According to [96, 165] a positive torque is produced by the $(1-2s)f$ sideband current when $s < 0.5$ since the flux is rotating forwards with respect to the stator, and a negative torque when $s > 0.5$ since the flux wave then rotates backwards with respect to the stator. These torques are low and can be considered as an asynchronous torque. At a slip of 0.5 the sideband current and resultant asynchronous torque are zero.

Based on the above discussion, if the speed oscillation is neglected since the $(1+2s)f$ current is low, there will be two unknown stator current components and three unknown rotor currents; i.e., there is an additional $(1-2s)f$ stator current component. These unknown currents can be related to each other and to the stator voltages using the coupling impedance concept as shown in the next section.

5.2 Rotor Faults Detection Using Impedance Matrix

Rotor faults can be added to the impedance matrix in (3.21) through representing appropriate relationships between various rotor currents and reducing the size of the coupling impedance matrix. For example, if one of the rotor phases is open, the impedance matrix is modified by deleting the row and the column that relate to the phase. In the case of an asymmetrical rotor fault, negative-sequence voltages will be included in the matrix.

For this reason, it is necessary to add other components in the impedance matrix to accommodate the $(1-2s)f$ current. The voltage is assumed to be zero for this component

so that this frequency is assumed shorted through the supply. The impedance matrix includes all impedances in (3.21) which are functions of the three-phase windings on the stator and rotor so that

$$\begin{bmatrix} \bar{V}_{s_f} \\ 0 \\ 0 \\ 0 \\ 0 \end{bmatrix} = \begin{bmatrix} \bar{Z}_{s,s_f} & 0 & \bar{Z}_{s_f,r_1} & \bar{Z}_{s_f,r_2} & \bar{Z}_{s_f,r_3} \\ 0 & \bar{Z}_{s,s_b} & \bar{Z}_{s_b,r_1} & \bar{Z}_{s_b,r_2} & \bar{Z}_{s_b,r_3} \\ \bar{Z}_{r_1,s_f} & \bar{Z}_{r_1,s_b} & \bar{Z}_{r_1,r_1} & \bar{Z}_{r_1,r_2} & \bar{Z}_{r_1,r_3} \\ \bar{Z}_{r_2,s_f} & \bar{Z}_{r_2,s_b} & \bar{Z}_{r_2,r_1} & \bar{Z}_{r_2,r_2} & \bar{Z}_{r_2,r_3} \\ \bar{Z}_{r_3,s_f} & \bar{Z}_{r_3,s_b} & \bar{Z}_{r_3,r_1} & \bar{Z}_{r_3,r_2} & \bar{Z}_{r_3,r_3} \end{bmatrix} \begin{bmatrix} \bar{I}_{s_f} \\ \bar{I}_{s_b} \\ \bar{I}_{r_1} \\ \bar{I}_{r_2} \\ \bar{I}_{r_3} \end{bmatrix} \quad (5.1)$$

The rotor voltage vectors are assumed to be zero because the windings are short-circuited on the slip ring side. The field that rotates forwards with respect to the rotor has the subscript f . The field that rotates backwards with respect to the rotor when there is rotor asymmetry has the subscript b . The stator is symmetrical so can be analysed on a per phase basis. The stator harmonic n is neglected because it is assumed unity and s , r_1 , r_2 , and r_3 correspond to stator and rotor phase windings of the machine. \bar{I}_{s_f} is the main stator current (the stator forward current) and \bar{I}_{s_b} the $(1-2s)$ times mains-frequency component (the stator backward current). Since these stator currents have different frequencies, they are not linked so the values of \bar{Z}_{s_b,s_f} and \bar{Z}_{s_f,s_b} are equal to zero.

5.2.1 Coupling and Mutual Impedances Including General Rotor

Asymmetry

By comparing both matrices in (3.21) and (5.1), it becomes clear by adding some backward components that the rotor asymmetry case modifies the coupling and mutual impedances. The coupling and mutual impedances which were described in Chapter 3 represent the forward components in the matrix only. Here they will be written with

suffix f . The expressions for the backward components of the impedance matrix are given in this section:

- [1] Stator-stator coupling impedance: the air-gap field was expressed using (3.11) and hence the back-EMF in the stator winding. This was related to the supply current, by the stator impedance and stator-stator coupling impedance and as in (3.22) and (3.23) with reference to the forward rotating fluxes. Here the stator impedance in (3.22) will be written with labelling (suffixes) f to indicate that it is the forward component. Hence The stator impedances with reference to the forward rotating fluxes and backward rotating fluxes are

$$\begin{aligned}\bar{Z}_{s,s_f} &= R_s + jX_s + jX_{ss} \\ \bar{Z}_{s,s_b} &= R_s + j(2s-1)(X_s + X_{ss})\end{aligned}\quad (5.2)$$

The magnetising reactance for the three-phase winding was defined in (3.23). Obviously, the backward component of the stator current is a negative sequence for ($s > 0.5$) and a positive sequence for ($s < 0.5$).

- [2] Stator-rotor coupling impedance: the expressions for forward coupling impedances were described in (3.26) and they can be linked to backward component. The EMFs induced in the rotor windings by the stator air-gap flux wave that rotates backwards with respect to the rotor have equal amplitude, but the phase progression is reversed. Hence, the backwards coupling impedances are

$$\bar{Z}_{r,s_b} = -\bar{Z}_{r,s_f} \quad (5.3)$$

- [3] Rotor-stator coupling impedance: the forward components of the stator-rotor coupling impedances were directly derived from their rotor-stator counterparts by

applying suitable transformations as in (3.29). The backward components $\bar{Z}_{s_b,r}$ are equal to $\bar{Z}_{s_f,r}$ but multiplied by s_b instead of s_f , where $s_b = s_f(2s-1)$.

$$\bar{Z}_{s_b,r} = \bar{Z}_{s_f,r} \Big|_{s_b=s_f(2s-1)} \quad (5.4)$$

5.2.2 Determination of Backward Components of Currents and

Torque

The electromagnetic torque can be determined from the current density distributions of the stator and rotor as discussed earlier in Section 3.5. Since the current density is modified here to include the fault condition, the torque will be modified to include the backwards components.

The stator and rotor currents densities are $j_s(y,t)$ and $j_r(y,t)$ respectively, including the forward and backward components. The torque can be given as

$$T = \frac{2\pi r^2 \mu_o L_{st}}{p_m \mathcal{G}} \operatorname{Re} \left\{ j \left(\bar{J}_{st_b} \bar{J}_{r_b}^* - \bar{J}_{st_f} \bar{J}_{r_f}^* \right) + j \left(\bar{J}_{st_b} \bar{J}_{r_f} - \bar{J}_{st_f} \bar{J}_{r_b} \right) e^{j2s\omega t} \right\} \quad (5.5)$$

The stator current density, which includes the forward and backward components and only includes the fundamental ($n = 1$), is

$$j_s(y,t) = \operatorname{Re} \left\{ \bar{J}_{st_f} e^{j(\omega t - p_m k y)} + \bar{J}_{st_b} e^{j((2s-1)\omega t + p_m k y)} \right\} \quad (5.6)$$

For a balanced 3-phase current set, and using the identity $a = e^{(j2\pi/3)}$, the forward and backward components of the MMF are given as

$$\begin{aligned} \bar{J}_{sf} &= \bar{N}_{st} (1 + a^1 a^{-1} + a^{-1} a^1) \bar{I}_s = 3\bar{N}_{st} \bar{I}_s \\ \bar{J}_{sb} &= 3\bar{N}_{st}^* \bar{I}_s \end{aligned} \quad (5.7)$$

The rotor currents set up fundamentally distributed rotating MMF waves, which can be expressed in the stator coordinates as:

$$i_R(\mathcal{Y}, t) = \text{Re} \left\{ \bar{J}_{R_f} e^{j(\omega t - p_m k y)} + \bar{J}_{R_b} e^{j((2s-1)\omega t + p_m k y)} \right\} \quad (5.8)$$

It is assumed that $n = 1$ again, where

$$\begin{aligned} \bar{J}_{R_f} &= \bar{I}_{R_1} \bar{N}_r + a^1 \bar{I}_{R_2} \bar{N}_r + a^{-1} \bar{I}_{R_3} \bar{N}_r \\ \bar{J}_{R_b} &= \bar{I}_{R_1} \bar{N}_r^* + a^{-1} \bar{I}_{R_2} \bar{N}_r^* + a^1 \bar{I}_{R_3} \bar{N}_r^* \end{aligned} \quad (5.9)$$

It is worth noting that the torque expression in (5.5) includes the state steady and oscillating components developed by the machine. From equation (5.5), the steady state torque is obtained:

$$T_{steady} = \frac{1}{\omega} p_{rot} \quad (5.10)$$

where

$$p_{rot} = 3 |\bar{I}_r|^2 \frac{R_r}{s} \quad (5.11)$$

5.2.3 Wound Rotor-Equivalent Circuit with Backward Components

The currents in the stator and rotor winding are related to the main supply voltage by means of the matrix equation. The matrix equation defined in (5.1) assumes that the rotor phases are short-circuited. In Section 3.5, the general steady state equivalent circuit has been shown for a wound-rotor machine with rotor symmetry. In this section, the forward and backward components of the machine with rotor asymmetry are coupled via a coupling circuit, which in general, can be an asymmetrical T-type or PI-type network.

Using the single-phase equivalent circuit shown in Figure 5.1 can be used to obtain the machine currents (e.g. forward and backward stator current components), electromagnetic torque (forward and backward components), stator and rotor losses, etc. It was derived

and simplified in [154, 155, 166], and it can be used to obtain the amplitude of the pulsating torque which is due to rotor asymmetry. The asymmetry is confined to a single-phase of the wound-rotor in order to simplify the analysis. This leads to an expression for the ratio of I_{sf}/I_{sb} . An external rotor resistance is used to represent a wound-rotor induction machine with rotor asymmetry. The resultant equivalent circuit is converted to constant frequency through the system. The rotor components are referred to the stator using the turns ratio in (3.43). The skew is removed so the skew coefficient will be unity and the skew reactance disappears. The core loss resistance is incorporated in the circuit. The stator impedance can be written with reference to the forward and backward components. The backward component varies since it contains by $(2s-1)$.

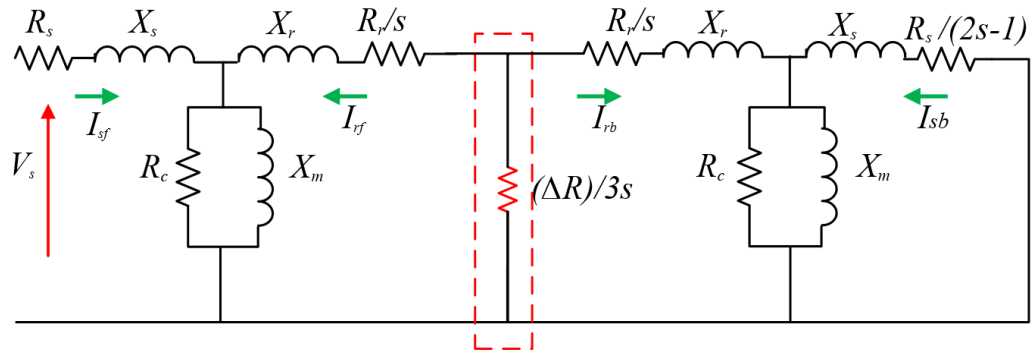


Figure 5.1. Single-phase equivalent circuit containing ΔR in wound-rotor phase.

The slip can be assumed close to the rated one, so the effective rotor reactances are small compared to the resistances. A three-phase wound-rotor machine can be analysed by approximating using a per-phase machine circuit affected by an increased resistance ΔR . The model can be simplified, in the case where the magnetising current is negligible and the resistance terms are assumed to be dominant. This will lead to defining the ratio I_{sf}/I_{sb} using a current divider where

$$\frac{I_{sb}}{I_{sf}} \approx \left(\frac{\Delta R}{3s} \right) / \left(\frac{R_r}{s} + \frac{\Delta R}{3s} \right) \quad (5.12)$$

5.3 Simulation of Wound Rotor Faults Using MATLAB

The simulation of rotor faults was carried out in the MATLAB environment through identifying appropriate relationships between various rotor currents and reducing the coupling impedance matrix. If the rotor windings are asymmetrical, then negative-sequence voltages will be generated. The matrix was programmed in MATLAB with different sets of external resistors. MATLAB/Simulink could be used to simulate the slip energy recovery system, which can simultaneously incorporate the rotor faults.

5.3.1 Implementation of Wound Rotor Faults

The rotor winding is connected to a combination of resistor bank. These series of resistors are connected to the rotor winding through the slip rings and are controlled by breakers. They were used with two of the phases short-circuited and the remaining phase connected to a small resistor as in Figure 5.2.

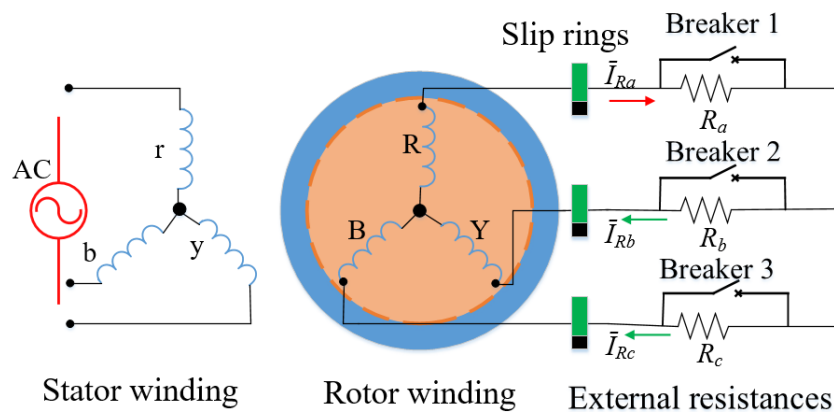


Figure 5.2. Simulation of wound rotor connected with external resistance.

For example, at the beginning the rotor phases were connected to a group of balanced resistors (2Ω). Then phases A and C are short-circuited (the breaker across the external resistances R_a and R_c are closed), and phase B is connected to a small resistor (2Ω). This

resistor (2Ω) represents a referred resistance of approximately (to the stator side) 8Ω in the equivalent circuit. Finally, the comparison was made between different cases. In this simulation, the opening times used for the circuit breaker were 4 s, 7 s. and 9 s.

5.3.2 Results of Implementation of Wound Rotor Faults

The implementation of the machine model is included in parts; the first part is to program the impedance matrix of a healthy wound rotor machine in MATLAB. The different sets of external resistors are then put into the matrix. The results from the different set of resistors are compared. The second part is to simulate the wound rotor induction using MATLAB/Simulink model in Appendix E.

The rotor resistance method described above is applied, which is normally used for the speed control of a wound-rotor induction motor. The transient torques for the healthy machine are shown in Figure 5.3. The simulations were run from no load up to full load or light load. The time step was 1 ms at the beginning and then it was increased up to 6 ms. Figure 5.4 shows the torque for a healthy motor, a motor with asymmetrical resistance (R_a and R_c short-circuited, and $R_b = 2 \Omega$), and a healthy motor with symmetrical resistances.

Traditionally the resistances that are connected in series with rotor phases to increase the starting torque and reduce the starting rotor current in general and this is presented in Figure 5.4, Figure 5.5 and Figure 5.6.

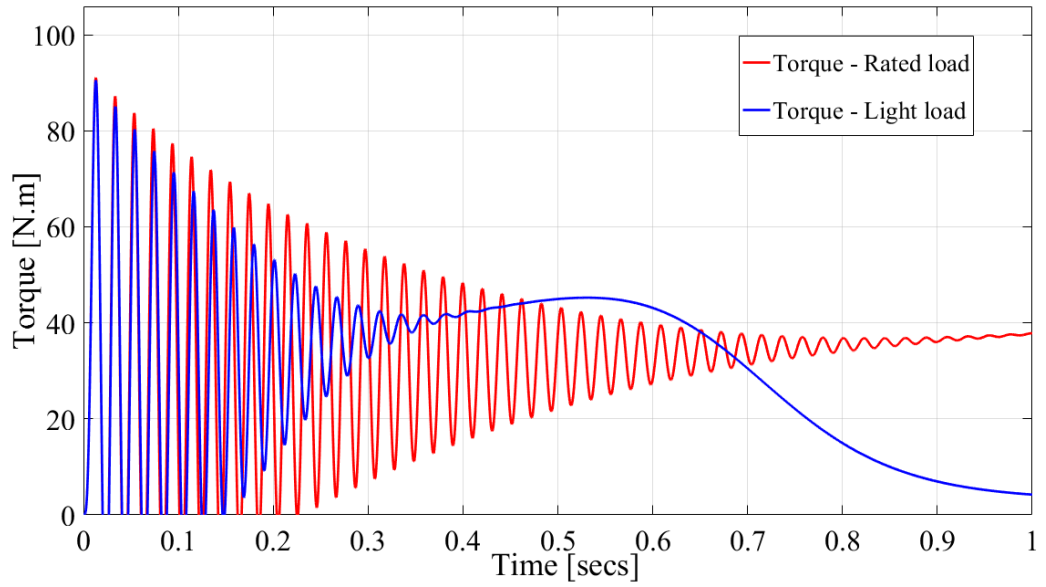


Figure 5.3. Run-up torque with different loads.

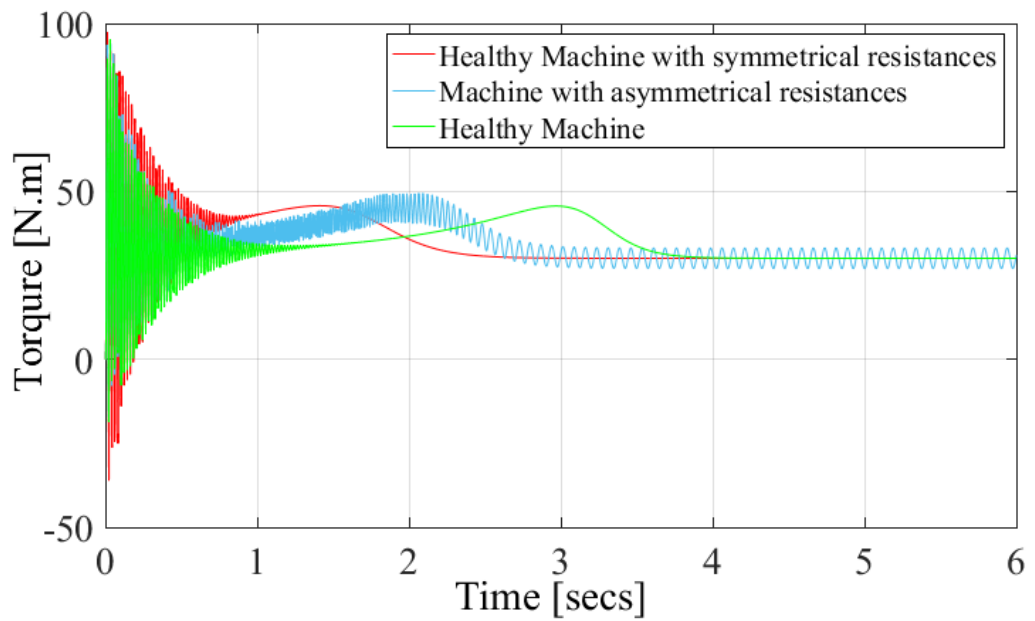


Figure 5.4. Electromagnetic torque developed by the machine with rated load.

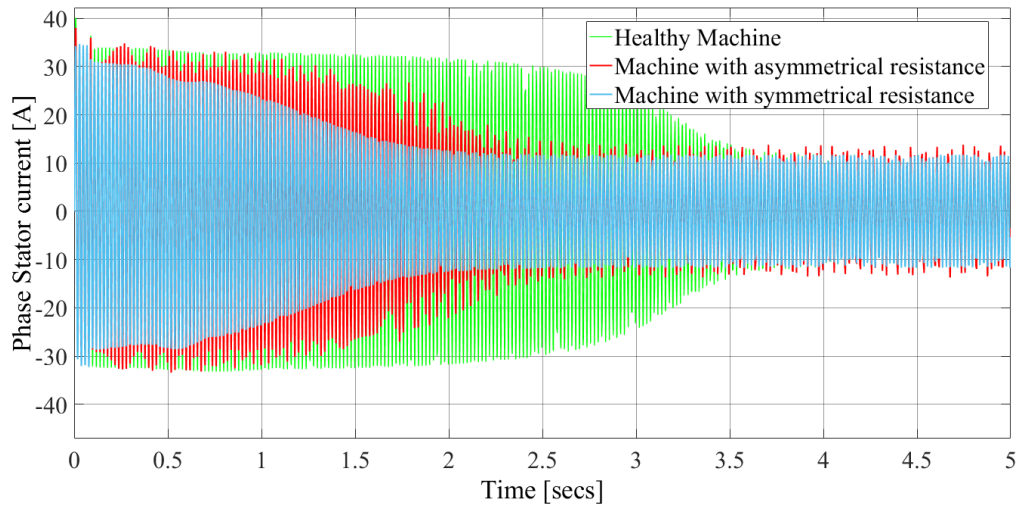


Figure 5.5. Simulated phase stator currents v.s. time response under different conditions.

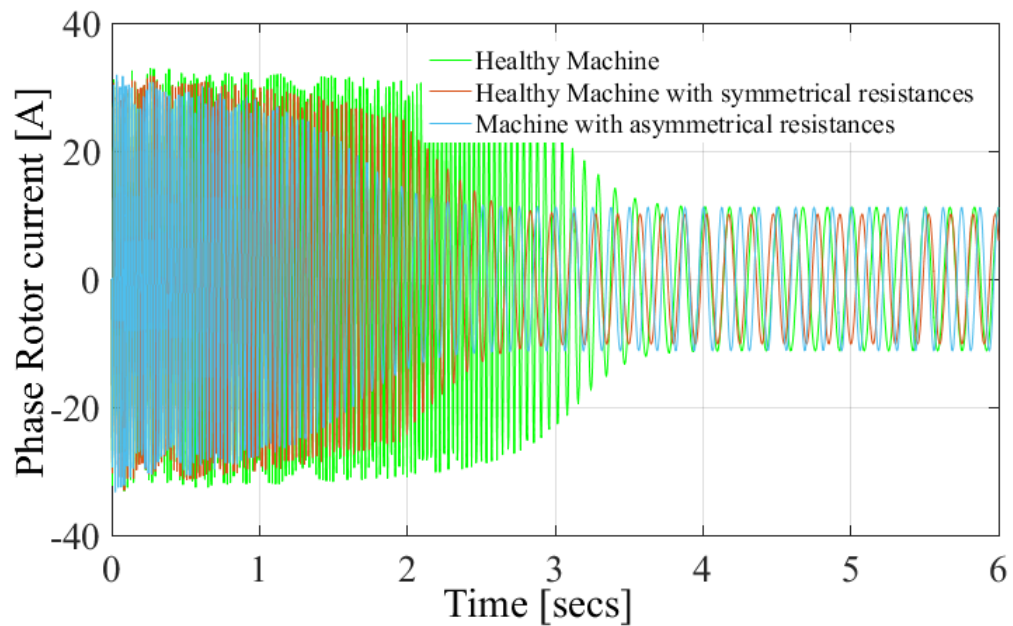


Figure 5.6. Simulated rotor currents v.s. time response under different conditions.

The time to achieve steady-state stator current is reduced when additional rotor resistance. An unbalanced rotor will introduce a loss of the steady torque and produce more torque oscillation. The torque ripple in the steady state substantially increases when the rotor is asymmetric. The three rotor winding currents are not equal and the current harmonics

increase significantly. The losses in the rotor increase after adding external resistance to the rotor. The losses increase even more if the symmetrical resistances are added.

The machine requires 1.5 extra seconds to reach steady state when connected to unbalanced resistors. The stator losses increase during the transient state after adding both the symmetrical and asymmetrical resistances as shown in Figure 5.7. The asymmetrical resistances result in oscillation in the stator power loss. Adding the symmetrical resistance enables the stability of the machine to be achieved in less time.

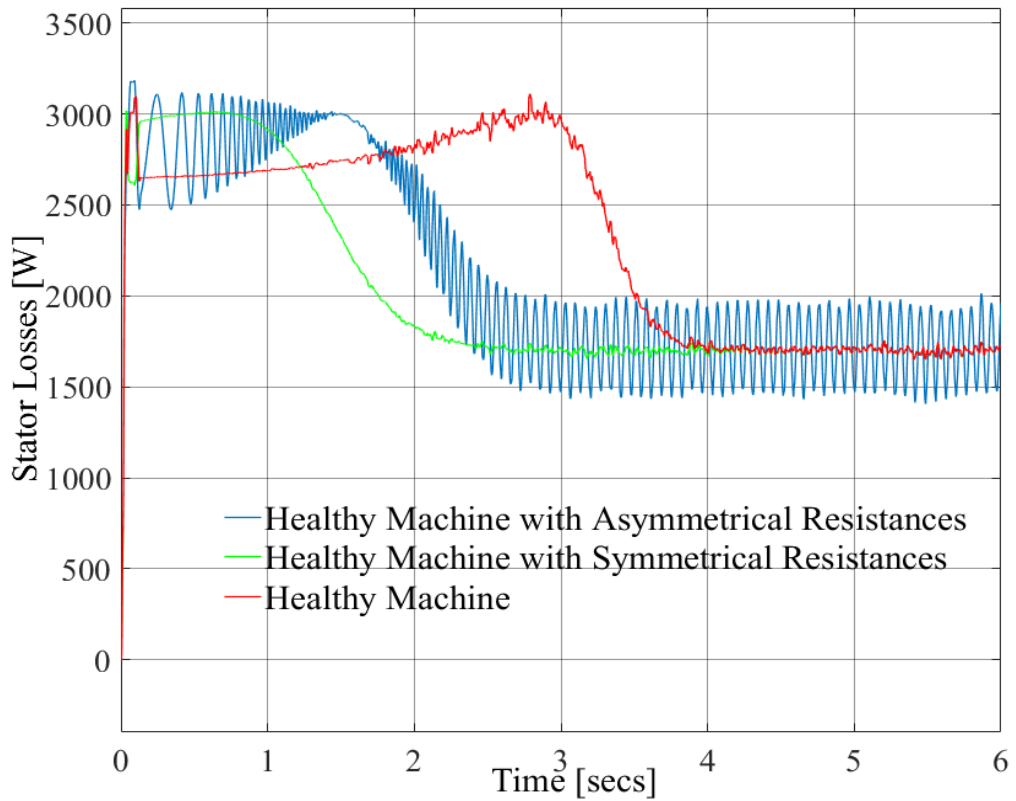


Figure 5.7. Simulated stator power losses v.s. time under different conditions.

A negative dip in the state steady torque occurs at slip = 0.5 (half synchronous speed point) as shown in Figure 5.8. The main oscillating torque generated by the backward rotor field is at a frequency of $2sf$ and this oscillating torque occurs when the machine is

run at half speed with an unbalanced rotor. The impact of asymmetrical resistors on the three rotor phase currents is shown in Figure 5.9. The variation of the three rotor currents reflects the imbalance of the external rotor resistors. Figure 5.10 shows the forward and backward stator currents. It can be seen that I_{sb} is almost equal to zero in a healthy machine and it has non-negligible value in a machine connected with asymmetrical resistances. In addition, it rapidly drops to zero at the half speed point in case of asymmetrical resistances. This occurs when the backward field generated by the asymmetrical rotor is stationary with respect to the stator, and hence cannot produce EMFs in the stator coils. Regarding operating conditions, simulation tests at different speeds show constant values of the ratio I_{sb}/I_{sf} around the rated slip value, according to the equivalent circuits. The results are reported in Figure 5.11 and Figure 5.12; the backward current components at rated speed can be detected. Figure 5.12 shows the percentage of the stator backward component to the forward component, and as expected, the amplitude falls to zero at $s = 0.5$. In a small induction machine, the backward components have very small amplitude compared to the main stator current component so careful measurement is necessary. The analysis and simulation indicate that the stator and rotor power losses increase in the fault condition, which is also reported in Figure

5.13. There is a jump in the rotor winding loss in the fault condition during the starting time.

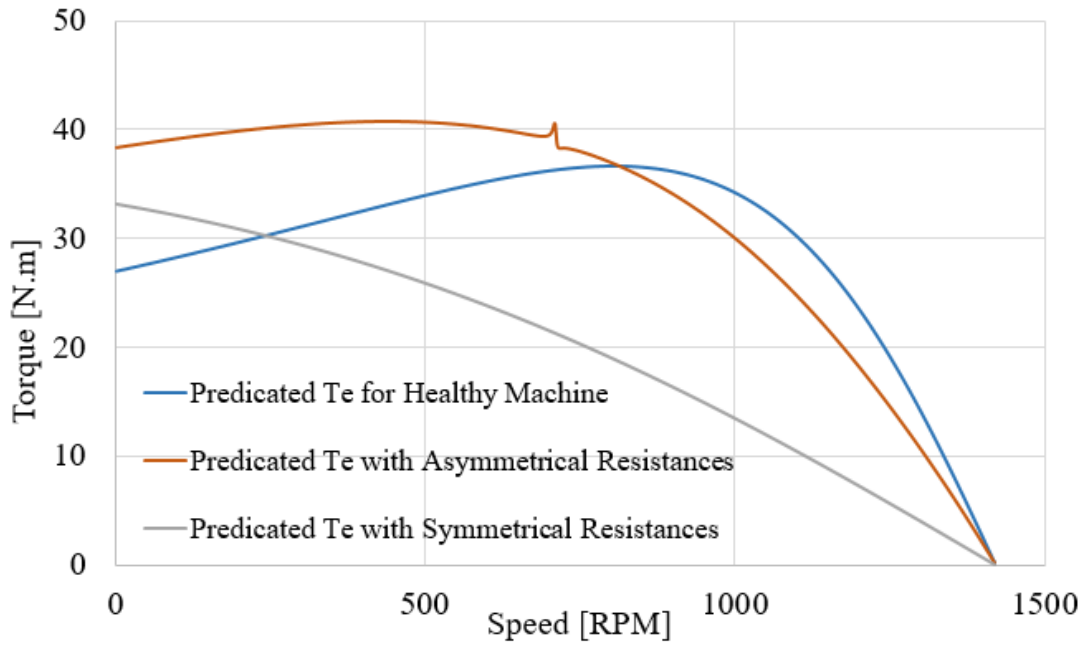


Figure 5.8. Characteristics of steady state torque developed by the machine v.s. speed.

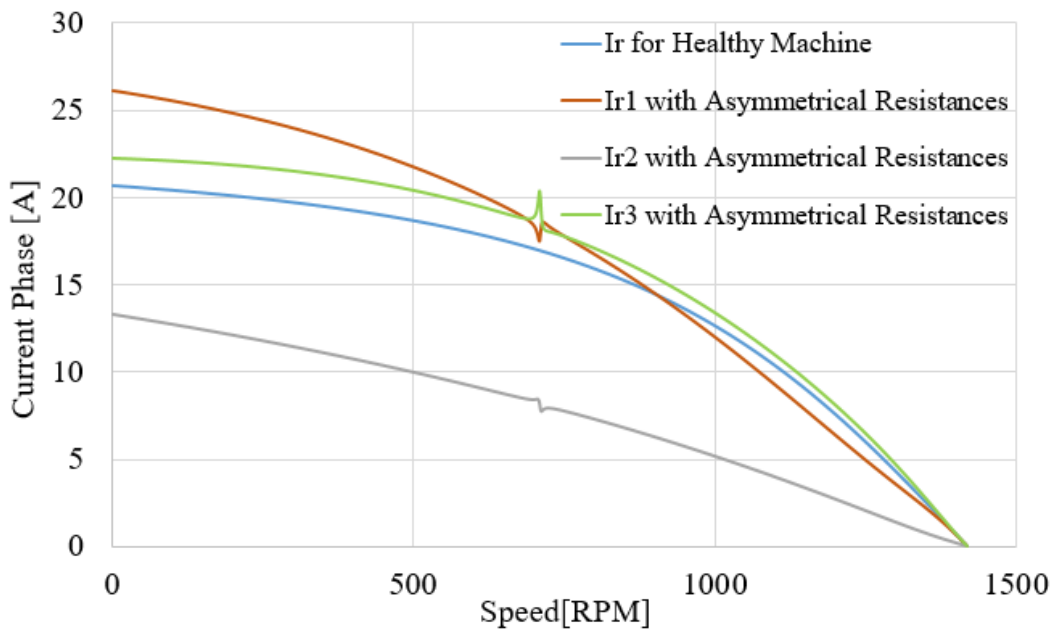


Figure 5.9. Predicted three phase rotor currents v.s. speed characteristics for balanced and unbalanced rotors.

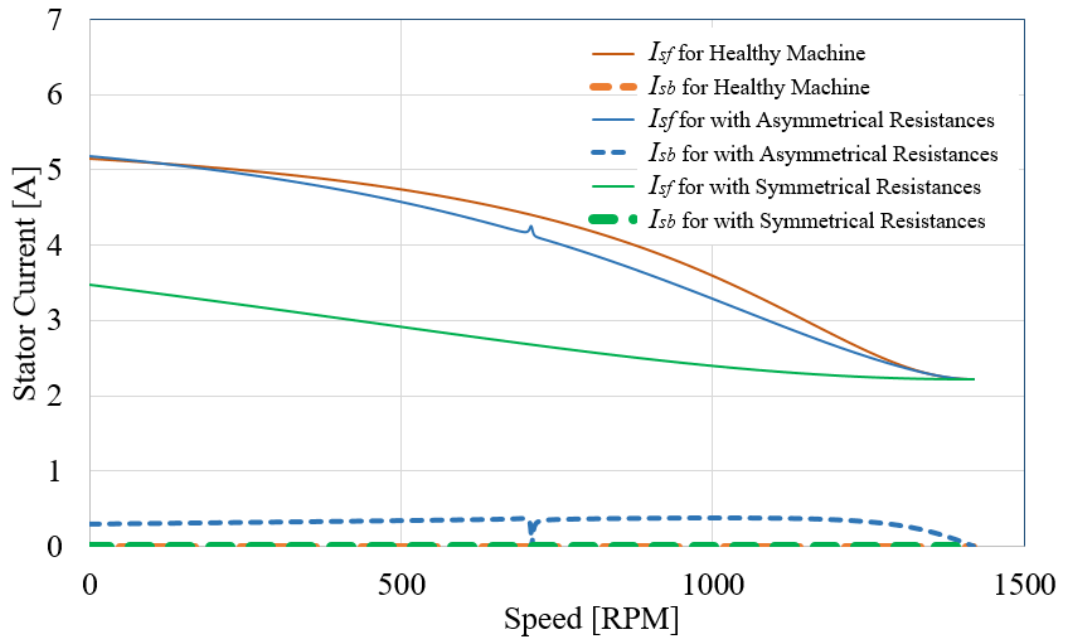


Figure 5.10. The forward and backward components of stator current for balanced and unbalanced rotors.

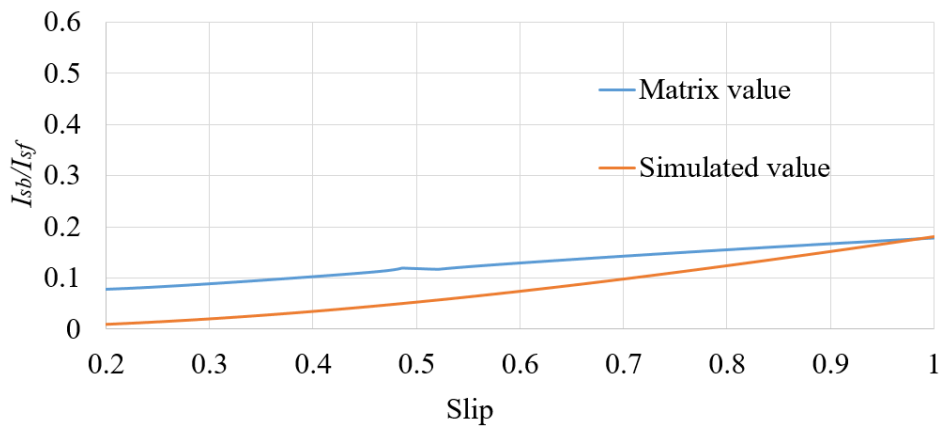


Figure 5.11. Curve I_{sb}/I_{sf} versus slip for wound rotor machine with asymmetrical resistances.

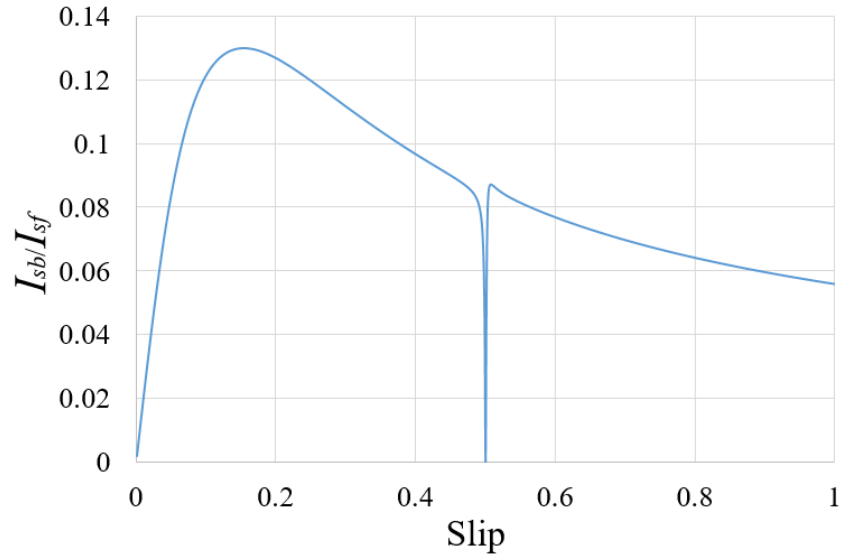


Figure 5.12. Percentage of the backward component over forward component of stator current v.s slip for a machine connected to asymmetrical resistances, showing the drop point at half speed.

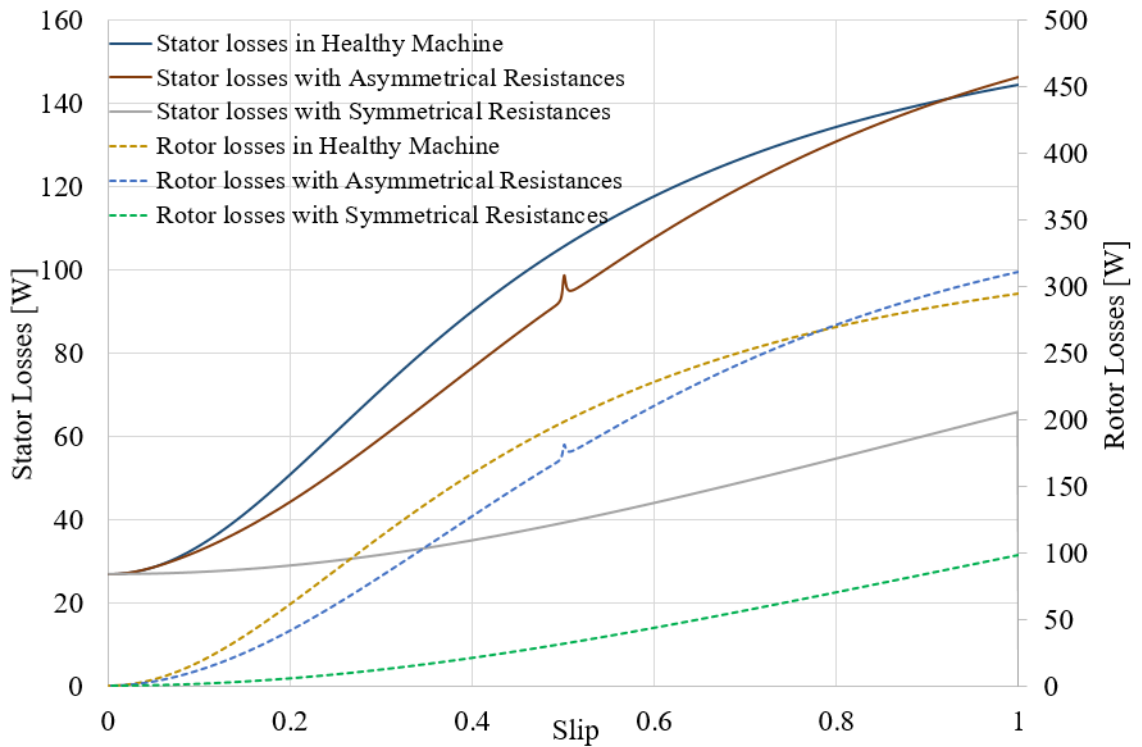


Figure 5.13. Stator and rotor losses vs. slip for a healthy machine, machine with asymmetrical resistances connected to the rotor, and machine with asymmetrical resistances connected to the rotor.

5.4 Experimental Work and Results

5.4.1 Experimental Test Set-up and Testing Procedure

The experimental investigation in this Section was carried out on a 7.46 kW three-phase four-pole wound rotor induction machine. This machine was utilised to evaluate the mathematical analysis. Data for this machine are given in Appendix C. A number of tests were performed to obtain the machine parameters, such as an open circuit (running light test) and a short circuited (locked rotor test) tested, etc. as described in Appendix D. The setup of the experiment involving the test machine, DC motor, external resistances, and measurement equipment is shown in Figure 5.14. The slip rings were connected to three variable resistors (1 to 5 Ω). The machine was coupled to a DC machine through a shaft mounted torque unit. The system speed was controlled using the Ward-Leonard system, as will be described.

In this experiment, the test machine (WRIM) drives a DC generator. The field of the DC generator is excited separately. The DC generator is loading by means of a resistor load rack. Since the motor drives a load, it must exert more torque. The induced torque is proportional to the product of flux and current, so with increasing load the relative speed (slip) between the rotor and the rotating magnetic field will also increase. However, the no-load current of the test machine is as high as 30 % to 40 % of the full-load value. The performance of the induction machine can be determined indirectly by loading a DC generator coupled to its shaft as shown in Figure 5.14. Torque transducer was added to continuously measure the speed and torque of the machine. The test machine supplied by an AC drive operating under scalar (open-loop) constant Volts per Hertz control was tested in the laboratory.

The parameters of the DC machine (generator) are listed in Table 5.1. The armature and field winding of the DC machine are electrically separated from each other. The field winding is excited by a separate DC source as the block diagram in Figure 5.15 illustrates.

Table 5.1. DC machine parameters.

| Name plate details | |
|-------------------------------|------|
| Power [HP] | 2 |
| Speed [rpm] | 1000 |
| Stator voltage [V] | 100 |
| Stator rated current [A] | 1.2 |
| Rotor Voltage [V] | 100 |
| Rated rotor current [A] | 26.1 |
| Measured resistances | |
| R Armature (room temp.) [Ohm] | 1.49 |
| R Field (room temp.) [Ohm] | 68.8 |

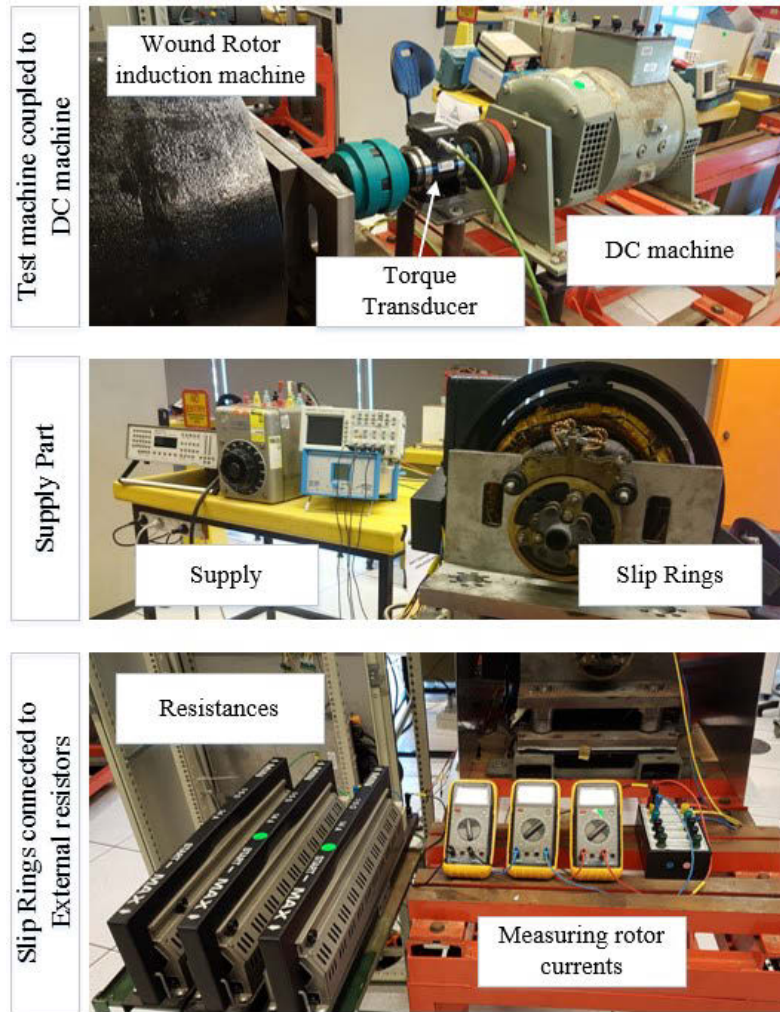


Figure 5.14. Laboratory set up of the experiment involving the test machine, external resistances, and measurement equipment.

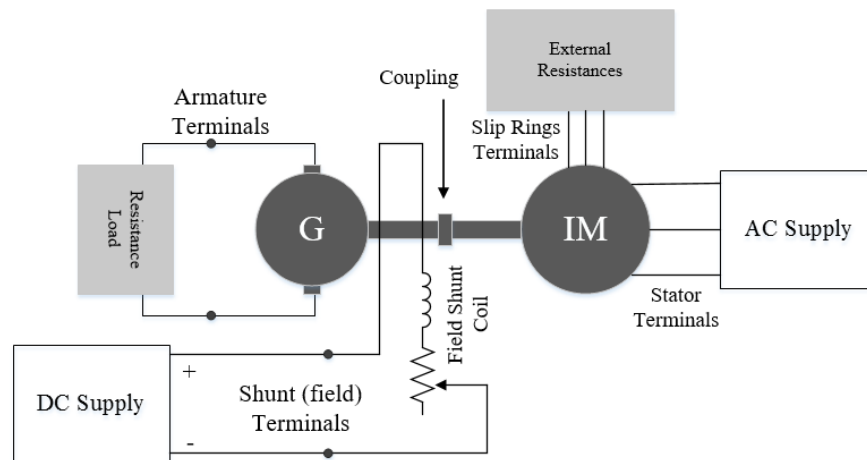


Figure 5.15. Schematic diagram of the connection for load testing of the wound rotor.

The test machine was connected in star with a line voltage. The stator voltage is reduced to values (100 V, 75 V, and 50 V) during the tests, facilitating greater stability of the machine. Reducing the stator voltage also minimises the magnetic saturation effects and oscillation torque that could be generated by an unbalanced condition.

In the next section, an extensive series of tests on the wound rotor machine are reported. There are a range of rotor faults and a variety of load conditions which are carried out to evaluate the induction machine behaviour in healthy and faulty conditions. The torque, the stator current, and the rotor currents are measured for a short-circuit rotor and when the rotor is connected to a symmetrical and asymmetrical bank of resistors. Finally, these outcomes are compared with the calculated variations of the same quantities. This allows the influence of rotor faults to be examined.

5.4.2 Results and Discussion

The induction machine was tested under healthy working conditions and with unbalanced rotor (asymmetrical) conditions at various speeds. The stator and rotor current measurements were made at no load and rated load. The machine ran at various line voltages, and the torque-speed curves were measured for these cases. All these measurements were compared with calculated values.

Figure 5.16 and Figure 5.17 show the experimental variations of rotor and stator current with speed. They are compared with the predicted variations of the same quantities for the healthy and faulty conditions. There is a good agreement which is evidence of the ability of the impedance matrix to predict the induction machine behaviour accurately. However, there are some differences in the results. These measurements were considered satisfactory; hence, the small backward current components proved useful in detecting

rotor faults. Figure 5.18 illustrates the effect of asymmetrical resistances on the fundamental rotor phase currents. The variation between rotor phase currents is substantial.

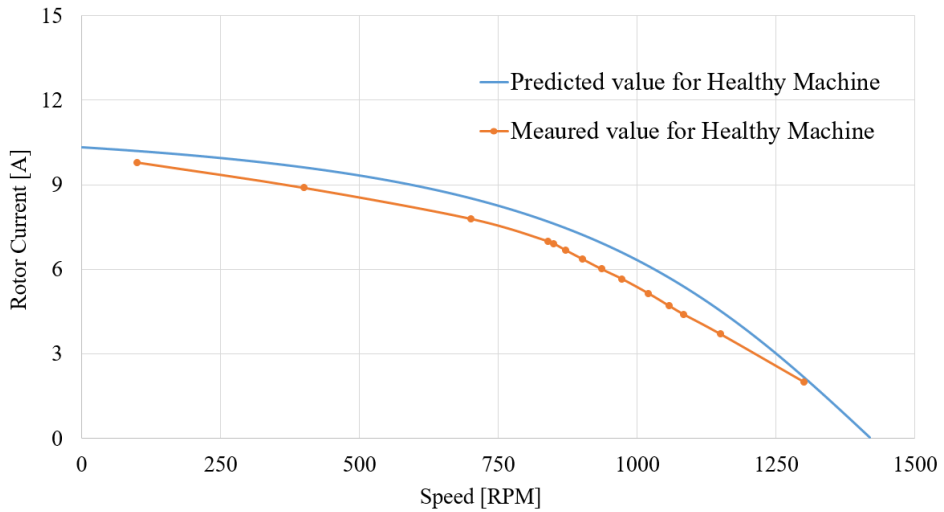


Figure 5.16. Variation of rotor current with speed for a healthy machine.

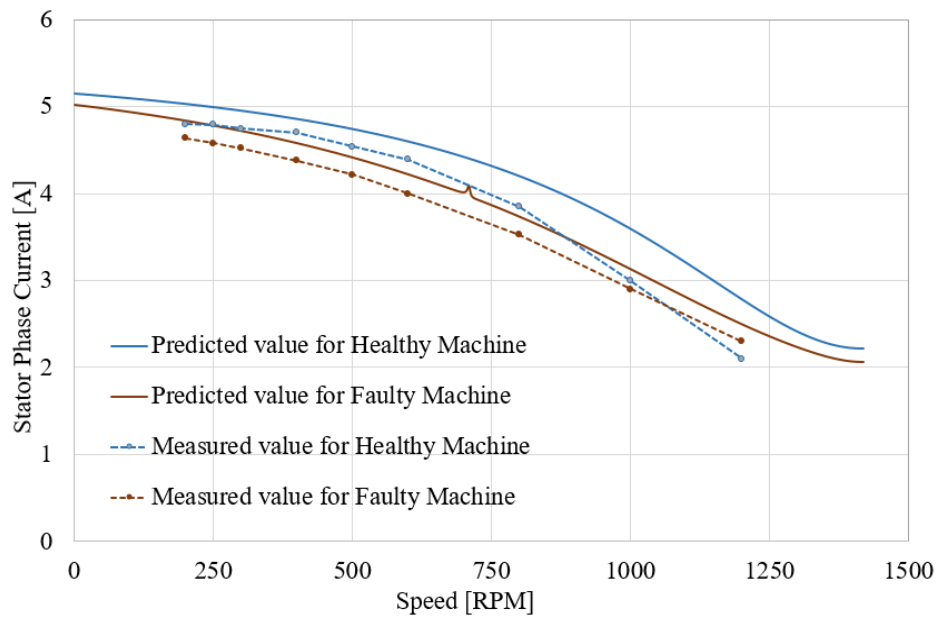


Figure 5.17. Variation of line current with speed for a machine in healthy condition, and a faulty machine with one rotor phase connected with asymmetrical resistance (2Ω).

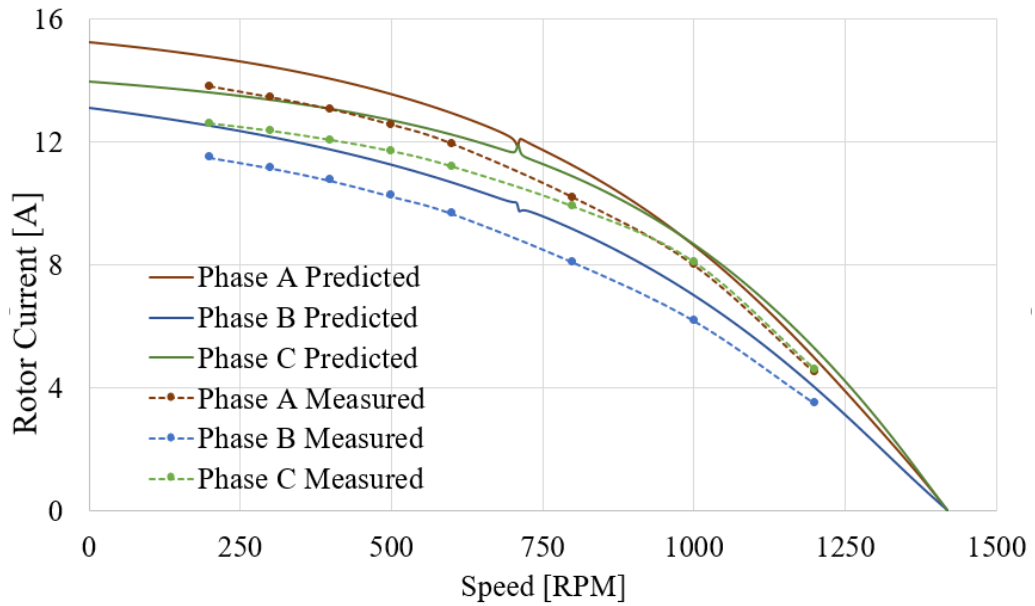


Figure 5.18. Measured and predicted rotor phase currents for unbalanced rotor (one rotor phase connected with 2Ω , and the other two phases are short-circuited).

Figure 5.19 shows the variation of rotor currents under two fault conditions. In the first condition, one of the rotor phases was connected to a 5Ω resistor, and in the second one it was connected to a 2Ω resistor. The variation increases with increasing unbalance of the external resistances. The torque speed curve is obtained under fault conditions and is shown in Figure 5.20. The oscillating torque occurs if the machine runs at half speed with asymmetrical resistance. During the tests, there is some vibration around this speed. In addition, the speed was not measured at half speed because the test machine was not stable. The measured results agree well with the analysis presented earlier in this chapter. The variation of the $(2s-1)f$ backward components of the stator current for two fault conditions are shown in Figure 5.21. It was expected that these components would rapidly drop to zero at half speed, corresponding to $s = 0.5$. Although these components increase with increasing unbalance, it is very difficult to record due to their small amplitude. This will occur when the backward field generated by the asymmetrical rotor is stationary with

respect to the stator, and hence no EMFs are induced into the stator coils. During all tests, the backward components amplitude did not exceed 6 % of the mains stator current. However, it was observed experimentally that these components do not vary between the various fault conditions.

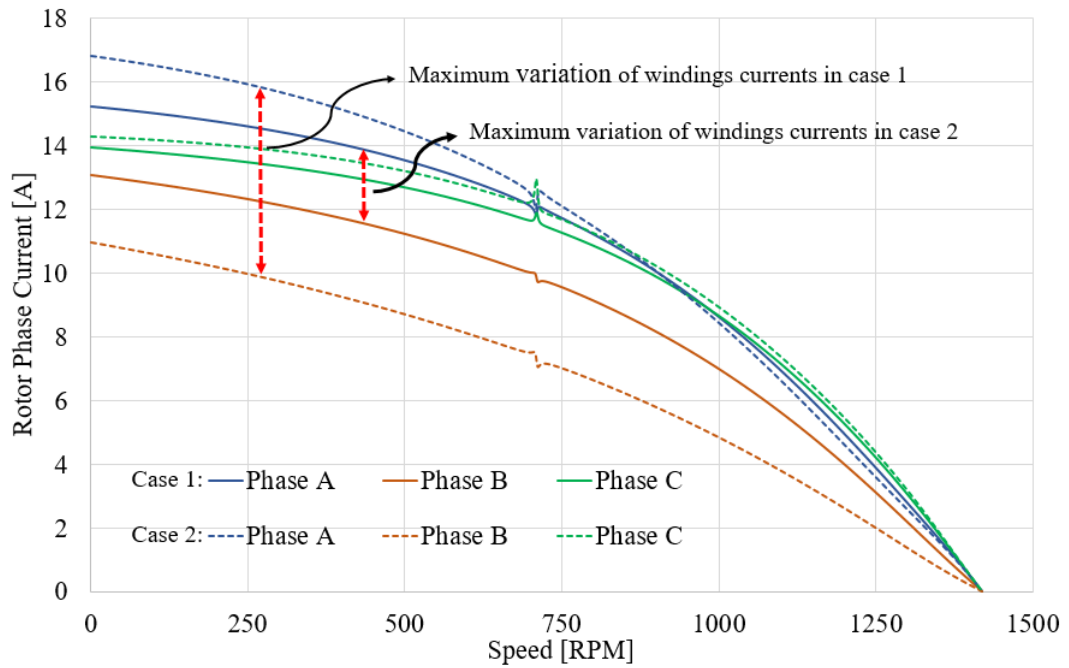


Figure 5.19. Variation of rotor phase currents for the two fault conditions. In the first condition, one of the rotor phases was connected to 2Ω , and in the second condition it was connected to 5Ω .

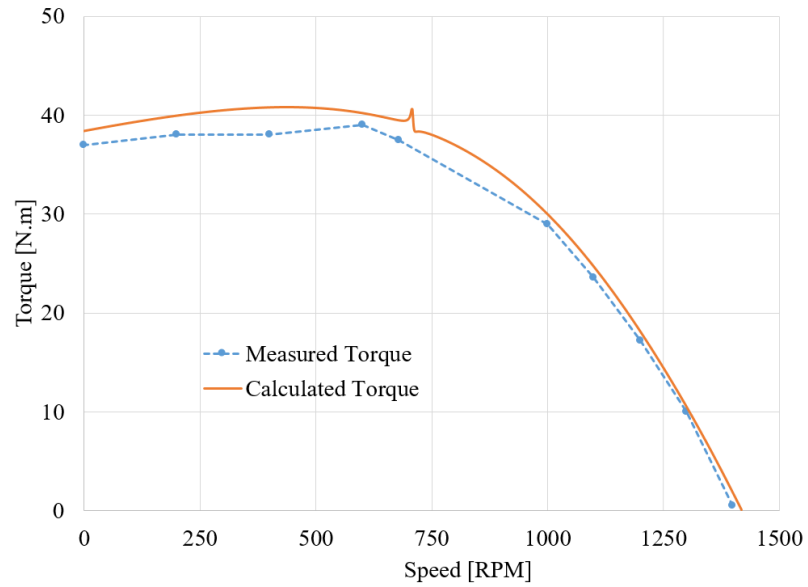


Figure 5.20. Variation of measured and calculated steady torque with speed for machine connected with asymmetrical resistances (2Ω).

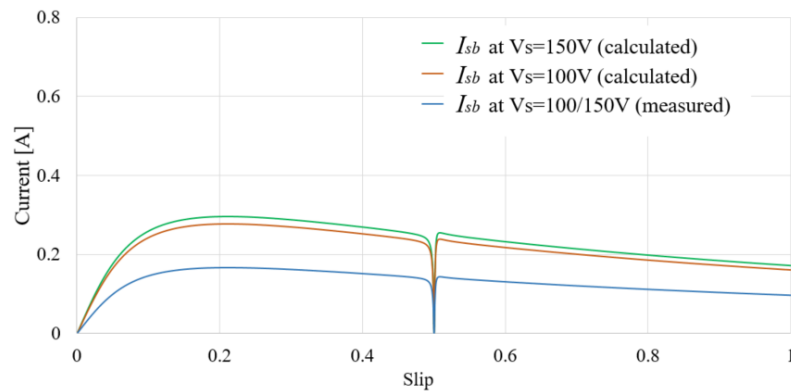


Figure 5.21. The backward components of stator current vs. slip for machine connected with asymmetrical resistances (2Ω), and the machine runs with 100 V and 150 V respectively.

5.5 Chapter Summary

The focus of the chapter was on several important aspects related to the impedance matrix method when used to identify the characteristics of rotor winding faults. Variations in the amplitude of stator current components are used to detect the rotor faults. The transient

and steady-state operation of the induction machine with asymmetrical rotor has been simulated. The steady state performance of the wound rotor machine was investigated by means of an equivalent circuit which included the rotor asymmetries. It is tested successfully on three-phase balanced and unbalanced induction machine operating conditions.

The technique is an induction motor fault diagnostic method, which investigates induction machine performance. The coupling impedance approach minimises the complexity of the analysis for an unbalanced three-phase induction machine in general. Experimental verification of this analysis was carried out to show how it is possible to use this type of analysis to improve condition monitoring of induction machines. It is possible to use stator current components for detection purposes in a large induction machine. In a small induction machine, the backward components have very small amplitude compared to the main stator current component so careful measurement is necessary. At different speeds, the amplitude of these components is around 6 % of the mains stator current. An unbalanced rotor increases the oscillating torque and reduces the steady state torque. Another advantage of this approach is that the same process of analysis could be used to consider the effect of winding harmonics.

Chapter 6: Study of Wound Rotor Induction Machines Including Air-gap Eccentricity Fault

This chapter puts forward a concept for measuring rotor eccentricity in a wound rotor induction machine. A simple method using pole-specific search coils is introduced to evaluate the degree of air-gap eccentricity in the induction machine. The UMP characteristics in the induction machine are described and then UMP is accurately calculated. The analysis is fully developed in the theory section, then an experimental rig for measuring UMP is described and measurements are taken. The reader is assumed to be familiar with fundamental air-gap magnetic flux density produced in an induction machine. However, some basic context and supporting information are provided.

6.1 Analysis of Air-gap Flux Changes Due to Eccentricity in Wound-Rotor

Induction machines are commonly designed to generate flux density that is as sinusoidal as possible in the air-gap, so they only one significant spatial harmonic of air-gap flux density. The pole-pair number of the machine winding p_m determines the harmonic number for the main flux component. For example, in 2 pole machine, the harmonic number for the main harmonic of the air-gap flux is $n = p_m = 1$, often called the fundamental harmonic. Therefore, there are no radial magnetic forces in an ideal machine (a purely theoretical model). However, this not true for real machines. In the case of rotor eccentricity, the air-gap permeance loses symmetry and the current density produces more than one spatial flux density harmonic that can interact to produce UMP. Such eccentricity often appears due to manufacturing tolerances. Inaccuracy of installation is

another reason for increasing UMP, for example, when the bearings are incorrectly positioned or worn.

The UMP in a wound-rotor machine can vary greatly from its cage-rotor equivalent [3, 141] and it is substantially higher. To describe this phenomenon, Figure 6.1 shows the main spatial harmonics that will be presented in a cage induction machine when there is low-level eccentricity. Figure 6.2 shows these for the wound rotor machine. It is clear that a series of MMF waves must be considered, which should correspond to the winding harmonics. The differential waves in the cage machines are discussed in detail in [141]. The authors conclude that the profile of the air-gap harmonics change with speed. At full-load speed the main pole-number flux wave dominated the air-gap harmonics, while at start, it has substantial differential flux wave components. In addition, authors observed that there are missing rotor MMF waves in the wound-rotor machine.

In Chapter 3, Figure 3.4 shows how this assumption could be extended to a four pole wound rotor machine. It breaks down the air-gap MMF and flux waves in terms of a four-pole machine and represents the interaction of these. The main difference is the lack of two-pole and six-pole MMF waves on the rotor that can damp the additional flux waves generated by the rotor eccentricity, hence reducing the UMP. This is because the cage structure has many effective parallel paths, which even out the air-gap flux and reduces the radial pull. The use of additional damper windings has been investigated in [3-6] and a similar theme is investigated here. However, this is combined with using pole-specific search coils to assess the degree of eccentricity.

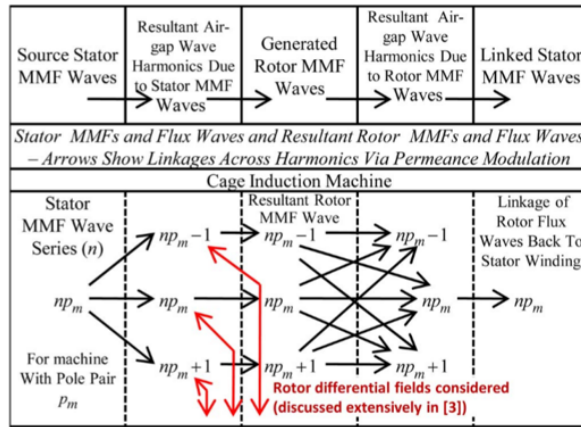


Figure 6.1. Air-gap flux waves accounted for in this study, showing linkages between MMF waves in a cage rotor machine and associated air-gap harmonic waves; for three-phase winding, $n = 1, 5, 7$, etc [50].

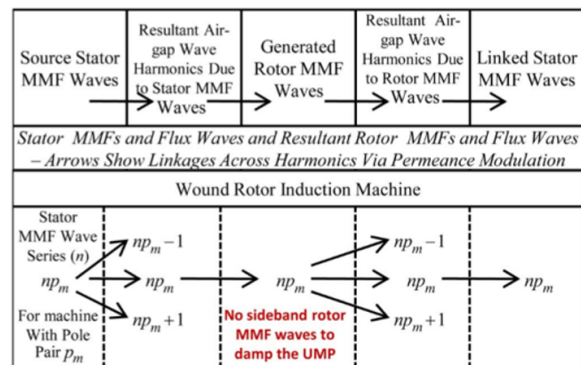


Figure 6.2. Air-gap flux waves accounted for in this study, showing linkages between MMF waves in a wound rotor machine and associated air-gap harmonic waves; for three-phase winding, $n = 1, 5, 7$, etc [50].

6.2 Variation of Air-gap Length Due to Eccentricity

The aim of this section is to investigate air-gap length in the case of rotor eccentricity. To simplify the analysis, the air-gap length is described in terms of the circumferential distance around the air-gap (y direction) and axial length down the stator bore (x direction). Considering the stator and rotor as circles, as shown in Figure 6.3, $\varepsilon = \frac{d}{g_{av}}$ is the degree in per-unit terms of eccentricity of the mean air-gap length g , k is the inverse of the mean air-gap radius r , and θ is the angle for the reference circumferential zero point

where the air-gap is minimum. The inner surface of the stator bore, in polar coordinates, is $r_1(\theta) = R_s$. The rotor circumference is expressed as

$$R_r^2 = (x-d)^2 + y^2 \quad (6.1)$$

To simplify the analysis and using the format $x^2 + y^2 = h^2$, this equation can be converted into polar coordinates. It can be rearranged to

$$r_2(\theta) = d \cos \theta + \sqrt{R_r^2 - (d \sin \theta)^2} \quad (6.2)$$

However, the length of the air-gap equals the difference between r_1 and r_2 ; hence, the air-gap length is

$$g(\theta) = R_s - d \cos \theta - R_r \sqrt{1 - \left(\frac{d}{R_r}\right)^2 \sin^2 \theta} \quad (6.3)$$

In practical cases $R_r \gg d$, hence

$$g(\theta) = R_s - d \cos \theta - R_r \quad (6.4)$$

The above expression represents the air-gap between the stator and rotor of the induction machine in the case of static eccentricity (the position of minimum air-gap length is fixed in space during the operating time). For g_{av} which is the effective air gap length when the rotor is concentric

$$g \cong g_{av} (1 - \varepsilon \cos \theta) \quad (6.5)$$

where the relative eccentricity is $d = \varepsilon g_{av}$, and equation (6.5) can be expressed in axial (x) and circumferential (y) directions so that

$$g(x, y) = g_{av} (1 - d(x) \cos(ky - \theta(x))) \quad (6.6)$$

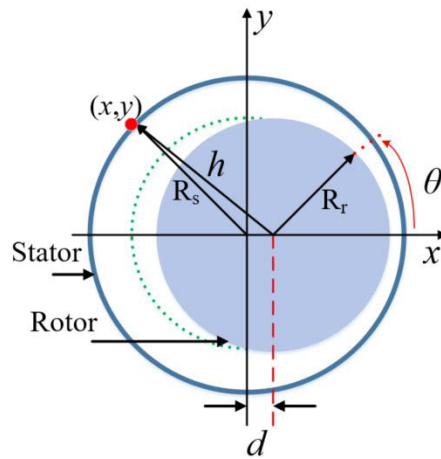


Figure 6.3. Schematic representation of air-gap eccentricity, showing the rotor and stator position.

If the shaft assembly is sufficiently rigid, the level of static eccentricity remains constant. Static eccentricity tends to produce a steady pull in one direction, while dynamic eccentricity creates a UMP vector rotating in synchronism with the rotor. The analysis model for dynamic eccentricity can be derived in the same way as for static eccentricity [84].

For the static eccentricity:

$$g_s(y) = g_{av} (1 - \varepsilon_s \cos(ky)) \quad (6.7)$$

For the dynamic eccentricity, which is a function of time t

$$g_d(y) = g_{av} (1 - \varepsilon_d \cos(\omega_r t - ky)) \quad (6.8)$$

6.3 Non-uniform Static Eccentricity

The degree of eccentricity can vary between the Drive End side of the machine (DE) and the Non-Drive End side of the machine (NDE). This is illustrated in Figure 6.4. The vector

direction of the eccentricity is different at each end which will lead to a vector rotation of the UMP on the rotor down the axial length.

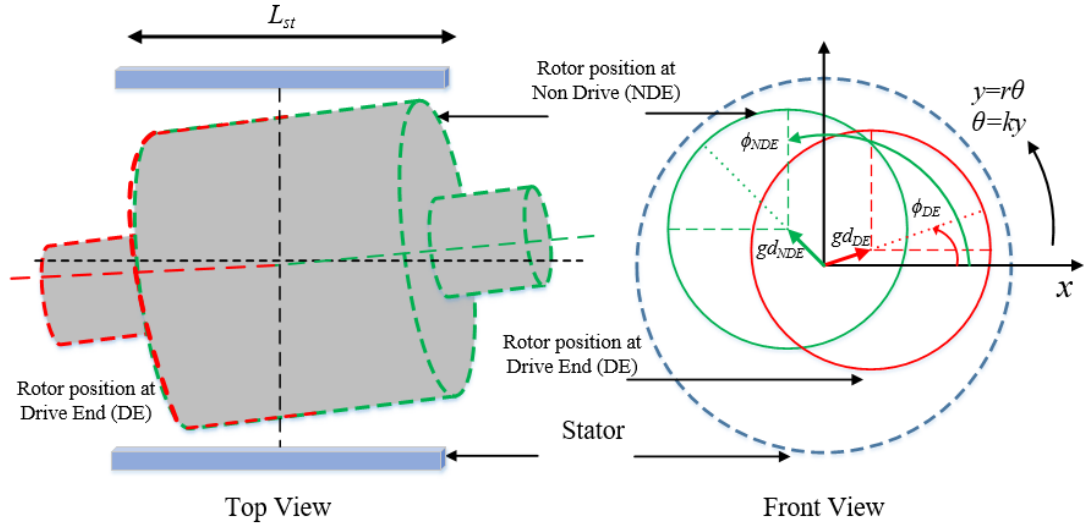


Figure 6.4. Definition of DE and NDE eccentricity.

Using equation (6.6)

$$\begin{aligned}
 g_s(x, y) &= g \left(1 - d(x) \cos(ky - \phi(x)) \right) \\
 &= \left(1 - \frac{d(x)}{2} \left(e^{j(ky - \phi(x))} + e^{-j(ky - \phi(x))} \right) \right)
 \end{aligned} \tag{6.9}$$

thus

$$= g \left(1 - 0.5 \left(\begin{aligned} &d_{ED}(x) e^{j(ky - \phi_{DE})} + d_{NED}(x) e^{j(ky - \phi_{NDE})} \\ &+ d_{ED}(x) e^{-j(ky - \phi_{DE})} + d_{NED}(x) e^{-j(ky - \phi_{NDE})} \end{aligned} \right) \right) \tag{6.10}$$

where ϕ is the angle for the reference circumferential point, where the air gap is at its minimum at each end. The functions of $d_{ED}(x)$ and $d_{NED}(x)$ are explored in the next section where an inverse is taken.

6.4 Permeance Harmonic Analysis

It is important to obtain an expression for the permeance in a convenient form. Applying Ampere's law, this will lead to an expression for the flux density distribution and hence to expressions for the coupling impedances.

The presence of rotor slots, stator slots, eccentricity of the rotor, and magnetic saturation results in a permeance wave in the air gap. From the analysis presented above, and supposing that the eccentricity degree is not high, the average permeance is the inverse of the air-gap length so that, for a cylindrical stator and rotor:

$$\Lambda(x, y)_s = \frac{1}{g(x, y)} = \frac{1}{g_{av}} \left(1 + \sum_{n=-\infty}^{\infty} \lambda^n(x) \cos(kny - \phi(x)) \right) \quad (6.11)$$

$$\begin{aligned} &\approx \frac{1}{g_{av}} \left(1 + \bar{\delta}(x) \left(e^{j(ky - \phi(x))} - e^{-j(ky - \phi(x))} \right) \right) \\ &= \frac{1}{g_{av}} \left(1 + \left(\begin{array}{l} \delta_{DE}(x) e^{j(ky - \phi_{DE})} + \delta_{NDE}(x) e^{j(ky - \phi_{NDE})} \\ + \delta_{DE}(x) e^{-j(ky - \phi_{DE})} + \delta_{NDE}(x) e^{-j(ky - \phi_{NDE})} \end{array} \right) \right) \end{aligned} \quad (6.12)$$

assuming $n=1$, if the L_{st} is the axial length, the coefficients can be defined by

$$\begin{aligned} \delta_{DE}(x) &= \left(\frac{(L_{st} + 2x)}{2d_{DE}L_{st}} \right) \\ \text{and } \delta_{NDE}(x) &= \left(\frac{(L_{st} - 2x)}{2d_{NDE}L_{st}} \right) \end{aligned} \quad (6.13)$$

where x defines that axial centre of the machine. The permeance must be expressed in rotor co-ordinates so Ampere's law can be applied to the rotor using the rotor reference frame.

In (6.13) the eccentricity is assumed low. But in [112, 135, 167, 168], the permeance was represented as Fourier series and the permeance harmonics were given as

$$\Lambda_{s,d}(y,t) = \sum_{n=0}^{\infty} \Lambda_n(t) \cos n(\omega_r t - kny)$$

$$\Lambda_n(t) = \begin{cases} \frac{\mu_o A_\delta}{g_{av}} \frac{1}{\sqrt{1-\varepsilon^2}} & n = 0 \\ \frac{2\mu_o A_\delta}{g_{av}} \frac{1}{\sqrt{1-\varepsilon^2}} \left(\frac{1-\sqrt{1-\varepsilon^2}}{\varepsilon} \right)^n & n > 0 \end{cases} \quad (6.14)$$

where A_δ is the area of the air-gap. This would be the case for high eccentricity. Smith and Dorrell [131, 135] applied the full series in their study. Belmans *et al.* in [169] moved toward linearizing the permeance series with respect to eccentricity. They found that the eccentricity often introduces only two additional spacial harmonics to the air gap. Again, Dorrell and Smith [135] verified this approach experimentally.

6.5 Generation of Additional Air-gap Flux Waves

It was stated in Section 6.1 that rotor eccentricity produces flux waves that have spatial harmonic numbers. These are usually below and above the main pole number. For example, a 4-pole machine produces 2-pole and 6-pole flux waves. In order to develop expressions for the air-gap flux waves, the air-gap flux needs to be related, as a series of flux waves, to the surface MMFs on the stator and rotor surfaces. These MMFs will be pole-specific depending on the winding harmonic. Ampere's circuital law can be applied to relate the air-gap flux using equation (3.14) for the ideal machine, which leads to a distribution for the air-gap flux due to the stator MMF waves.

Ampere's law, when applied to Figure 6.5 and considering the stator windings only, is of the form

$$\left(b_s(y,t) + \frac{\delta b_s(y,t)}{\delta y} \Delta y \right) \left(g(y) + \frac{\delta g(y)}{\delta y} \Delta y \right) - b_s(y,t)g(y) = \mu_0 j_s(y,t) \Delta y \quad (6.15)$$

The previous equation assumes that the iron infinitely permeable, therefore Δy tends to zero as derived by Dorrell in [47, 141]. Equation (6.15) can be written as

$$\begin{aligned} b_s(x,y,t) &= \frac{\int \mu_0 j_s(y,t) \cdot dy + C_{Homopolar}}{g_{s,d}(x,y,t)} \\ &= \Lambda_{s,d}(x,y,t) \left(\int \mu_0 j_s(y,t) \cdot dy + C_{Homopolar} \right) \end{aligned} \quad (6.16)$$

So that [131, 170]

$$\begin{aligned} b_s(x,y,t) &= \text{Re} \sum_{n=-\infty}^{\infty} \left[\begin{aligned} &\bar{B}_s^{np_m} e^{j(\omega t - np_m ky)} \\ &+ \bar{B}_s^{np_m - 1}(x) e^{j(\omega t - k(np_m - 1)y)} \\ &+ \bar{B}_s^{np_m + 1}(x) e^{j(\omega t - k(np_m + 1)y)} \end{aligned} \right] \\ \bar{B}_s^{np_m}(x) &= \frac{j\mu_0 \bar{J}_s^n}{knp_m g} \quad \text{and} \quad \bar{B}_s^{np_m \pm 1}(x) = \frac{j\mu_0 \bar{J}_s^n}{knp_m g} \bar{\delta}(x) \end{aligned} \quad (6.17)$$

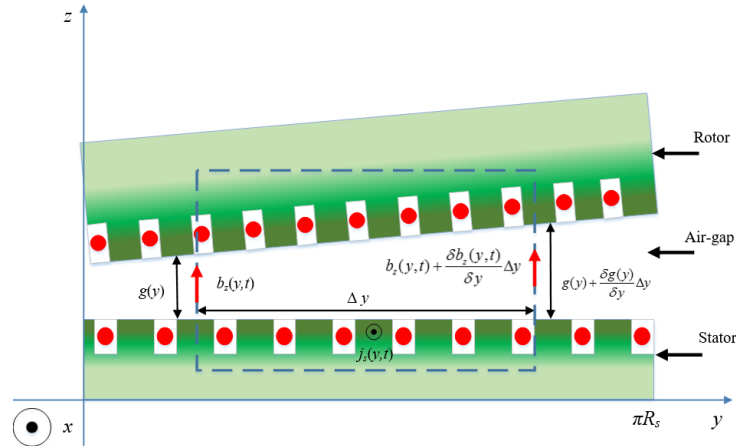


Figure 6.5. Ampere's Law Applied to a Non-Uniform Air-Gap. (after 360 mechanical degrees, the air-gap length is again the same value)

This means that the air-gap flux density distribution is written in Fourier series form. The constant $C_{Homopolar}$ is the homopolar flux term control as described in [131, 141]. The second and third terms in (6.17) explain the production of the additional flux density wave terms which appear significant when there is rotor eccentricity [3, 141]. Again, if the winding harmonics are ignored so that $n = 1$ only, then the air-gap flux is approximately

$$b_s(x, y, t) \approx \text{Re} \left(\begin{array}{l} \bar{B}_s^{p_m} e^{j(\omega t - p_m k y)} \\ + \bar{B}_s^{p_m-1}(x) e^{j(\omega_1 t - k(p_m-1)y)} \\ + \bar{B}_s^{p_m+1}(x) e^{j(\omega_2 t - k(p_m+1)y)} \end{array} \right) \quad (6.18)$$

where the field magnitude coefficients are

$$\begin{aligned} \bar{B}_s^{p_m}(x) &= \frac{j\mu_0 \bar{J}_s}{kp_m g} \\ \text{and,} & \\ \bar{B}_s^{p_m \pm 1}(x) &= \frac{j\mu_0 \bar{J}_s}{kp_m g} \bar{\delta}(x) = \frac{j\mu_0 \bar{J}_s}{kp_m g} \left(\delta_{DE}(x) e^{\pm(\phi_{DE})} + \delta_{NDE}(x) e^{\pm(\phi_{NDE})} \right) \end{aligned} \quad (6.19)$$

For the static eccentricity [131, 141]:

$\omega_1 = \omega_2 = \omega$ (i.e., a constant radial force in that direction).

For the dynamic eccentricity [131, 141]:

$\omega_1 = \omega - \omega_r$ and $\omega_2 = \omega + \omega_r$ (i.e. there is a rotational frequency radial vibration which corresponds to a rotating force vector).

In the case of the four-pole machine (which is commonly used in wind turbines as a generator pole number [171]), then, at low slip

$\omega_1 \approx \omega/2$ and $\omega_2 \approx 3\omega/2$.

The flux waves have to be transformed into the rotor reference frame in order to calculate

the EMFs induced in the rotor and so that the rotor current and MMF can be obtained. This can be done as explained in Section 3.2.3 and using equation (3.9).

$$b_{rt}(y', t) \approx \text{Re} \left(\begin{array}{l} \bar{B}_s^{p_m} e^{j(s\omega t - p_m k y')} \\ + \bar{B}_s^{p_m-1} e^{j(\omega_{1r} t - k(p_m-1)y')} \\ + \bar{B}_s^{p_m+1} e^{j(\omega_{2r} t - k(p_m+1)y')} \end{array} \right) \quad (6.20)$$

where ω_{1r} and ω_{2r} are in rotor reference frame [141]. These have instantaneous value at time t with main supply frequency ω as in [3].

For static eccentricity

$$\begin{aligned} \omega_{1r} &= \left[1 - \left(1 - \frac{1}{p_m} \right) (1-s) \right] \omega \\ \omega_{2r} &= \left[1 - \left(1 + \frac{1}{p_m} \right) (1-s) \right] \omega \end{aligned} \quad (6.21)$$

and at $s \ll 1$, these approximate to ω/p_m and $-\omega/p_m$, respectively.

For dynamic eccentricity

$$\omega_{1r} = \omega_{2r} = s\omega \quad (6.22)$$

[131, 141] show that both static and dynamic eccentricities produce their own $p_m \pm 1$ field components. The only difference between them being their rotational velocity. It can be shown from the above analysis that the frequencies of the induced EMFs are slip and pole specific, and that dynamic eccentric UMP is not damped when the slip is close to zero. Conversely there is no rotor damping of the $p_m \pm 1$ pole-pair flux waves in case of the wound rotor [135, 136]. There are no parallel circuits in the wound rotor to incorporate into the calculation as in the cage rotor. This parallel circuit damps the UMP. Hence, using parallel stator windings can also damp the UMP.

The rotor air-gap flux wave can be obtained from the expressions of the stator air-gap flux waves. Ignoring the differential waves then

$$b_r(y,t) = \text{Re} \sum_{n=-\infty}^{\infty} \left[\begin{array}{l} \bar{B}_{r(np_m, np_m \pm 1)}^{np_m} e^{j(\omega t - p_m ky)} \\ + \bar{B}_{r(np_m, np_m \pm 1)}^{np_m - 1} e^{j(\omega_1 t - k(np_m - 1)y)} \\ + \bar{B}_{r(np_m, np_m \pm 1)}^{np_m + 1} e^{j(\omega_2 t - k(np_m + 1)y)} \end{array} \right] \quad (6.23)$$

The rotor field magnitudes are

$$\bar{B}_r^{np_m}(x) = \frac{j\mu_0 \bar{J}_r^n}{knp_m g} \quad \text{and,} \quad \bar{B}_r^{np_m \pm 1}(x) = \frac{j\mu_0 \bar{J}_r^n}{knp_m g} \bar{\delta}(x) \quad (6.24)$$

However, air-gap components for additional spatial currents of $np_m \pm 1$ only exist for the cage rotor and can be calculated, but in the case of the wound rotor there are no additional spatial currents of $np_m \pm 1$. This implies that there would be a higher UMP in the wound rotor because the sideband spatial flux components would not be damped. The pole-specific search coil method can be used to predict both static and dynamic eccentricity and to damp UMP, since the EMF induced in the additional windings is influenced by the air-gap flux density. This will be presented here. This aspect not only opens the door for better understanding of the electromagnetic radial forces in different types of induction machines, but also helps to diagnose machine vibration in an industrial environment. Once the terms for the additional air-gap flux waves are obtained as in the above analysis, the UMP can be calculated.

6.6 Calculation of UMP Forces

Many different methods have been developed for electromagnetic force calculation due to eccentricity faults in the induction machine for about a century. These can be organised into two main categories: analytical methods and numerical methods. Both analytical and

numerical methods have their own benefits and drawbacks in studying induction machines, as illustrated in Table 6.1. In both, the rotor movement is assumed to be fixed, and forces and currents are calculated. In this project, the UMP that acts between the stator and eccentric rotor is studied by analytical means. The analytical method which uses standard rotating air-gap harmonic field theory demonstrates the substantial influence of the winding harmonics and rotor skew on the UMP. This provides valuable information to the induction machine designers. However, the accuracy of the UMP calculation can be maintained with acceptable calculation times. In addition, the rotor movement will be described by differential equations in order to control the eccentricity.

Table 6.1. Comparing the analytical and numerical methods.

| | Analytical Methods | Numerical Methods |
|--------------------------------------------------------------|-----------------------|----------------------|
| Prompt results | ✓ | |
| Simple interpretation | ✓ | |
| Evaluate accurately the effects of magnetic saturation | | ✓ |
| Evaluate accurately the effects of circulating currents | | ✓ |
| Evaluate accurately the effects of stator and rotor slotting | | ✓ |
| Provide high degree of accuracy in the final solution | | ✓ |
| Require computational power of computers and time consuming | | ✓ |

UMP is caused by asymmetric magnetic flux distribution in the air-gap. Many researchers reported that the pull is proportional to the square of the flux density [8, 82, 84, 172, 173]. The force pulls the rotor out of alignment. In other words, if the flux distribution is denser on one side of the rotor than the other. This force pulls the rotor towards the denser side.

In the previous section, expressions were derived for the air-gap flux density distribution of the wound rotor machine. Using these expressions, the unbalanced magnetic pull can be calculated by applying the Maxwell stress around the surface of either the rotor or the stator. The total magnetic flux density is divided into normal (radial) and tangential components. The force is determined by integrating the tensor around the air-gap surface as shown in Figure 6.6. The Maxwell stress force acting normally (radially) and tangentially to a point on the surface is

$$\sigma_n = \frac{B_n^2(\theta) - B_t^2(\theta)}{2\mu_0}, \text{ and } \sigma_t = \frac{B_n(\theta)B_t(\theta)}{\mu_0} \quad (6.25)$$

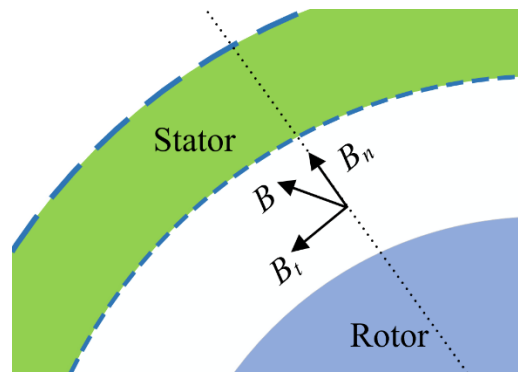


Figure 6.6. Normal and tangential components of the flux density.

where n and t are the normal and tangential components respectively. B_t is quite small relative to B_n in equation (6.25), so the effect of the tangential stress (force) on the UMP may not be noticeable under high torque conditions. In study [137], the tangential flux density was examined using coils connected to the rotor. The authors concluded that the tangential component is only responsible for about 10 % of the total magnetic force and thus can be neglected.

This means that the equation becomes

$$\sigma_n = \frac{B_n^2(\theta)}{2\mu_0} \quad (6.26)$$

Using Maxwell stresses with force components in x and y directions, the UMP is then calculated from

$$F_x = \int_0^{2\pi} \sigma r L_{st} \cos(\theta) . d\theta , \text{ and } F_y = \int_0^{2\pi} \sigma r L_{st} \sin(\theta) . d\theta \quad (6.27)$$

In [47] the full derivation is provided. However, to simplify the analysis, an example of a machine consisting of a pair of poles is considered to explain the UMP calculation process as shown in Figure 6.7(a). The rotor of the machine is set symmetrically within the stator bore. The rotor and stator are purely cylindrical, so the length of the air-gap is uniform. The rotor rotates as a result of the formation of poles of opposite polarity on the stator and rotor which exert a tangential force on the rotor. However, a much stronger magnetic force of attraction takes place between the stator and the rotor poles acting along a direction perpendicular to the rotor shaft axis. These forces therefore act radially. In a symmetrical machine, the MMF per pole and the area per pole are the same for all poles. Assume that the flux density B is uniform in the air-gap, and the MMF required for the iron parts is negligible. The forces of attraction between stator and rotor poles in the top and bottom are equal and act in the opposite direction to each other as below:

$$\begin{aligned} F_1 &= \frac{1}{2} \frac{B^2}{\mu_0} A = \frac{1}{2} \mu_0 \left(\frac{MMF}{g} \right)^2 A \\ F_2 &= \frac{1}{2} \frac{B^2}{\mu_0} A = \frac{1}{2} \mu_0 \left(\frac{MMF}{g} \right)^2 A \end{aligned} \quad (6.28)$$

where A is the area per pole.

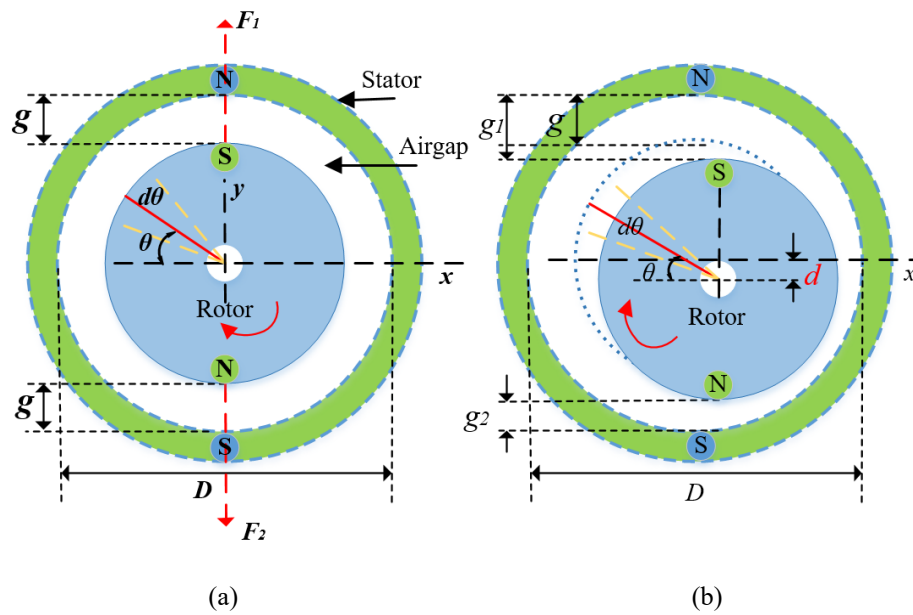


Figure 6.7. Radial magnetic forces in a 2 pole machine: (a) Radial magnetic forces in a symmetrical machine, and (b) machine with rotor displaced vertically downwards.

The forces are of equal magnitude and hence their resultant is equal to zero. There is no resultant radial magnetic pull on the rotor. In the analysis given above, the flux density distribution has been assumed uniform in the air-gap. In reality, the flux density distribution is almost sinusoidal, considering an elemental angle $d\theta$ at an angle θ from axis x . It is evident that if $g_1 > g_2$ as in Figure 6.7(b), force F_2 is greater than F_1 , and hence a resultant radial force acts on the rotor in the downward direction. It should be noticed that it is not only the abnormality of the air-gap that causes UMP but also any other asymmetry in the air-gap flux density distribution or in the winding. When the rotor is not concentric with the stator, the air-gap is not uniform over periphery. UMP is produced, which tends to draw the rotor over to the side where the air-gap is smaller. It was demonstrated earlier that the UMP is inversely proportional to the square of the length of the air-gap. Consider the case of a rotor when moved vertically downwards as shown in Figure 6.7(b). The total UMP acting on the rotor then becomes

$$F_{UMP}(x) = \frac{DL_{st}}{4\mu_0} B^2 \delta(x) \int_0^\theta (\sin \theta)^2 d\theta \quad (6.29)$$

The analysis given above assumes the case of static eccentricity, and hence the stator and rotor axes remain parallel during the running time. In (6.29), it has been assumed that the peak value of the flux density remains the same irrespective of the eccentricity, which is not true in reality. Therefore, the UMP has been calculated for the worst case. Nevertheless, as described in many studies, for a given air-gap eccentricity and flux density, the UMP increases with rotor diameter and rotor length.

Returning to equation (6.27), if α and β are Cartesian coordinates for a cross-section and the eccentricity and force are in α direction, the forces are given in quadrature by:

$$\begin{aligned} F_\alpha &= \frac{L_{st}}{2\mu_0} \int_0^{2\pi r} \sigma(y,t) \cos(ky) .dy \\ &= \frac{L_{st}}{4\mu_0} \int_0^{2\pi r} |b(y,t)|^2 (e^{jky} + e^{-jky}) .dy \end{aligned} \quad (6.30)$$

In the case of static eccentricity for simplicity, this will create a steady force. In the case of dynamic eccentricity, a rotating force vector will develop. Rewriting, the air-gap flux density waves are:

$$b(y,t) = \text{Re} \left\{ \bar{B} \left(e^{j(\omega t - p_m ky)} + \delta_s \left(e^{j(\omega t - k(p_m - 1)y)} + e^{j(\omega t - k(p_m + 1)y)} \right) \right) \right\} \quad (6.31)$$

For the 2-pole force waves (as in the earlier example) which are generated by flux waves with $p_m \pm 1$. Equation (6.29) becomes

$$\begin{aligned} F_\alpha &= \frac{L_{st}}{8\mu_0} \delta_s |\bar{B}^{p_m}|^2 \int_0^{2\pi r} \text{Re} \left\{ (e^{jky} + e^{-jky}) \times (e^{jky} + e^{-jky}) \right\} dy \\ &= \frac{\pi L_{st} r}{2\mu_0} \delta_s |\bar{B}^{p_m}|^2 \end{aligned} \quad (6.32)$$

6.7 New Approach to Eccentricity Detection Depending on Specific Search windings

The aim of the section is to investigate and demonstrate an effective detection of rotor eccentricity using a pole-specific winding method. The analysis described earlier was developed to illustrate that rotor eccentricity leads to the generation of air-gap flux waves with pole-pairs of $p_m \pm 1$. For instance, a 4-pole machine will produce 2-pole and 6-pole flux waves. If a machine with p_m pole pairs has search coils designed with $p_m \pm 1$ pole pairs then the analysis goes on to illustrate how the electromotive forces (EMFs) induced in these coils can be used to assess the degree of eccentricity as shown in Figure 6.8. These influenced by the air-gap flux density. The EMFs can be calculated and give a clear indication of the eccentricity degree in the induction machine. Two-phase search winding is used to address this conception; however, only one phase of the search winding has been shown in Figure 6.8.

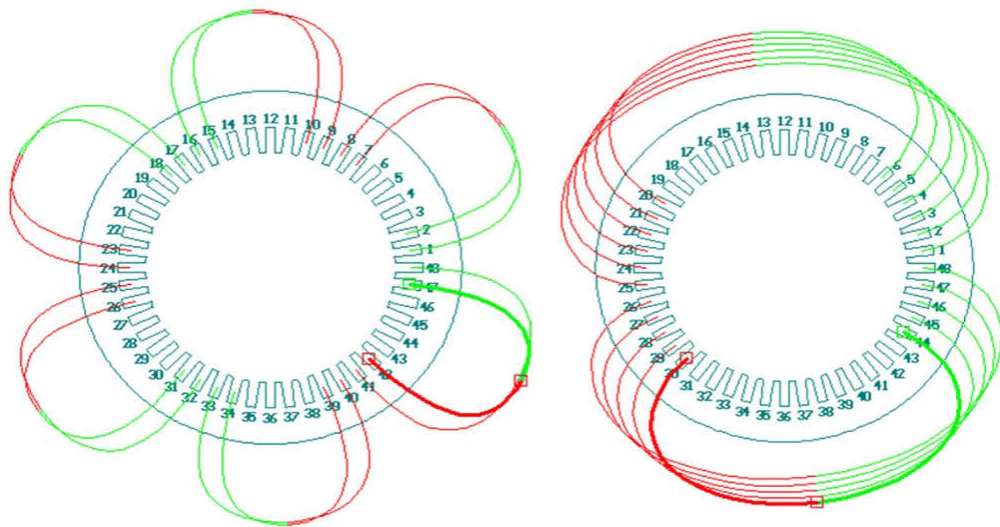


Figure 6.8. Two-phases distributed search winding: 6-pole search coils, 12 coils per phase, and 44 turns per coil and 2-pole search coils, 12 coils per phase, and 15 turns per coil – only one phase of each shown.

The main MMF harmonics in the air-gap are of order p_m and $p_m \pm 1$ when the other harmonics are neglected. The interaction between flux waves of p_m and $p_m \pm 1$ are examined for the same purpose. The impedance matrix is developed to predict the winding voltages as a function of eccentricity. However, the impedance matrix is couched in terms of a wound rotor induction motor rather than a cage machine.

To summarise the UMP and search coils voltages calculations, a flowchart is given in Figure 6.9. This illustrates the stepwise methodology required to obtain the UMP. The mathematical approach is also quite straightforward for obtaining search coil voltages. The principle equations will be explained in this section.

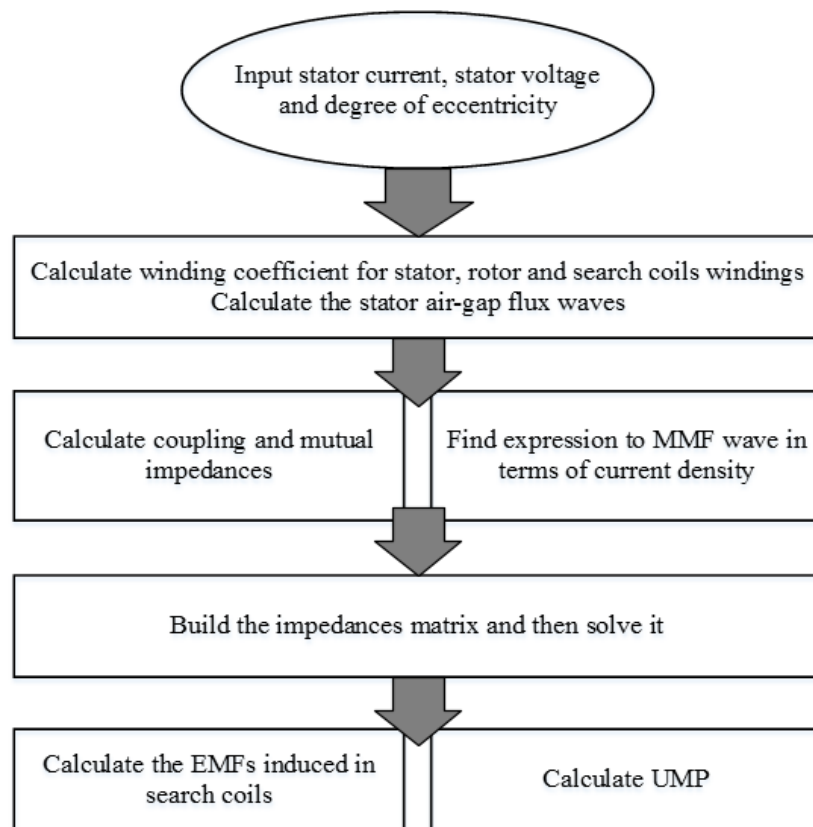


Figure 6.9. Flowchart of UMP and search coils voltages calculation.

6.7.1 Eccentricity Detection

Once the terms for the additional air-gap flux waves have been obtained, the UMP can be calculated as illustrated earlier. To get the EMF induced in the pole-specific search coils, the air-gap electric field needs to be calculated, which can be obtained from:

$$e^p(x, y, t) = \frac{db^p(x, y, t)}{dt} dy = \bar{E}_s^{p_m \pm 1}(x) e^{j(\omega t - k(p_m \pm 1)y)} \quad (6.33)$$

where

$$\bar{E}_s^{p_m \pm 1}(x) = \frac{-\bar{B}_s^{np_m \pm 1}(x)}{k(p_m \pm 1)} = \frac{-j\mu_0\omega\bar{J}_s^n}{k^2 p_m(p_m \pm 1)g} \bar{\delta}(x) \quad (6.34)$$

For a machine with p_m pole-pairs, it can be assumed that there are two pole-specific search windings with pole-pair numbers of $p_m \pm 1$. Each pole-pair has two windings in quadrature on the α and β axes. The EMFs induced into these windings can be obtained from:

$$u_{(SC+1)_{(\alpha, \beta)}}(t) = \text{Re} \int_{-L_{st}/2}^{L_{st}/2} \int_0^{2\pi r} -e^{p_m+1}(x, y, t) n_{(SC+1)_{(\alpha, \beta)}}^{p_m+1}(y) dy dx \quad (6.35)$$

$$u_{(SC-1)_{(\alpha, \beta)}}(t) = \text{Re} \int_{-L_{st}/2}^{L_{st}/2} \int_0^{2\pi r} -e^{p_m-1}(x, y, t) n_{(SC-1)_{(\alpha, \beta)}}^{p_m-1}(y) dy dx$$

The search winding coefficients are, for the p_m+1 pole-pairs and for p_m-1 pairs:

$$n_{(SC+1)_\alpha}^{p_m+1}(y) = \left(\bar{N}_{(SC+1)}^{p_m+1} \right)^* e^{-j(p+1)ky}$$

$$n_{(SC+1)_\beta}^{p_m+1}(y) = \left(j\bar{N}_{(SC+1)}^{p_m+1} \right)^* e^{-j(p+1)ky} \quad (6.36)$$

$$n_{(SC-1)_\alpha}^{p_m-1}(y) = \left(\bar{N}_{(SC-1)}^{p_m-1} \right)^* e^{-j(p-1)ky}$$

$$n_{(SC-1)_\beta}^{p_m-1}(y) = \left(j\bar{N}_{(SC-1)}^{p_m-1} \right)^* e^{-j(p-1)ky}$$

where

$$\bar{N}_{SC+1}^{p_m+1} = \frac{k}{2\pi} \sum_{w=1}^{N_w} k_s C_{w(SC+1)} e^{jn(p_m+1)ky_w}, \text{ and } \bar{N}_{SC-1}^{p_m-1} = \frac{k}{2\pi} \sum_{w=1}^{N_w} k_s C_{w(SC-1)} e^{jn(p_m-1)ky_w} \quad (6.37)$$

where C_w is the number of conductors of the search coil winding.

For simplicity, it is assumed that the α winding is on the real axis and the β winding is on the imaginary axis. Phase a of the main winding is also located on the real axis. This is the expression for the voltage induced in the search coil by a rotating flux wave set up by a balanced 3-phase current. If the current set is unbalanced, then a backward rotating flux wave will be set up. This can be accounted for and will be the focus of further work. If the winding harmonics are ignored such that $n = 1$ only, then the air-gap flux is approximately as in equation (6.18). The EMF induced into the additional windings is influenced by the air-gap flux density. Hence, the pole-specific search coil method can be used to predict both static and dynamic eccentricity. Now there is a need to develop the theory for calculating the EMFs induced into pole-specific search coils in the induction machine.

6.7.2 Development of the Impedance Matrix for Condition Monitoring

An impedance matrix can be developed that incorporates both eccentricity and the pole-specific search windings. The coupling impedance matrix expressed in (3.21) can be developed for this purpose. The additional pole-specific search windings have linkage impedances and self impedances, hence some columns and rows must be added. If we focus on the condition monitoring function of the search coils, and the first case when the rotor is an open circuit, then:

$$\begin{bmatrix} V_{s-ph} \\ V_{pm-1}^\alpha \\ V_{pm-1}^\beta \\ V_{pm+1}^\alpha \\ V_{pm+1}^\beta \end{bmatrix} = [\bar{Z}] \begin{bmatrix} I_{s-ph} \\ 0 \\ 0 \\ 0 \\ 0 \end{bmatrix} = \begin{bmatrix} \bar{Z}_{s,s} & 0 & 0 & 0 & 0 \\ \bar{Z}_{pm-1,s}^\alpha & 0 & 0 & 0 & 0 \\ \bar{Z}_{pm-1,s}^\beta & 0 & 0 & 0 & 0 \\ \bar{Z}_{pm+1,s}^\alpha & 0 & 0 & 0 & 0 \\ \bar{Z}_{pm+1,s}^\beta & 0 & 0 & 0 & 0 \end{bmatrix} \begin{bmatrix} I_{s-ph} \\ 0 \\ 0 \\ 0 \\ 0 \end{bmatrix} \quad (6.38)$$

where

$$\begin{aligned} \bar{Z}_{pm-1,s}^\alpha &= j \frac{3\pi\mu_0\omega L_{st}\bar{N}_{st}^1}{k^3 p_m (p_m - 1)g} \bar{\delta}(\text{mean}) \left(\bar{N}_{(SC-1)}^{p_m-1} \right)^* \\ \bar{Z}_{pm-1,s}^\beta &= j \frac{3\pi\mu_0\omega L_{st}\bar{N}_{st}^1}{k^3 p_m (p_m - 1)g} \bar{\delta}(\text{mean}) \left(j\bar{N}_{(SC-1)}^{p_m-1} \right)^* \\ \bar{Z}_{pm+1,s}^\alpha &= j \frac{3\pi\mu_0\omega L_{st}\bar{N}_{st}^1}{k^3 p_m (p_m + 1)g} \bar{\delta}(\text{mean}) \left(\bar{N}_{(SC+1)}^{p_m+1} \right)^* \\ \bar{Z}_{pm+1,s}^\beta &= j \frac{3\pi\mu_0\omega L_{st}\bar{N}_{st}^1}{k^3 p_m (p_m + 1)g} \bar{\delta}(\text{mean}) \left(j\bar{N}_{(SC+1)}^{p_m+1} \right)^* \end{aligned} \quad (6.39)$$

$Z_{s,s}$ is the stator-stator coupling impedance defined in equation (3.22). The voltage vector also includes the EMF induced in the search coils. Most of the matrix elements are zeros because the search coils are open circuit, meaning no current is produced in these coils. This is the most basic form of the impedance matrix. The leakage reactance includes all the end effects, slot leakage. The induced voltages in the windings are calculated for a given phase current and eccentricity as

$$\begin{aligned} V_{pm-1,s}^\alpha &= j \frac{3\pi\mu_0\omega L_{st}\bar{N}_{st}^1}{k^3 p_m (p_m - 1)g} \bar{\delta}(\text{mean}) \left(\bar{N}_{(SC-1)}^{p_m-1} \right)^* \left(I_{s-ph} \right) \\ V_{pm-1,s}^\beta &= j \frac{3\pi\mu_0\omega L_{st}\bar{N}_{st}^1}{k^3 p_m (p_m - 1)g} \bar{\delta}(\text{mean}) \left(j\bar{N}_{(SC-1)}^{p_m-1} \right)^* \left(I_{s-ph} \right) \\ V_{pm+1,s}^\alpha &= j \frac{3\pi\mu_0\omega L_{st}\bar{N}_{st}^1}{k^3 p_m (p_m + 1)g} \bar{\delta}(\text{mean}) \left(\bar{N}_{(SC+1)}^{p_m+1} \right)^* \left(I_{s-ph} \right) \\ V_{pm+1,s}^\beta &= j \frac{3\pi\mu_0\omega L_{st}\bar{N}_{st}^1}{k^3 p_m (p_m + 1)g} \bar{\delta}(\text{mean}) \left(j\bar{N}_{(SC+1)}^{p_m+1} \right)^* \left(I_{s-ph} \right) \end{aligned} \quad (6.40)$$

Assuming the phase current is constant, the relationship between the induced voltages and eccentricity degree is linear below a certain level of eccentricity. It is illustrated from (6.38) that monitoring the voltage in these coils can be used to assess the rotor eccentricity.

6.7.3 Development of the Impedance Matrix for UMP Control

The matrix can be further developed to include an additional winding current and active UMP control. The search winding could be either current driven or voltage driven. If passive damping is used, i.e. the windings are short circuited, then

$$\begin{bmatrix} V_{s-ph} \\ 0 \\ 0 \\ 0 \\ 0 \end{bmatrix} = \begin{bmatrix} \bar{Z}_{s,s} & \bar{Z}_{s,p_m-1}^\alpha & \bar{Z}_{s,p_m-1}^\beta & \bar{Z}_{s,p_m+1}^\alpha & \bar{Z}_{s,p_m+1}^\beta \\ \bar{Z}_{p_m-1,s}^\alpha & \bar{Z}_{p_m-1,SC}^\alpha & 0 & 0 & 0 \\ \bar{Z}_{p_m-1,s}^\beta & 0 & \bar{Z}_{p_m-1,SC}^\beta & 0 & 0 \\ \bar{Z}_{p_m+1,s}^\alpha & 0 & 0 & \bar{Z}_{p_m+1,SC}^\alpha & 0 \\ \bar{Z}_{p_m+1,s}^\beta & 0 & 0 & 0 & \bar{Z}_{p_m+1,SC}^\beta \end{bmatrix} \begin{bmatrix} I_{s-ph} \\ I_{p_m-1}^\alpha \\ I_{p_m-1}^\beta \\ I_{p_m+1}^\alpha \\ I_{p_m+1}^\beta \end{bmatrix} \quad (6.41)$$

For $p_m - 1$, the linkage and self impedances are given by:

$$\begin{aligned} \bar{Z}_{s,p_m-1}^\alpha &= j \frac{\pi \mu_0 \omega L_{st} \bar{N}_{st}^{-1}}{k^3 p_m (p_m - 1) g} \bar{\delta}(\text{mean}) \left(\bar{N}_{(SC-1)}^{p_m-1} \right) \\ \bar{Z}_{s,p_m-1}^\beta &= j \frac{\pi \mu_0 \omega L_{st} \bar{N}_{st}^{-1}}{k^3 p_m (p_m - 1) g} \bar{\delta}(\text{mean}) \left(j \bar{N}_{(SC-1)}^{p_m-1} \right) \\ \bar{Z}_{p_m-1,SC}^\alpha &= R_{SC-1} + j \frac{\pi \mu_0 \omega L_{st} \bar{N}_{(SC-1)}^{p_m-1}}{k^3 (p_m - 1)^2 g} \left(\bar{N}_{(SC-1)}^{p_m-1} \right)^* \\ \bar{Z}_{p_m-1,SC}^\beta &= R_{SC-1} + j \frac{\pi \mu_0 \omega L_{st} \bar{N}_{(SC-1)}^{p_m-1}}{k^3 (p_m - 1)^2 g} \left(j \bar{N}_{(SC-1)}^{p_m-1} \right)^* \end{aligned} \quad (6.42)$$

For $p_m + 1$, the linkage and self impedances are given by:

$$\begin{aligned}
 \bar{Z}_{s,pm+1}^{\alpha} &= j \frac{\pi\mu_0\omega L_{st} \bar{N}_{st}^{-1}}{k^3 p_m (p_m + 1) g} \bar{\delta}(\text{mean}) \left(\bar{N}_{(SC+1)}^{p_m+1} \right) \\
 \bar{Z}_{s,pm+1}^{\beta} &= j \frac{\pi\mu_0\omega L_{st} \bar{N}_{st}^{-1}}{k^3 p_m (p_m + 1) g} \bar{\delta}(\text{mean}) \left(j\bar{N}_{(SC+1)}^{p_m+1} \right) \\
 \bar{Z}_{pm+1,SC}^{\alpha} &= R_{SC+1} + j \frac{\pi\mu_0\omega L_{st} \bar{N}_{(SC-1)}^{p_m-1}}{k^3 (p_m + 1)^2 g} \left(\bar{N}_{(SC+1)}^{p_m+1} \right)^* \\
 \bar{Z}_{pm+1,SC}^{\beta} &= R_{SC+1} + j \frac{\pi\mu_0\omega L_{st} \bar{N}_{(SC-1)}^{p_m-1}}{k^3 (p_m + 1)^2 g} \left(j\bar{N}_{(SC+1)}^{p_m+1} \right)^*
 \end{aligned} \tag{6.43}$$

R_{SC-1} and R_{SC+1} are $p_m - 1$ and $p_m + 1$ pole winding resistances respectively. The self-inductances of these windings are almost constant. The mutual inductances between the two windings of each winding set are zero, because these windings are 2-phase and wound in quadrature, and there are no speed terms.

In the real case, there is rotor current. Therefore, the UMP detection matrix can be developed to include the rotor current so that

$$\begin{bmatrix} V_{s-ph} \\ V_{r-ph} \\ V_{pm-1}^{\alpha} \\ V_{pm-1}^{\beta} \\ V_{pm+1}^{\alpha} \\ V_{pm+1}^{\beta} \end{bmatrix} = [\bar{Z}] \begin{bmatrix} I_{s-ph} \\ I_{r-ph} \\ 0 \\ 0 \\ 0 \\ 0 \end{bmatrix} = \begin{bmatrix} \bar{Z}_{s,s} & \bar{Z}_{s,r} & 0 & 0 & 0 & 0 \\ \bar{Z}_{r,s} & \bar{Z}_{r,r} & 0 & 0 & 0 & 0 \\ \bar{Z}_{pm-1,s}^{\alpha} & \bar{Z}_{pm-1,r}^{\alpha} & 0 & 0 & 0 & 0 \\ \bar{Z}_{pm-1,s}^{\beta} & \bar{Z}_{pm-1,r}^{\beta} & 0 & 0 & 0 & 0 \\ \bar{Z}_{pm+1,s}^{\alpha} & \bar{Z}_{pm+1,r}^{\alpha} & 0 & 0 & 0 & 0 \\ \bar{Z}_{pm+1,s}^{\beta} & \bar{Z}_{pm+1,r}^{\beta} & 0 & 0 & 0 & 0 \end{bmatrix} \begin{bmatrix} I_{s-ph} \\ I_{r-ph} \\ 0 \\ 0 \\ 0 \\ 0 \end{bmatrix} \tag{6.44}$$

where I_{r-ph} is the rotor current. The rotor coupling and mutual impedances are added to this matrix. Z_{r-r} , Z_{s-r} , and Z_{r-s} are defined in (3.31), (3.29), and (3.28) respectively. The linkage impedances with the rotor are

$$\begin{aligned}
 \bar{Z}_{pm-1,r}^{\alpha} &= j \frac{3\pi\mu_0\omega L_{st} \bar{N}_r^1}{k^3 p_m (p_m - 1) g} \bar{\delta}(\text{mean}) \left(\bar{N}_{(SC-1)}^{p_m-1} \right)^* \\
 \bar{Z}_{pm-1,r}^{\beta} &= j \frac{3\pi\mu_0\omega L_{st} \bar{N}_r^1}{k^3 p_m (p_m - 1) g} \bar{\delta}(\text{mean}) \left(j \bar{N}_{(SC-1)}^{p_m-1} \right)^* \\
 \bar{Z}_{pm+1,r}^{\alpha} &= j \frac{3\pi\mu_0\omega L_{st} \bar{N}_r^1}{k^3 p_m (p_m + 1) g} \bar{\delta}(\text{mean}) \left(\bar{N}_{(SC+1)}^{p_m+1} \right)^* \\
 \bar{Z}_{pm+1,r}^{\beta} &= j \frac{3\pi\mu_0\omega L_{st} \bar{N}_r^1}{k^3 p_m (p_m + 1) g} \bar{\delta}(\text{mean}) \left(j \bar{N}_{(SC+1)}^{p_m+1} \right)^*
 \end{aligned} \tag{6.45}$$

It is likely that the search coils will not eliminate all UMP. The UMP controlled by the search coil currents can be obtained as

$$\begin{bmatrix} F_{\alpha} \\ F_{\beta} \end{bmatrix} = \begin{bmatrix} F_{\alpha,ph} & F_{\alpha,pm-1}^{\alpha} & F_{\alpha,pm-1}^{\beta} & F_{\alpha,pm+1}^{\alpha} & F_{\alpha,pm+1}^{\beta} \\ F_{\beta,ph} & F_{\beta,pm-1}^{\alpha} & F_{\beta,pm-1}^{\beta} & F_{\beta,pm+1}^{\alpha} & F_{\beta,pm+1}^{\beta} \end{bmatrix} \begin{bmatrix} I_{s-ph} \\ I_{pm-1}^{\alpha} \\ I_{pm-1}^{\beta} \\ I_{pm+1}^{\alpha} \\ I_{pm+1}^{\beta} \end{bmatrix} \tag{6.46}$$

The equation was written in arbitrary Cartesian coordinates with α and β axes. In this equation, the middle matrix represents the flux densities multiplied by constants. Equation matrices (6.41) and (6.46) can be combined and active voltage control used for UMP reduction. The matrix equation is then

$$\begin{bmatrix} V_{s-ph} \\ V_{pm-1}^{\alpha} \\ V_{pm-1}^{\beta} \\ V_{pm+1}^{\alpha} \\ V_{pm+1}^{\beta} \\ F_{\alpha} \\ F_{\beta} \end{bmatrix} = \begin{bmatrix} \bar{Z}_{s,s} & \bar{Z}_{s,pm-1}^{\alpha} & \bar{Z}_{s,pm-1}^{\beta} & \bar{Z}_{s,pm+1}^{\alpha} & \bar{Z}_{s,pm+1}^{\beta} \\ \bar{Z}_{pm-1,s}^{\alpha} & \bar{Z}_{pm-1,CS}^{\alpha} & 0 & 0 & 0 \\ \bar{Z}_{pm-1,s}^{\beta} & 0 & \bar{Z}_{pm-1,CS}^{\beta} & 0 & 0 \\ \bar{Z}_{pm+1,s}^{\alpha} & 0 & 0 & \bar{Z}_{pm+1,CS}^{\alpha} & 0 \\ \bar{Z}_{pm+1,s}^{\beta} & 0 & 0 & 0 & \bar{Z}_{pm+1,CS}^{\beta} \\ F_{\alpha,ph} & F_{\alpha,pm-1}^{\alpha} & F_{\alpha,pm-1}^{\beta} & F_{\alpha,pm+1}^{\alpha} & F_{\alpha,pm+1}^{\beta} \\ F_{\beta,ph} & F_{\beta,pm-1}^{\alpha} & F_{\beta,pm-1}^{\beta} & F_{\beta,pm+1}^{\alpha} & F_{\beta,pm+1}^{\beta} \end{bmatrix} \begin{bmatrix} I_{s-ph} \\ I_{pm-1}^{\alpha} \\ I_{pm-1}^{\beta} \\ I_{pm+1}^{\alpha} \\ I_{pm+1}^{\beta} \end{bmatrix} \tag{6.47}$$

There is no rotor current here. Obviously (6.46) can be developed to also include the rotor current and combined with (6.44) to show UMP control with stator and rotor current.

$$\begin{bmatrix} V_{s-ph} \\ V_{r-ph} \\ V_{pm-1}^\alpha \\ V_{pm-1}^\beta \\ V_{pm+1}^\alpha \\ V_{pm+1}^\beta \\ F_\alpha \\ F_\beta \end{bmatrix} = \begin{bmatrix} \bar{Z}_{s,s} & \bar{Z}_{s,r} & \bar{Z}_{s,pm-1}^\alpha & \bar{Z}_{s,pm-1}^\beta & \bar{Z}_{s,pm+1}^\alpha & \bar{Z}_{s,pm+1}^\beta \\ \bar{Z}_{r,s} & \bar{Z}_{r,r} & \bar{Z}_{r,pm-1}^\alpha & \bar{Z}_{r,pm-1}^\beta & \bar{Z}_{r,pm+1}^\alpha & \bar{Z}_{r,pm+1}^\beta \\ \bar{Z}_{pm-1,s}^\alpha & \bar{Z}_{pm-1,r}^\alpha & \bar{Z}_{pm-1,CS}^\alpha & 0 & 0 & 0 \\ \bar{Z}_{pm-1,s}^\beta & \bar{Z}_{pm-1,r}^\beta & 0 & \bar{Z}_{pm-1,CS}^\beta & 0 & 0 \\ \bar{Z}_{pm+1,s}^\alpha & \bar{Z}_{pm+1,r}^\alpha & 0 & 0 & \bar{Z}_{pm+1,CS}^\alpha & 0 \\ \bar{Z}_{pm+1,s}^\beta & \bar{Z}_{pm+1,r}^\beta & 0 & 0 & 0 & \bar{Z}_{pm+1,CS}^\beta \\ F_{\alpha,s-ph} & F_{\alpha,r-ph} & F_{\alpha,pm-1}^\alpha & F_{\alpha,pm-1}^\beta & F_{\alpha,pm+1}^\alpha & F_{\alpha,pm+1}^\beta \\ F_{\beta,s-ph} & F_{\beta,r-ph} & F_{\beta,pm-1}^\alpha & F_{\beta,pm-1}^\beta & F_{\beta,pm+1}^\alpha & F_{\beta,pm+1}^\beta \end{bmatrix} \begin{bmatrix} I_{s-ph} \\ I_{r-ph} \\ I_{pm-1}^\alpha \\ I_{pm-1}^\beta \\ I_{pm+1}^\alpha \\ I_{pm+1}^\beta \end{bmatrix} \quad (6.48)$$

6.8 Experimental Work Using New Test Rig

This section provides a detailed description of the test set-up; the test machine and the force transducers that are used in the experimental work. It explains the calibration method of the rig, and describes the different approaches and measurement techniques used.

6.8.1 Laboratory Test Equipment

The same 4-pole wound rotor induction machine that was used earlier is used. The basic machine specifications are listed in Appendix C. The stator core winding diagram is also shown in Appendix C. The geometry of the machine is 48 stator slots, with a 72 slot rotor with 1 stator slot skew as shown in Figure 6.10 (with removed slip rings).



Figure 6.10. 72 slot wound rotor with 1 stator slot skew (removed slip rings).

The stator was rewound with a double layer winding. This design aims to achieve the best possible winding in terms of MMF and its harmonics [174]. In the stator, the number of coils per phase is 16, and the number of coils per pole per phase is 4 (two coil sides per slot). A distributed winding was used in this machine.

This test machine is set up on a pair of metal plates and bolted tightly to reduce the vibration due to the rotor motion, and end-caps of the machine were removed. The metal plates are set on both the Drive End (DE) and Non-Drive End (NDE) of the machine. The rotor for the test machine was separately mounted on pedestals which included piezoelectric force transducers; these allowed the direct measurement of the UMP on each bearing. The pedestals and plates were used to set the air-gap between the rotor and stator during the experiment. The experimental strategy was to change the rotor displacement and then measure the 2 and 6 search coil voltages that are influenced by force on the rotor. Figure 6.11 shows the laboratory set up.

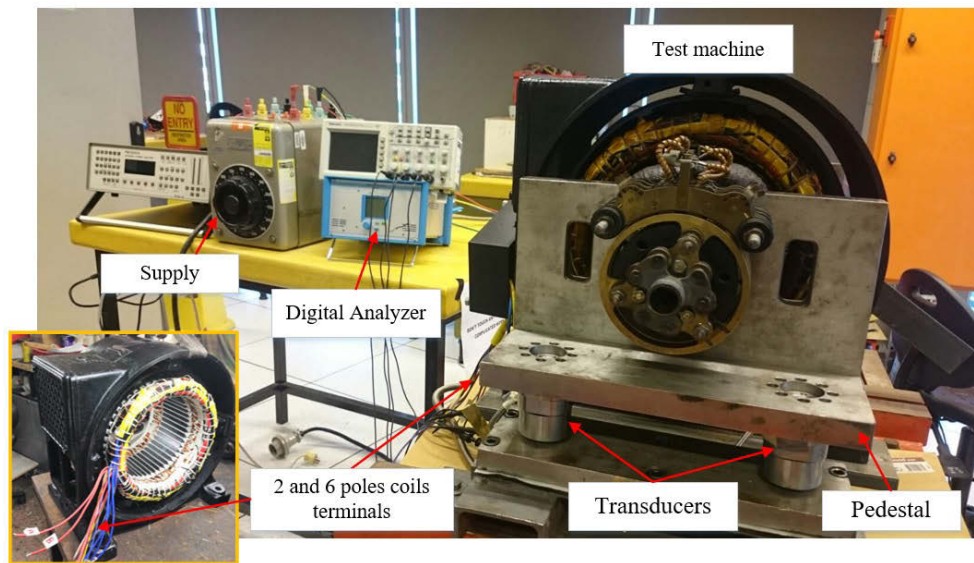


Figure 6.11. Laboratory set up of the experiment involving the test machine (Dive End side), search coils, piezoelectric force transducers, and other measurement equipment.

In the experiment, a set of 4 transducers are utilised to measure the active force. These are able to measure both compression and tensile forces in any direction. The transducer includes 3-component force sensors which measure the force introduced through the top plate. These sensors are linked to a summing box through integrated three-wire cables. The transducers and summing box are attached under the test machine on a metal plate on which the motor is also installed as shown in Figure 6.11. This plate has dimensions 500 x 630 mm as shown in Figure 6.12. The summing box is connected to a multichannel change amplifier (digital analyser) to complete the measuring system. It works using the piezoelectric measurement concept, where sensors convert mechanical signals into an electric voltage. The measurement values are proportional to the acting forces.

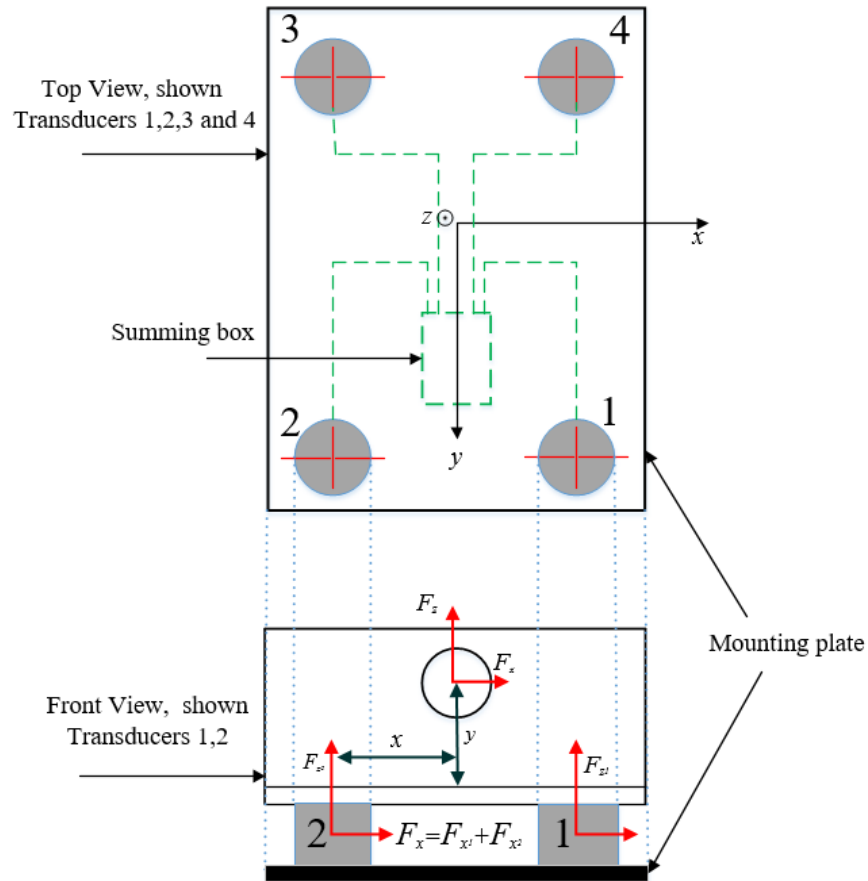


Figure 6.12. Transducers arrangement. The distance between the vertices of the shaft axis to the transducers is defined as x and the distance between shaft axis and the top point of the transducer is defined as y . (Transducers 1 and 2 in DE of the machine).

There are three channels per rotor end. Therefore, the total forces are defined in the machine sides as F_{x12} , F_{z1} and F_{z2} for the drive end (DE) and F_{x34} , F_{z3} and F_{z4} for the non-drive end (NDE). The total forces can be then calculated in three directions by summation as follows

$$\begin{aligned}
 F_x &= F_{x12} + F_{x34} \\
 F_y &= F_{y14} + F_{y23} \\
 F_z &= F_{z1} + F_{z2} + F_{z3} + F_{z4}
 \end{aligned}
 \tag{6.49}$$

The machine was coupled to a D.C. machine. The D.C. machine provides a load for the test motor using the Ward-Leonard arrangement described in Chapter 5.

6.8.2 Implementation of Air-gap Eccentricity

The rotor of the test machine is separately mounted on pedestals, allowing free movement of the rotor and adjusting the air-gap between the stator and rotor. Initially, the stator was adjusted in the x direction. The rotor and stator mountings were shimmed to get the rotor and stator at the same height, and to centre the rotor. Feeler gauges were used to adjust the air-gap at each end of the machine in both horizontal and vertical positions. The rotor mountings were shimmed to reset to identical heights. These shims were measured to be 0.35 mm by Vernier calliper. Then, various levels of eccentricity can be applied and measured.

In order to measure eccentricity, feeler gauges were slid into the air-gap at each end of the machine in both horizontal and vertical positions. However, this method was not accurate enough to measure the eccentricity. The stator and rotor positions were adjusted using clock gauges to obtain more accurate measurements as shown in Figure 6.13. After a number of trials the rotor was adjusted to be nominally centred with an air gap of 0.55 mm. Various levels of eccentricity were applied by moving the stator in the horizontal direction.

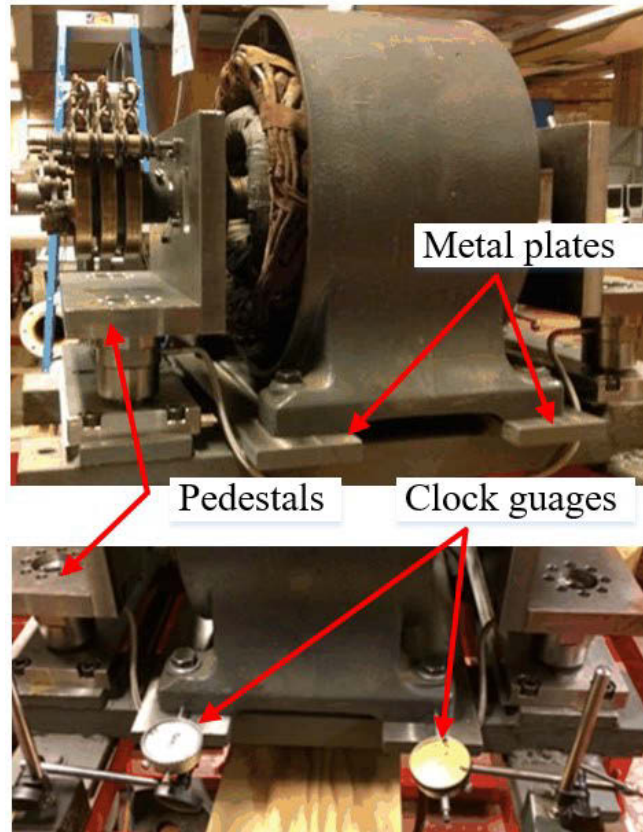


Figure 6.13. Experiment with test machine showing the air-gap adjustment using Clock gauges.

6.8.3 Implementation of Auxiliary Windings

As the start of the study, the stator was modified to include the simple pole-specific search windings with 2 poles and the initial induced voltage was recorded. Then the 6 poles were mounted and the results of 2 and 6 poles induced voltage were recorded together as illustrated in Figure 6.14. The slot top wedges originally held the main winding, and these were removed and the space was used to insert search windings. The 6-pole search windings consisted of 24 coils with two turns per coil. The span of each coil was 8 slots and half of the slots had a 6-pole coils side in the slot top. There were two 2-pole windings in quadrature. These were formed from 12 coils of one turn and a 24 slot pitch. Each slot

had one 2-pole coil side in it. Thinner wedges were made and used to hold the search windings.

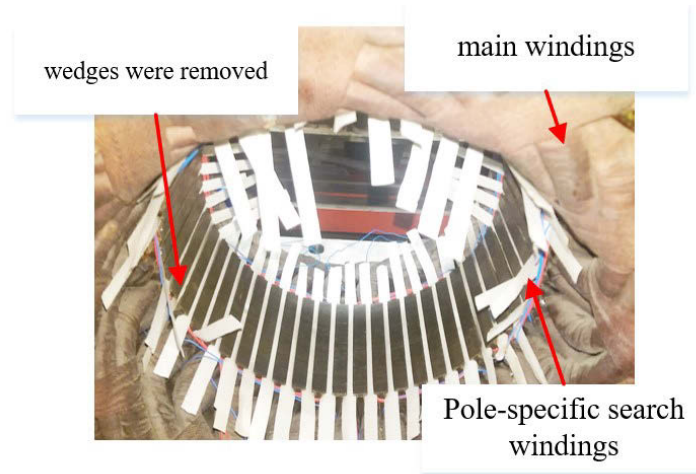


Figure 6.14. Search coils being fitted: single 6-pole winding; red coils down top of slots; and blue coils wound round winding only next to the end of core.

The initial test concluded that if the simple pole-specific search windings have sufficient turns and conductor current carrying capacity, they can be used to control the UMP (hence the later rewinding). This gave accurate results, as discussed in the next section.

The second step was to design new functional search coils. The stator was rewound with the same 4-pole 3-phase winding. However, the search windings were inserted and these were designed with more turns. They had two phases that were in quadrature. All the windings were correctly placed in the slots with suitable wedging. The winding schemes for the 6-pole and 2-pole search windings are shown in Figure 6.8 and the search windings details are listed in Table 6.2. More details are provided in Appendix C.

Table 6.2. Winding parameters of main winding and functional search coils.

| | |
|--------------------------|------------------------------------------------|
| Four-pole main winding | |
| Phases | 3 |
| Parallel paths | 1 |
| Effective turns per slot | 34 |
| Connection | Star |
| Resistance (Room Temp.) | 1.4 Ohm |
| Six-pole winding | |
| Phases | 2 (in quadrature on α and β axes) |
| Parallel paths | 1 |
| Effective turns per slot | 44 |
| Connection | Short-Circuit |
| Resistance (Room Temp.) | 22.5 Ohm |
| Two-pole winding | |
| Phases | 2 (in quadrature on α and β axes) |
| Parallel paths | 1 |
| Effective turns per slot | 15 |
| Connection | Short-Circuit |
| Resistance (Room Temp.) | 14.3 Ohm |

6.8.4 Measurement Setup and Testing Procedure

The testing began by aligning the bearings and the rotor of the test machine into the correct location; the rotor position is needed when calculating eccentricity and UMP. These procedures were the most difficult and the most time-consuming part of setting up the test since it required a manual procedure each time the eccentricity level was changed. The rotor was set at an original centre location and then at 5%, 20%, and 40% off-centre. The rotor was positioned at the centre by manual alignment with the feeler gauges. It was demonstrated to be about 4 % eccentric even when nominally centred. The clock gauges

were used for moving the rotor from the nominal centre and this produced about 5 % error. The different position measurements had to be iterated several times, and finally the initial eccentricity was reduced as much as possible. Therefore, all the previous steps were done with continuous recording of the induced voltage in the search coils. The measured and calculated search coil voltages were then compared. These search windings can be used to inject current to adjust and damp the UMP. The search windings were provided with current of around 0.5 A in order to adjust and reduce the UMP.

The open-circuit (equivalent to running a light-load test) and short-circuit (equivalent to a locked rotor test) tests were performed to measure UMP at different positions of the rotor. When there is a load, UMP and torque exist together. Under the locked rotor condition, UMP and torque can be separated depending on whether the locking bar is blocked against the rotor mounting or stator bed. This can be done by measurement of forces in both cases. In the first case, there is no detected torque. In the second case, there are both detected torque and UMP. Torque transducers can be used to separate UMP and torque if the machine is running.

To investigate this, Figure 6.15 shows the moments around the point located between the transducers (1 and 2), which meets the vertices of the shaft. If we define the distance between the shaft axis and the centre of the transducer 2 as x , and define the distance between the centre of the transducers and the shaft as y , angle γ can be defined as

$$\tan(\gamma) = \frac{x}{y} \quad (6.50)$$

The net z direction force is

$$F_{z_T} = F_{z_1} + F_{z_2} + F_{z_3} + F_{z_4} \quad (6.51)$$

The net x direction force is obtained by taking moments about the centre point between the transducers

$$F_{x_T} = \frac{x}{y} (F_{z_1} - F_{z_2} - F_{z_3} + F_{z_4}) \quad (6.52)$$

The torque expression is given by taking moments around the shaft so that

$$\begin{aligned} \text{Torque} &= Fd \sin(\gamma) \\ &= \left[\begin{aligned} &F_{x_1} \sin(\gamma) + F_{x_2} \sin(\gamma) + \\ &(F_{z_1} - F_{z_2}) \cos(\gamma) + (F_{z_4} - F_{z_3}) \cos(\gamma) \end{aligned} \right] \end{aligned} \quad (6.53)$$

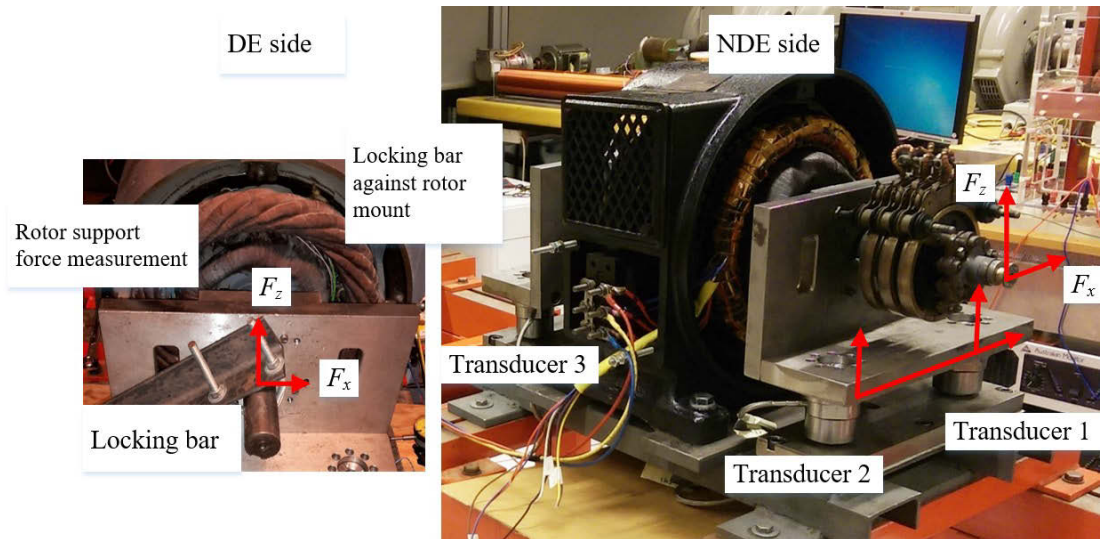


Figure 6.15. Illustration of NDE and DE sides of the test machine, and UMP measurement rigs using piezoelectric transducers.

6.8.5 The Main Features of the Experimental Setup

The UMP test rig allows direct measurement of the electromagnetic forces in the induction machine when the rotor is not aligned with the stator. The rig is also suitable for accurately measuring both steady radial pulls and vibrations on individual bearings.

A variety of UMP scenarios including axial variation of the eccentricity and vibration effects due to broken rotors (in case of cage-rotor) can be applied. This also enables the study of the mechanical imbalance in a variety of machines.

Although eccentricity models are assumed to be uniform down the axial bore, in some cases there will be variation in the eccentricity level between the DE and NDE sides in the machine, which produces non-uniform eccentricity. This unique rig allows the study of non-uniform axial eccentricity and will be discussed in the following results section.

The test rig also allows study of the effects of the $p_m \pm 1$ search windings to reduce the UMP. This arrangement of the force transducers enables examination of an arrangement of auxiliary windings.

6.9 Results and Discussion

In this section, the experimental verification of the diagnosis and measurement of UMP in wound-rotor induction machine is presented. The results given here validate the new approach, which depends on the specific search coils, and is used for detecting and damping the UMP.

As stated earlier, the test machine initially has 4 % eccentricity even when nominally centred. The rotor position was adjusted using simple clock gauges from the nominal centre giving about a 5% error. The characteristics of UMP against rotor eccentricity for the different supply voltages is presented in Figure 6.16 [48]. Rotor position can be assessed more accurately for further measurement when the rotor was both open-circuit and short-circuit. It is clear that the UMP is proportional to the eccentricity. Initially, the measured UMPs are matched with the results obtained in [48] using Finite Element Analysis (FEA). This work was done by Dorrell and Kayani (2014). It was then found

that the measured UMP closely matched with the FEA results. Figure 6.17 is used to relate the variation of supply voltage with eccentricity values. It shows the variation of UMP with voltage at 4 %, 20 %, 30 %, and 40 % eccentricity. As predicted, it is proportional to the square of the voltage because it is a function of the square of the flux density.

Dorrell and Kayani tested the machine when the rotor bar was locked using a locking bar as shown in Figure 6.15. The test machine was excited and several results were obtained when the rotor was short-circuited. The test was done at low voltage (50V). A comparison was shown between the measurement and FEA simulation results, and they were found to match, as illustrated in Figure 6.18. However, the test machine initially has 4 % eccentricity even when nominally centred. This introduces variation between the normal and the estimated results. In case of the skewed analytical simulation, the measured UMP is considered significantly higher than the un-skewed simulations at any particular eccentricity. This is because the skew increases the UMP as explained in [170].

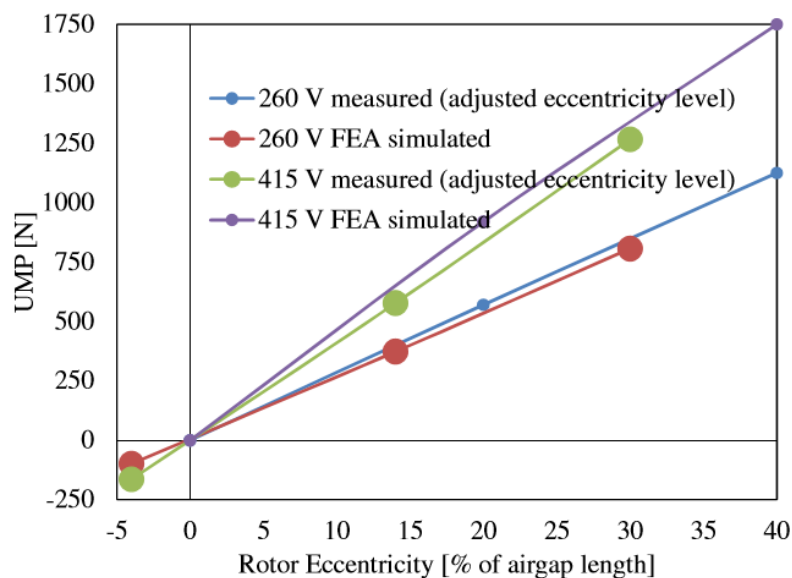


Figure 6.16. Open-circuit rotor UMP measurement results – comparison to adjust static eccentricity [48].

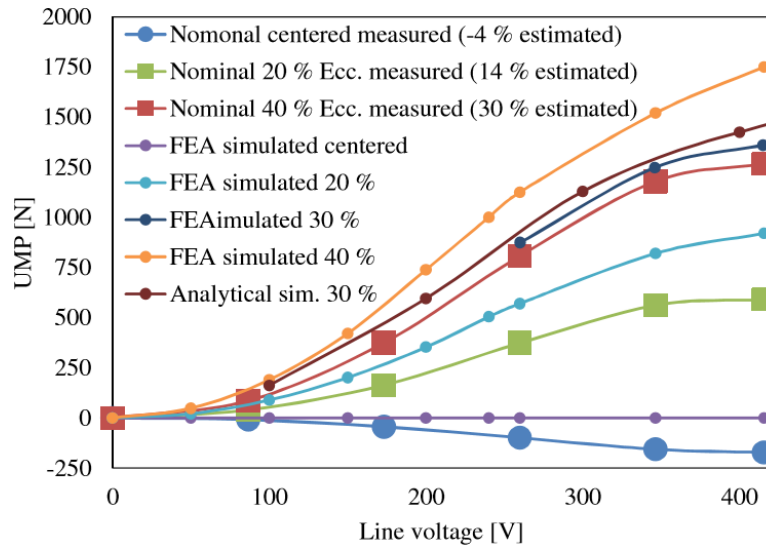


Figure 6.17. Variation of UMP with line voltage for several eccentricities, at open-circuit condition [48].

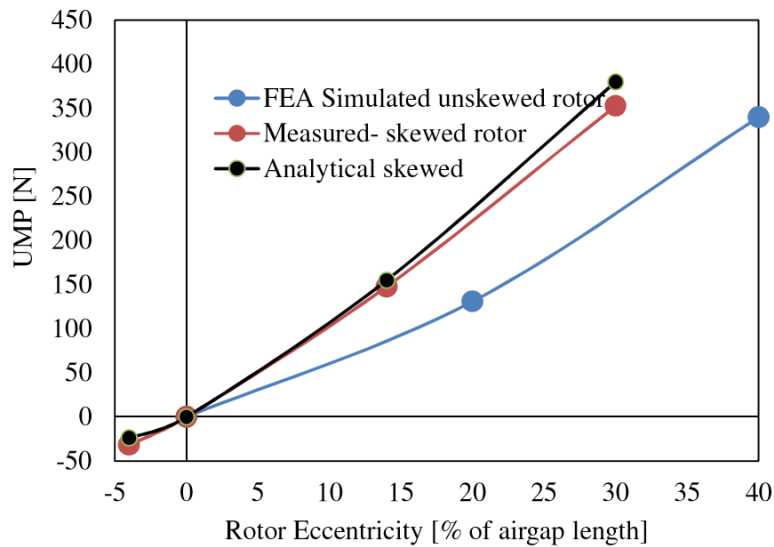


Figure 6.18. Short-circuit rotor UMP measurement results.

6.9.1 Separate Static and Dynamic Eccentricity in the Test Machine

The value of 4 % eccentricity was assumed as to be static at the beginning of the study.

A test was done to validate this assumption. The rotor was centred and the shaft of the machine was manually rotated by 90 degrees. The force was measured at this position.

This was repeated at 180, 270, and 360 degrees and every time the UMP was measured. The value of UMP changes while moving the shaft. The characteristics of UMP in Table 6.3 confirmed that the initial value of inherent 4 % eccentricity includes both static and dynamic eccentricity which explained why it was difficult to remove.

The average static force was 53 N. From Figure 6.16 the static eccentricity was estimated to be about 3 %. However, by rotating the shaft of the test machine by 90 degrees, the average force varied as discussed above and the direction of the net force vector changed, hence suggesting there is also a dynamic eccentricity in the machine. The forces were analysed and separated into static and dynamic. The average dynamic force was 30 N, and the dynamic eccentricity was found to be 1.7%.

Table 6.3. UMP measurements due to changing rotor position.

| Angle of Movement [Degree] | F_x [N] | F_z [N] | F_T [N] | Angle of F_T [Degree] |
|----------------------------|-----------|-----------|-----------|-------------------------|
| 0 | 1.2 | -54 | 54 | -88.7 |
| 90 | -1.2 | -93 | 93.8 | 82.6 |
| 180 | -36 | -48 | 60 | 53.1 |
| 270 | -17 | -9 | 19.2 | 27.9 |
| 360 | 1.4 | -52 | 52 | -88.5 |

It was assumed that the rotor was nominally centred when there was about 4 % eccentricity with an air-gap of 0.55 mm. Although, at 20 % eccentricity it was found to be 4 %, at 40 % eccentricity it was found to be about 30 % eccentricity. This is likely due to issues with setting the eccentricity accurately with high eccentricity. In Figure 6.17 various curves are given. The measured and simulated values at 30 % eccentricity are shown to match. The UMP should increase in proportion to the voltage squared if saturation is ignored. In practice, the attenuation of UMP will occur with iron saturation.

6.9.2 Separating Torque and UMP in the Test Machine

The torque can be obtained when the machine was tested with a locking bar (short-circuited). It is extracted from measured forces when the rotor was locked against the stator bed. The locked rotor test produced a reasonable correlation and the torque value was found to be 5.1 Nm (measured) and 4 Nm (simulated) [48]. The test was performed with the line voltage and line current equal to 48 V and 11.1 A respectively. The locked-rotor torque is not easy to predict, as any skew will increase the effective rotor resistance. A torque transducer is used to separate UMP and torque if the machine is running.

6.9.3 Non-constant Eccentricity and the Net Force Direction

Section 6.4 showed that the eccentricity can vary between the DE and NDE sides of the machine. In order to investigate the axial variation of the eccentricity in the test machine, the test was implemented with changing rotor positions at the DE and NDE to create unequal air-gap at each end.

The rotor position was set so that the NDE was centred and the DE was at 40 % eccentricity as shown in Figure 6.19. This was then repeated so that the DE was centred and the NDE was at 40 % eccentricity. In the first case, the DE was found to have a higher force acting on it as illustrated in Figure 6.19. In the second case, the NDE was found to have a higher force acting on it.

It can be concluded that the net force vector (shown as a green arrow in the above figure) is no longer in the axial centre of the machine since the eccentric end will experience a higher force than the centred end. Figure 6.20 shows the experimental results of the test under the open-circuit condition, indicating validation of this assumption. If the rotor was were closer to the bearings, the difference in the forces would be more notable [48]. The

rotor core of the test machine is 101 mm long but the bearings are about 220 mm away from the core.

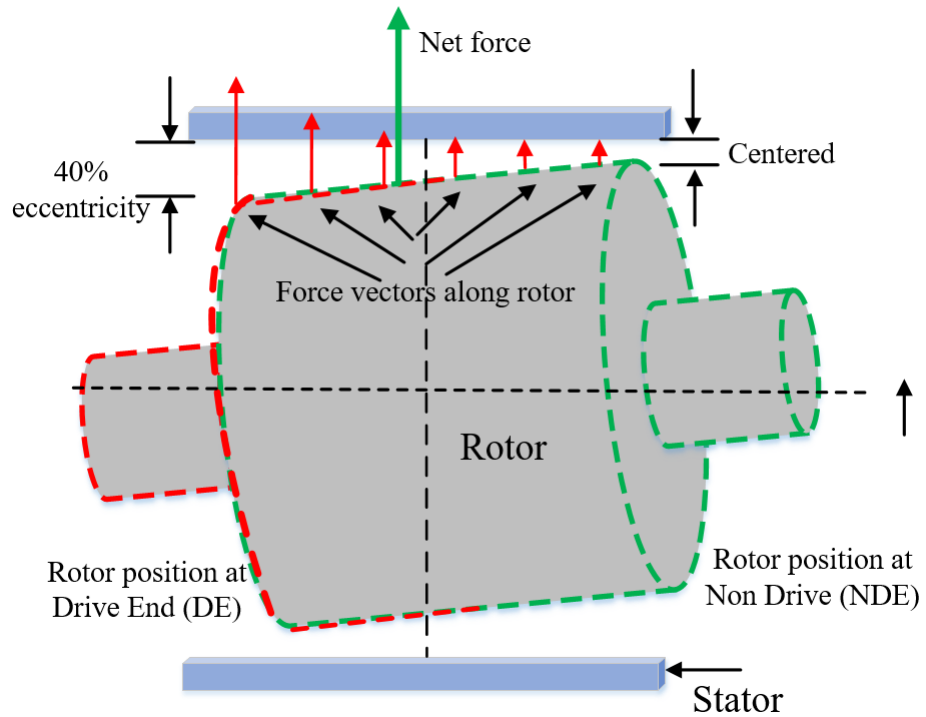


Figure 6.19. Axial variation of eccentricity and the direction of UMP.

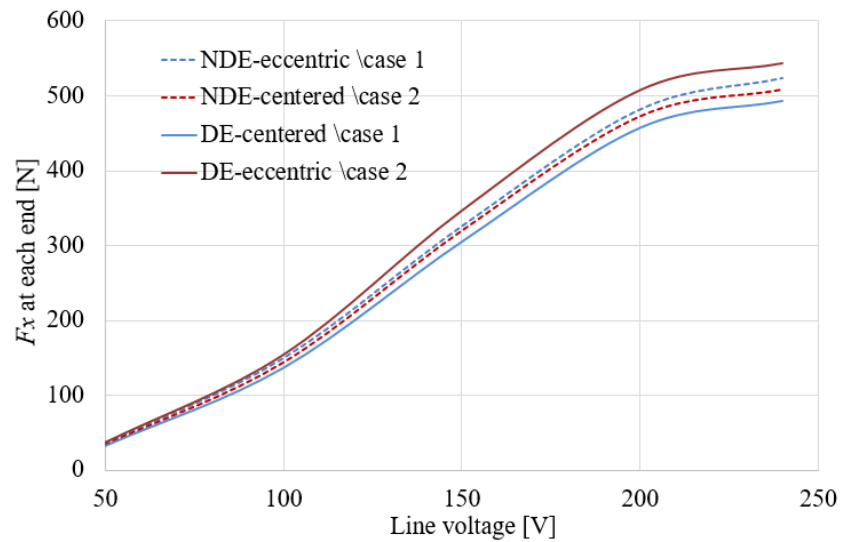


Figure 6.20. Axial variation of eccentricity.

6.9.4 Variation of UMP with Eccentricity for the Test Machine

The UMP was measured for a variety of eccentricities, with rotor displacement in the horizontal direction. In the case of an eccentric rotor, a steady pull was directed towards the point of narrowest air-gap. The variation of UMP with eccentricity at line voltage of 200 V is shown in Figure 6.21 when there rotor was open circuit. The agreement between the calculated results from the impedance matrix method and the measured results shows high consistency. A slight divergence appeared due to the difficulty in the exact repositioning the rotor at the given set of eccentricities.

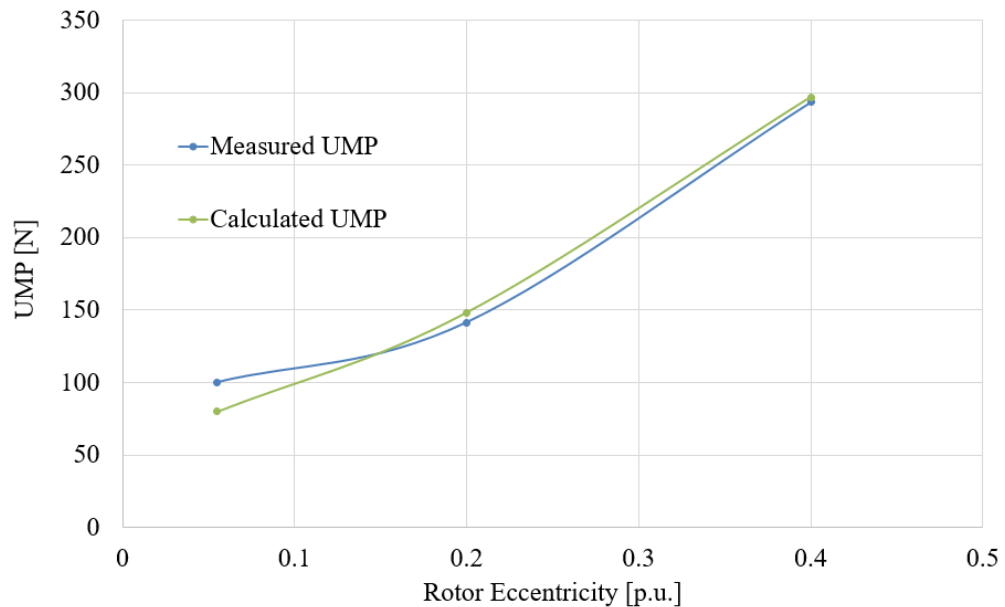


Figure 6.21. Variation of measured and predicted UMP with eccentricity degrees for the open-circuit test with 200 V.

6.9.5 Induced Voltages in the Simple Search Coils

The machine was modified to include simple pole-specific search windings as mentioned earlier. Initially, the 6-pole search winding was inserted.

The results appear in Figure 6.22 and Figure 6.23, and are visibly almost linear. The open-circuit (running light) and short circuit (locked rotor) results have different values. The degrees of eccentricity are not precise as presented above and there is a degree of eccentricity variation down the axial length of the machine. The results match reasonably well given the approximate nature of the eccentricity measurements. These findings clearly contribute to the validation of the search coils method.

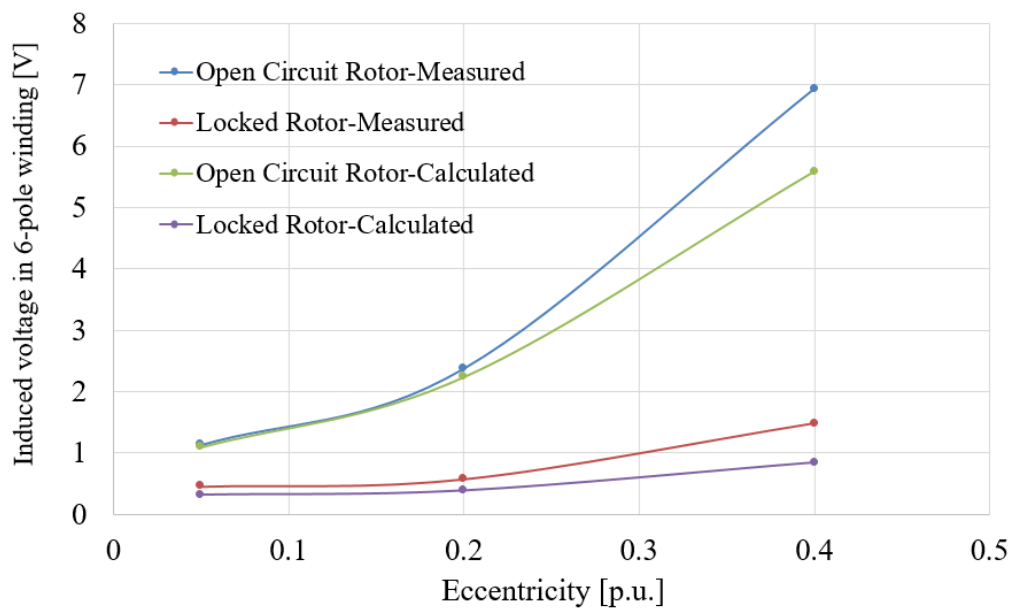


Figure 6.22. Induced 6-pole search winding voltages with a variation of eccentricity, illustrating the predicted and measured values.

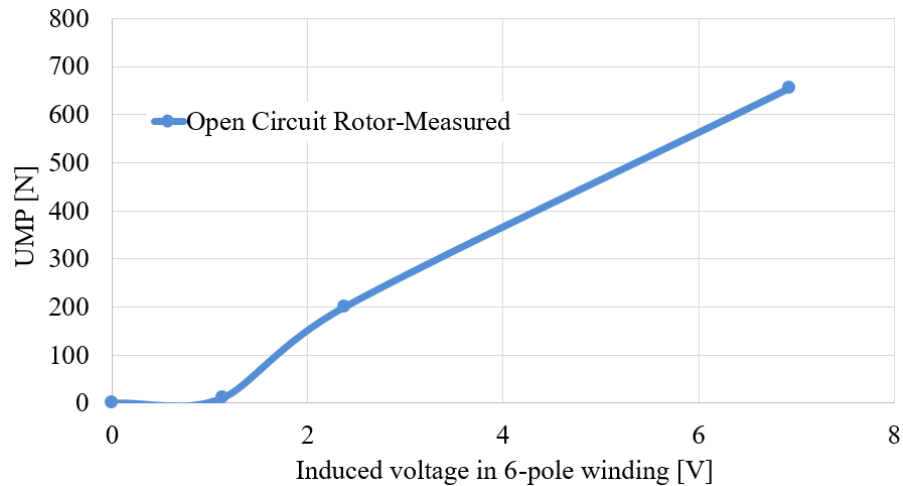


Figure 6.23. Variation of measured UMP with 6-pole induced voltages for the open-circuit test at 200 V.

The machine was dismantled and two 2-pole search windings were inserted in quadrature axes (d and q). The 2-pole and 6-pole search winding voltages are represented in Figure 6.24 for the open-circuit (running light) and the approximate linearity is clear. These were the initial results before designing the functional coils. For testing the theory developed in Section 6.8, the induced voltages in the windings were calculated for a given phase current and eccentricity. It is clear in the figure that 20% eccentricity represents approximately 15% since the test machine initially has approximately 4 % eccentricity.

Again, there is a linear characteristic, although the eccentricity was seen to be less in these tests. The short circuit test was done at 50 V and, if linearity is assumed, these results should be four times less. However, an induction machine demagnetises as it is loaded, so the results are lower. If these windings are suitably robust with sufficient turns and conductor current carrying capacity, they can be used to control the UMP (hence the later rewinding).

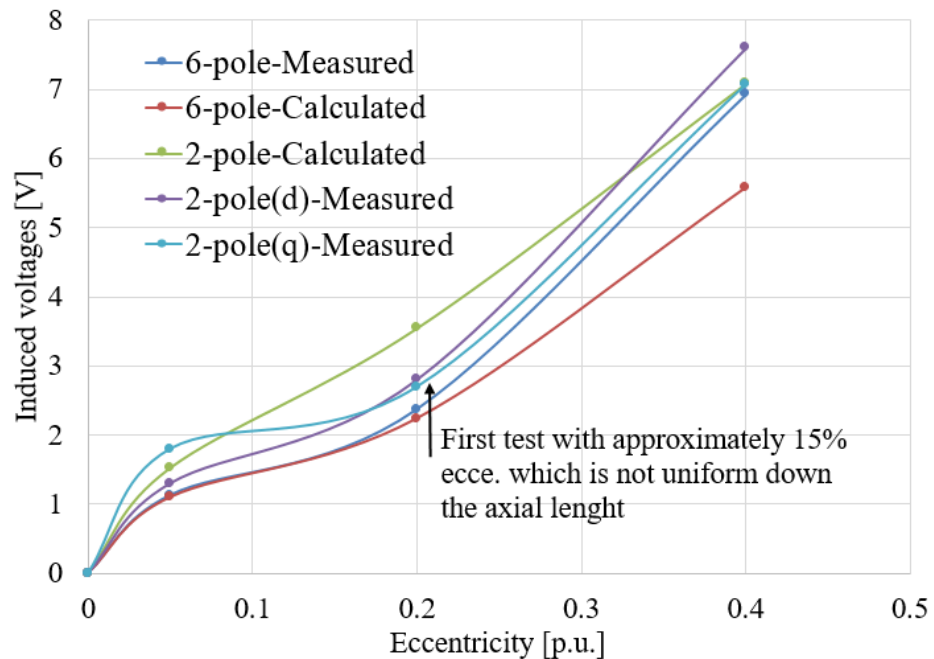


Figure 6.24. Induced voltages with a variation of eccentricity with 2 and 6 pole search windings for open circuit operation.

6.9.6 Induced Voltages in the Functional Search Coils

The stator was then rewound with the same 4-pole 3-phase winding and new six and two pole search windings were inserted as discussed in Section 6.8.3. The new six and two pole search windings were designed with more turns and they have two phases. These two phases are laid in two electrical axes with 90-degrees between them (in quadrature). The windings were then correctly placed in the slots with suitable wedging.

The induced voltages are illustrated in Figure 6.25 for the open circuit operation and the locked rotor test. It again shows approximate linearity. The voltages induced into the 2-pole and 6-pole coils are almost identical and this can be accounted for by addressing the total turns and flux linkage per pole using (6.16) and (6.17). These equations show that the peak flux densities of the 2-pole and 6-pole flux waves and the frequencies are the

same. The total turns per phase for the 6-pole winding is 528 with a peak flux of Φ_6 such that the flux linkage is $528\Phi_6$. Therefore, the flux linkages per pole for the two and six-pole flux waves are approximately $\Phi_2 = 3\Phi_6$. The total turns per phase for the two-pole winding is 180 so that the flux linkage is $180 \Phi_2 = 540 \Phi_6$. Hence, with the same frequency, the induced open-circuit search winding voltages are almost equal.

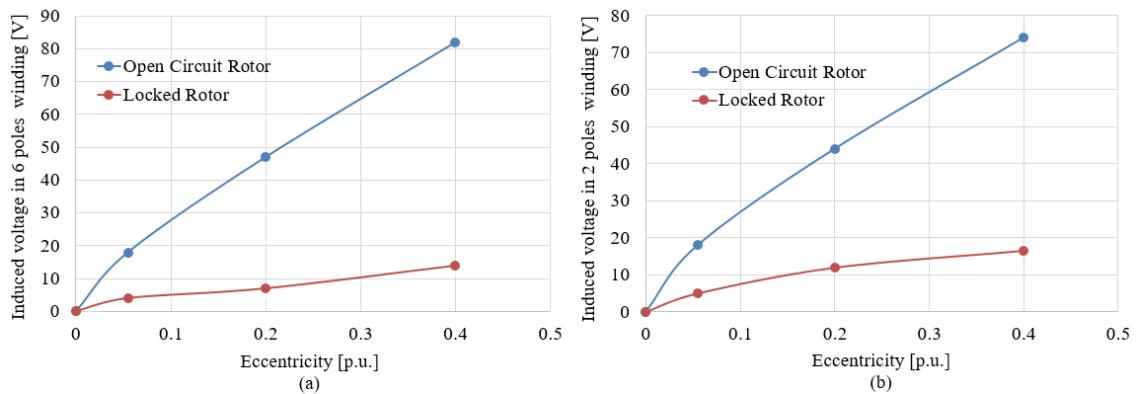


Figure 6.25. Induced voltages in the functional coils with a variation of eccentricity. Open circuit rotor test and locked rotor test were run at (200V, 1.0A) and (50V, 3.50A) respectively.

Figure 6.26 and Figure 6.27 show the calculated and measured induced voltages in the 2-pole and 6-pole windings with a variation of eccentricity and UMP. The voltages are now much higher than induced voltages in the first simple search coil arrangements due to the increased number of turns. The voltages are close and the differences are due to the variation between the nominal eccentricity setting and the actual setting. The 5 % eccentricity setting is probably close to 10 %, and the 40 % eccentricity setting is probably close to 35 % eccentricity. The two-pole winding is measuring a lower voltage because the machine is designed as a four-pole machine so the stator yoke is narrower than an equivalent two-pole machine; hence, there would be some finite MMF drop around the core-back and a lowering of the two-pole flux. However, the results appear reasonable.

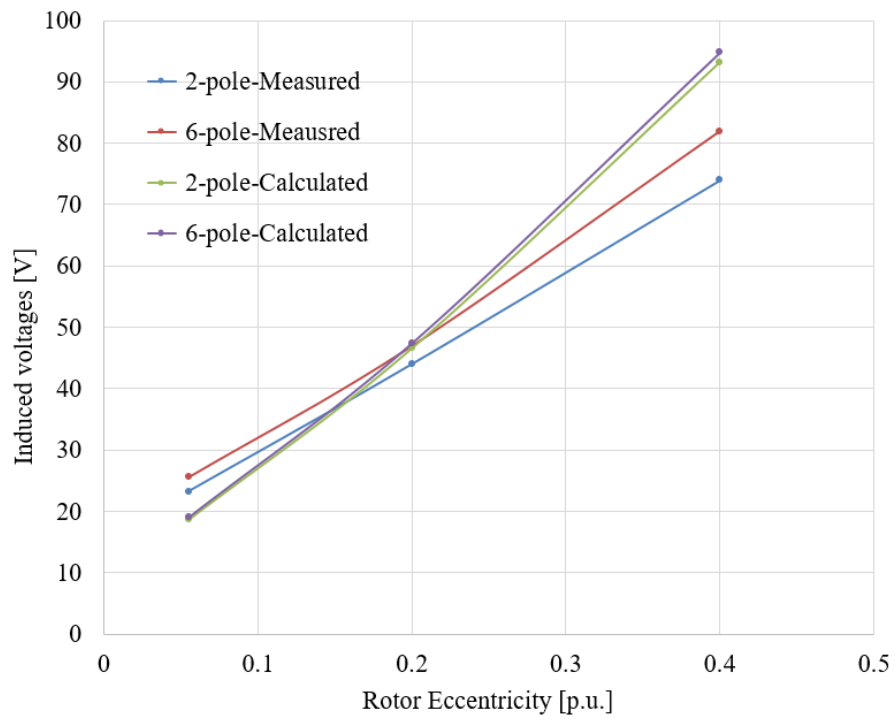


Figure 6.26. Calculated and measured voltages in the search windings with a variation of eccentricity with an open-circuit rotor.

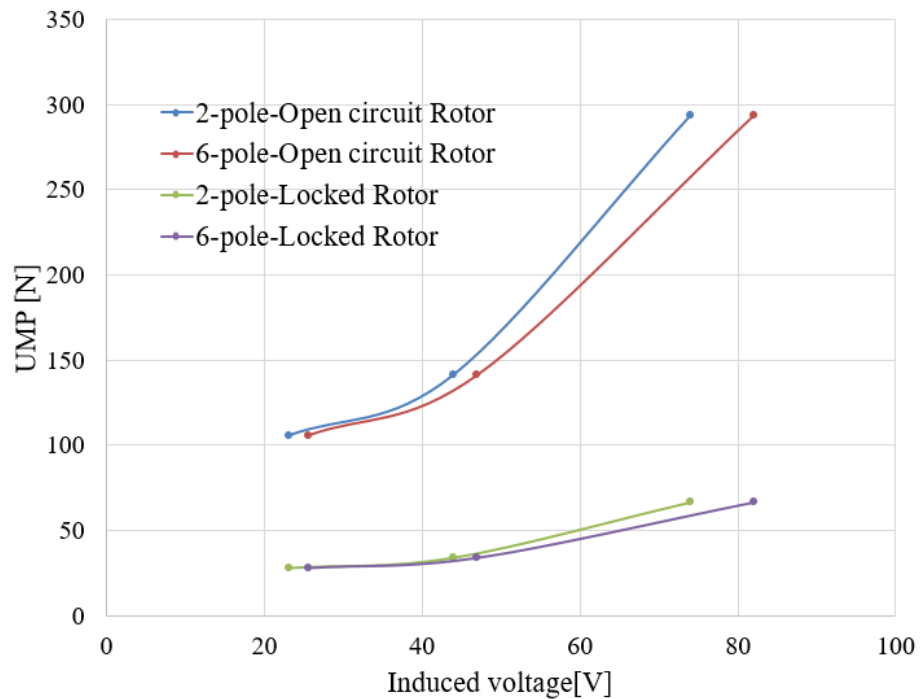


Figure 6.27. Variation of measured UMP with induced search windings voltages.

6.9.7 Investigation on Non-constant Eccentricity

In order to investigate non-constant eccentricity, the rotor was moved again to record the induced voltages in the 2-pole and 6-pole windings and the variation in the UMP values. The rotor was nominally centred and then moved one end at a time starting with 40 % eccentricity at the DE (case 1 in Figure 6.28). The rotor was moved in the horizontal plane in opposite directions at each end. These movements were simplified in Figure 6.28 and the positions shown in cases 1 to 6 which led to a non-uniform eccentricity. The average UMPs, due to the same degree of eccentricity applied in the one end, are almost equal as illustrated in Figure 6.29, which demonstrates the accuracy of the measurements. Figure 6.30 shows the motor end movements and the eccentricity. It shows that the electromagnetic forces are different in both ends. However, there is also some low-level residual vertical eccentricity. Investigation of non-constant eccentricity plays a vital role in the evaluation of UMP. It will be shown in the next section how effective it is in reducing the average UMP in the machine. Generally, the UMP and search coil voltages (simple search coils) decrease with average eccentricity as shown in Figure 6.31. The 6-pole search coil winding voltage is much less than the 2-pole winding, as previously stated.

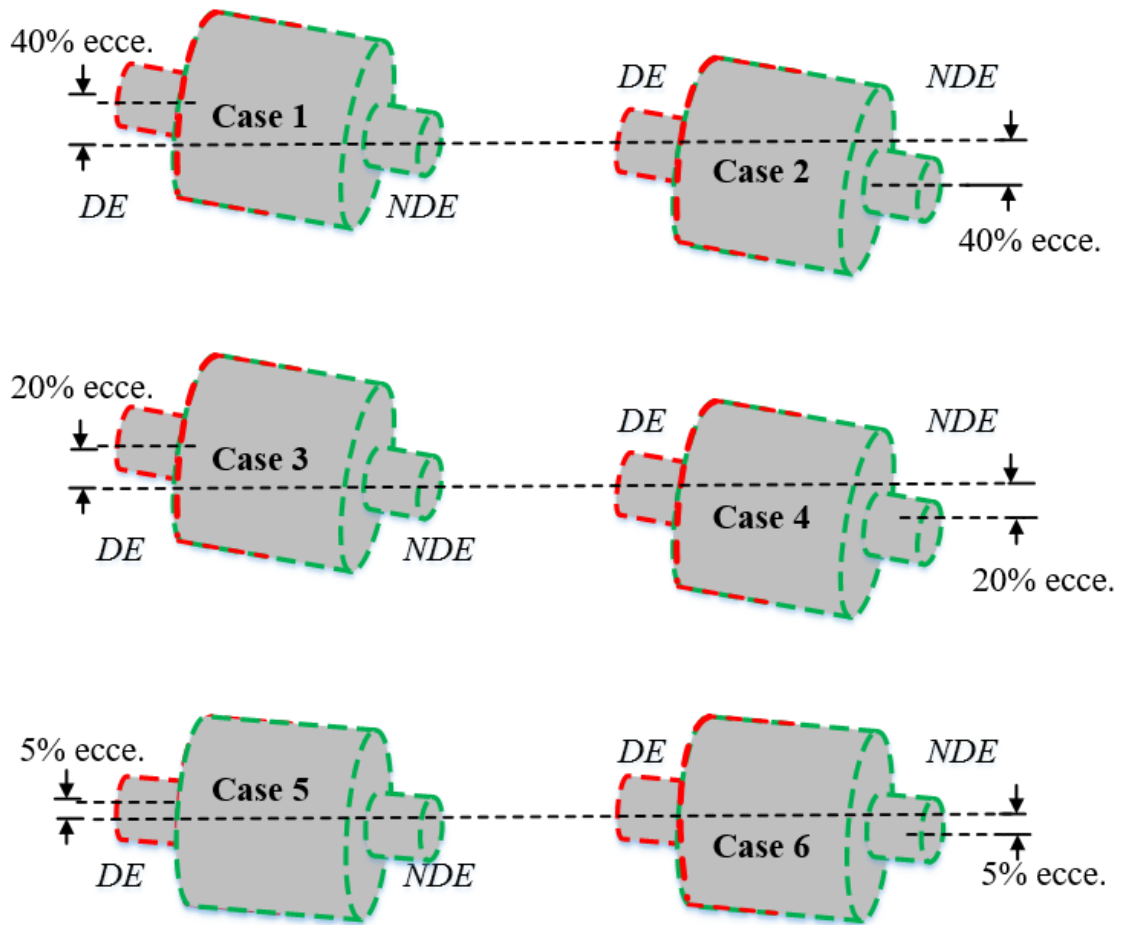


Figure 6.28. Variation of the rotor in stator bore and the illustration of 6 cases of movement strategies.

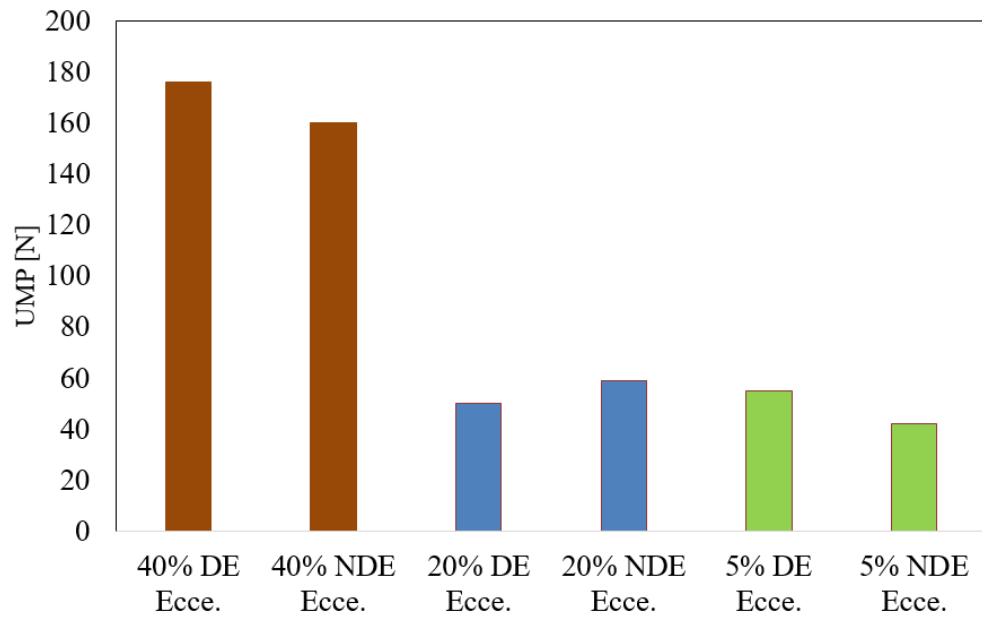


Figure 6.29. Average unbalanced magnetic pull due to rotor end movement with variation of eccentricity.

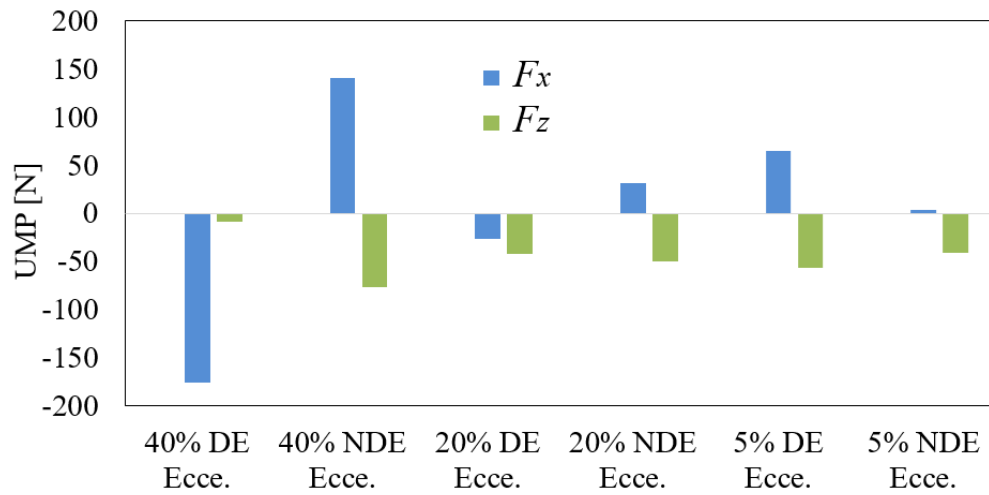


Figure 6.30. Unbalanced magnetic pull due to rotor end movement with variation of eccentricity.

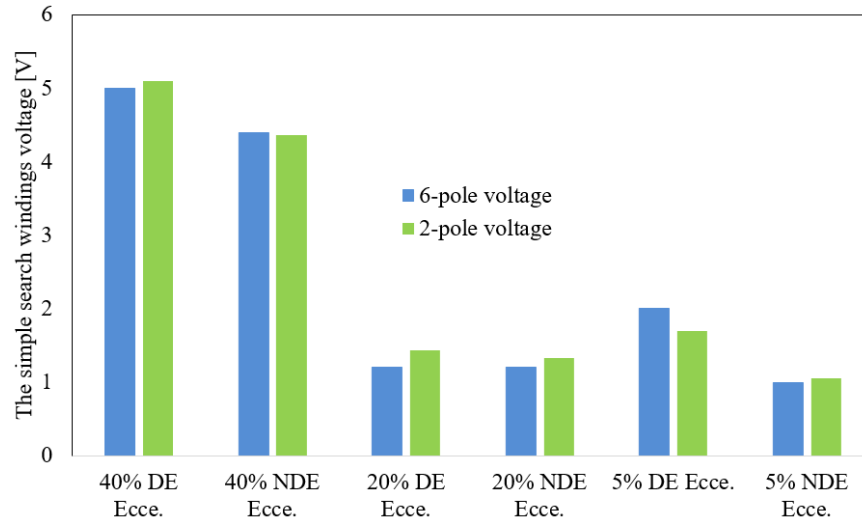


Figure 6.31. Search coil voltages with motor end movement.

6.9.8 Production of Effective Damper Windings

In this part of the project, some tests were done to evaluate the damping of UMP using the search coils. The functional search windings are now short-circuited to produce effective damper windings. The measured and calculated damper currents are illustrated in Figure 6.32 and appear close given the issues with setting the degree of eccentricity. The search winding currents increase rapidly with the eccentricity degree because of the related changes in flux density distribution around the air-gap. These are also matching between the predicted and measured values.

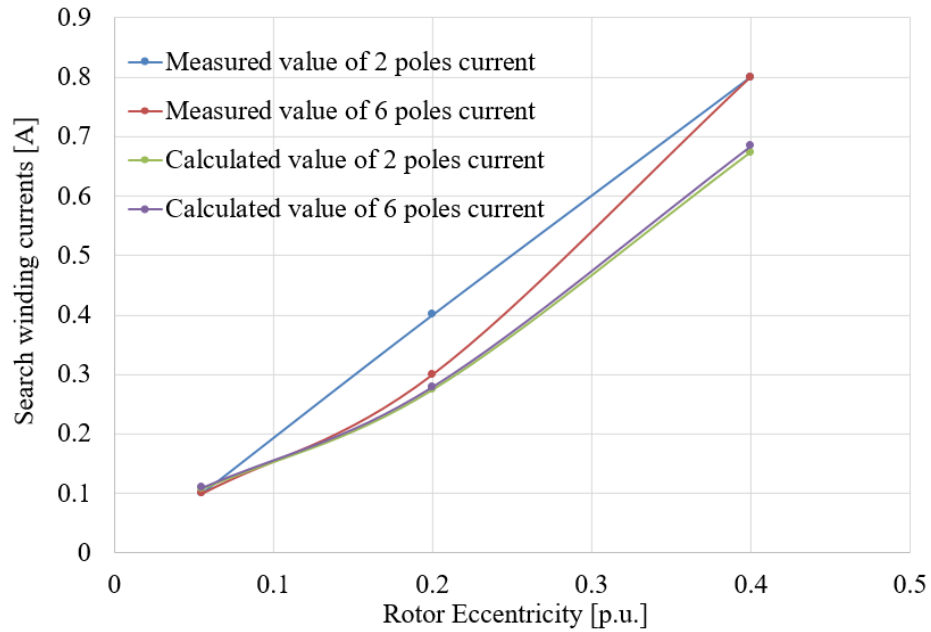


Figure 6.32. Calculated and measured currents in the functional search windings with variation of eccentricity.

The UMP characteristics are presented in Figure 6.33; these show the UMP results with the search coils winding open-circuited so there is no damping current. These results are compared with the UMP results with the winding short-circuited. The damper windings significantly damp the UMP at the synchronous speed, but the effect is much reduced when the rotor is locked. This is because as the slip increases the machine demagnetises and the fundamental stator and rotor MMFs cancel each other. However, the winding harmonics begin to influence the UMP. This was also discussed in [47] and [131, 135]. The damping effect of the 2-pole and 6-pole windings occurs within the fundamental flux wave, so it is to be expected that the UMP damping is much lower under locked rotor conditions. A doubly-fed induction generator (DFIG) operates at between about $s = 0.25$ and $s = -0.25$ [27] under controlled stator and rotor currents so that the damping windings will be effective under these conditions.

The matrices in (6.38) and (6.41) were used to calculate the UMP, as shown in Figure 6.34. The measured and calculated values of the UMP are close and the differences are due to the variation between the nominal eccentricity setting and actual setting as explained earlier. The reduction in measured values of the UMP is less than the predicted values for the same reason.

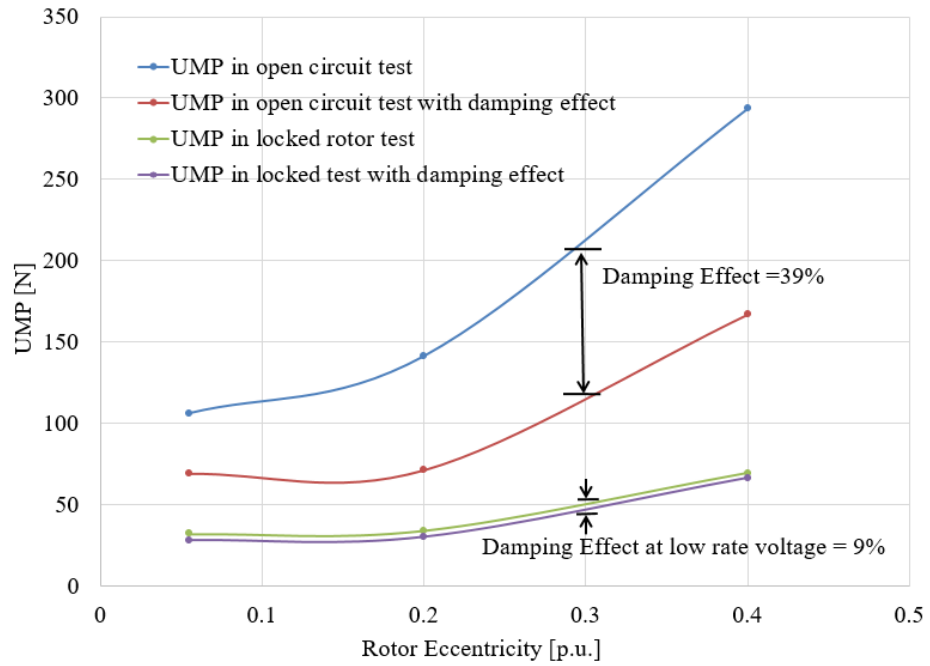


Figure 6.33. Variation of measured UMP with eccentricity variation in the open circuit test and locked rotor test.

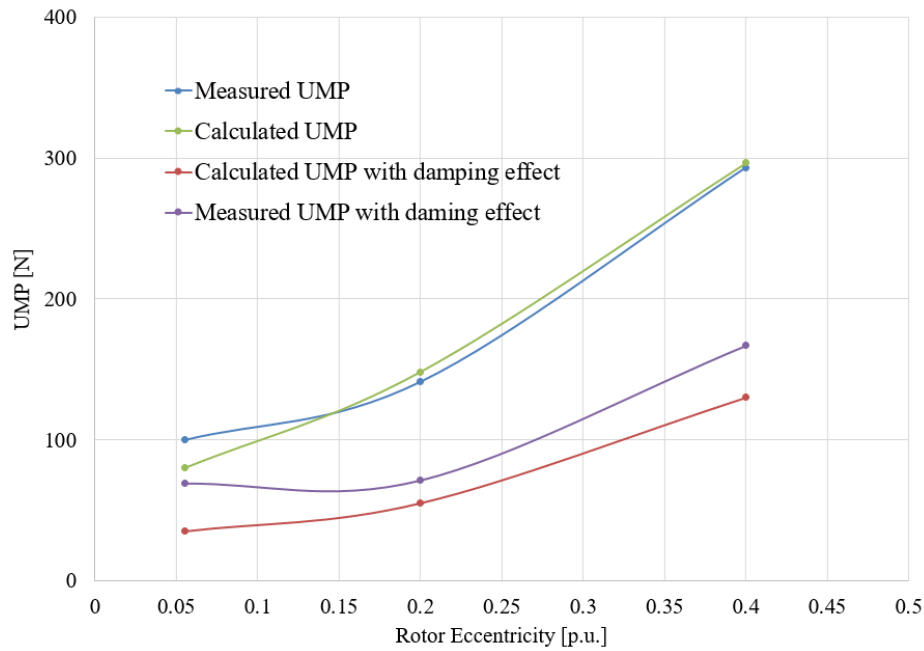


Figure 6.34. Comparison of calculated and measured UMP with a variation of eccentricity, and comparison of calculated and measured UMP with and without damping effect. The test was done with open-circuit operation.

6.9.9 Copper Losses in the Damper Windings

A comparison between the measured and calculated search coil losses was made, when the coils were short-circuited, as shown in Figure 6.35. The loss in the 6-pole winding was more than that in the 2-pole since it has higher resistance than the 2-pole winding. Obviously, the losses increase with increasing eccentricity. The difference between measured and calculated losses is due to the difference between the measured and calculated currents as shown in Figure 6.32. It can be illustrated that the current that generates the search winding copper losses could be used in the detection of eccentricity failure. The level of losses is low (30 W, measured at 40 % eccentricity maximum) since they are not involved in electromechanical energy conversion. This can be accommodated in the design of the cooling system. When manufacturing a machine, additional slot space

can be taken into account during the design process. The amount of space required for the damper windings is relatively low (4% - 8% of total space).

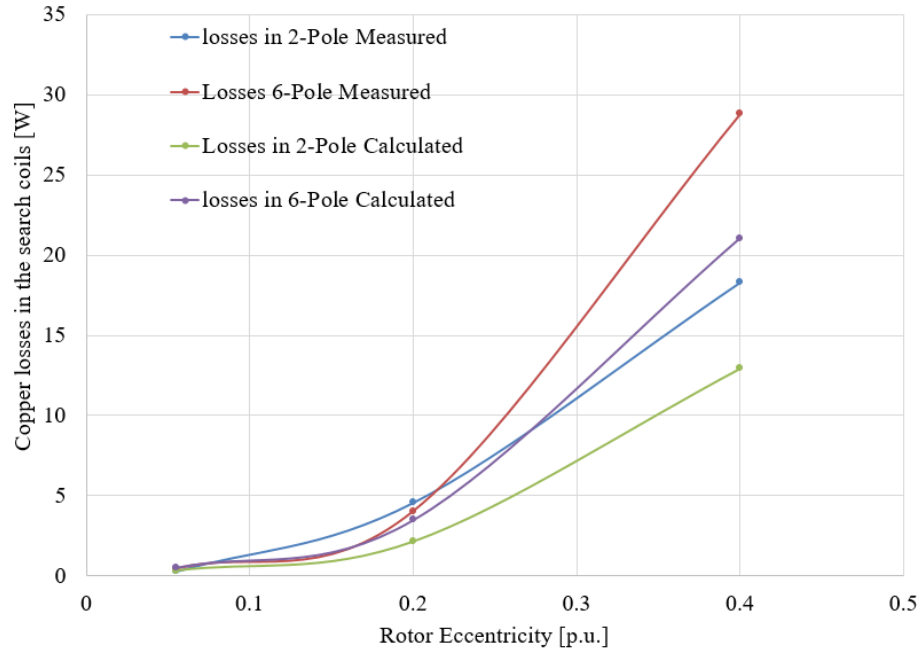


Figure 6.35. Calculated and measured copper losses in the functional search winding with a variation of eccentricity.

6.9.10 The Vibration Measurements

In order to evaluate the effectiveness of the auxiliary winding method, the following test was performed. A set of vibration sensors were used to measure the vibrations due to the eccentricity failure. The vibration signals were recorded by installing an accelerometer on the top of the drive end bearing in the radial direction, and another accelerometer in the middle of the machine in the axial direction as shown in Figure 6.36.

The vibration was sensed on the stator frame and on the bearing housing in open-circuit operation and the machine had 40 % eccentricity. The vibration spectra are presented in Figure 6.37. The results again show that the amplitude of the principal harmonic in the

motor was reduced after shorting the additional windings. The black circles in the figure highlight the reduction in amplitude. These agree with the measured bearing forces.

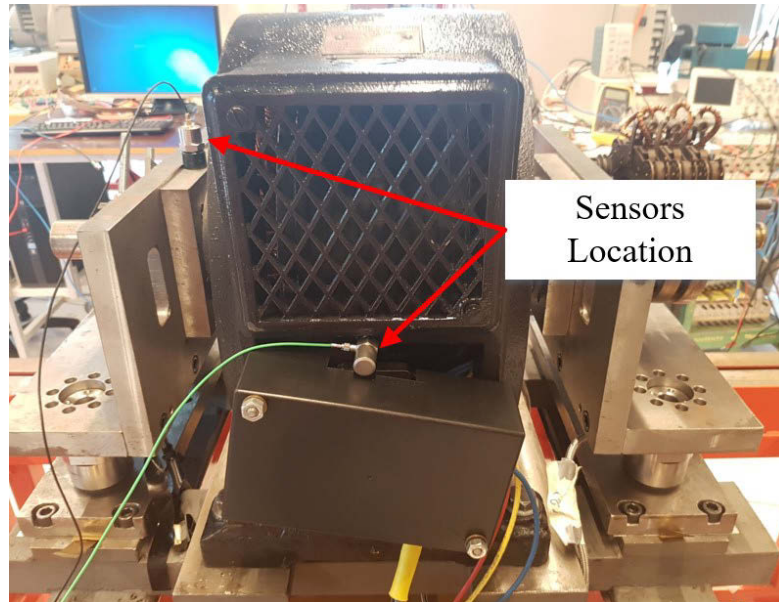


Figure 6.36. Vibration monitoring sensors position.

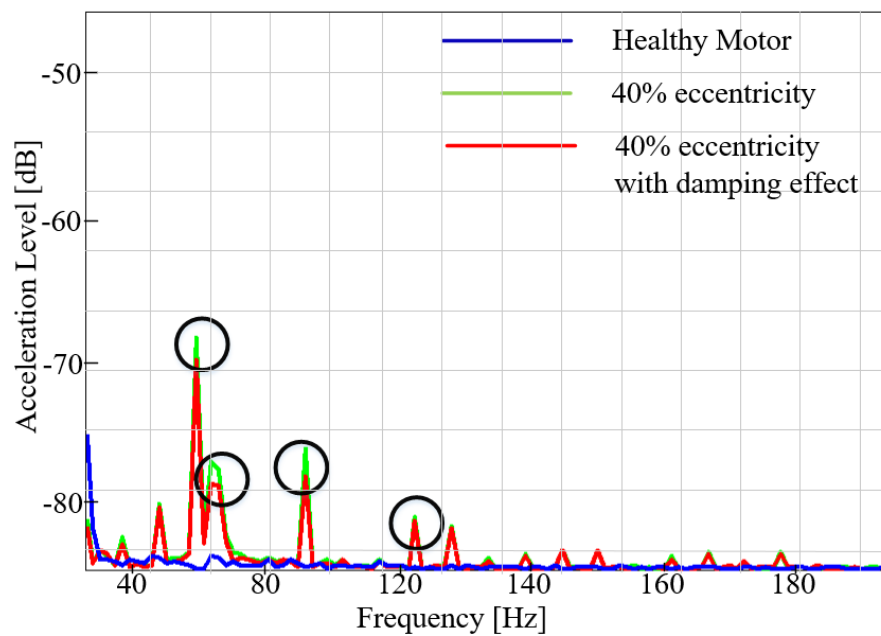


Figure 6.37. Stator frame vibration zoom spectrum for a uniform air-gap, and 40% static eccentricity.

6.9.11 Investigation of Injecting a DC Current in the Auxiliary

Windings

In this test, injection of a DC current in the 2-pole and 6-pole search coils was undertaken in order to note the UMP as in Figure 6.38. The search windings were supplied with 0.5A current and an attempt was made to note the drop in UMP. The DC current produces static flux waves in the machine. The stator winding produces a 4-pole flux wave. The 2-pole and 6-pole windings will clearly generate 2- and 6-pole flux waves. These do not move. In the absence of eccentricity, the UMP would be proportional to the main current and to the search winding currents.

At the beginning, the test was done using the original inserted search coils and this showed a marginal change in the UMP, while the expected results were much greater. This mismatch was due to the too low MMF to result in an effective UMP. To produce a steady pull, the 2-pole and 6-pole windings need to have many more turns to carry higher loads and hence to be effective.

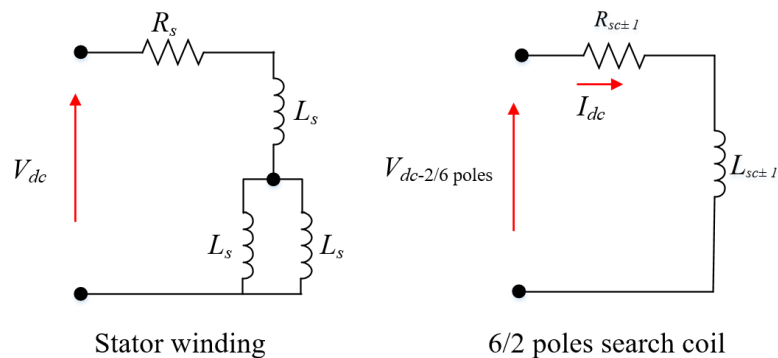


Figure 6.38. Illustration of the test where a DC current is input in the 2- and 6-pole search coils.

This test was done again using search windings inserted during the rewinding of the stator and the results are shown in Figure 6.39. Obviously, the UMP is proportional to the search

winding currents. Therefore, these windings can be used to inject current to adjust and damp the UMP in induction machines.

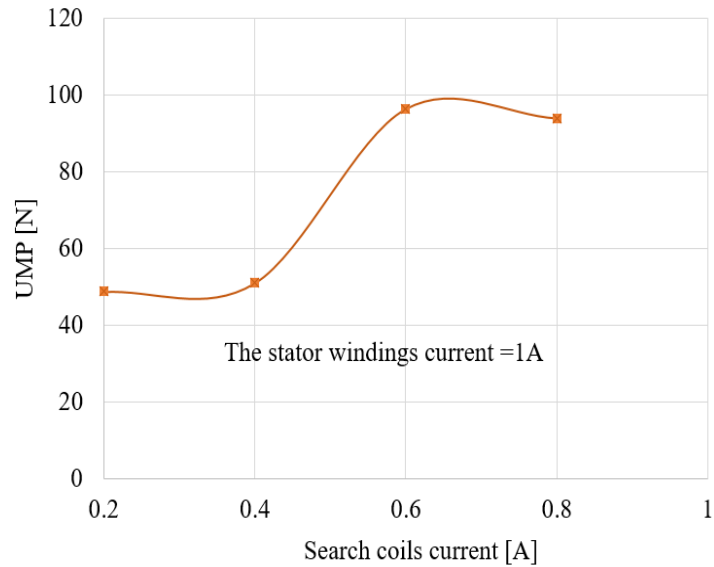


Figure 6.39. Variation of measured UMP with induction of a DC current in the 2-pole and 6-pole search coils.

6.10 Chapter Summary

This chapter has developed the theory for calculating EMFs induced into pole-specific search coils inserted in a 4-pole wound-rotor induction machine. Impedance matrices were also developed for both condition monitoring and UMP calculation. A test rig was constructed that could measure the search coil voltages and set the rotor in a non-centred manner. A 4-pole wound rotor induction motor was adapted to include pole-specific windings with 2- and 6-poles and it was illustrated that monitoring the voltage in these can be used to assess the rotor eccentricity. A method of incorporating damper windings in order to reduce the UMP, and hence bearing wear has been assessed. It was discussed in Section 6.2 that wound rotor induction machines experience higher levels of UMP

compared to the cage rotor equivalent since the cage rotor effectively damps the UMP. Therefore, it is reasonable to assume rotor eccentricity issues and the associated wear and vibrations are higher in wound rotor machines.

Chapter 7: Conclusions and Suggestions for Further Work

This chapter reviews and summarises the thesis with a general summary of the contributions in the previous chapters, and discussing significant and novel results as well as identifying the important areas for further research.

7.1 Summary and Conclusions

The review of the literature on wound-rotor induction machine faults produced a few models able to predict the behaviour of these machines in healthy and faulty conditions. In addition, the limitations of these approaches were not verified experimentally. Condition monitoring of induction machines has been a challenging task for the engineers and researchers although there are now several commercial systems available to the industry; they are mostly aimed at the monitoring of the cage-rotor induction machine.

A literature review of existing condition monitoring methods was presented in Chapter 2. Their features and limitations were discussed. The most common detection method is the stator current monitoring (MCSA), since the stator current is readily available in most applications. Focusing on eccentricity fault detection, the methods developed are couched in terms of cage induction machines, which may not be applicable to wound rotor machines as studied here.

This thesis proposes a model that can accurately predict the behaviour of these machines in healthy and faulty conditions using the harmonic conductor density technique. The model proved very successful in expressing induction machine performance. A relatively simple, yet powerful model is proposed that can accurately analyse the behaviour of a WRIM or DFIG with rotor-wound faults. The model is based upon standard rotating air-

gap harmonic field theory, which highlights importance of the influence of the stator and rotor winding harmonics. The model is required to build the impedance matrix that includes all the mutual and coupling impedances. The aim of the method here is to diagnose and detect unbalanced rotor-phase impedances and rotor eccentricity on a four-pole wound rotor.

The work presented here is divided into three main parts: construction of the impedance matrix, development of this matrix to incorporate unbalanced rotor-phase impedances, and development of this matrix again to incorporate rotor eccentricity. The accuracy demonstrated through the experimental test suggests that the impedance matrix method is a powerful tool for wound-rotor induction machine fault detection.

It can be concluded that the variations in the amplitudes of stator current components in the induction machine are used in this project to detect rotor faults, such as unbalanced rotor-phase impedances. The transient and steady-state operation of the induction machine with asymmetrical external rotor resistances has been simulated. The steady state performance of the wound rotor machine has been investigated by means of an equivalent circuit, including rotor asymmetries. The project also involved programming all forms of the matrices in the MATLAB environment to carry out the mathematical analysis. It was concluded that it is possible to use stator current components for detection purposes in the large-scale induction machine. For detection purposes, there is a difficulty using these current components in very small induction machines, as the backward components have a small amplitude compared to the main stator current component. Over different speeds, the amplitude of these components is only around 6 % of the mains stator current. As expected, an unbalanced rotor leads to an increase in oscillating torque, thus a loss of steady-state torque.

The accuracy demonstrated through the experimental test suggests that the impedance matrix method is a powerful tool for air-gap eccentricity fault detection. Furthermore, this method can reduce the UMP in the induction machine when search windings are inserted. UMP calculation can be complex. Here, the UMP calculation process is simplified and discussed with a direct example.

A 4-pole wound rotor induction motor was adapted to include pole-specific windings with 2 and 6 poles and it was illustrated that monitoring the induced voltage in these can be used to assess the rotor eccentricity. Once again, it is not easy to obtain the induced voltages using hand calculations, so it is reasonable to use MATLAB for calculations. The project investigated the UMP when only one end of the machine was misaligned (e.g. incorrect fitting of one bearing or end-cap), which is called non-constant eccentricity. It was concluded that the net force vector is no longer in the axial centre of the machine since the eccentric end will experience a higher force than the centred end.

The practical applicability of this research mainly rests within the domain of large machines with low critical speeds which can be inaccessible, for example, the doubly-fed induction generator (DFIG) as used in many wind turbine generators. Faults in cage rotor induction machines have been studied by both the IEEE and Electrical Power Research Institute (EPRI) since they are by far the most common form of induction machine. Rotor eccentricity is one common mechanical fault reported earlier in the literature review. It can be concluded that the wound rotor induction machine will eliminate faults concerned with the cage structure but include faults related to the slip rings and rotor windings. It was discussed in Chapter 6 that wound rotor induction machines experience higher levels of UMP compared with the cage rotor equivalents, since the cage rotor effectively damps the UMP. Therefore, it is reasonable to assume rotor eccentricity issues and the associated

wear and vibrations are generally higher in wound rotor machines. Wind turbines are a relatively new application and their size has increased rapidly in recent years.

7.2 Further Work

One of the interesting extensions of the project would be to combine the vibration analysis introduced in Section 6.10.11 with flux distribution analysis in order to evaluate the reduction in the vibration due to the search coils currents.

A further development would be to investigate mixed UMP in the matrix. Static and dynamic conditions can exist together in a real application, and the eccentricity is not necessarily constant down the bore. However, to diagnose mixed eccentricity, it is necessary to concentrate on monitoring voltage harmonics. Voltage harmonics are larger than current harmonics, so detection is more sensitive and reliable.

The electromagnetic forces between the stator and the rotor vary quickly. Certain aspects of an induction machine such as magnetic saturation, skew effect, the effect of slots, and uneven distribution of field are difficult to incorporate in the calculation although not impossible. However, more experiments need to be carried out to further evaluate the reliability and sensitivity with very small degrees of air gap eccentricity, machine size, load types, and installations. In the case of very small degrees of eccentricity and a small machine, any detection scheme may fail because of insignificant fault harmonics. Hence it is important to address these issues experimentally.

More experimental testing and evaluation under real conditions are required for the reliable condition monitoring. There is a strong need to undertake research in the area of eccentricity detection of closed-loop drive-fed motors. It is important also to compare

how the UMP is affected by the parallel paths in the stator side and the parallel paths in the rotor side.

APPENDICES

Appendix A: Internet Multimedia

The below URL contains:

- A.1 Thesis Softcopy
- A.2 Thesis Figures
- A.3 Lab Videos and Photos

URL: <https://sites.google.com/view/ahmadsalah/thesis>



Appendix B: Rotor Skew

Induction machines can have rotor or stator slots that are skewed with respect to one another. Therefore, there is a need to include this in the analysis. Considering Figure B.1, the axial centre is described by $x = 0$, and the skewing factor k_{sk} can be expressed as

$$k_{sk} = \frac{\sin(np_m b / D_R)}{np_m b / D_R} \quad (\text{B.1})$$

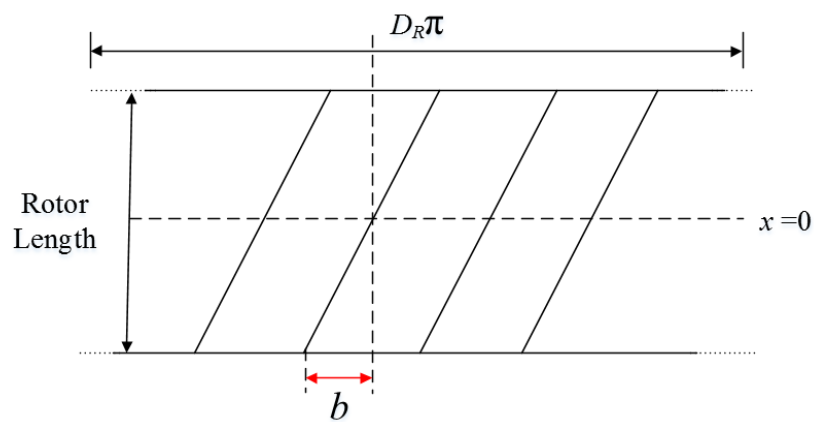


Figure B.1. Rotor surface with skewed slot.

where b is the circumferential displacement of the one end of the slot from the un-skewed position, and D_r is rotor diameter. Therefore, the rotor skew can be incorporated into the harmonic conductor density method easily.

Appendix C: Machine Specifications

In this project, a three-phase, four-pole induction machine is investigated. The basic machine specifications are listed in Table D.1; some data were obtained from simulating the machine in *SPEED* software [34]. The geometry of the machine is set to 48 stator slots, 72 rotor slots, and 4 poles. The stator core winding diagram is shown in different styles in Figure D.1 and Figure D.2.

The pole pitch (τ) measured in slot which is $\tau = N_s/2p_m = 48/4 = 12$. The coil throw (span) y was reduced such that $y = 11\tau/12$. The double layer winding was applied, and the total number of coils is equal to the number of slots. So the number of the coils is 48, and coils per phase are equal to $48/3 = 16$. There are 16 slots occupied by one phase in each layer, 8 with inward and 8 with outward current directions. In each layer, each phase produces four poles in this case. The second layer was displaced to the left by $\tau - y = 12 - 11 = 1$ slot with respect to the first layer.

Pole-specific search coils (2-pole and 6-pole windings) are shown in Figure D.3, Figure D.4 and Figure D.5. In the case of 6-pole winding, the number of slots per pole is equal to $48/6 = 8$, and there are 4 coil groups per phase. A single layer winding was used. The number of turns per coil is 44. The windings were concentric with 12 coils per phase, and the total number of coils for both phases is 24. The two series windings in quadrature for each pole set (i.e., 2 phases α, β) were considered.

In the case of 2-pole winding, the number of slots per pole equal to $48/2 = 24$. The number of coils per phase is 12 with 15 turns. The single layer (one coil-side per slot) was used, so the number of slots per phase band is 12. The number of coils is 24. The diameter of wire is 0.5 mm.

Table C.1. Test machine specification.

| Name plate details | |
|-----------------------------|-------------------------------------|
| Power [HP] | 10 (or 7.46 kW) |
| Speed [rpm] | 1420 |
| Frequency [Hz] | 50 |
| Stator voltage [V] | 400/440 Delta |
| Stator rated current [A] | 13 |
| Rotor voltage [V] | 200 |
| Rated rotor current [A] | 22 |
| Number of poles | 4 |
| Measured geometry [mm] | |
| Axial length of rotor core | 103.9 |
| Axial length of stator core | 100.9 |
| Stator outer diameter | 353 |
| Stator inner diameter | 228.15 |
| Rotor outer diameter | 226.42 |
| Shaft diameter | 120 |
| Airgap length | 0.5 |
| Stator slots | 48 |
| Stator slot opening | 3.9 |
| Turns per slot | 34 in series |
| Stator wire diameter | 1.534 |
| Stator winding | Double layer lap with 12 slot pitch |
| Coils per pole per phase | 4 |
| Stator slot depth | 26.82 |
| Stator tooth width | 8.22 |
| Stator tooth tip depth | 1 |
| Stator slot type | Round bottom, parallel tooth |
| Rotor slot number | 72 |
| Rotor slot opening | 3 |
| Rotor slot depth | 22.5 |
| Rotor tooth tip depth | 1 |

| | |
|-------------------------------------|----------------------------|
| Rotor slot type | Parallel slot, flat bottom |
| Slot width | 3.5 |
| Rotor wire diameter | 1.9 mm from <i>SPEED</i> |
| Turns per coil | 17 in series |
| Coils per phase | 16 |
| Rotor connection | Star through 3 slip rings |
| Rotor inertia | 0.1734 kg/m ² |
| Measured resistances [ohm] | |
| Rph stator (DC, temp) | 2.1 |
| Rph rotor (DC, temp) | 0.23 |
| Equivalent Circuit Parameters [ohm] | |
| R _r | 3.01 |
| X _s | 5.23 |
| X _r | 3.37 |
| X _{ss} (X _m) | 198 |
| R _c | 10k |

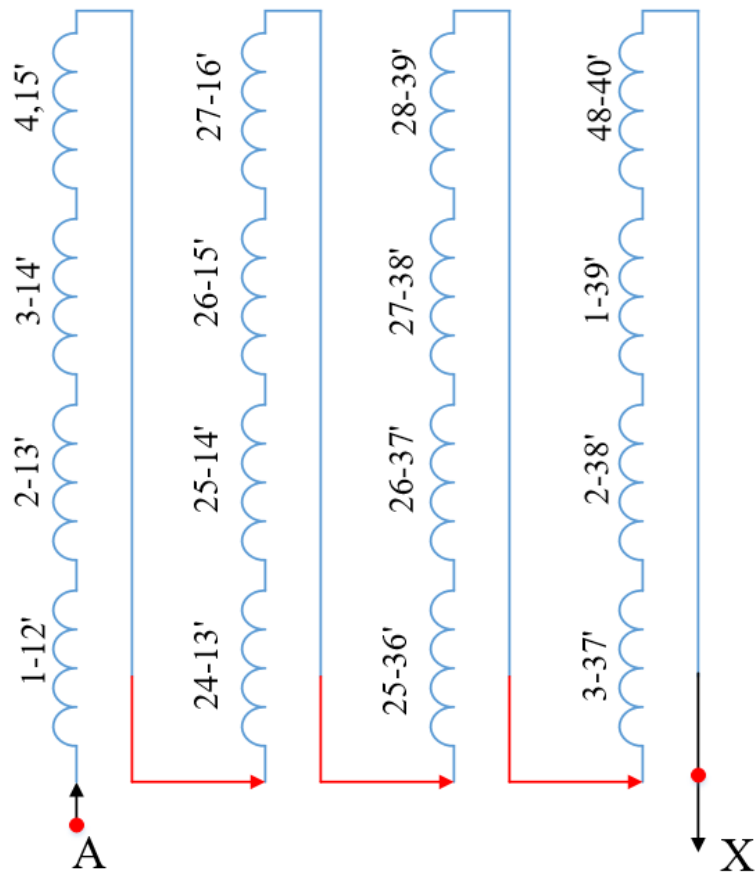


Figure C.1. Double-layer winding, 4 poles, $q=4$, $y/\tau = 11/12$, $N_s = 48$ slots, and $a = 1$ current path.

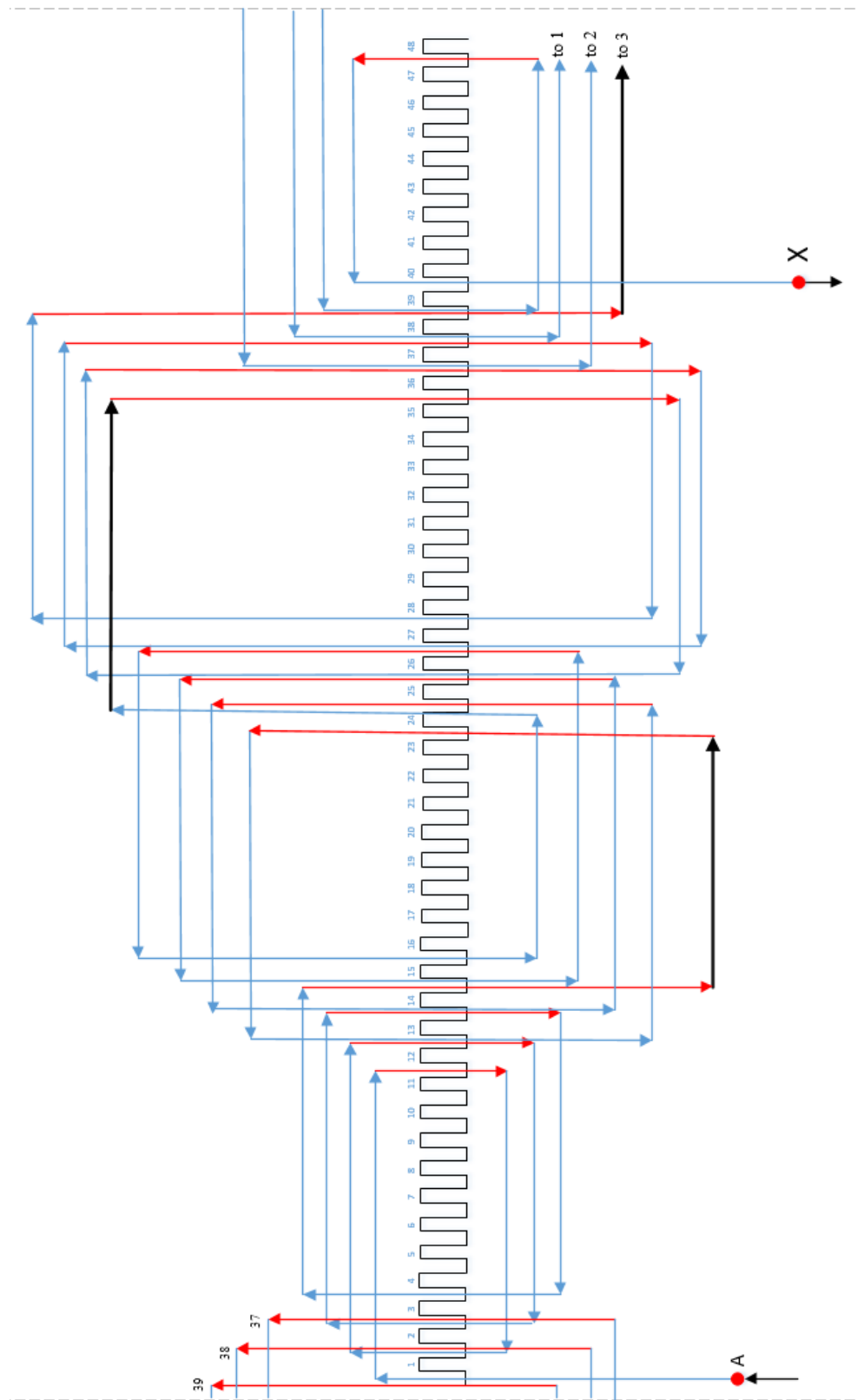


Figure C.2. Four pole main windings (Phase A only), blue wires located in the first layer, red wires located in the second layer, black wires illustrating the jumping to the next pole.

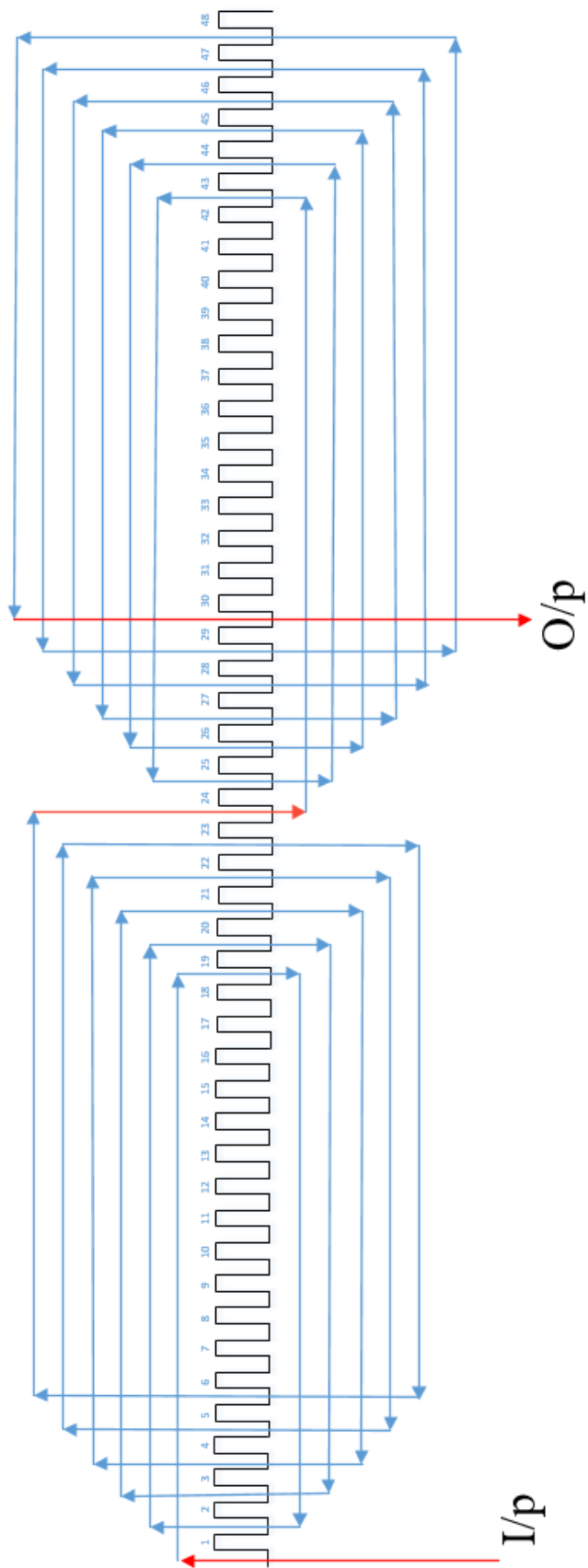


Figure C.3. Two pole search windings, phase α .

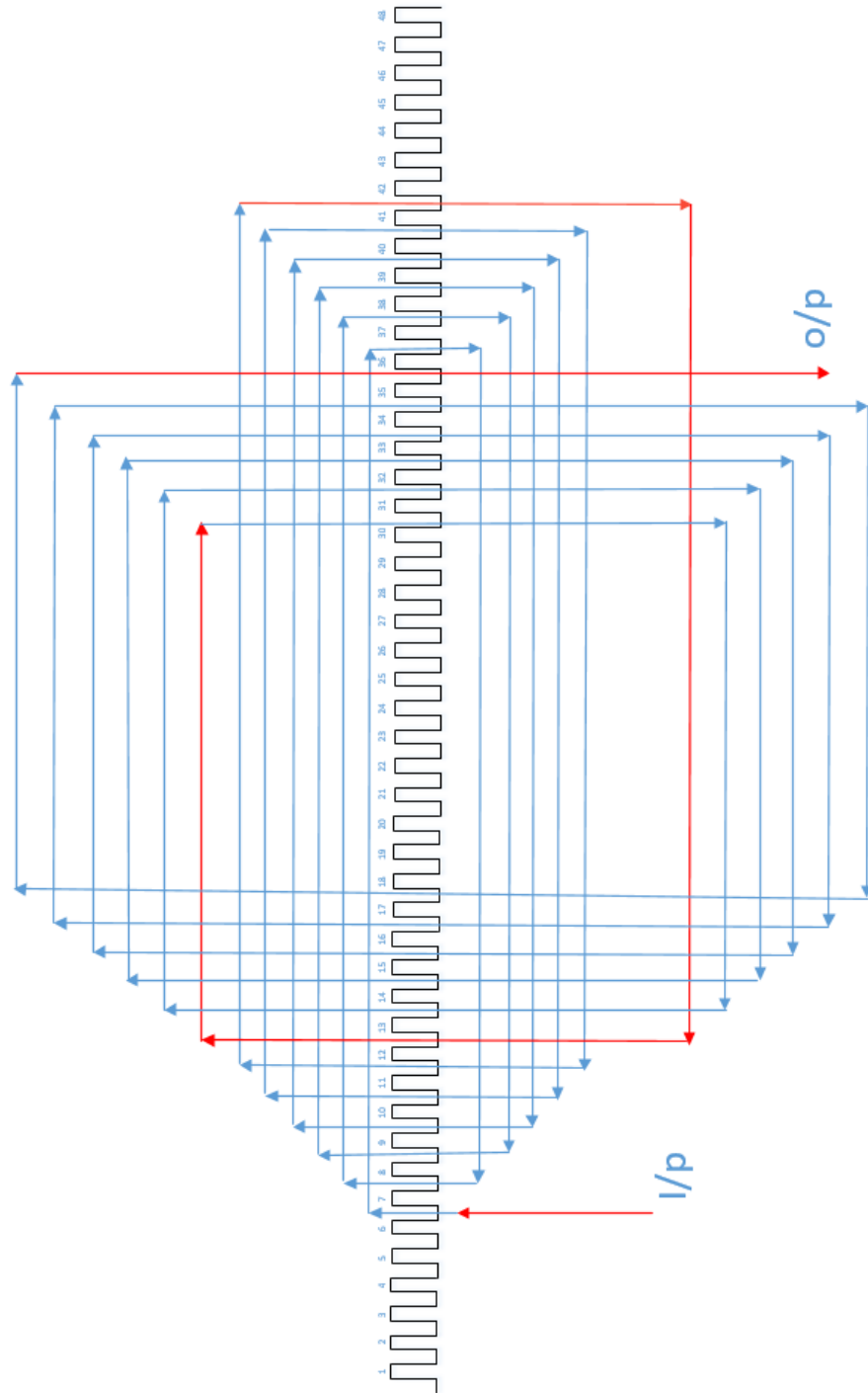


Figure C.4. Two pole search windings, phase β .

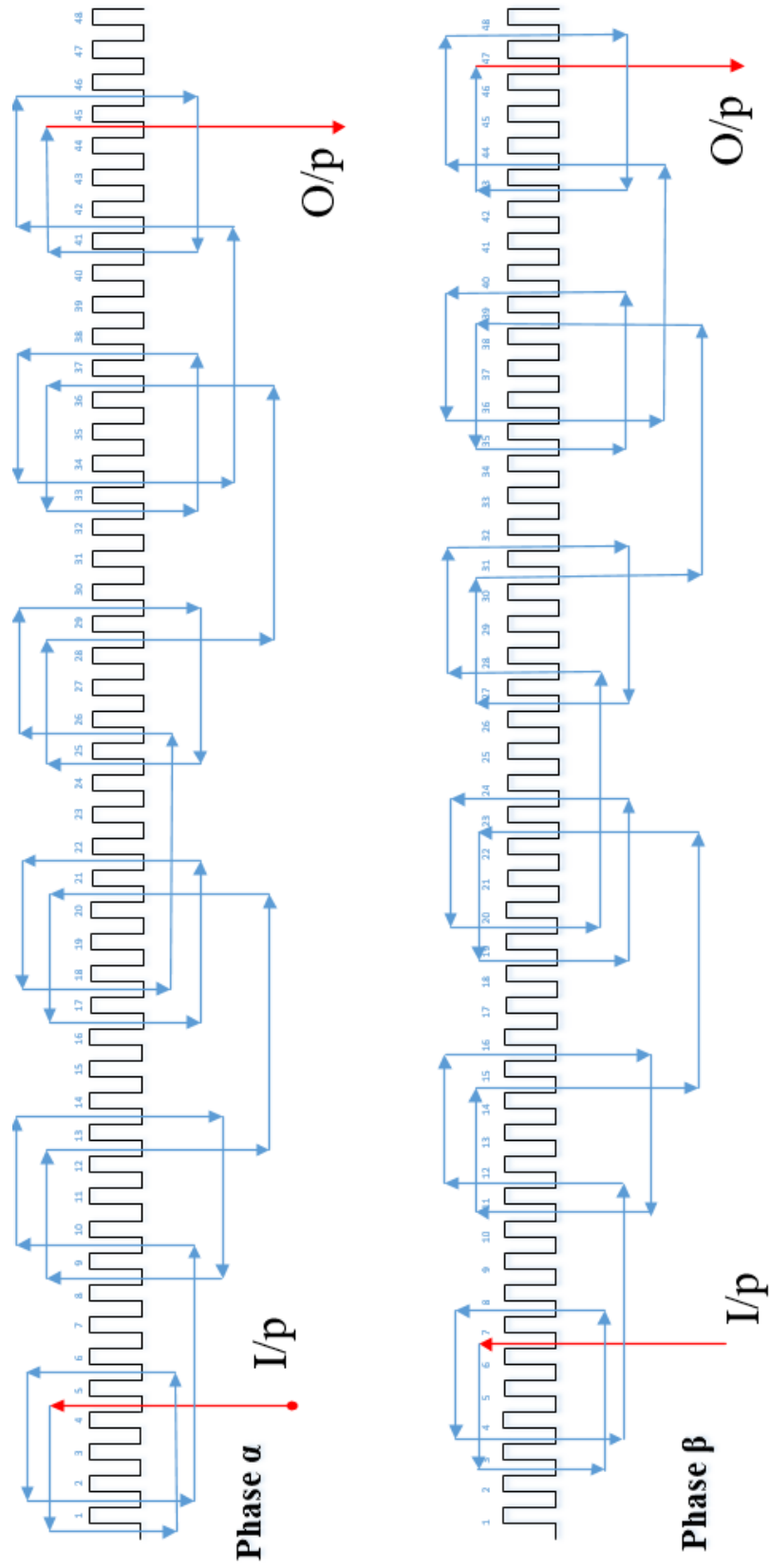


Figure C.5. Six pole search windings, phases α and β .

Appendix D: Induction Machine Equivalent Circuit Parameters

The most common method is to determine induction motor parameters manually. Some parameters are obtained by testing machine under no-load and locked rotor conditions.

D.1 Stator and Rotor Resistances

In order to obtain stator and rotor winding resistances, voltage was applied across these windings. For the rotor, since the star connection point is usually inside the machine and not accessible. Voltages and currents were measured across two phases while the third phase was left open. By applying Kirchhoff voltage law, the windings resistances can be obtained.

For stator resistance, if it is start connected:

$$2R_s = \frac{V}{I} = \frac{1.653}{0.434}, R_s = 1.91 \Omega \quad (\text{D.1})$$

For rotor resistance, which is invariably hard-wired as a star:

$$2R_r = \frac{0.1898}{0.411}, R_r = 0.2312 \Omega \quad (\text{D.2})$$

D.2 No load Test

The no-load test gives information about exciting current and rotational losses. The test is performed by applying rated voltage on the stator windings. The small power required by the machine is due to core losses, friction and winding losses. The machine will rotate at almost synchronous speed, which makes the slip nearly zero. The magnetising resistance and core losses can be obtained from

$$\begin{aligned}\cos \theta &= \frac{\text{power}}{VI} = 0.1871 \\ X_m &= \frac{V}{I \sin \theta} = 218.05 \Omega \\ R_c &= \frac{V}{I \cos \theta} = 1191.6 \Omega\end{aligned}\tag{D.3}$$

D.3 Locked Rotor Test

The locked rotor test is the same as short circuit test on a transformer and provides the information about leakage impedances and rotor resistance. The rotor is at stand still while low voltage is applied to stator windings to generate rated current. Since there is no rotation, the slip is one. The magnetisation reactance is much larger than leakage impedance, so the former can be ignored. Using this test L_s , and L_r can be determined from X_{eq} – with the inductances split equally. Hence

$$\begin{aligned}\cos \theta &= \frac{\text{power}}{VI} \\ Z_{sc} &= \frac{V}{I} = 11.406 \Omega \\ X_{eq} &= Z_{sc} \cos \theta = 10.36 \Omega = \omega(L_s + L_r) \\ R_{eq} &= Z_{sc} \sin \theta = 4.77 \Omega\end{aligned}\tag{D.4}$$

$$\begin{aligned}R_{eq} &= R_s + \left(\frac{N_{st}}{N_r}\right)^2 R_r \\ \left(\frac{N_{st}}{N_r}\right) &= 3.6\end{aligned}\tag{D.5}$$

Appendix E: MATLAB/ Simulink Model of the Wound Rotor Induction Motor

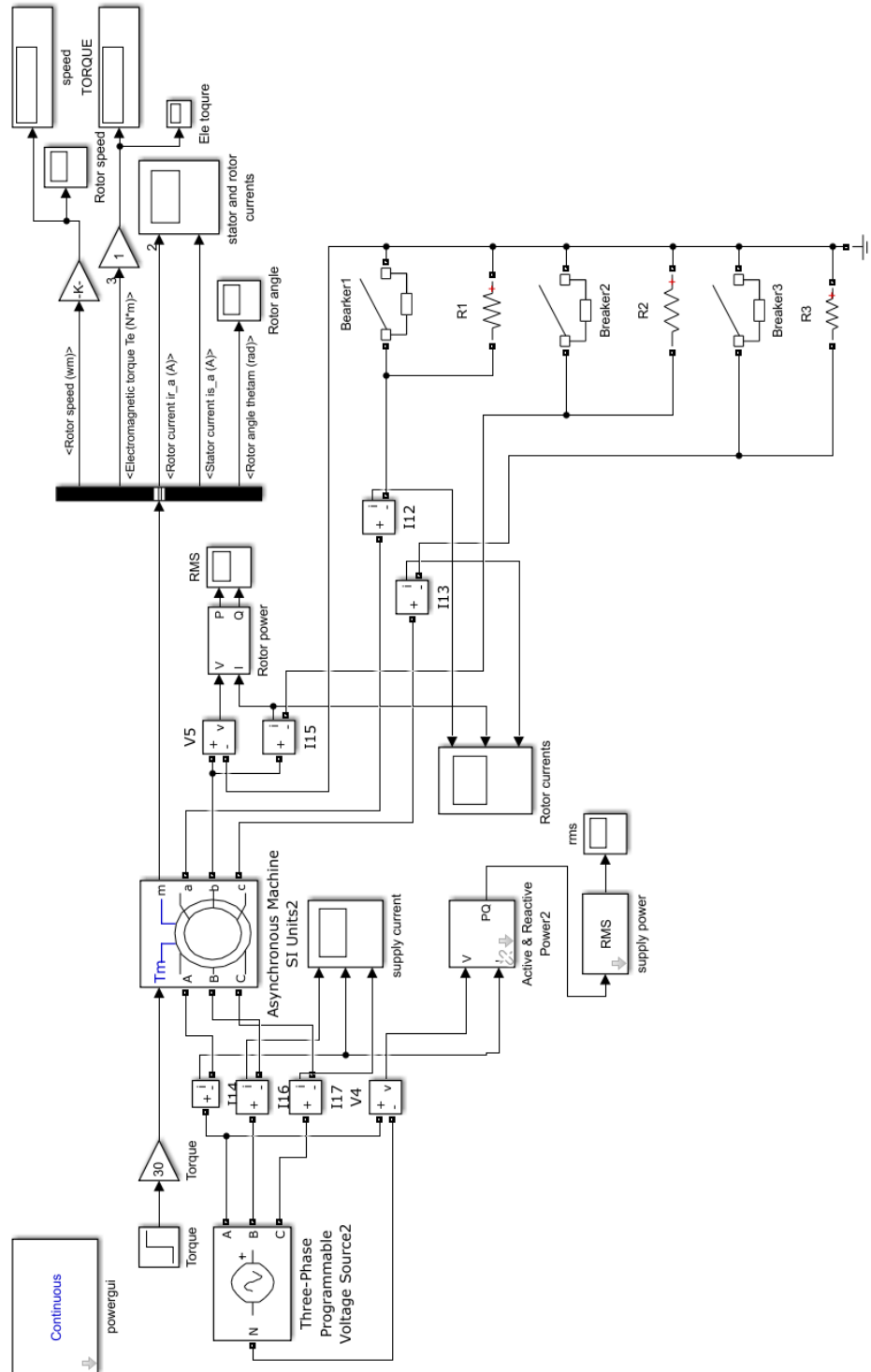


Figure E.1. MATLAB/simulink model of the three-phase wound rotor induction motor.

Biography



Ahmad Salah  (S'16–M'16) was born in Maan, Jordan, in 1985. He received the B.Eng. degree in electrical engineering from Yarmouk University, Irbid, Jordan, in 2008, and the M.Sc. degree in electrical and computer engineering from the New York Institute of Technology, Amman, Jordan, in 2012. He is currently working toward the Ph.D. degree in electrical engineering at the University of Technology Sydney, Ultimo, NSW, Australia. He was a Lecturer at Al-Hussein Bin Talal University, Maan, where he also worked as the Director of the Maintenance Department. His main research interests include fault detection of induction machines and condition monitoring of doubly fed induction generator.



Prof. **Youguang Guo**  (S'02–M'05–SM'06) was born in Hubei, China, in 1965. He received the B.E. degree from the Huazhong University of Science and Technology, Wuhan, China, in 1985; the M.E. degree from Zhejiang University, Hangzhou, China, in 1988; and the Ph.D. degree from the University of Technology Sydney (UTS), Ultimo, NSW, Australia, in 2004, all in electrical engineering. He is currently an Associate Professor with the School of Electrical and Data Engineering, UTS. His research interests include measurement and characterization of magnetic properties of magnetic materials, numerical analysis of electromagnetic field, electrical machine design and optimization, power electronic drives, and motor control.



Prof. **David G. Dorrell**  (M'95–SM'08) is a native of St. Helens, U.K. He received the B.Eng. (Hons.) degree in electrical and electronic engineering from the University of Leeds, Leeds, U.K., in 1988; the M.Sc. degree in power electronics engineering from the University of Bradford, Bradford, U.K., in 1989; and the Ph.D. degree in engineering from the University of Cambridge, Cambridge, U.K., in 1993. Since 2015, he has been a Professor of electrical machines with the University of KwaZulu-Natal, Durban, South Africa. He has held lecturing positions at Robert Gordon University, Aberdeen, U.K., and the University of Reading, Reading, U.K. He was a Senior Lecturer at the University of Glasgow, Glasgow, U.K., for several years. In 2008, he took up a post as a Senior Lecturer at the University of Technology Sydney, Ultimo, NSW, Australia, and he was promoted to an Associate Professor in 2009. He is also an Adjunct Associate Professor with National Cheng Kung University, Tainan, Taiwan. His research interests include the design and analysis of various electrical machines, and also renewable energy systems. Dr. Dorrell is a Chartered Engineer in the U.K. and also a fellow of the Institution of Engineering and Technology.

References

- [1] S. Williamson and M. Mueller, "Calculation of the impedance of rotor cage end rings," in *IEE Proceedings B (Electric Power Applications)*, 1993, vol. 140, no. 1, pp. 51-60: IET.
- [2] S. Williamson and M. Abdel-Magied, "Steady-state analysis of double-cage induction motors with rotor-cage faults," in *IEE Proceedings B (Electric Power Applications)*, 1987, vol. 134, no. 4, pp. 199-206: IET.
- [3] D. G. Dorrell, J. K. Shek, M. A. Mueller, and M.-F. Hsieh, "Damper windings in induction machines for reduction of unbalanced magnetic pull and bearing wear," *Industry Applications, IEEE Transactions on*, vol. 49, no. 5, pp. 2206-2216, 2013.
- [4] A. Sinervo, A. Laiho, and A. Arkkio, "Low-frequency oscillation in rotor vibration of a two-pole induction machine with extra four-pole stator winding," *Magnetics, IEEE Transactions on*, vol. 47, no. 9, pp. 2292-2302, 2011.
- [5] A. Laiho, A. Sinervo, J. Orivuori, K. Tammi, A. Arkkio, and K. Zenger, "Attenuation of harmonic rotor vibration in a cage rotor induction machine by a self-bearing force actuator," *IEEE Transactions on Magnetics*, vol. 45, no. 12, pp. 5388-5398, 2009.
- [6] A. Chiba, T. Fukao, and M. A. Rahman, "Vibration suppression of a flexible shaft with a simplified bearingless induction motor drive," *IEEE Transactions on Industry Applications*, vol. 44, no. 3, pp. 745-752, 2008.
- [7] L. Wu, Z. Zhu, J. Chen, and Z. Xia, "An analytical model of unbalanced magnetic force in fractional-slot surface-mounted permanent magnet machines," *IEEE Transactions on Magnetics*, vol. 46, no. 7, pp. 2686-2700, 2010.
- [8] Z. Zhu, D. Ishak, D. Howe, and J. Chen, "Unbalanced magnetic forces in permanent-magnet brushless machines with diametrically asymmetric phase windings," *IEEE Transactions on Industry Applications*, vol. 43, no. 6, pp. 1544-1553, 2007.
- [9] D. Jee and N. Patel, "V/f control of induction motor drive," 2013.
- [10] P. Vas, *Parameter estimation, condition monitoring, and diagnosis of electrical machines*. Oxford University Press, USA, 1993.
- [11] W. R. Finley and R. R. Burke, "Troubleshooting motor problems," *Ind. Appl., IEEE Trans.*, vol. 30, no. 5, pp. 1383-1397, 1994.
- [12] R. Belmans and K. Hameyer, "Different approaches to the preventive maintenance of induction motors," in *Proc. ICEM 1996*, 1996, vol. 2, pp. 423-428.
- [13] H. Toliyat and S. Nandi, "Condition monitoring and fault diagnosis of electrical machines—A review," in *Proc. IEEE-IAS 1999 Annu. Meeting*, 1999, vol. 1, pp. 3-7.
- [14] W. Thomson, D. Rankin, and D. G. Dorrell, "On-line current monitoring to diagnose airgap eccentricity in large three-phase induction motors—industrial case histories verify the predictions," *IEEE Trans. Energy Convers.*, vol. 14, no. 4, pp. 1372-1378, 1999.
- [15] M. El Hachemi Benbouzid, "A review of induction motors signature analysis as a medium for faults detection," *IEEE Trans. Ind. Appl.*, vol. 47, no. 5, pp. 984-993, 2000.
- [16] J. Cameron, W. Thomson, and A. Dow, "Vibration and current monitoring for detecting airgap eccentricity in large induction motors," in *Proc. IEEE B (Elect. Power Appl.)*, 1986, vol. 133, no. 3, pp. 155-163: IET.
- [17] D. Basak, A. Tiwari, and S. Das, "Fault diagnosis and condition monitoring of electrical machines—A Review," in *Ind. Tech. ICIT 2006. IEEE Int. Conf.*, 2006, pp. 3061-3066.
- [18] R. Krishnan, *Electric motor drives: modeling, analysis, and control*. Prentice Hall, 2001.
- [19] I. Boldea, *The induction machines design handbook*. CRC press, 2009.
- [20] M. Group, "Report of large motor reliability survey of industrial and commercial installations, Part II," *IEEE Trans. Ind. Appl.*, vol. 21, no. 4, pp. 865-872, 1985.
- [21] EPRI, "Improved Motors for Utility Applications," *EPRI Final Report*, 1982.
- [22] R. Pena, J. Clare, and G. Asher, "Doubly fed induction generator using back-to-back PWM converters and its application to variable-speed wind-energy generation," *IEE Proceedings-Electric Power Applications*, vol. 143, no. 3, pp. 231-241, 1996.
- [23] D. Reljić, J. Tomić, and Ž. Kanović, "Application of the Goertzel's algorithm in the airgap mixed eccentricity fault detection," *Serbian Journal of Electrical Engineering*, vol. 12, no. 1, pp. 17-32, 2015.
- [24] M. R. Mehrjou, N. Mariun, M. H. Marhaban, and N. Mison, "Rotor fault condition monitoring techniques for squirrel-cage induction machine—A review," *Mechanical Systems and Signal Processing*, vol. 25, no. 8, pp. 2827-2848, 2011.
- [25] C. I. Hubert, *Electric machines: theory, operation, applications, adjustment and control*. 1991.
- [26] S. Chapman, *Electric machinery fundamentals*. Tata McGraw-Hill Education, 2005.

- [27] J. Fletcher and J. Yang, "Introduction to the doubly-fed induction generator for wind power applications," in *Paths to Sustainable Energy*: InTech, 2010.
- [28] M. Tazil *et al.*, "Three-phase doubly fed induction generators: an overview," *IET Electric Power Applications*, vol. 4, no. 2, pp. 75-89, 2010.
- [29] S. Muller, M. Deicke, and R. W. De Doncker, "Doubly fed induction generator systems for wind turbines," *IEEE Industry applications magazine*, vol. 8, no. 3, pp. 26-33, 2002.
- [30] L. Xu and W. Cheng, "Torque and reactive power control of a doubly fed induction machine by position sensorless scheme," *IEEE transactions on Industry Applications*, vol. 31, no. 3, pp. 636-642, 1995.
- [31] D. Zhi and L. Xu, "Direct power control of DFIG with constant switching frequency and improved transient performance," *IEEE Transactions on Energy Conversion*, vol. 22, no. 1, pp. 110-118, 2007.
- [32] S. V. Bozhko, R. Blasco-Gimenez, R. Li, J. C. Clare, and G. M. Asher, "Control of offshore DFIG-based wind farm grid with line-commutated HVDC connection," *IEEE Transactions on Energy Conversion*, vol. 22, no. 1, pp. 71-78, 2007.
- [33] I. Boldea, "Control of electric generators: a review," in *Industrial Electronics Society, 2003. IECON'03. The 29th Annual Conference of the IEEE*, 2003, vol. 1, pp. 972-980: IEEE.
- [34] D. G. Dorrell, A. Hermann, and B. B. Jensen, "Analysis of unbalanced magnetic pull in wound rotor induction machines using finite element analysis-Transient, motoring and generating modes," in *Industrial Electronics Society, IECON 2013-39th Annual Conference of the IEEE*, 2013, pp. 7307-7312: IEEE.
- [35] J. Robinson, C. D. Whelan, and N. K. Haggerty, "Trends in advanced motor protection and monitoring," *IEEE Transactions on Industry Applications*, vol. 40, no. 3, pp. 853-860, 2004.
- [36] L. K. Singh and P. K. S. Komal, "Condition Monitoring of Induction Motor," 2015.
- [37] Y. Amirat, M. E. H. Benbouzid, E. Al-Ahmar, B. Bensaker, and S. Turri, "A brief status on condition monitoring and fault diagnosis in wind energy conversion systems," *Renewable and sustainable energy reviews*, vol. 13, no. 9, pp. 2629-2636, 2009.
- [38] I. Ahmed, R. Supangat, J. Grieger, N. Ertugrul, and W. Soong, "A baseline study for on-line condition monitoring of induction machines," in *AUPEC 2004, Australasian Universities Power Engineering Conference, Brisbane, 2004*.
- [39] R. R. Schoen, T. G. Habetler, F. Kamran, and R. Bartfield, "Motor bearing damage detection using stator current monitoring," *Industry Applications, IEEE Transactions on*, vol. 31, no. 6, pp. 1274-1279, 1995.
- [40] J. Sottile Jr and J. L. Kohler, "An on-line method to detect incipient failure of turn insulation in random-wound motors," *Energy Conversion, IEEE Transactions on*, vol. 8, no. 4, pp. 762-768, 1993.
- [41] S. B. Lee, R. M. Tallam, and T. G. Habetler, "A robust, on-line turn-fault detection technique for induction machines based on monitoring the sequence component impedance matrix," *Power Electronics, IEEE Transactions on*, vol. 18, no. 3, pp. 865-872, 2003.
- [42] T. A. Lipo, *Introduction to AC machine design*. Wisconsin Power Electronics Research Center, University of Wisconsin, 2004.
- [43] S.-B. Lee and T. G. Habetler, "An on-line stator winding resistance estimation technique for temperature monitoring of line-connected induction machines," in *Industry Applications Conference, 2001. Thirty-Sixth IAS Annual Meeting. Conference Record of the 2001 IEEE*, 2001, vol. 3, pp. 1564-1571: IEEE.
- [44] A. H. Bonnett and G. C. Soukup, "Cause and analysis of stator and rotor failures in three-phase squirrel-cage induction motors," *IEEE Transactions on Industry applications*, vol. 28, no. 4, pp. 921-937, 1992.
- [45] J. Cros and P. Viarouge, "Synthesis of high performance PM motors with concentrated windings," *IEEE transactions on energy conversion*, vol. 17, no. 2, pp. 248-253, 2002.
- [46] J. L. Kohler, J. Sottile, and F. C. Trutt, "Condition monitoring of stator windings in induction motors. I. Experimental investigation of the effective negative-sequence impedance detector," *IEEE Transactions on Industry Applications*, vol. 38, no. 5, pp. 1447-1453, 2002.
- [47] D. G. Dorrell, "Calculation of unbalanced magnetic pull in cage induction machines," Thesis, University of Cambridge, 1993.
- [48] D. G. Dorrell and O. Kayani, "Measurement and Calculation of Unbalanced Magnetic Pull in Wound Rotor Induction Machine," *Magnetics, IEEE Transactions on*, vol. 50, no. 11, pp. 1-4, 2014.
- [49] G. M. Joksimović, "Dynamic simulation of cage induction machine with air gap eccentricity," *IEE Proceedings-Electric Power Applications*, vol. 152, no. 4, pp. 803-811, 2005.
- [50] D. G. Dorrell, "Sources and characteristics of unbalanced magnetic pull in three-phase cage induction motors with axial-varying rotor eccentricity," *Industry Applications, IEEE Transactions on*, vol. 47, no. 1, pp. 12-24, 2011.
- [51] S. Nandi, R. M. Bharadwaj, and H. A. Toliyat, "Mixed eccentricity in three phase induction machines: analysis, simulation and experiments," in *Industry Applications Conference, 2002. 37th IAS Annual Meeting. Conference Record of the*, 2002, vol. 3, pp. 1525-1532: IEEE.

- [52] M. Osama and T. Lipo, "A new induction machine model for analysis of eccentric rotor magnetic pull," in *Proc. of Symposium on Power Electronics, Electrical Drives, Advanced Electrical Motors, SPEEDAM '94 Taormina*, 1994, pp. 173-177.
- [53] W. T. Thomson and R. J. Gilmore, "Motor current signature analysis to detect faults in induction motor drives—fundamentals, Data interpretation, and industrial case histories," in *Proceedings of 32nd Turbo machinery Symposium, A&M University, Texas, USA*, 2003.
- [54] P. J. Tavner and J. Penman, *Condition monitoring of electrical machines*. Research Studies Pre, 1987.
- [55] W. T. Thomson and M. Fenger, "Current signature analysis to detect induction motor faults," *Industry Applications Magazine, IEEE*, vol. 7, no. 4, pp. 26-34, 2001.
- [56] H. Niaoqing, Y. Zhang, G. Fengshou, Q. Guojun, and B. Andrew, "Early, Fault Detection Using a Novel Spectrum Enhancement Method for Motor Current th Signature Analysis," in *7 WSEAS Int. Conf. on Artificial Intelligence Knowledge Engineering and Data Bases (AIKED'08), University of Cambridge*, 2008, pp. 470-475.
- [57] M. Rigoni, N. Sadowski, N. Batistela, J. Bastos, S. Nau, and A. Kost, "Detection and analysis of rotor faults in induction motors by the measurement of the stray magnetic flux," *Journal of Microwaves, Optoelectronics and Electromagnetic Applications*, vol. 11, no. 1, pp. 68-80, 2012.
- [58] J. Pons-Llinares, J. A. Antonino-Daviu, M. Riera-Guasp, M. Pineda-Sanchez, and V. Climente-Alarcon, "Induction motor diagnosis based on a transient current analytic wavelet transform via frequency B-splines," *IEEE Transactions on Industrial Electronics*, vol. 58, no. 5, pp. 1530-1544, 2011.
- [59] B. Li, M.-Y. Chow, Y. Tipsuwan, and J. C. Hung, "Neural-network-based motor rolling bearing fault diagnosis," *Industrial Electronics, IEEE Transactions on*, vol. 47, no. 5, pp. 1060-1069, 2000.
- [60] V. Kontargyri *et al.*, "An expert system for fault diagnosis, repairing and maintenance of electrical machines," in *Proceedings of the 6th conference on Applications of electrical engineering*, 2007, pp. 166-171: Citeseer.
- [61] W. T. Thomson and A. Barbour, "On-line current monitoring and application of a finite element method to predict the level of static airgap eccentricity in three-phase induction motors," *Energy Conversion, IEEE Transactions on*, vol. 13, no. 4, pp. 347-357, 1998.
- [62] M. E. H. Benbouzid, M. Vieira, and C. Theys, "Induction motors' faults detection and localization using stator current advanced signal processing techniques," *IEEE Transactions on power electronics*, vol. 14, no. 1, pp. 14-22, 1999.
- [63] W. T. Thomson and R. J. Gilmore, "Motor current signature analysis to detect faults in induction motor drives—fundamentals, data interpretation, and industrial case histories," in *Proceedings of the thirty-second turbomachinery symposium*, 2003, pp. 145-156.
- [64] W. T. Thomson, "On-line MCSA to diagnose shorted turns in low voltage stator windings of 3-phase induction motors prior to failure," in *Electric Machines and Drives Conference, 2001. IEMDC 2001. IEEE International*, 2001, pp. 891-898: IEEE.
- [65] M. E. H. Benbouzid, "A review of induction motors signature analysis as a medium for faults detection," *IEEE transactions on industrial electronics*, vol. 47, no. 5, pp. 984-993, 2000.
- [66] J. F. Martins, V. F. Pires, and A. Pires, "Unsupervised neural-network-based algorithm for an on-line diagnosis of three-phase induction motor stator fault," *IEEE Transactions on Industrial Electronics*, vol. 54, no. 1, pp. 259-264, 2007.
- [67] A. M. C. MA Cruz, S, "Rotor cage fault diagnosis in three-phase induction motors by extended Park's vector approach," *Electric Machines & Power Systems*, vol. 28, no. 4, pp. 289-299, 2000.
- [68] A. M. Cardoso and E. S. Saraiva, "Computer-aided detection of airgap eccentricity in operating three-phase induction motors by Park's vector approach," *IEEE Transactions on Industry Applications*, vol. 29, no. 5, pp. 897-901, 1993.
- [69] J. Zarei and J. Poshtan, "An advanced Park's vectors approach for bearing fault detection," *Tribology International*, vol. 42, no. 2, pp. 213-219, 2009.
- [70] M. E. H. Benbouzid and G. B. Kliman, "What stator current processing-based technique to use for induction motor rotor faults diagnosis?," *IEEE Transactions on Energy Conversion*, vol. 18, no. 2, pp. 238-244, 2003.
- [71] Q. Wu and S. Nandi, "Fast single-turn sensitive stator interturn fault detection of induction machines based on positive- and negative-sequence third harmonic components of line currents," *IEEE Transactions on Industry Applications*, vol. 46, no. 3, pp. 974-983, 2010.
- [72] S. B. Lee, R. M. Tallam, and T. G. Habetler, "A robust, on-line turn-fault detection technique for induction machines based on monitoring the sequence component impedance matrix," *IEEE Transactions on Power Electronics*, vol. 18, no. 3, pp. 865-872, 2003.
- [73] R. M. Tallam, T. G. Habetler, and R. G. Harley, "Transient model for induction machines with stator winding turn faults," *IEEE Transactions on Industry Applications*, vol. 38, no. 3, pp. 632-637, 2002.
- [74] R. Beguenane and M. E. H. Benbouzid, "Induction motors thermal monitoring by means of rotor resistance identification," *Energy Conversion, IEEE Transactions on*, vol. 14, no. 3, pp. 566-570, 1999.
- [75] P. Milanfar and J. H. Lang, "Monitoring the thermal condition of permanent-magnet synchronous motors," *Aerospace and Electronic Systems, IEEE Transactions on*, vol. 32, no. 4, pp. 1421-1429, 1996.

- [76] S. Bachir, S. Tnani, J.-C. Trigeassou, and G. Champenois, "Diagnosis by parameter estimation of stator and rotor faults occurring in induction machines," *IEEE Transactions on Industrial Electronics*, vol. 53, no. 3, pp. 963-973, 2006.
- [77] N. Zhao, Z. Zhu, and W. Liu, "Thermal analysis of permanent magnet motor and generator," *Magnetics, IEEE Transactions on*, vol. 47, no. 10, pp. 4199-4202, 2011.
- [78] A. Siddique, G. Yadava, and B. Singh, "A review of stator fault monitoring techniques of induction motors," *Energy conversion, IEEE transactions on*, vol. 20, no. 1, pp. 106-114, 2005.
- [79] D. G. Dorrell, "Combined thermal and electromagnetic analysis of permanent-magnet and induction machines to aid calculation," *IEEE Transactions on Industrial Electronics*, vol. 55, no. 10, pp. 3566-3574, 2008.
- [80] I. Boldea and S. A. Nasar, *The induction machine handbook*. CRC press, 2010.
- [81] D. Mori and T. Ishikawa, "Force and vibration analysis of induction motors," *IEEE Transactions on magnetics*, vol. 41, no. 5, pp. 1948-1951, 2005.
- [82] A. Belahcen, A. Arkkio, P. Klinge, J. Linjama, V. Voutilainen, and J. Westerlund, "Radial forces calculation in a synchronous generator for noise analysis," in *Proceeding of the Third Chinese International Conference on Electrical Machines*, 1999, pp. 199-122.
- [83] H. Toliyat, M. Arefeen, and A. Parlos, "A method for dynamic simulation and detection of air-gap eccentricity in induction machines," in *Industry Applications Conference, 1995. Thirtieth IAS Annual Meeting, IAS'95., Conference Record of the 1995 IEEE*, 1995, vol. 1, pp. 629-636: IEEE.
- [84] D. G. Dorrell, W. T. Thomson, and S. Roach, "Analysis of airgap flux, current, and vibration signals as a function of the combination of static and dynamic airgap eccentricity in 3-phase induction motors," *Industry Applications, IEEE Transactions on*, vol. 33, no. 1, pp. 24-34, 1997.
- [85] L. Frosini, A. Borin, L. Girometta, and G. Venchi, "Development of a leakage flux measurement system for condition monitoring of electrical drives," presented at the Diagnostics for Electric Machines, Power Electronics & Drives (SDEMPED), 2011 IEEE International Symposium on, 2011.
- [86] A. Ceban, R. Pusca, and R. Romary, "Study of rotor faults in induction motors using external magnetic field analysis," *Industrial Electronics, IEEE Transactions on*, vol. 59, no. 5, pp. 2082-2093, 2012.
- [87] D.-H. Hwang, J.-H. Chang, D.-S. Kang, J.-H. Lee, and K.-H. Choi, "A Method for Dynamic Simulation and Detection of Air-gap Eccentricity in Induction Motors by Measuring Flux Density," in *Electromagnetic Field Computation, 2006 12th Biennial IEEE Conference on*, 2006, pp. 69-69: IEEE.
- [88] J. Penman, M. Dey, A. Tait, and W. Bryan, "Condition monitoring of electrical drives," in *IEE Proceedings B (Electric Power Applications)*, 1986, vol. 133, no. 3, pp. 142-148: IET.
- [89] D.-H. Hwang, K.-C. Lee, J.-H. Lee, Y.-J. Kim, K.-H. Choi, and J.-H. Lee, "A Method for Dynamic Simulation and Detection of Air-Gap Eccentricity in Induction Motors," *2004 12th ICPE 논문집*, pp. 725-728, 2004.
- [90] J. S. Hsu, "Monitoring of defects in induction motors through air-gap torque observation," *Industry Applications, IEEE Transactions on*, vol. 31, no. 5, pp. 1016-1021, 1995.
- [91] J. Hsu, H. Woodson, and W. Weldon, "Possible errors in measurement of air-gap torque pulsations of induction motors," *Energy Conversion, IEEE Transactions on*, vol. 7, no. 1, pp. 202-208, 1992.
- [92] F. Filippetti, M. Martelli, G. Franceschini, and C. Tassoni, "Development of expert system knowledge base to on-line diagnosis of rotor electrical faults of induction motors," in *Industry Applications Society Annual Meeting, 1992., Conference Record of the 1992 IEEE*, 1992, pp. 92-99: IEEE.
- [93] S. Nandi, H. Toliyat, and X. Li, "Condition monitoring and fault diagnosis of electrical motors-a review," *Energy Conversion, IEEE Transactions on*, vol. 20, no. 4, pp. 719-729, 2005.
- [94] A. M. Da Silva, R. J. Povinelli, and N. A. Demerdash, "Induction machine broken bar and stator short-circuit fault diagnostics based on three-phase stator current envelopes," *IEEE Transactions on Industrial Electronics*, vol. 55, no. 3, pp. 1310-1318, 2008.
- [95] G. Kliman, R. Koegl, J. Stein, R. Endicott, and M. Madden, "Noninvasive detection of broken rotor bars in operating induction motors," *IEEE Transactions on Energy Conversion*, vol. 3, no. 4, pp. 873-879, 1988.
- [96] T. Barton and B. Doxey, "The operation of three-phase induction motors with unsymmetrical impedance in the secondary circuit," *Proceedings of the IEE-Part A: Power Engineering*, vol. 102, no. 1, pp. 71-79, 1955.
- [97] N. M. Elkasabgy, A. R. Eastham, and G. E. Dawson, "Detection of broken bars in the cage rotor on an induction machine," *IEEE transactions on industry applications*, vol. 28, no. 1, pp. 165-171, 1992.
- [98] W. Thomson and I. Stewart, "Online current monitoring for fault diagnosis in inverter fed induction motors," in *Power Electronics and Variable-Speed Drives, Third International Conference on*, 1988, pp. 432-435: IET.
- [99] F. Filippetti, G. Franceschini, C. Tassoni, and P. Vas, "AI techniques in induction machines diagnosis including the speed ripple effect," *IEEE Transactions on Industry Applications*, vol. 34, no. 1, pp. 98-108, 1998.
- [100] A. C. Smith, "Harmonic field analysis for slip-ring motors including general rotor asymmetry," *Industry Applications, IEEE Transactions on*, vol. 26, no. 5, pp. 857-865, 1990.

- [101] R. Roshanfekar, H. Aliakbar, and A. Jalilian, "Performance analysis of 3-phase wound rotor induction motor under asymmetrical fault conditions in stator and rotor windings," in *Power Electronics, Drive Systems and Technologies Conference (PEDSTC), 2014 5th*, 2014, pp. 323-328: IEEE.
- [102] S. Djurović, D. Vilchis-Rodriguez, and A. Smith, "Vibration monitoring for wound rotor induction machine winding fault detection," in *Electrical Machines (ICEM), 2012 XXth International Conference on*, 2012, pp. 1906-1912: IEEE.
- [103] D. Razafimahefa, E. Randrianarisoa, E. J. R. Sambatra, and N. Heraud, "Modeling and faults detection of small power wound rotor induction machine," in *Electrical and Power Engineering (EPE), 2014 International Conference and Exposition on*, 2014, pp. 311-316: IEEE.
- [104] P. Trickey, "Test analysis and calculation of polyphase hysteresis motors," *IEEE Transactions on Power Apparatus and Systems*, no. 5, pp. 1855-1862, 1972.
- [105] A. Covo, "Unbalanced magnetic pull in induction motors with eccentric rotors," *Transactions of the American Institute of Electrical Engineers. Part III: Power Apparatus and Systems*, vol. 73, no. 2, pp. 1421-1425, 1954.
- [106] R. Robinson, "The calculation of unbalanced magnetic pull in synchronous and induction motors," *Transactions of the American Institute of Electrical Engineers*, vol. 62, no. 10, pp. 620-624, 1943.
- [107] A. Gray and J. Pertsch, "Critical review of the bibliography on unbalanced magnetic pull in dynamo-electric machines," *Transactions of the American Institute of Electrical Engineers*, vol. 37, no. 2, pp. 1417-1424, 1918.
- [108] H. Frohne, "The practical importance of unbalanced magnetic pull, possibilities of calculating and damping it," *Conti Elektro Berichte*, vol. 13, pp. 81-92, 1967.
- [109] R. Robinson, "Line-frequency magnetic vibration of ac machines," *Transactions of the American Institute of Electrical Engineers. Part III: Power Apparatus and Systems*, vol. 81, no. 3, pp. 675-679, 1962.
- [110] E. W. Summers, "Vibration in 2-pole induction motors related to slip frequency," *Transactions of the American Institute of Electrical Engineers. Part III: Power Apparatus and Systems*, vol. 74, no. 3, pp. 69-72, 1955.
- [111] G. Rai, *Airgap eccentricity in induction motors*. ERA Technology Limited, 1974.
- [112] R. Belmans, A. Vandenput, and W. Geysen, "Electromagnetic influence on the radial vibrations of two-pole induction motors," in *Vibrations and Audible Noise in Alternating Current Machines*: Springer, 1988, pp. 81-97.
- [113] J. Eastham and S. Williamson, "Generalised theory of induction motors with asymmetrical airgaps and primary windings," in *Proceedings of the Institution of Electrical Engineers*, 1973, vol. 120, no. 7, pp. 767-775: IET.
- [114] S. Williamson and A. C. Smith, "Steady-state analysis of 3-phase cage motors with rotor-bar and end-ring faults," in *IEE Proceedings B (Electric Power Applications)*, 1982, vol. 129, no. 3, pp. 93-100: IET.
- [115] S. Williamson, M. Abdel-Magied, and A. C. Smith, "Effects of Rotor Cage Asymmetry on the Performance of Three-Phase Induction Motors," in *Vibrations and audible noise in alternating current machines*: Springer, 1988, pp. 485-498.
- [116] S. Williamson and M. Abdel-Magied, "Unbalanced magnetic pull in induction motors with asymmetrical rotor cages," in *IEE Conf. Publ*, 1985, vol. 254, pp. 218-222.
- [117] S. Swann, "Effect of rotor eccentricity on the magnetic field in the air-gap of a non-salient-pole machine," in *Proceedings of the Institution of Electrical Engineers*, 1963, vol. 110, no. 5, pp. 903-915: IET.
- [118] D. G. Dorrell and A. C. Smith, "Calculation of UMP in induction motors with series or parallel winding connections," *IEEE Transactions on Energy Conversion*, vol. 9, no. 2, pp. 304-310, 1994.
- [119] A. Tenhunen, T. P. Holopainen, and A. Arkkio, "Effects of saturation on the forces in induction motors with whirling cage rotor," *IEEE Transactions on Magnetics*, vol. 40, no. 2, pp. 766-769, 2004.
- [120] D. G. Dorrell, "Experimental behaviour of unbalanced magnetic pull in 3-phase induction motors with eccentric rotors and the relationship with tooth saturation," *IEEE transactions on energy conversion*, vol. 14, no. 3, pp. 304-309, 1999.
- [121] B. Heller and A. Jokl, "Tangential forces in squirrel-cage induction motors," *IEEE Transactions on Power Apparatus and Systems*, no. 4, pp. 484-492, 1969.
- [122] A. Stavrou and J. Penman, "Modelling dynamic eccentricity in smooth air-gap induction machines," in *Electric Machines and Drives Conference, 2001. IEMDC 2001. IEEE International*, 2001, pp. 864-871: IEEE.
- [123] L. Vandeveld and J. Melkebeek, "Theoretical and experimental study of radial forces in relation to magnetic noise of induction motors," in *Proceedings of the International Conference on Electrical Machines (ICEM), 5-8 September Vol. 3*, 1994, pp. 419-424.
- [124] M. Berman, "On the reduction of magnetic pull in induction motors with off-centre rotor," in *Industry Applications Society Annual Meeting, 1993., Conference Record of the 1993 IEEE*, 1993, pp. 343-350: IEEE.
- [125] S. Nandi and H. A. Toliyat, "Novel frequency-domain-based technique to detect stator interturn faults in induction machines using stator-induced voltages after switch-off," *IEEE Transactions on Industry Applications*, vol. 38, no. 1, pp. 101-109, 2002.
- [126] H. A. Toliyat and T. A. Lipo, "Transient analysis of cage induction machines under stator, rotor bar and end ring faults," *IEEE Transactions on Energy Conversion*, vol. 10, no. 2, pp. 241-247, 1995.

- [127] D. S. Kirschen, D. W. Novotny, and T. A. Lipo, "Optimal efficiency control of an induction motor drive," *IEEE Transactions on Energy Conversion*, no. 1, pp. 70-76, 1987.
- [128] S. Nandi, S. Ahmed, and H. A. Toliyat, "Detection of rotor slot and other eccentricity related harmonics in a three phase induction motor with different rotor cages," *IEEE Transactions on Energy Conversion*, vol. 16, no. 3, pp. 253-260, 2001.
- [129] N. Al-Nuaim and H. Toliyat, "A novel method for modeling dynamic air-gap eccentricity in synchronous machines based on modified winding function theory," *IEEE Transactions on energy conversion*, vol. 13, no. 2, pp. 156-162, 1998.
- [130] G. M. Joksimovic, M. D. Durovic, J. Penman, and N. Arthur, "Dynamic simulation of dynamic eccentricity in induction machines-finding function approach," *IEEE Transactions on Energy Conversion*, vol. 15, no. 2, pp. 143-148, 2000.
- [131] A. C. Smith and D. G. Dorrell, "Calculation and measurement of unbalanced magnetic pull in cage induction motors with eccentric rotors. Part 1: Analytical model," *IEE Proceedings-Electric Power Applications*, vol. 143, no. 3, pp. 193-201, 1996.
- [132] D. G. Dorrell, "The influence of rotor skew on unbalanced magnetic pull in cage induction motors with eccentric rotors," 1995.
- [133] D. G. Dorrell, "Modelling of non-uniform rotor eccentricity and calculation of unbalanced magnetic pull in 3-phase cage induction motors," in *International conference on electrical machines*, 2000, pp. 1820-1824.
- [134] H. M. Kelk, A. Eghbali, and H. A. Toliyat, "Modeling and analysis of cage induction motors under rotor misalignment and air gap eccentricity," in *Industry Applications Conference, 2005. Fourtieth IAS Annual Meeting. Conference Record of the 2005*, 2005, vol. 2, pp. 1324-1328: IEEE.
- [135] D. G. Dorrell and A. C. Smith, "Calculation and measurement of unbalanced magnetic pull in cage induction motors with eccentric rotors. Part 2: Experimental investigation," *IEE Proceedings-Electric Power Applications*, vol. 143, no. 3, pp. 202-210, 1996.
- [136] A. Burakov and A. Arkkio, "Comparison of the unbalanced magnetic pull mitigation by the parallel paths in the stator and rotor windings," *IEEE Transactions on Magnetics*, vol. 43, no. 12, pp. 4083-4088, 2007.
- [137] K. Binns and M. Dye, "Identification of principal factors causing unbalanced magnetic pull in cage induction motors," *Proceedings of the Institution of Electrical Engineers*, vol. 120, no. 3, pp. 349-354, 1973.
- [138] M. DeBortoli, S. Salon, D. Burow, and C. Slavik, "Effects of rotor eccentricity and parallel windings on induction machine behavior: A study using finite element analysis," *IEEE Transactions on Magnetics*, vol. 29, no. 2, pp. 1676-1682, 1993.
- [139] S. Salon, M. DeBortoli, D. Burow, and C. Slavik, "Calculation of circulating current between parallel windings in induction motors with eccentric rotors by the finite element method," *Proceedings of ICEM '92*, pp. 371-375, 1992.
- [140] A. Burakov, *Modelling the unbalanced magnetic pull in eccentric-rotor electrical machines with parallel windings*. Helsinki University of Technology, 2007.
- [141] D. G. Dorrell, "Sources and characteristics of unbalanced magnetic pull in three-phase cage induction motors with axial-varying rotor eccentricity," presented at the Industry Applications, IEEE Transactions on, 2011.
- [142] R. S. Konwar, K. Kalita, A. Banerjee, and W. K. S. Khoo, "Electromagnetic analysis of a bridge configured winding cage induction machine using finite element method," *Progress In Electromagnetics Research B*, vol. 48, pp. 347-373, 2013.
- [143] O. Poncelas, J. A. Rosero, J. Cusidó, J. A. Ortega, and L. Romeral, "Motor fault detection using a Rogowski sensor without an integrator," *IEEE Transactions on Industrial Electronics*, vol. 56, no. 10, pp. 4062-4070, 2009.
- [144] M.-J. Kim, B.-K. Kim, J.-W. Moon, Y.-H. Cho, D.-H. Hwang, and D.-S. Kang, "Analysis of inverter-fed squirrel-cage induction motor during eccentric rotor motion using FEM," *IEEE Transactions on Magnetics*, vol. 44, no. 6, pp. 1538-1541, 2008.
- [145] D. G. Dorrell and A. Salah, "Detection of rotor eccentricity in wound rotor induction machines using pole-specific search coils," in *Magnetics Conference (INTERMAG), 2015 IEEE*, 2015, pp. 1-1: IEEE.
- [146] D. G. Dorrell, A. Salah, and Y. Guo, "The detection and suppression of unbalanced magnetic pull in wound rotor induction motors using pole-specific search coils and auxiliary windings," *IEEE Transactions on Industry Applications*, vol. 53, no. 3, pp. 2066-2076, 2017.
- [147] A. Balan, "Theoretical and experimental investigations on radial electromagnetic forces in relation to vibration problems of induction machines," 1997.
- [148] D. G. Dorrell and K. Makhoba, "Detection of Inter-turn Stator Faults in Induction Motors Using Short Term Averaging of Forwards and Backwards Rotating Stator Current Phasors for Fast Prognostics," *IEEE Transactions on Magnetics*, 2017.
- [149] D. G. Dorrell, "Matrix analysis techniques in cage induction machines," *International Journal of Computer Applications in Technology*, vol. 36, no. 2, pp. 69-76, 2009.
- [150] C. Jha and S. S. Murthy, "Generalised rotating-field theory of wound-rotor induction machines having asymmetry in stator and/or rotor windings," in *Proceedings of the Institution of Electrical Engineers*, 1973, vol. 120, no. 8, pp. 867-873: IET.
- [151] S. Williamson and K. Mirzoian, "Analysis of cage induction motors with stator winding faults," *IEEE transactions on power apparatus and systems*, no. 7, pp. 1838-1842, 1985.
- [152] D. G. Dorrell, "Design requirements for doubly-fed reluctance generators," in *Power Electronics and Drive Systems, 2007. PEDS'07. 7th International Conference on*, 2007, pp. 981-988: IEEE.

- [153] D. G. Dorrell, T. Miller, and C. Rassmussen, "Inter-bar currents in induction machines," in *Industry Applications Conference, 2001. Thirty-Sixth IAS Annual Meeting. Conference Record of the 2001 IEEE*, 2001, vol. 2, pp. 729-736: IEEE.
- [154] F. Filippetti, G. Franceschini, and C. Tassoni, "Neural networks aided on-line diagnostics of induction motor rotor faults," *IEEE Transactions on Industry Applications*, vol. 31, no. 4, pp. 892-899, 1995.
- [155] F. Filippetti, G. Franceschini, C. Tassoni, and P. Vas, "Broken bar detection in induction machines: comparison between current spectrum approach and parameter estimation approach," in *Industry Applications Society Annual Meeting, 1994., Conference Record of the 1994 IEEE*, 1994, vol. 1, pp. 95-102: IEEE.
- [156] F. Filippetti, G. Franceschini, and C. Tassoni, "Neural networks aided on-line diagnostics of induction motor rotor faults," in *Industry Applications Society Annual Meeting, 1993., Conference Record of the 1993 IEEE*, 1993, pp. 316-323: IEEE.
- [157] D. G. Dorrell, D. Staton, and M. McGilp, "A combined electromagnetic and thermal approach to the design of electrical machines," *IECON 2006*, 2006.
- [158] A. Salah, Y. Guo, and D. G. Dorrell, "Impedance matrix analysis technique in wound rotor induction machines including general rotor asymmetry," in *Industrial Electronics Society, IECON 2016-42nd Annual Conference of the IEEE*, 2016, pp. 1821-1826: IEEE.
- [159] K. Shahzad, Y. Guo, L. Li, and D. G. Dorrell, "Design of high speed permanent magnet generator for solar co-generation system using motor-CAD," presented at the Electrical Machines and Systems (ICEMS), 2017 20th International Conference on, 2017.
- [160] J. Goss, M. Popescu, and D. Staton, "A comparison of an interior permanent magnet and copper rotor induction motor in a hybrid electric vehicle application," in *Electric Machines & Drives Conference (IEMDC), 2013 IEEE International*, 2013, pp. 220-225: IEEE.
- [161] D. G. Dorrell, N. Paterson, and J. Watson, "The causes and quantification of sideband currents for use in rotor fault detection systems for cage induction motors," *Proc. ICEM'96*, vol. 2, pp. 414-419, 1996.
- [162] X. Deng, S. Palko, T. Jokinen, and A. E. Ritchie, "Rotor Faults Analysis of Induction Motors by Dynamic Model and Finite Element Method," in *Rotor Faults Analysis of Induction Motors by Dynamic Model and Finite Element Method*, 1995: KTH Mechanics, Royal Institute of Technology.
- [163] Y. Liao and T. A. Lipo, "Effect of saturation third harmonic on the performance of squirrel-cage induction machines," *Electric machines and power systems*, vol. 22, no. 2, pp. 155-171, 1994.
- [164] E. Ritchie, X. Deng, S. Palko, and T. Jokinen, "Rotor fault analysis of induction motors by dynamic model and finite element method," in *Stockholm Power Tech. Conf.*, 1995, pp. 368-372.
- [165] P. Vas, "Induction motors with unbalanced rotor," *Periodica Polytechnica Electrical Engineering*, vol. 20, no. 2, pp. 119-128, 1976.
- [166] S. Murthy, H. Rai, and A. Tandon, "A novel self-excited self-regulated single phase induction generator. II. Experimental investigation," *IEEE transactions on energy conversion*, vol. 8, no. 3, pp. 383-388, 1993.
- [167] B. Wu, W. Sun, Z. Li, and Z. Li, "Circular whirling and stability due to unbalanced magnetic pull and eccentric force," *Journal of Sound and vibration*, vol. 330, no. 21, pp. 4949-4954, 2011.
- [168] A. Di Gerlando, G. M. Foglia, and R. Perini, "Analytical modelling of unbalanced magnetic pull in isotropic electrical machines," in *Electrical Machines, 2008. ICEM 2008. 18th International Conference on*, 2008, pp. 1-6: IEEE.
- [169] R. Belmans, A. Vandenput, and W. Geysen, "Influence of unbalanced magnetic pull on the radial stability of flexible-shaft induction machines," in *IEE Proceedings B (Electric Power Applications)*, 1987, vol. 134, no. 2, pp. 101-109: IET.
- [170] D. G. Dorrell, "Calculation of unbalanced magnetic pull in small cage induction motors with skewed rotors and dynamic rotor eccentricity," *IEEE transactions on energy conversion*, vol. 11, no. 3, pp. 483-488, 1996.
- [171] D. Aguglia, P. Viarouge, R. Wamkeue, and J. Cros, "Selection of gearbox ratio and power converters ratings for wind turbines equipped with doubly-fed induction generators," in *Electric Machines & Drives Conference, 2007. IEMDC'07. IEEE International*, 2007, vol. 1, pp. 447-452: IEEE.
- [172] B.-T. Kim, B.-I. Kwon, and S.-C. Park, "Reduction of electromagnetic force harmonics in asynchronous traction motor by adapting the rotor slot number," *Magnetics, IEEE Transactions on*, vol. 35, no. 5, pp. 3742-3744, 1999.
- [173] D. Guo, F. Chu, and D. Chen, "The unbalanced magnetic pull and its effects on vibration in a three-phase generator with eccentric rotor," *Journal of Sound and vibration*, vol. 254, no. 2, pp. 297-312, 2002.
- [174] J. Pyrhonen, T. Jokinen, and V. Hrabovcova, *Design of rotating electrical machines*. John Wiley & Sons, 2013.